UNIVERSITAT DE BARCELONA

Strategies to synthesize carbon-supported elctrocatalysts with reduced Pt content and increased activity for use in low temperature fuel cells

Júlia Garcia Cardona

Document signat digitalment per: Julia Garcia Cardona

Document signat digitalment per: Julia Garcia Cardona

UNIVERSITAT DE BARCELONA

Programa de Doctorat en
Electroquímica. Ciència i Tecnologia

STRATEGIES TO SYNTHESIZE CARBON-SUPPORTED ELECTROCATALYSTS WITH REDUCED Pt CONTENT AND INCREASED ACTIVITY FOR USE IN LOW-TEMPERATURE FUEL CELLS

Memòria presentada per optar al

Grau de Doctor per la Universitat de Barcelona

Julia Garcia Cardona

Directors

Dr. Pere L. Cabot Julià
Professor Catedràtic

Dr. Ignacio Sirés Sadornil
Professor Agregat

Tutor Acadèmic

Dr. Pere L. Cabot Julià
Professor Catedràtic

Barcelona, Setembre de 2023

Document signat digitalment per: Julia Garcia Cardona

UNIVERSITAT DE BARCELONA

Facultat de Química

Departament de Ciència de Materials i Química Física

Secció de Química Física

STRATEGIES TO SYNTHESIZE CARBON-SUPPORTED ELECTROCATALYSTS WITH REDUCED Pt CONTENT AND INCREASED ACTIVITY FOR USE IN LOW-TEMPERATURE FUEL CELLS

Julia Garcia Cardona

PhD Thesis

Laboratori d'Electroquímica dels Materials i del Medi Ambient (LEMMA)

Barcelona, Setembre de 2023

Document signat digitalment per: Julia Garcia Cardona

Acknowledgements

First, I want to thank my thesis supervisors, Prof. Pere L. Cabot and Prof. Ignacio Sirés, for their guidance and help throughout this long period. It has been a great experience to work and learn with you. I would also like to thank Prof. Enric Brillas and Dr. Francisco Alcaide for their helpful suggestions, and Prof. Elvira Gómez for her career advice and guidance when having doubts about this thesis.

All my colleagues at LEMMA group have been wonderful. I would like to give a special mention to Roger Oriol, with whom I've shared my ups and downs and who has been a great colleague and friend during these hard years.

My friends have also been an incredible support, especially when times were tough, and I would like to thank all of them for being there no matter what. From my school friends, (Judit, Maria and Marc) to my university classmates, both from chemistry degree (Anna and Ruben) and computer engineering degree (Lobitos), with whom we've created an incredible group of friends.

My aunts, Olga and Àngels, my uncle, Fede, and my cousin, Marina, have been an incredible support and have helped me to disconnect from work, enjoying the holidays all together. To my dad, I would like to thank him for sharing tips and listening to my issues, since he had experienced similar problems while doing his thesis. My mum has always been in my thoughts and heart these years.

Finally, I would like to thank my husband, Iago, for his love and support. These years have been challenging for both of us and our careers, but we've also had time to create an incredible family with our son, Àlex.

I'm sure I'm missing someone to thank, so thank you all who have been there for me.

Document signat digitalment per: Julia Garcia Cardona

ABSTRACT

Conventional catalysts for polymer electrolyte fuel cells are based on Pt supported on porous carbons, generally carbon blacks. However, Pt is expensive and scarce and is poisoned by CO, which is present in the hydrogen obtained by reforming natural gas and it is also generated as an intermediate in the oxidation of methanol. In addition, carbon blacks have some drawbacks, such as their microporosity, impurities, and low electrochemical and thermal stability. In this thesis, nanoparticle catalysts with a core-shell structure have been synthesised and characterised, with the Ni or Cu core and the Pt shell supported on advanced carbons, in order to reduce the amount of Pt used and increase its catalytic activity against the reduction of oxygen and the oxidation of methanol and CO, as well as its stability. Different procedures have been used to synthesize the catalysts, with initial deposition of Ni or Cu nanoparticles by chemical reduction on different carbons and subsequent galvanic exchange with Pt. The catalysts have been characterised by transmission electron microscopy, X-ray photoelectron spectroscopy, voltammetry cyclic and linear scanning voltammetry on rotating disk electrode. The results of the structural and electrochemical analyses, supported by computational calculations of model atomic clusters, are consistent with the formation of nanoparticles with a diameter of 2-5 nm, a nucleus enriched with Ni or Cu and an essentially Pt shell. They presented greater tolerance to CO than the commercial Pt/C, due to the electronic effect of the metallic nucleus on the Pt, which enhanced the desorption of CO. The calculation of the CO adsorption energies on different active centres showed that the presence of surface defects could affect the CO tolerance of the catalysts, which could be critical for nanoparticles that are too small, as observed experimentally.

In the case of PtNi, the two anodic peaks observed in the oxidation of CO suggest the presence of two distinct structural domains on the catalyst surface, probably Pt in Ni-rich hexagonal domains and in Pt-rich cubic domains, without forming a solid solution between Ni and Pt. Its activity against methanol oxidation is also greater than that of Pt/C due to the ligand effect of Ni on Pt, which also increases with the incorporation of Ru species due to its bifunctional effect. Contrary to the case of PtNi, a solid solution of Cu is formed in Pt, attributable to its compatibility of size and crystallization system, cubic (hexagonal in the case of Ni). Also, in the case of PtCu, better catalytic activity is

observed against the oxidation of methanol than for commercial Pt/C, due to the geometric and ligand effects of Cu on Pt. This makes them interesting for the reduction of oxygen in the cathodes of direct methanol fuel cells, since it decreases the negative effect of methanol transport through the membrane.

The dispersion of PtCu nanoparticles on commercial carbon nanofibers and nanotubes, as well as commercial and synthetic mesoporous carbons, also leads to catalysts that are more tolerant to CO than commercial Pt/C, due to the electronic effects of Cu on Pt discussed above. Better activities for oxygen reduction than on commercial Pt/C, both mass and specific, are achieved on various supports, while its relative stability is increased with respect to the latter. Mesoporous carbon supports synthesised from chitosan are of special interest, since chitosan is an abundant, non-toxic, nitrogen-rich natural polysaccharide present in crustacean shells. Also taking into account that P20 silicon oxide was used as a template in the synthesis procedure, the mesoporous carbon obtained was low cost and of great added value. Adjusting the microporosity-mesoporosity ratio of the carbons through different synthetic procedures, specific activities against oxygen reduction and methanol oxidation were obtained with mesoporous carbons derived from chitosan, greater than those of Pt/C and that of PtCu catalysts supported on commercial mesoporous carbons.

LIST OF ACRONYMS

AFC	Alkaline fuel cell
CB	Carbon black
CHP	Combined heat and power
CNF	Carbon nanofiber
CNT	Carbon nanotube
CV	Cyclic voltammetry
CVD	Chemical vapor deposition
DFT	Density functional theory
DMFC	Direct methanol fuel cell
DOMC	Disordered mesoporous carbon
ECSA	Electrochemical surface area
EDS	Energy dispersive spectroscopy
EDTA	Ethylenediaminetetraacetic acid
FC	Fuel cell
FWHM	Full width at half maximum
GC	Glassy carbon
GDE	Gas diffusion electrode
GDL	Gas diffusion layer
GNF	Graphitic carbon nanofiber
HER	Hydrogen evolution reaction
HOMO	Highest occupied molecular orbital
HOR	Hydrogen oxidation reaction

LUMO	Lowest unoccupied molecular orbital
LSV	Linear sweep voltammetry
MC	Mesoporous carbon
MCFC	Molten carbonate fuel cell
MEA	Membrane electrode assembly
MOR	Methanol oxidation reaction
MWCNT	Multi-walled carbon nanotube
NMC	N-doped mesoporous carbon
OMC	Ordered mesoporous carbon
OMS	Ordered mesoporous silica
ORR	Oxygen reduction reaction
PAFC	Phosphoric acid fuel cell
PEFC	Polymer electrolyte fuel cell
PEM	Proton exchange membrane
PEMFC	Proton exchange membrane fuel cell
PFSA	Perfluorosulfonic acid
PTFE	Polytetrafluoroethylene
PVP	Polyvinylpyrrolidone
RDE	Rotating disc electrode
RHE	Reversible hydrogen electrode
SEM	Scanning electron microscopy
SRM	Steam reforming of methane
SOFC	Solid oxide fuel cell

STEM	Scanning transmission electron microscopy
TEM	Transmission electron microscopy
XPS	X-ray photoelectron spectroscopy
XRD	X-ray diffraction

Document signat digitalment per: Julia Garcia Cardona

TABLE OF CONTENTS

1. Introduction 1
   1.1. Fuel cells 2
      1.1.1. Origin 2
      1.1.2. Concept 3
      1.1.3. Classification 4
   1.2. Proton exchange membrane fuel cells 6
      1.2.1. PEMFC components 7
      1.2.2. PEMFCs applications 9
   1.3. Direct methanol fuel cells 10
   1.4. Fuel cell thermodynamics 11
   1.5. Fuel cell kinetics 13
   1.6. Hydrogen oxidation reaction 15
      1.6.1. Pt-based catalysts for H_2 oxidation 16
      1.6.2. H_2 oxidation in presence of CO 18
   1.7. Methanol oxidation reaction 18
   1.8. Oxygen reduction reaction 20
   1.9. Latest trends in PEMFCs 23
      1.9.1. Catalyst supports 23
      1.9.2. Core-shell catalysts for PEMFCs 28
      1.9.2.1. PtCu catalysts 30
      1.9.2.2. PtNi catalysts 30
2. Objectives 33
3. Experimental section 35
   3.1. Materials and Reagents 35
   3.2. Carbon support 35
      3.2.1. Carbon activation 36
      3.2.2. Carbon from chitosan 36
   3.3. Synthesis of PtCu catalysts 36
      3.3.1. Synthesis A 37
      3.3.2. Synthesis B 37

3.3.3. Synthesis C 38
3.3.4. Galvanic replacement 38
3.4. Synthesis of PtNi catalysts 39
3.5. Structural characterization 39
3.5.1. X-ray diffraction 39
3.5.2. Transmission electron microscopy 40
3.5.3. X-ray photoelectron spectroscopy 42
3.6. Electrochemical characterization 43
3.6.1. Working electrode preparation 44
3.6.2. Cyclic voltammetry 44
3.6.3. Linear sweep voltammetry 47
3.6.4. Accelerated degradation tests 48
4. Results and discussion 51
4.1. Catalysts supported on carbon blacks 51
4.1.1. Synthesis and Evaluation of PtNi Electrocatalysts for CO and Methanol Oxidation in Low Temperature Fuel Cells 51
4.1.2. Nanostructuring Determines Poisoning: Tailoring CO Adsorption on PtCu Bimetallic Nanoparticles 75
4.2. Electrochemical Performance of Carbon-Supported Pt(Cu) Electrocatalysts for Low-Temperature Fuel Cells 97
4.3. PtCu supported on mesoporous carbons 111
4.3.1. Testing PtCu Nanoparticles Supported on Highly Ordered Mesoporous Carbons CMK3 and CMK8 as Catalysts for Low-Temperature Fuel Cells 111
4.3.2. On the Viability of Chitosan-Derived Mesoporous Carbons as Supports for PtCu Electrocatalysts in PEMFC 137
5. Conclusions 159
6. References 163
Publications and Meetings 179

1. Introduction

The current energy crisis can be explained by the sum of different factors. First, the unceasing increase of the world population experienced in the last decades, with an annual growth rate of 1-2 % [1], has boosted the demand of energy and material resources. At present, such rise in energy needs is still mostly fulfilled by employing fossil fuels, which are considered as non-renewable energy sources. In addition, their use as fuels and the consequent contamination is thought to be intimately linked to global warming, owing to the emission of greenhouse gases, and they also become a menace to human health due to hazardous pollutant emissions. Therefore, there is an urgent need to change the current energy supply scheme, replacing the finite non-renewable energy sources by greener and more sustainable alternatives, eventually decreasing the emission of noxious substances but still fulfilling the current and future energy demand [2].

The main drawbacks of the most widely used renewable energy sources (i.e., solar energy, wind or hydraulic energy) are the long distance from production plants to the places where energy may be needed, thus posing the problem of energy transport, and the discontinuous production of energy, being highly dependent on weather conditions.

Taking into account that a large percentage of emissions, in particular CO_2, is directly linked to transport based on combustion engines, electric vehicles moved by H_2 appear as a greener alternative. Although hydrogen-based energy economy is, at the moment, costly and at its infancy, technological progress can play in its favour when clean and reliable energy supply is required with massive energy storage. Furthermore, hydrogen can be employed as a vector to store intermittent renewable energy, which means that it is a substance that facilitates the transportation and storage of energy, offering the possibility of usage in a future time and/or distant space from the primary production site [3].

Fuel cells fed with hydrogen have received an increasing interest as an alternative green energy source in recent years, because of their near zero carbon emission, their higher efficiency as compared to other energy sources, since they are not limited by the second law of thermodynamics, and the unlimited source of reactants, since H_2 and O_2 can be readily obtained via water splitting. Among their multiple applications, they can be used

to produce electrical energy on a large scale for heating systems in buildings, transport, and on a smaller scale for electronic devices (e.g., computers, mobile phones). Consequently, in the last years there has been considerable research in this field, with focus on different aspects such as production, storage and transport of hydrogen, which includes new sources of hydrogen, catalytic materials and procedures [4].

1.1. Fuel cells

1.1.1. Origin

The origins of fuel cells (FCs) can be set more than 200 years ago. In 1801, the research led by Humphry Davy, a British chemist, on electrolysis using the voltaic cell to split up common compounds brought the discovery of several new metals, such as sodium or potassium. This laid the scientific foundations for the FCs as we know them nowadays, which were designed by Christian Friedrich Schönbein, a German-Swiss chemist, in 1838. At the same time, William Grove really invented the technology, when he discovered that electricity could be produced using hydrogen and oxygen, proving that the electrolysis of water was reversible. The experiment was performed with four cells, each one consisting of two inverted tubes, one with hydrogen and the other with oxygen, immersed in dilute sulfuric acid and using platinum wires as the electrodes. Using the current generated by this system, Grove was able to electrolyse the water in a fifth cell, generating hydrogen and oxygen. Although he was not the first to publish about this phenomenon, Grove proclaimed himself the discoverer of this technology, which he called “gaseous voltaic battery” [5].

The term “fuel cell” was not introduced until fifty years later, in 1889, by Charles Mond and Ludwig Langer, whose research focused on FCs using coal gas as a fuel. From 1920, the gas diffusion electrode (GDE) began to be used for low temperature operation. Schmid was the first to introduce a tubular electrode made of carbon catalysed with platinum, tubular, which together with an air electrode of similar design has been introduced into operational FCs. However, the FC technology remained obscure until 1932, when Francis Bacon modified the equipment of Mond and Langer to develop the first fuel cell (with alkaline electrolyte), but it was only in 1959 that he was able to demonstrate a practical 5 kW fuel cell system.

Between the late 50s and 60s, the FCs were developed and used in space missions of NASA (Gemini space program), and the research work started to focus on the development of FCs for stationary power supply and transport. Meanwhile, in the Soviet Union, the FCs were being developed for military applications.

1.1.2. Concept

Fuel cells can be defined as electrochemical devices that continuously convert chemical energy stored in fuels such as hydrogen, methanol or ethanol into electrical energy through their indirect combustion by an oxidant (usually O_2), being the fuel and oxidant continuously fed to the cell. They share some characteristics with batteries since both produce electrical energy through electrochemical reactions between fuels and oxidants. In the fuel cell, the whole reaction is split into two half reactions, where the fuel is oxidized at the anode, generating electrons that are transported through an external circuit to the cathode, at which oxygen reduction takes place. A separator, in most cases acting as the electrolyte, is placed between the electrodes to permit the flow of ions between the anode and cathode. The recombination of the ions with the oxidant takes place at the cathode, thus depleting the oxidant and yielding pure water.

In most of the fuel cells, the half reactions occurring at the anode and cathode are the hydrogen oxidation reaction (HOR, reaction (1)) and the oxygen reduction reaction (ORR, reaction (2)), respectively, giving rise to the overall reaction (3), as follows:

Anodic: $H_2 \rightleftharpoons 2H^+ + 2e^-$ (1)

Cathodic: $½\ O_2 + 2H^+ + 2e^- \rightleftharpoons H_2O$ (2)

Overall: $H_2 + ½\ O_2 \rightleftharpoons H_2O$ + electricity + heat (3)

The main difference between FCs and the other batteries is that the latter ones can produce a limited amount of energy that is determined by the amount of chemical reagents that are stored in the device, whereas FCs can produce energy in a continuous manner as far as fuel and oxygen are supplied to the electrodes. On the other hand, FCs produce electrical energy with higher efficiencies than any conventional thermo-mechanical system, which means that a greater amount of energy is obtained using a given amount of fuel [6].

A very promising feature of FCs is that they are not limited by the Carnot cycle efficiency, which is a common drawback in the direct combustion of fuel. Using FCs, the efficiency can be greater than 80%. Moreover, the fuel cell releases a lower amount of pollutants as compared to an internal combustion engine, and this release can be actually reduced to zero when H_2 is used as the fuel. Other advantages are that they do not have moving parts, therefore being silent, and present higher mechanical robustness, and can be modular, meaning they can be stacked to produce a wide variety of power requirements, from hundreds to millions of watts [7].

1.1.3. Classification

Fuel cells can be classified according to the type of fuel, operation temperature, electrolyte type, reagents and their application. Depending on the electrolyte used, fuel cells can be classified in five major types: Alkaline fuel cells (AFCs), polymer electrolyte fuel cells (PEFCs) and phosphoric acid fuel cells (PAFCs), which are the ones operating at low temperatures; in addition, there are molten carbonate fuel cells (MCFCs) and solid oxide fuel cells (SOFCs), which operate at high temperatures. The electrolytes can be of three types: aqueous, molten or solid. AFCs use an alkaline electrolyte and pure hydrogen and oxygen as reactants. PEFCs use a hydrated acidic polymer membrane as the electrolyte, platinum-catalysed electrodes and mainly hydrogen or methanol as fuels. When H_2 is used, we refer normally to proton exchange membrane fuel cells (PEMFCs) and in the case of using methanol as the fuel, as direct methanol fuel cells (DMFCs). PAFCs use an anode and a cathode made of a finely dispersed platinum catalyst on carbon and a silicon carbide structure that holds the concentrated phosphoric acid electrolyte. MCFCs use a molten carbonate salt embedding a porous ceramic matrix as the electrolyte and a coal-derived gas, methane or natural gas as fuels. SOFC use a solid ceramic electrolyte. More information of the different types of fuel cells is summarized in Table 1 [8].

Aqueous electrolytes are generally used at low and intermediate temperatures. Molten electrolytes are typically used at high temperatures and only occasionally at intermediate ones. Finally, the solid electrolytes, such as oxide mixtures, are used at very high temperatures. For the low temperature fuel cells (AFCs, PEFCs and PAFCs), which

operate to 250 ºC, noble metals are required as electrocatalysts, since in these conditions the reaction kinetics are rather slow.

Table 1. Fuel cell types (adapted from [8]).

Parameter	**Type of FC**				
	AFC	**PEFC**	**PAFC**	**MCFC**	**SOFC**
Electrolyte	KOH/NaOH	Polymeric membrane	H_3PO_4	Li_2CO_3 K_2CO_3	Ceramic Solid oxide ZrO_2 with Y_2O_3
Fuel	H_2	H_2, CH_3OH and other liquid alcohols	Hydrocarbons	Hydrocarbons	Hydrocarbons
Oxidant	O_2 / air	O_2 / air	O_2	CO_2 / O_2 / air	O_2 / air
Electrode	Metal or Pt supported on carbon	Pt supported on carbon	Pt supported on carbon	Ni + Cr	Ni / Y_2O_3 / ZrO_2
Operating temperature (ºC)	50-200	50-110	150-210	600-800	500-1000
Power (kW)	10-100	0.01-1000	100-5000	1000-100000	100-100000
Efficiency (%)	60	60	55	55-65	60-65
Applications	*Transportation: -Fleet vehicles -Boats -Space shuttles	*Transportation *Power supplies *Portable equipment	*Combined heat and power (CHP) *Stationary power supplies	*CHP *Stationary power supplies	*CHP *Large-scale stationary power

Among the many kinds of fuel cells, PEMFCs are considered the most promising fuel cell technology for transport applications since they present suitable properties such as their low operating temperature, quick start-up capability, light mass, low noise, high efficiency and nearly zero emissions. They operate under 90 ºC because of the use of a hydrated proton-exchange polymer membrane, which could be dried at higher temperatures. They can run with different fuels apart from hydrogen, such as methanol,

ethanol and formic acid. However, hydrogen is at the top of the investigations due to its high energy density and because water is the only oxidation product.

1.2. Proton exchange membrane fuel cells

Fig. 1 shows the different elements that compose a PEMFC. An elementary unit (cell) is composed of an electrolyte membrane, two catalysed electrodes (anode and cathode), bipolar plates and gas diffusion layers. The polymeric membrane is known as proton exchange membrane (PEM) since it is made of a proton conducting polymer that is impermeable to gas. The most used is Nafion®, which is an excellent proton conductor with conductivity similar to that of sulphuric acid and keeps gas crossover and electron short circuit to a minimum. The use of this membrane is limited to around 80 ºC to avoid dehydration [9,10].

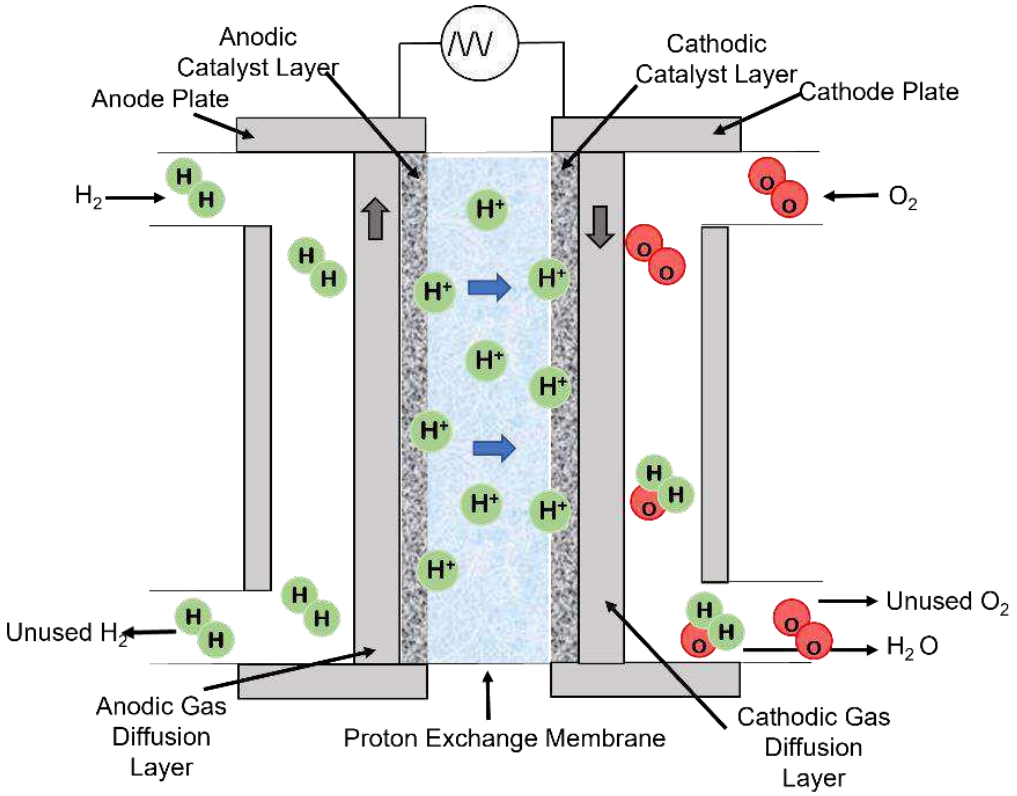

Figure 1. Proton exchange membrane fuel cell scheme.

The PEMFC starts its operation when hydrogen is supplied to the anode and oxygen to the cathode, where both gases enter through the channels of the bipolar plates of their respective electrodes and there, they are distributed along their entire surface through the

gas diffusion layers. Once the reactants have passed through the diffusion layer, they meet the catalyst layer, which is placed between the gas diffusion layer and the electrolyte. The hydrogen molecule is transformed into protons and electrons on the anode catalyst, while protons from the electrolyte react with the oxygen and electrons from the outer electric circuit on the cathode catalyst to yield water.

The most suitable catalyst for PEMFCs is Pt, as both reactions, hydrogen oxidation and oxygen reduction, which take place on the metal surface present faster kinetics compared to other metal catalysts. Therefore, the electrodes of the PEMFCs are Pt-based but, aiming to diminish the amount of Pt, the electrodes are made of Pt nanoparticles supported on porous carbonaceous materials with high specific area. This results in a high dispersion and narrow distribution of the nanoparticles, which is a requisite for a high catalytic performance of the catalysts. The most widely used carbon support is Vulcan XC-72, which is carbon black obtained by pyrolysis, because of its availability, conductivity, and low cost [7].

The electrodes are very expensive PEMFC components due to the use of Pt-based catalysts. In recent years, attempts have been made to reduce the amount of Pt needed for the operation. It is expected that in the near future these quantities can be decreased in order to reduce the overall cost of PEMFCs and make them viable for large-scale applications.

1.2.1. PEMFC components

1.2.1.1. Polymer electrolyte membrane

The membrane of a PEMFC must meet a series of characteristics. Among them, it must show a high proton conductivity, non-permeability to reagents flow, and mechanical and chemical stability during its operation. The polymeric material used for the membranes is based on derivatives of perfluorosulfonic acid (PFSA), a copolymer resulting from the combination of polytetrafluoroethylene (PTFE) and various perfluorosulfonated chains that contain sulfonic groups, which are responsible for ionic conduction. The most known and used is the Nafion® membrane, which is the commercial name of perfluorosulfonylfluoro-ethyl-propyl-vinyl ether manufactured by Dupont [11].

The proton conductivity of the membrane strongly depends on its water content and temperature. The degree of hydration of the polymer is affected by several factors such as the generation of water in the cathode, the electroosmotic transport of protons and that of the water molecules due to a concentration gradient.

Another aspect to consider is that the impermeability of the polymeric membrane against the transport of reactants is not complete, because the reactants are somewhat soluble in water, a phenomenon known as crossover [12], which produce a reduction of the output voltage of the PEMFC.

1.2.1.2. Catalytic layer

The active region of the PEMFC is the catalytic layer, in which the electrocatalyst is arranged, and on the surface of which the electron transfer takes place. The structure of the electrocatalyst and its mode of incorporation in the catalytic layer is of vital importance since the confluence in the reaction zone of the species involved and the exposure of the maximum electrode surface must be guaranteed.

The development of electrocatalysts based on metal particles, usually Pt supported on carbon, allows the metal load in the reaction zone to be reduced. The structure of a generic Pt/C electrocatalyst consists of Pt nanoparticles with an average size of 2 to 4 nm, which are distributed quite homogeneously on carbons with a high specific area and mesoporous structure. The most used carbonaceous substrates are carbon blacks, especially Vulcan XC-72. Carbon blacks are made up of almost spherical particles, 30-50 nm and with specific areas of about 250 $m^2\ g^{-1}$. In PEMFCs, the carbon support present in the cathode is subject to degradation, losing part of the carbon by an electrochemical oxidation mechanism. Consequently, the carbon support loses part of its structure and supporting properties. In the anode, when operating with pure hydrogen, the catalyst is relatively stable, but it is poisoned by sulphur and CO that originate from the fuel. The lower the operation temperature, the more severe is the poisoning effect. Different strategies have been proposed in order to solve these problems that will be discussed later [13].

The combination of the anodic and cathodic catalytic layers with the polymeric membrane is known as the membrane electrode assembly (MEA). It is possible to deposit the

catalytic layer on the porous electrode or directly on the polymeric membrane, by compression at high temperature to obtain an optimal assembly.

1.2.1.3. Gas diffusion layer

A GDE consists of the combination of the catalytic layer with the gas diffusion layer (GDL). The GDL must have a porous structure that enables the transport of reagents towards the catalytic layer and the removal of water produced in the cathode, as well as both electrical and thermal conductivity, and it is responsible for providing the MEA with sufficient mechanical stability [14].

A GDL is made up of carbonaceous materials such as carbon paper or carbon fibre fabric. To avoid flooding of the electrode compartments, it is necessary to provide the material with a certain hydrophobicity, so it is usual to incorporate a layer composed of PTFE and carbon black with a microporous structure between the catalytic layer and the diffusion layer [15].

1.2.2. PEMFCs applications

Considering the power that a PEMFC stack can generate (see Table 1), its application will be determined by its power, being the low power PEMFCs useful for mobile phones, personal computers and small electronic devices, while those with higher power can be used in the automotive industry, as auxiliary and stationary energy or in military applications [16].

The automotive sector constitutes one of the most promising field for application of PEMFC stacks, owing to their high efficiency as well as their environmental friendliness. Although the hydrogen necessary for the PEMFC operation is more expensive than the fuel used in conventional vehicles, the efficiency achieved is much greater, which results in a similar cost per km [17]. In addition, if PEMFC technology is compared with that of battery-based electric vehicles, there are also great differences, because long recharging times are not necessary, just the time needed to refuel, and they have a higher energy density than conventional batteries. As a result, they have greater autonomy.

Although stationary applications are often overshadowed by those in the automotive sector, the development carried out in the field of PEMFCs to generate stationary energy is satisfactory, since cheaper components can be used, the storage and supply of fuel is

simpler, and the dimension and weight are not critical parameters for these applications [18]. The most common application in this field is as part of the electrical supply and as an emergency generator.

The power density generated by PEMFCs positions them as a great competitor to the conventional batteries with which today, for example, mobile phones, portable computers, or music devices work. The main drawback to overcome in this field is how to store hydrogen in such a small device, since weight and size are important for these applications [19].

1.3. Direct methanol fuel cells

Considering fuel cells for their application as energy supply in portable devices, the DMFC is a primary topic of fuel cell research, as this type of FC has the appropriate characteristics for portable devices. DMFCs represent a promising source of energy that is readily applicable to modern life and can create a better environment for mankind. The DMFC technology is relatively new when compared to other fuel cells [20]. DMFCs market for notebook computers, mobile phones and other portable electronic devices is expected to grow significantly. They are expected to work in combination with thin film batteries, in order to create hybrid power systems, where fuel cells are useful for charging the thin film batteries.

They are similar to PEMFCs, since DMFCs use a polymer electrolyte. However, the latter use liquid methanol, diluted in water to 1.0-2.0 M, as fuel instead of hydrogen. During operation, methanol draws hydrogen without the need of an external reformer [21]. At the cathode, the protons supplied from the anode participate in the reduction of O_2 to water.

Normally a single DMFC can supply only 0.3–0.5 V, so it is mainly used to replace the batteries for cameras, notebook computers and other portable electronic applications in the range from 1 W to 1 kW [22]. One of the main advantages of DMFCs is that the anode catalyst itself draws the hydrogen from the methanol and reduces the overall cost due to the absence of a reformer. Their characteristics are similar to those of the PEMFC. However, its performance is limited by two important factors: crossover of methanol from

the anode to the cathode, which lowers the system efficiency, and the slow kinetics of the electrochemical oxidation of methanol at the anode.

The effect known as crossover is produced since, even though the electrolyte membrane should be "impermeable" to reagents, some of them get through it. Also, the fuel used has an enormous tendency to filter, so it also tends to cross the polymeric membrane. Thus, fuel molecules can pass through the Nafion® membrane and reach the cathode, where they would react without producing any electrical current [23]. The most immediate consequence is that the open circuit battery voltage is lower than expected, meaning that fuel is consumed without producing electricity.

1.4. Fuel cell thermodynamics

Thermodynamics is the key to understand the energy conversion processes. Traditionally, electrical energy is obtained by means of thermal energy produced by combustion and then converted to mechanical energy, which is a low efficiency process (ideally about 40% in internal combustion engines) and there is no solution to obtain a higher efficiency value because of the limitations posed by the thermodynamic laws. In fuel cells, however, since electrical energy is obtained from the chemical energy stored in fuels, the energy conversion is not limited by the Carnot cycle and therefore, the efficiency can be enhanced even over 70%. In fuel cells, when they are operated under thermodynamically reversible conditions, the maximum possible electrical energy output and the corresponding electrical potential difference between the cathode and the anode are achieved, although some of the energy is inevitably dissipated as heat [24].

The knowledge of the fuel cell thermodynamics is necessary to understand its performance by changing the different variables such as temperature, electrolyte concentration and gas pressure. These changes can affect and determine the properties of fuel cells when they are put into operation. The thermodynamic laws that must be used when studying the performance of the fuel cell are based on the conversion of chemical energy into electrical energy by means of electrochemical reactions.

In a PEMFC fed with H_2 and O_2, the overall electrochemical reaction (4) occurring at the fuel cell is a result of the anodic reaction that takes place in the anode, where hydrogen is transformed into protons and electrons (reaction (1)); once formed, the protons migrate

through the polymeric membrane to the cathode, while electrons are transferred to the cathode through the external electrical circuit, where they are combined with oxygen to produce water (reaction (2)).

$$H_2 + ½\ O_2 \rightarrow H_2O + \mathrm{W} + \mathrm{Q} \quad (4)$$

The term W in reaction (4) is the electrical work done by the system, while the Q is the heat transferred to the surroundings at constant temperature and pressure.

The electrical work can be described according to Eq. (5), where E is the ideal cell voltage, and I is the current generated by the electrons transferred from the anode to the cathode.

$$W = -E \cdot I \cdot \Delta t \quad (5)$$

The amount of electricity produced when the reaction takes place, which in Eq. (5) is expressed as $I{\cdot}\Delta t$, can be given by $n{\cdot}F$, where n are the mols of electrons transferred, and F is the Faraday constant, 96487 C. Therefore, the maximum electrical work, which is also the Gibbs free energy change, can be calculated as:

$$W = \Delta G = -n \cdot F \cdot E_{cell} \quad (6)$$

The Gibbs free energy change can also be given by Eq. (7), where ΔH is the enthalpy change, which is the total thermal energy available, and ΔS is the entropy change. In PEMFCs, where hydrogen is oxidized, the entropy change is negative, thus generating heat.

$$\Delta G = \Delta \mathrm{H} - \mathrm{T} \cdot \Delta S \quad (7)$$

For the overall cell reaction (4), the standard Gibbs free energy change is given by:

$$\Delta G° = G°_{H_2O} - G°_{H_2} - \frac{1}{2}\ G°_{O_2} \quad (8)$$

The Gibbs energy change of the reaction (ΔG) can be expressed by Eq. (9), where $\Delta G°$ is the standard Gibbs energy change of the reaction and a_i is the activity of the species i.

$$\Delta G = \Delta G° + RT \ln \frac{a_{H_2O}}{a_{H_2} \cdot a_{O_2}^{1/2}} \quad (9)$$

Considering Eq. (9), if ΔG is substituted by E, the Nernst Eq. (10) is obtained, which provides a relationship between the standard potential (E^o) and the equilibrium potential (E) of the cell. Fuel cells generally operate at pressures low enough to approximate the activity to the partial pressure of the gases involved in the reaction.

$$E = E° - \frac{RT}{nF} \ln \frac{a_{H_2O}}{a_{H_2} \cdot a_{O_2}^{1/2}} \quad (10)$$

In PEMFCs, the cell potential can be increased when operating at higher reactant pressures, which improves the fuel cell performance for a given temperature [25].

1.5. Fuel cell kinetics

As detailed in the previous section, the equilibrium potential of the system is the theoretical maximum potential that can be achieved in the absence of current flow. It depends on the cell conditions (temperature, pressure and concentration of the species).

The working conditions of FCs are very far from their equilibrium potential. The actual cell voltage is decreased from its ideal value because of several types of irreversible losses, which are often referred to as polarization, overpotential or overvoltage (see Fig. 2) [25]. The overpotential is the difference between the actual potential of the system E, which is measured between the terminals of the battery when an electric current flows, and the equilibrium potential E_{eq}, which coincides with the open circuit potential (E_{ocp}) when the FC is reversible.

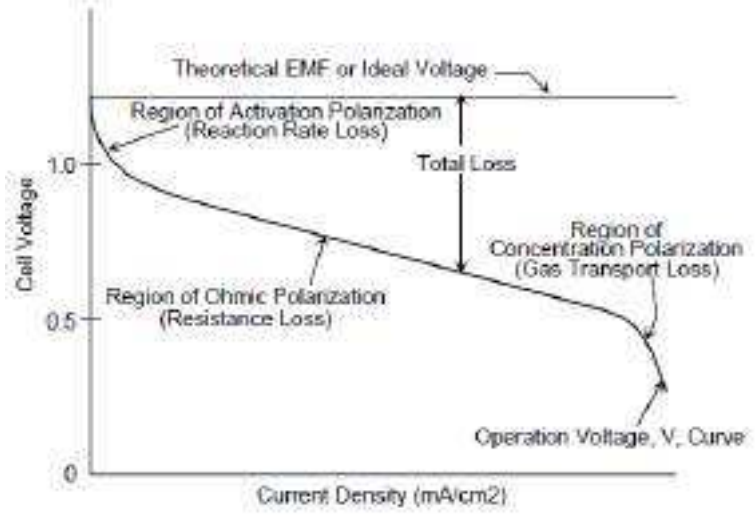

Figure 2. Ideal and actual fuel cell voltage/current profiles [25].

Fig. 2 represents the multiple factors that contribute to the FC polarization, which are activation, ohmic and mass-transport-related losses. The activation-related losses are due to the activation energy needed for the electrochemical reactions that take place at the electrodes, which means that they are related to the reaction rate and kinetics. These losses depend on the reactions, the electrocatalysts, both the materials used and the electrode microstructure, temperature and reactant activities. As can be seen in Fig. 2, this overpotential, known as activation overpotential, is dominant in the low current density region, which corresponds to the activation or kinetic zone [26]. It is expressed according to the Eq. (11), which is a form of the Tafel equation, where j is the current density, j_o the exchange current density, α the charge transfer coefficient, R the gas constant, b the Tafel slope and T the absolute temperature.

$$\eta_{act} = \frac{RT}{anF} \ln\left(\frac{j}{j_o}\right) = b \ln\left(\frac{j}{j_o}\right) \tag{11}$$

On the other hand, the ohmic losses are mainly caused by the ionic resistance of the electrolyte and the electronic resistance of the electrodes, current collectors and interconnectors, and contact resistances. These losses depend on the materials, geometry of the fuel cell stack and the temperature, and they are proportional to the current density. In the polarization curve (Fig. 2), the ohmic region is the linear region found in the intermediate values of current density, where there is a linear trend [27]. This overpotential is expressed according to Eq. (12), where R_i is the internal resistance of the system due to the electrolyte, active layer, electrodes and electrical connectors.

$$\eta_{ohm} = jR_i \tag{12}$$

The losses related to mass transport are the result of transport limitations of the reagents involved and depend strongly on the current density, reagents concentration and catalyst activity. They are originated by diffusion processes due to concentration gradients of reactants and products, electrode porosity and membrane permeability [26]. These phenomena are observed at high current densities in the fuel cell polarization curve (Fig. 2), since they are strongly affected by the reactant transport to the electrode surface. The overpotential related to these phenomena is known as concentration overpotential, Eq. (13), where j_L is the limiting current density. In order to reduce this overpotential, a higher

concentration of reactants can be set, as well as the decrease of electrode thickness and the use of catalysts with high surface area.

$$\eta_{act} = \frac{RT}{anF} \ln\left(1 - \frac{j}{j_L}\right) \quad (13)$$

1.6. Hydrogen oxidation reaction

The HOR is the fastest reaction that takes place in a PEMFC stack. The voltage drop in an $H_2|O_2$ fuel cell is generally due to the cathodic process, resulting from the slow kinetics of the oxygen reduction reaction. However, there are cases in which the voltage losses come from the anode.

The global anodic reaction in acidic medium is expressed according to reaction (1), and it takes place following adsorption and ionization steps. Adsorption on the catalyst sites can occur through reaction (14) (Tafel step) or reaction (15) (Heyrovsky step), depending on the catalyst activity [28]:

$$H_2 \rightarrow 2\ H_{ad} \quad (14)$$

$$H_2 \rightarrow H_{ad} + H^+ + e^- \quad (15)$$

Afterward, H_{ad} can be ionized through reaction (16) (Volmer step):

$$H_{ad} \rightarrow H^+ + e^- \quad (16)$$

the protons then migrating toward the membrane.

The adsorption of hydrogen on different metals such as Pt has been a very hot topic over the years. It has been shown that the hydrogen oxidation process in an acidic medium begins with the adsorption of the H_2 molecule on the electrode. By means of the cyclic voltammetry technique, it is possible to identify the hydrogen adsorptions that take place in the different crystallographic planes of the electrode surface [29].

However, the main problem for the anode it is not the HOR kinetics but the catalyst poisoning. The most common sources for obtaining hydrogen on a large scale are fossil fuels such as natural gas and crude oil, which contain impurities. Obtaining high purity hydrogen with high yields can be done by the electrolysis of aqueous solutions, but currently the large-scale cost of this process is very high [30]. The cheaper industrial

production of H_2 is mainly from fossil sources and therefore, it contains impurities. The most common is CO, which acts as a poison for the Pt catalyst in PEMFCs, since it adsorbs on the metal surface, thus blocking the active centres.

In the studies carried out with CO stripping, it is observed that the oxidation of CO on polycrystalline Pt does not start until reaching a potential of approximately 0.6 V vs. reversible hydrogen electrode (RHE), a value higher than the potential of the anode of a PEMFC and therefore, Pt becomes poisoned.

1.6.1. Pt-based catalysts for H_2 oxidation

For the H_2 oxidation in fuel cells, the process requires the presence of adsorbed H as intermediate to promote the subsequent electrochemical reaction, as shown in reactions (14)-(16) described above. The chemical and electronic state of adsorbed H affect both the mechanism and kinetics of the reaction, leading to a specific exchange current density and Tafel slope, which depend on the electrode material. Considering that in a reversible process the mechanism for the direct reaction is the same as that for the reverse one, the catalytic activity of different metals toward the H^+/H_2 couple can be studied considering the hydrogen evolution reaction (HER). The electroadsorption of H on metallic catalysts can occur both, in acidic and alkaline solutions, even in non-aqueous solutions where the H-containing acids dissolve.

When the H^+ ion (in the form of hydrated H_3O^+) meets the vicinity of the electrode, a charge-transfer takes place with the formation of electroadsorbed H according to the reverse of reaction (16), which can be written with more detail as reaction (17), where M represents an atom on the metal surface.

$$M + H^+ + e^- \rightarrow M - H_{ads} \quad (17)$$

Then, the H_{ads} species can undergo the subsequent reverse reactions (18) and (19), which come from reactions (15) and (14), respectively:

$$M - H_{ads} + H^+ + e^- \rightarrow M + H_2 \quad (18)$$

$$2\ M - H_{ads} \rightarrow M + H_2 \quad (19)$$

The electrochemical studies about the HER and the HOR reveal that two different types of adsorptions take place: (i) the under-potential deposition of H (H_{UPD}), and (ii) the over-

potential deposition of H (H_{OPD}). The H_{UPD} is a process that occurs only at specific noble metals, such as Pt, Rh, Pd and Ir, when the H adsorption takes place above the reversible potential of the HER [29].

It has been proven that the H_{UPD} often matches with anion adsorption, and it can only be observed in cyclic voltammetry measurements if the two processes do not occur at the same potential range, as it happens in diluted aqueous H_2SO_4 using Pt (111) as electrode (Fig. 3). The fact that the H_{UPD} and anion adsorption can take place at similar potentials points to analogous Gibbs energies of adsorption for the two processes.

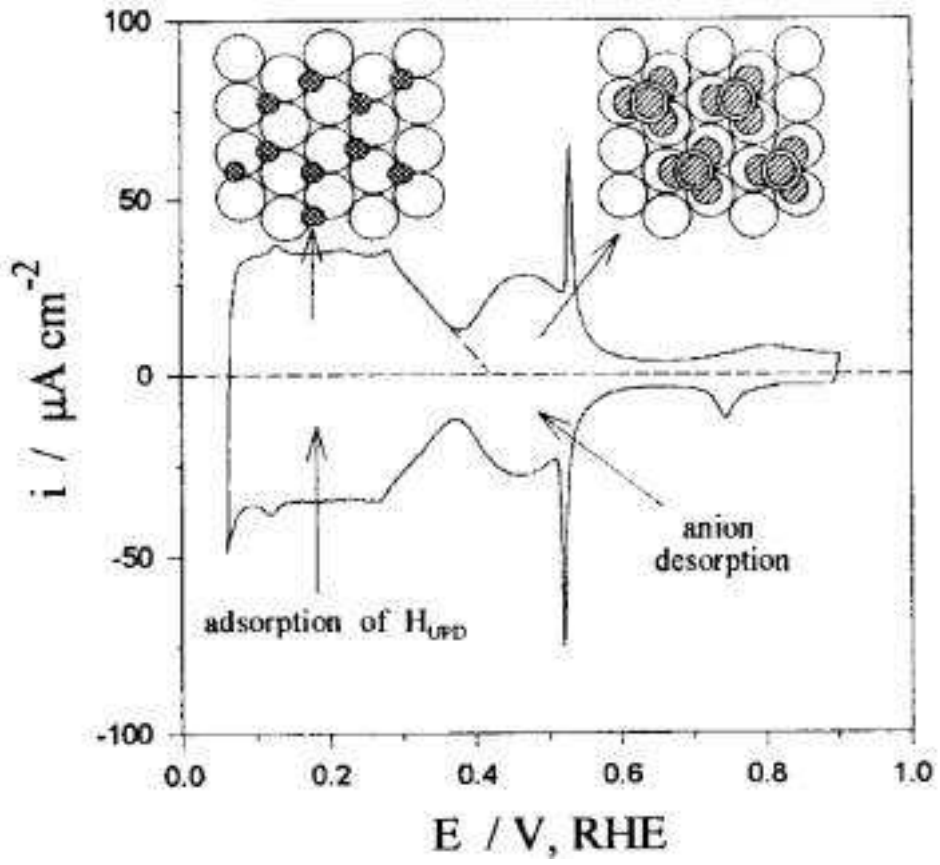

Figure 3. Cyclic voltammetry profile for Pt(111) in 0.05 M H_2SO_4 aqueous solution at 50 mV s^{-1} and 298 K, showing the regions of the H_{UPD} and anion adsorption with schematic representation of their structures [29].

Studies carried out on the reaction of hydrogen at the interface between Pt and the electrolyte, at different temperatures, have shown that in alkaline solutions the catalytic activity strongly depends on temperature, unlike in acidic solutions. From the exchange current density changes with temperature, it has been possible to determine the activation

energies, finding that the exchange current densities are markedly lower the higher the pH of the solution.

1.6.2. H_2 oxidation in presence of CO

When H_2 is produced by steam reforming of methane (SRM), a further CO removal is necessary, which can be both physical (adsorption at high pressures) or chemical (preferential catalytic oxidation of CO), since concentrations of about 10-50 ppm are obtained and its presence in H_2 used as a fuel in fuel cells interferes in the HOR. This interference is due to the adsorption of CO on metals, especially on Pt, since the active centres of the metal are blocked, producing the phenomenon known as catalyst poisoning. Therefore, it is very important to know the factors that influence this process in order to develop catalysts that are efficient for fuel cells [31].

CO adsorbs on all transition metals, forming a M-CO bond that occurs according to the donor-acceptor mechanism developed by Blyholder [32]. The model describes that the CO donates a pair of electrons from its highest occupied molecular orbital (HOMO) to the empty electron levels of the metal *d*-band, while the metal gives back electron density from the filled electron levels of its d-band to the lowest unoccupied molecular orbital (LUMO), which has an antibonding character. The transition elements of the periodic table can be divided according to the type of adsorption of the CO molecule, since the elements located to the right of Fe, Tc and W (including Pt) adsorb CO molecularly and those located to the left of these elements are adsorbed dissociatively. These two different ways of adsorbing CO occur because the stronger the M-C bond, the weaker the C-O bond, thus facilitating its dissociative adsorption.

1.7. Methanol oxidation reaction

Methanol oxidation reaction (MOR) is the reaction that occurs at the anode of a DMFC. This type of battery is very attractive since 6 electrons can be obtained for each molecule of methanol that is oxidized. Therefore, compared to the methanol as the fuel, it has the advantage of a high energy density. In addition, it can be safely transported and stored. Although it is an interesting reaction from the energetic point of view, its reaction mechanism is complex and the identification of intermediate species that are formed as well as the role of the catalyst in the reaction is still debated.

Under acidic conditions, the ideal process for the MOR is the fast oxidation of methanol to CO_2 on the electrode with six-electron transfer (26):

$$CH_3OH + H_2O \rightarrow CO_2 + 6H^+ + 6e^- \quad (20)$$

The reaction mechanism of methanol oxidation is in the focus of many studies, due to its complexity and its differences and similarities to the HOR on Pt when H_2 is contaminated with CO. In both cases there is the presence of CO molecules, which appear in the MOR as intermediate but the behaviour of Pt in each case is different, being an interesting area to investigate.

The ideal and most simple MOR reaction takes place according to the following stages: methanol adsorption (reaction (21)), dehydrogenation of carbon-containing intermediates (reactions (22)-(24)), and the generation of carbon dioxide (reaction (25)) [33]. The corresponding steps would be as follows:

$$CH_3OH \rightarrow CH_2OH_{ads} + H^+ + e^- \quad (21)$$

$$CH_2OH_{ads} \rightarrow CHOH_{ads} + H^+ + e^- \quad (22)$$

$$CHOH_{ads} \rightarrow COH_{ads} + H^+ + e^- \quad (23)$$

$$COH_{ads} \rightarrow CO_{ads} + H^+ + e^- \quad (24)$$

$$CO_{ads} + OH_{ads} \rightarrow CO_2 + H^+ + e^- \quad (25)$$

The occurrence of step (25) requires the adsorption of OH on Pt surface, as given by reaction (26):

$$H_2O \rightarrow OH_{ads} + H^+ + e^- \quad (26)$$

Once the methanol is absorbed on the platinum, reactions (20), (21) and (22) follow one another rapidly, while the oxidation kinetics of COH_{ads} is already slower and finally that of CO_{ads} oxidation, which is even more so, being the limiting step. Therefore, the intermediate products of the MOR such as CO_{ads}, cannot be avoided in the real process, which covers the active sites, reducing the catalyst performance and affecting the whole reaction.

The formation of CO_2 will be favoured at high temperatures as well as in electrodes with a high surface area. Even so, it must also be taken into account that factors such as methanol concentration, temperature and operation time influence the degree of dehydrogenation and recombination of intermediate species, obtaining products such as formaldehyde, formic acid or methyl formate.

1.8. Oxygen reduction reaction

The ORR is a complex reaction composed of a series of elementary steps that produce oxygenated reaction intermediates that interact and behave depending on the nature of the electrode used. This reaction is influenced, therefore, by the presence of adsorbed species on the electrode and intermediate products obtained in the oxygen reduction on the electrode surface.

The ORR can take place via the transfer of 4 electrons (direct route), which in an acidic medium is represented by reaction (27) and in alkaline medium by reaction (28) [34-35]:

$$O_2 + 4\ H^+ + 4e^- \rightarrow 2\ H_2O \qquad E^0 = 1.229\ V \qquad (27)$$

$$O_2 + 2\ H_2O + 4e^- \rightarrow 4\ OH^- \qquad E^0 = 0.401\ V \qquad (28)$$

For the direct route of oxygen reduction, it is necessary to reduce the chemical potential of the species by means of active metals such as platinum, palladium or silver.

Instead, the ORR can occur first via the transfer of 2 electrons (indirect route), with the formation of hydrogen peroxide in acidic medium, reaction (29), and subsequently, the reaction can continue to the formation of water, reaction (30):

$$O_2 + 2\ H^+ + 2e^- \rightarrow H_2O_2 \qquad E^0 = 0.695\ V \qquad (29)$$

$$H_2O_2 + 2\ H^+ + 2e^- \rightarrow 2\ H_2O \qquad E^0 = 1.776\ V \qquad (30)$$

However, H_2O_2 is sometimes the final product. In alkaline medium, the indirect route can be represented by the following reactions:

$$O_2 + H_2O + 2e^- \rightarrow HO_2^- + OH^- \qquad E^0 = -\ 0.065\ V \qquad (31)$$

$$HO_2^- + H_2O + 2e^- \rightarrow 3\ OH^- \qquad E^0 = 0.867\ V \qquad (32)$$

The reduction of oxygen can be described as a parallel competition between the direct and the indirect pathways. Therefore, the nature of the catalyst, its composition, and properties, as well as the electrolyte, influence the shift towards one path or another [36].

The 4-electron transfer reaction is of technological interest in PEFCs, whereas the 2-electron route is commonly used in the industry to produce hydrogen peroxide. According to the Nernst equation, the equilibrium potentials for such reactions decrease with increasing pH.

Different reaction schemes have been proposed for the ORR, which are described in the literature, the first and best known being those formulated by Damjanovic [37], Wroblowa [38] and Bagostki [39]. However, Wroblowa's simplification of the electroreduction of O_2 on a metal surface is the most illustrating in describing such a process. According to this scheme (Fig. 4), O_2 can be reduced directly to water and OH^- in acidic and basic media, respectively, with a reaction rate constant k_1, or through intermediates (indirectly) with a first transfer of 2 electrons with a rate constant k_2. Subsequently, the intermediates that are adsorbed (H_2O_2, OOH^-) can continue to react through another 2-electron transfer until water (k_3) and OH^-, an irreversible chemical decomposition (k_4) to O_2, and diffusion from the electrode surface towards the electrolyte or vice versa (k_5) [40].

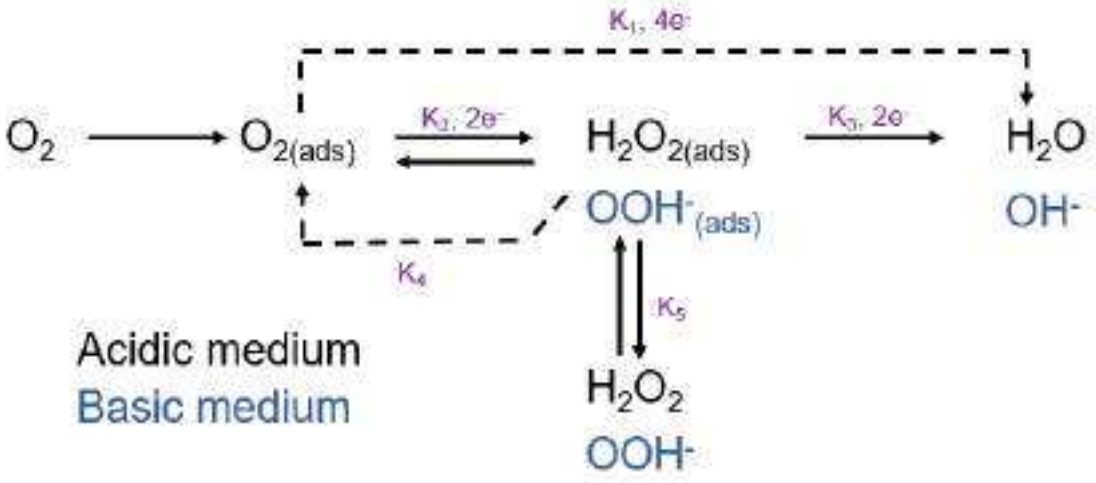

Figure 4. Scheme of the ORR in both acidic and basic medium. Adapted from [40].

The electroactivity of the different transition metals towards the ORR can be predicted by computational studies, using the density functional theory (DFT), taking into account the adsorption energies of all reaction intermediates as a function of the potential applied to the cathode. A volcano-type graph where the catalytic activity is represented against the binding energy of oxygen to the surface of each metal, as shown in Fig. 5, can be thus obtained. In the plot, Pt is the metal that shows the highest activity for the ORR, followed by Pd and the remaining transition metals. The oxygen interaction with the catalyst surface may predict the main reaction pathway.

The types of oxygenated intermediates formed on the surface of the catalyst will depend considerably on the electrolyte where the reaction takes place, as well as on the potential applied [34,35]. There is experimental evidence, supported by computational calculations [41], in that the mechanism of the ORR occurs through different mechanisms on the pure metal and on the oxidized metal surface.

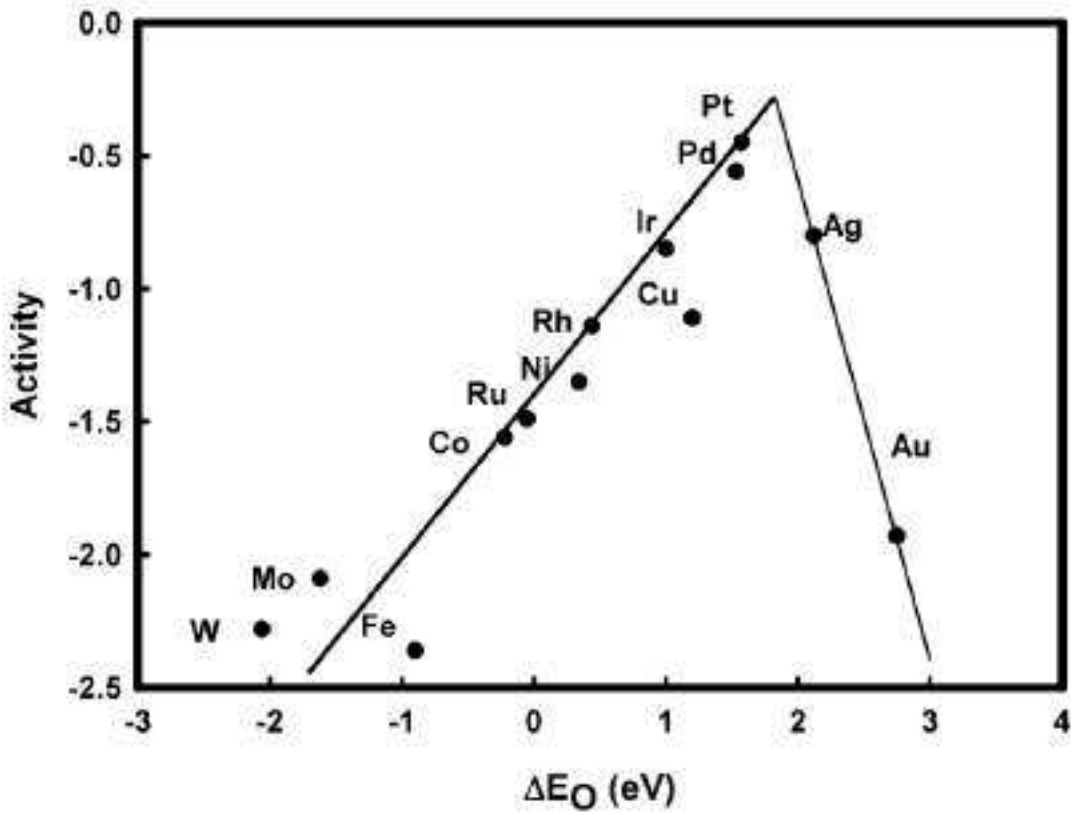

Figure 5. Trends in ORR catalytic activity of transition metals plotted as a function of the oxygen binding energy [41].

The ORR is therefore very sensitive to the structure of the catalyst and depends on its nature and state of the surface. The Tafel slopes obtained under the different conditions correlate with different pathways or rate-determining steps [42]. For example, in the Tafel curve of the ORR on Pt, regardless of the medium used, two slopes can be distinguished, one at low overpotentials and another at high overpotentials. Both slopes describe two different surface structures, the ORR on the pure metal and on the oxidized one, respectively, thus corresponding to different mechanisms.

In summary, the kinetics of the ORR depend on the catalyst, the electron transfer, and the adsorption and desorption of oxygen intermediates formed during the process.

1.9. Latest trends in PEMFCs

Nowadays, the research on PEMFCs is mainly focused on improving PEMFC performance and a line of research to fulfil this goal is focused on increasing the intrinsic activity of the catalysts and reducing its cost [43-46]. In a standard PEMFC structure, the catalyst layer is made of Pt, carbon support, and Nafion®. Pt acts as the catalyst, whereas the carbon contributes to the electrical conductivity and catalyst dispersion, and Nafion® behaves as the binder and the proton conducting medium.

Platinum is, by far, the most efficient catalytic material, which was first applied in a fuel cell system in 1839. Still now, Pt nanoparticles usually supported on porous carbon are the only practical choice for PEMFCs. In comparison to other metals, it is one of the most expensive metals and has restricted accessibility, which makes unviable the preparation of millions of cars with Pt-based electrocatalysts, since considering all the components in the PEMFC, they contribute more than half to the total cost [47].

To decrease the Pt loading without influencing the performance of the PEMFC, it is mandatory to improve the activity and durability of the Pt-based electrocatalyst. There are different strategies that researchers have been studying, concerning both the catalyst support and the catalyst nanoparticles.

1.9.1. Catalyst supports

The use of a catalyst support is necessary to obtain a high dispersion and a narrow distribution of the catalyst nanoparticles. The supporting materials, therefore, have an influence in the cost, performance, and the durability of PEMFCs and DMFCs. The

catalytic layers must be relatively thin to minimise the decrease of the cell performance related to the proton transport rate within the layer and the mass transfer rate of the chemical reactants and products to and from the active sites. This can contribute to an overpotential or electrode polarization, which can limit the cell performance.

There are some requirements for supporting materials, such as high specific surface area (to provide a high substrate area to favour a good dispersion of the nanoparticles), low reactivity with oxygen under both dry and humid air conditions at the PEMFCs operating temperatures, high electrochemical stability in fuel cell conditions, high electronic conductivity, easily recoverable metal in the used catalysts, and a strong interaction between the support material and the catalysts (this can influence the electronic structure of the Pt catalyst improving its catalytic properties, activity and can enhance the electrocatalyst stability) [48].

The most used support materials are carbon-based since they present exceptional properties such as a good resistance to both alkaline and acid environments, a high surface area with the possibility to control the morphology and porosity, high electrical conductivity and excellent graphitic nature.

1.9.1.1. Carbon blacks

Carbon blacks (CBs) have been the most widely used supports for PEMFCs due to their unique characteristics of high surface area, high availability, good electrical conductivity, porosity, and low cost. They are amorphous forms of graphitic carbon, which usually consist of near-spherical particles, with an average size of 20-50 nm, which can form aggregates of about 250 nm. The most known carbon black suitable for fuel cells is Vulcan XC-72, which can be obtained from Cabot Corporation [49].

They are used in their activated form in order to increase both, metal dispersion and catalytic activity. The carbon activation can be performed by a chemical treatment, a thermal treatment or both. The chemical activation is an oxidative treatment in which various oxidants can be used like nitric acid, hydrogen peroxide or ozone, and it is performed to generate oxygen groups on the carbon surface. They are expected to act as nucleation centres for the catalysts nanoparticles and favour their dispersion, thus

increasing the performance of the fuel cell. The thermal treatment is used to remove impurities on the carbon surface, such as metal oxides and sulphides [50].

The main disadvantage of using CBs is that they present insufficient electrochemical stability, since they tend to corrode fast, especially in on/off operation conditions. The degradation of the carbon support by corrosion induces the detachment of the supported nanoparticles of Pt, which then tend to agglomerate or are washed away from the electrode surface. The corrosion of the support affects the surface properties of the electrodes, such as increasing the electrode hydrophobicity. Because of all these factors, carbon corrosion leads to the collapse of the MEA structure [51,52]. Moreover, they have high density of surface defects and despite of their high surface area, CBs present micropores of less than 1 nm that make that part of surface area not useful. Micropores of higher diameter can also trap metal nanoparticles, thus making them inaccessible to reactants.

1.9.1.2. Carbon nanotubes

One of the carbon materials that has been investigated as a possible alternative for CBs are carbon nanotubes (CNTs), a carbon material with tubular structure which makes them unique. They can be synthesised in the laboratory, showing a remarkable mechanical and electrical properties as well as good thermal conductivity. CNTs consist of layers of graphite rolled forming cylinders and can be single walled (one graphene sheet) or multiwalled (several coaxially arranged graphene sheets), the latter designed by the acronym MWCNTs [53].

Compared with CBs, CNTs have a higher surface area, better electrical conductivity, lower weight, a perfect hexagonal formation, and remarkable mechanical, electrical and chemical features. Because of these properties, CNTs can improve the fuel cell performance since they enhance the catalytic performance, catalyst steadiness and corrosion resistance. They also provide a high surface area and allows a better dispersion of Pt nanoparticles, resulting in a decrease of Pt use and therefore a decrease in the fuel cell cost [54,55].

The higher activity of the catalysts supported on CNTs with respect to those supported on CBs was ascribed to different factors [56]: *i*) the higher conductivity; *ii*) the better

accessibility of the reactants due to the graphitic interspaces and the hollow cavity; *iii*) the increased activity due to the *d* band modification of the Pt and *iv*) the presence of more active sites.

1.9.1.3. Carbon nanofibers

Carbon nanofibers (CNFs) are a specific variety of carbons that are formed from the interaction of gases that contain carbon in their composition with metal catalyst particles at high temperatures. Unlike conventional graphite materials and nanotubes where the basal plane is exposed, in the structure of CNFs, only the edge regions are exposed. The main difference between nanotubes and nanofibers consists of the lack of a hollow cavity in the latter.

The carbon nanofibers are synthesised by the two most popular synthesis methods, one being chemical vapor deposition (CVD) and the second one electrospinning [57]. The nanofibers synthesised by these two methods differ in many ways, including morphology, graphitization, electrical conductivity, graphene layer arrangement, and synthesis conditions themselves.

Among all carbon supports, graphitic carbon nanofibers (GNFs), sometimes also termed as CNFs, have received great attention as catalyst support materials due to their structure, since its fibrous and highly graphitic nature gives them excellent electronic properties. Also, referring to the properties of the metal deposition, we can observe a good metal interaction with the nanofiber surface and a specific crystallographic orientation of the supported metal nanoparticles, and the lower susceptibility of the deposited nanoparticles toward CO poisoning, compared to other carbon supports.

The use of CNFs as carbon supports in fuel cells can be explained due to their pore geometry, which has a big influence on the mass transportation of the reactants and the removal of the resulting products from the catalyst layer. Using CNFs, the mass transfer effects are generally reduced improving the porosity and tortuosity of the catalyst layer, because CNFs have less than 1% of micropores and a pore volume can reach up to 0.7 $cm^3\ g^{-1}$, which is a bigger pore volume than in Vulcan XC-72. Furthermore, Vulcan carbon has a bigger percentage of interior pores where the metal nanoparticles are trapped, making them inaccessible for reactants [58].

1.9.1.4. Mesoporous carbons

MCs are referred to carbon solid-based materials containing pores in the range of 2 to 50 nm, according to IUPAC [59]. They can be classified in two categories according to its structure and morphology: ordered mesoporous carbons (OMCs), which are usually synthesised by nanocasting ordered mesoporous silica (OMS) templates or by directly templating triblock copolymer structure-directing species, and disordered mesoporous carbons (DOMCs) with irregular pore structures [60]. Although DOMCs show mesoporosity, the mesopores do not lead to interesting properties as catalyst supports because they are isolated or irregularly interconnected in most cases. Thus, OMCs are preferred as catalyst supports due to their higher specific surface area, electrical conductivity, and mass transport [59].

The synthesis procedure to obtain mesoporous carbon involves infiltration of the pores of an ordered mesoporous silica template with appropriate carbon precursor, such as furfuryl alcohol, sucrose, acenaphthene and mesophase pitch, etc., followed by carbonization, and subsequent template removal [61].

The ordered mesoporous carbons have recently received great attention because of their potential use as catalytic supports in fuel cell electrodes. They have controllable pore sizes, high surface areas, and large pore volumes [62]. Nanoporous carbons with 3D ordered pore structures have shown improved mass transport of reactants and products during fuel cell operation, resulting in a higher limiting current. In addition, oxidation-resistant graphitic MCs with strong catalyst-support interactions are expected to provide a substantial improvement in stability and durability to a fuel cell catalyst.

The textural characteristics of the mesoporous carbons depend especially on the type of template and carbonization temperature. A type of OMC named CMK-3 was synthesised using a 2D hexagonal SBA-15 template, and another named CMK-8 was prepared using 3D cubic KIT-6. These OMCs are characterised by a high BET surface area, hydrophobic surface, chemical stability, and the easy modification of their surface chemistry. To decrease their hydrophobicity, they must be usually activated when used as the catalyst support [63].

Other interesting mesoporous carbon materials can be used as catalyst supports, such as those obtained from chitosan. Chitosan is a linear copolymer generally obtained from the deacetylation of chitin, the second most abundant polysaccharide after cellulose and can be extracted from crustacean shells by means of alkaline reagents [64]. Therefore, the waste obtained from shellfish industry can be used as the main source of chitin and in consequence of chitosan, making this last one a cheap, abundant, and renewable biomass source, which is rich in N and therefore can be used to produce N-doped carbon materials, including mesoporous carbons [65].

The benefits of using chitosan as a precursor for carbonaceous materials to be used in different applications include its low-cost, sustainability, suitable hydrophilicity, chemical stability, the presence of metal anchoring functional groups, and easy customization of their properties through chemical and/or physical modifications [66]. For example, Perazzolo et al. studied by DFT the deposition of Pt nanoparticles on N-doped and S-doped MCs [67,68], and Perini et al. synthesised and studied Pt and Pd nanoparticles supported on N-doped MCs [57]. On the other hand, Daniel et al. reported the use of chitosan as a precursor to obtain mesoporous carbon for its application in heterogeneous catalysis [69].

1.9.2. Core-shell catalysts for PEMFCs

By definition, a catalyst is that substance that modifies and increases the rate of reaction without being consumed in said process. Catalysts play an important role in chemical reactions, so the selection of the catalyst for each type of reaction is essential, since it must have high activity and selectivity.

For FCs, a high-performance catalyst is expected to possess high-density of active sites (with matching energy levels), high stability in fuel cell operation conditions, high electrical conductivity, and moderate surface adsorption. A strong adsorption would mean that final products could not be easily released, whereas weak adsorption would mean that only small amounts of reactants would be adsorbed on the surface, thus resulting in slow reaction rates. Considering these properties, the catalyst composition, morphology, and structure have a great impact on both, catalytic activity and stability, thus meaning that it is important to optimize these factors for the development of catalysts to obtain good performance FCs [70].

Pt is at present the best catalyst for both reactions that take place in a PEMFC. However, the scarcity in the earth and high cost of Pt make necessary to search for new synthesis methods leading to optimal particle size and distribution with decreasing amounts of Pt.

A line of investigation to obtain improved catalysts for PEMFCs with lower Pt content consists of the synthesis and testing of other metals from the Pt metal group and/or Pt-based alloys, starting from the material design and going to the optimization of the electrode structure. However, under acidic conditions, non-platinum group metals in Pt alloys are easily dissolved from the surface under electrochemical tests, thus leading to the instability of the Pt alloy structure and affecting the activity of the catalyst. For this reason, particular attention was focused on core-shell structure nanoparticles, with cheap transition metal cores and thin Pt shells [70-72]. In these structures the amount of Pt is significantly reduced while the ORR is still performed by Pt and sometimes its catalytic activity can be enhanced. Studies of core-shell structures have shown that the catalyst activity in front of the ORR can be greatly improved because the transition metal of the core is able to modify the electronic properties of Pt [71,72].

Figure 6 shows the activity and stability prediction from DFT calculations of Corona et al. [72] for different core-shell systems.

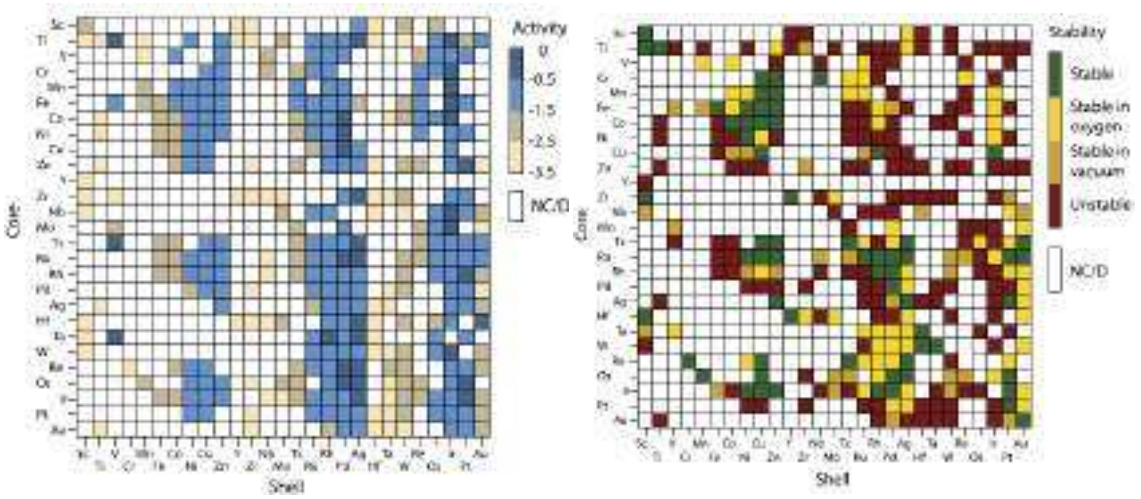

Figure 6. Activity (left) and stability (right) of core@shell NPs for the ORR [72].

According to such DFT studies, the enhancement of the ORR activity in the core-shell structures in which Pt is the shell, is due to the modification of the electronic structure of Pt by the transition metal core. This leads to a change in the oxygen binding energy on Pt

and therefore adjusting their ORR activity. However, two interesting systems have not been studied by these calculations that have been showing interesting experimental results in literature, which are Pt(Cu) and Pt(Ni) core-shell nanoparticles [73-111].

1.9.2.1. PtCu catalysts

The PtCu bimetallic systems, including PtCu alloys, Pt(Cu) core-shells and Cu dealloyed PtCu supported on carbon black, have been the object of interest in recent years, because of their interesting properties in front of CO, methanol and ethanol oxidation as well as in the ORR [73-87]. The role of superficial and near-surface Cu on the catalysed oxidation of CO has been also studied by DFT calculations [88-90].

Most of the Pt(Cu) core-shell catalysts studied have been mainly supported on Vulcan carbon XC-72 and XC-72R. The synthesis procedure in aqueous media was either by direct electrochemical [73-76] or electroless deposition of Cu using different reducing reagents such as $NaBH_4$ [75,77], formaldehyde [78] and water-ethylene glycol mixtures with $NaBH_4$ and ascorbic acid [79-83]. The deposited Cu nanoparticles were then partially replaced with Pt by galvanic exchange.

In more recent studies, alternative carbon supports have been used to study this bimetallic system as PEMFC catalyst, such as CNTs [84-86] and mesoporous carbons [87], in which a higher stability and an increased activity of the catalysts were obtained.

1.9.2.2. PtNi catalysts

The PtNi bimetallic systems have also been the object of interest in recent years because, as in the case of PtCu, they show good results in front of CO, methanol and ethanol oxidation as well as in the ORR [91-111].

A single crystalline $Pt_3Ni(111)$ surface was found to be more active against the ORR than the commercial Pt/C catalyst [91], 90 times higher in terms of mass activity. Since then, many other researchers studied different PtNi systems. They were octahedral PtNi nanoparticles [92-96] with high ORR mass activity, and PtNi alloys with improved methanol [97-105] and ethanol oxidation [106-109]. They normally presented better results than using Pt/C and similar PtM alloys in the absence of Ni. However, these nanoparticles typically show low durability because Ni is easily leached out during the ORR under acidic conditions [110]. In order to decrease the Ni leaching, Wang et al.

reported core-shell structures, where a PtNi alloy core was covered with a PtRu shell by impregnation and reduction at high temperature [111].

To sum up, it can stated that the conventional Pt/C catalysts for PEFCs have been extensively studied and improved by reducing the Pt content, by optimizing the nanoparticle dispersion and size on the catalyst supports, usually CBs, as well as studying alternative supporting materials for enhancing their catalytic activities and stability. However, the use of Pt is still a problem because of its price, scarcity and its low tolerance to CO, which is present in the H_2 obtained by hydrocarbon reforming and it is also an intermediate in the methanol oxidation. In the last years, Pt-based nanoparticles having a core-shell structure, with a non-noble metal core and a Pt shell, supported on CBs, have shown some interesting advantages. Nonetheless, CBs present some drawbacks, such as their microporosity, impurities and low electrochemical and thermal stability.

2. Objectives

Considering all the aforementioned previous works found in the literature, Pt-based nanoparticle catalysts with core-shell structure, composed of Ni or Cu as the core and a Pt shell, supported on advanced carbons, have been synthesised and characterised in this thesis. The general objective was to explore some potential solutions to the main current drawbacks of conventional Pt-based PEFCs: their cost in the large-scale production due to the amount of Pt needed; their low CO tolerance; the slow kinetics at the cathode because of the sluggish ORR; and their reduced catalytic activity in front of the MOR because of the methanol crossover to the cathode.

This thesis has been divided into three parts, related to the synthesis and characterization of carbon-supported Pt(Cu) and Pt(Ni) catalysts, each one with the following specific objectives:

1. **Pt(Cu) and Pt(Ni) supported on carbon black.**
   - Develop synthetic methods allowing the obtention of active Pt(Cu) and Pt(Ni) CO-tolerant core-shell nanoparticles, with Cu or Ni-rich cores and Pt-rich shells, optimal mean size about 3 nm, and a good distribution on the carbon support.
   - Evaluate the structural properties of the catalysts and analysing their influence on their CO tolerance, supported by computational calculations of the CO adsorption energies for different nanoparticle structures.
   - Test the MOR catalytic activity of the catalysts as compared to that of commercial ones.

2. **Pt(Cu) supported on carbon nanotubes and carbon nanofibers.**
   - Synthesize and characterizing (structurally and electrochemically) the Pt(Cu) supported on MWCNTs and CNFs. Then, comparing the obtained results to those for Pt(Cu) supported on carbon black XC-72 and for commercial PtCu/C and Pt/C.
   - Evaluate the activity of the synthesised catalysts in front of the CO oxidation and of the ORR, compared to Pt(Cu)/XC-72, PtCu/C and Pt/C.
   - Evaluate the stability of the catalysts by means of accelerated degradation tests, as compared to that of Pt(Cu)/XC-72, PtCu/C and Pt/C.

- Test the effect of the activation of MWCNTs, CNFs and XC-72 as supports of the Pt(Cu) on the catalyst performance.

3. Pt(Cu) supported on commercial and chitosan-derived mesoporous carbons

- Synthesize and characterizing (structurally and electrochemically) the Pt(Cu) supported on activated and non-activated commercial ordered mesoporous carbons CMK-3 and CMK-8.
- Evaluate the CO tolerance and catalytic activity in front of the ORR of Pt(Cu) supported on CMK-3 and CMK-8, as compared to the properties of commercial Pt/C.
- Evaluate the stability of Pt(Cu)/CMK3 and Pt(Cu)/CMK8 as compared to that of Pt/C by means of accelerated degradation tests.
- Synthesize and characterizing (structurally and electrochemically) the Pt(Cu) supported on chitosan-derived mesoporous carbons showing different mesoporosity to microporosity ratio.
- Evaluate the CO tolerance and catalytic activity in front of the ORR and the MOR of Pt(Cu) supported on the chitosan-derived mesoporous carbons, as compared to the properties of Pt(Cu)/CMK3 and commercial Pt/C.

3. Experimental section

3.1. Materials and Reagents

High-purity water (resistivity > 18.2 MΩ cm at 25 ºC) obtained from a Milli-Q water purification system (Merck KGaA, Darmstadt, Germany) has been used to prepare all the solutions.

For the synthesis of the catalysts, all the reagents were of analytical grade. HNO_3, NaOH, H_2SO_4 (98 wt.%), $CuSO_4.5\ H_2O$, ethanol (96 wt.%), acetone (99.5 wt.%) and 2-propanol (dry) were from Panreac. Formaldehyde (CH_2O) 37 wt.%, ethylenediaminetetraacetic acid disodium salt (Na_2-EDTA), $NaBH_4$, HCl (40 wt.%), n-heptane, poly(ethylene glycol)-dodecyl ether (surfactant Brij-30) and the Nafion® solution (5 wt.%) were from Sigma-Aldrich. Polyvinylpyrrolidone (PVP), with a M_w of 56 $kg \cdot mol^{-1}$, was from Avocado. The H_2PtCl_6 aqueous solution (10 wt.%) used for the galvanic replacement was from Merck.

For the electrochemical testing, a Metrohm glassy carbon (GC) of 5 mm diameter was used as a support electrode to carry out the electrochemical tests of the obtained catalysts. To polish the surface of the GC, deagglomerated Buehler alumina (Al_2O_3) suspensions of 0.3 and 0.05 µm and a Buehler PSA Polishing felt cloth were used. The catalysts obtained were compared to Pt/C (20 wt.%) and PtCu/C (1:1, 20 wt.%) commercial catalysts from Premetek, which employ Vulcan XC-72 as the carbonaceous support. N_2 and CO gases were Linde 3.0 (purity 99.9%).

3.2. Carbon support

The carbon supports used were carbon black Vulcan XC-72 from Cabot (particle size between 20 and 50 nm and BET surface area around 250 $m^2\ g^{-1}$), MWCNTs (diameter between 110 and 170 nm, length 5-9 µm) and CNFs (diameter around 100 nm and length between 2 and 200 µm) from Sigma-Aldrich, and mesoporous carbons CMK-3 (particle size around 1 µm, pore diameters of about 3.8-4.0 nm and a specific surface area of over 900 $m^2\ g^{-1}$) and CMK-8 (particle size around 1 µm, pore diameters in the range of 3.2-6.6 nm and a specific surface area over 500 $m^2\ g^{-1}$) from ACS materials.

3.2.1. Carbon activation

Activation is normally performed to introduce oxygenated groups that favour the particle anchoring and narrow distribution of the nanoparticles on the carbonaceous surface. The different carbon supports have been activated in order to compare if they enhance the catalytic activity of the catalysts, and those catalysts containing activated carbon will be differentiated by adding the symbol "-A" to the carbon support.

The activation procedure consists of an aqueous thermochemical treatment of the carbon supports and was chosen between different carbon activation procedures described before by Calvillo et al. [112]. In this activation treatment, the carbon supports were first suspended in a 2.0 M HNO_3 solution with the help of a ultrasonic bath. Then, they were heated and left at boiling temperature for 30 min. Afterwards, they were left to cool down at room temperature and filtered using a porous plate. The precipitate was rinsed several times with water in order to remove impurities and acid traces, and finally with ethanol. The powder containing the activated carbon support was left to dry overnight at 80 ºC.

3.2.2. Carbon from chitosan

The mesoporous carbons obtained from chitosan as a precursor were synthesised in the University of Padova by Durante's group [113]. Chitosan was used as the precursor and silica P20 as the inorganic template. Four different types of acids were used for the dissolution of chitosan, H_2SO_4, CH_3COOH, HCl and CH_3COONH_4, and the carbons obtained were respectively named from CH1 to CH4. The characterization of these carbons were made at the University of Padova by means of N_2 adsorption, elemental analysis, TEM, X-ray photoelectron spectroscopy (XPS) and Raman spectroscopy.

3.3. Synthesis of PtCu catalysts

The different PtCu catalysts studied were synthesised by different procedures in order to study the synthesis influence and to improve the synthetic method. They all consisted in a two-step synthesis where carbon-supported Cu nanoparticles (Cu/C, the catalyst precursor) were firstly obtained by different deposition methods. The different electroless deposition methods to obtain Cu nanoparticles were performed using basic aqueous medium with high concentration of NaOH, with formaldehyde (Synthesis A) or $NaBH_4$ (Synthesis B) as reducing agents, and also $NaBH_4$ in water-in-oil microemulsion

(Synthesis C). Later, once the Cu/C was formed, a partial galvanic replacement was performed in order to obtain the PtCu/C specimens.

3.3.1. Synthesis A

Synthesis A (**SA**) consists of the preparation of the Cu/C catalyst precursor utilizing formaldehyde as the reducing agent in basic medium, following the work of Georgieva et al. [78]. PtCu/C was synthesised in this form, where C stands for the carbon support, Vulcan XC-72 in this case, which was used both as received and activated.

First, the carbon powder was dispersed in 100 mL of a solution containing 10 mM $CuSO_4 \cdot 5H_2O$ as the Cu precursor, 30 mg L^{-1} CH_2O as the reducing agent, 50 mM Na_2-EDTA as the complexing agent, 5 mM PVP as the surfactant and 125 mg of the carbon support, Vulcan XC-72. Then, the pH was raised up to 12.5-13.0 with 1.0 M NaOH solution. Once the suspension was set for the reaction, it was kept at 45 ± 1 ºC in a water bath under stirring for 30 min. The suspended solid was centrifuged at 9500 rpm for 15 min and then re-suspended in ultrapure ethanol and centrifuged again several times to remove the surfactant. The powder of Cu/C nanoparticles were left to dry under vacuum overnight.

3.3.2. Synthesis B

Synthesis B (**SB**) consists of the preparation of the Cu/C catalyst precursor using $NaBH_4$ as the reducing agent in basic medium, following the work of Mintsouli et al. [76]. PtCu/C was synthesised by this procedure, where the carbon supports tested were Vulcan XC-72, CNTs, CNFs, CMK-3 and CMK-8, which were used both as received and activated.

First, 65 mg of the carbon support and 120 mg of $CuSO_4.5\ H_2O$ were sonicated in 50 mL of a 1.0 M NaOH solution for 30 min, until the carbon support was completely dispersed. Then, a determined amount of $NaBH_4$ powder was slowly added to the suspension in order to obtain the Cu nanoparticles. Different syntheses were previously performed to obtain the optimal $CuSO_4.5H_2O$:$NaBH_4$ weight ratio, which was 1:2. Once all the $NaBH_4$ powder was poured to the suspension, this one was left for 30 min in the ultrasonic bath until the Cu reduction was completed and then the suspension was filtered and cleaned several times with ethanol. The powder obtained (Cu/C precursor) was then subjected to a galvanic exchange.

3.3.3. Synthesis C

Synthesis C (**SC**) consists of the preparation of the Cu/C catalyst precursor using a water-in-oil microemulsion and $NaBH_4$ as the reducing agent, based on the work of Solla-Gullón et al. [114]. The synthesised PtCu/C catalysts were supported on the commercial carbons Vulcan XC-72 and CMK-3 and also on carbons obtained from chitosan, CH1, CH2, CH3 and CH4.

First, 50 mL of microemulsion consisting of n-heptane, Brij-30 and an aqueous solution of $CuSO_4$, with a water-to-surfactant molar ratio of 7:1, were prepared. Once the microemulsion was homogeneous, $NaBH_4$ in powder was slowly added to the magnetically stirred microemulsion to form the Cu nanoparticles, with a reductant-to-metal molar ratio of 9:1 and a total stirring time of 2 h. After this time, the reducing agent was completely removed both for its usage in the chemical reaction and its decomposition in aqueous media. Then, 0.5 mL of the 8 wt.% H_2PtCl_6 solution was slowly dropped to perform the galvanic exchange, keeping the magnetic stirring for 1 h. Finally, 21 mg of the carbon support were dispersed to the microemulsion, also stirring for 1 h and then, acetone was added for the phase separation. Once the organic phase was clean, it was separated from the aqueous phase and the powder was filtered. To assure that the nanoparticles obtained by this procedure became fully covered by Pt, the recently prepared PtCu/C precursor was subjected to a further galvanic exchange.

3.3.4. Galvanic replacement

The powder containing the Cu/C or the PtCu/C precursor was slowly added to 20 mL of a 5 mM H_2PtCl_6 in 0.1 M $HClO_4$ solution and sonicated. Then, it was left under continuous stirring for 45 min, where a spontaneous galvanic partial replacement of the surface Cu by Pt occurs, which can be described as in reaction (33) (E^0= 0.404 V vs. RHE):

$$2\ Cu + PtCl_6^{2-} \rightarrow 2\ Cu^{2+} + Pt + 6\ Cl^- \qquad (33)$$

Once the reaction was completed, the suspension was filtered using a Nalgene filtration system and cellulose acetate filter, under vacuum conditions. Then, the powder was rinsed with abundant water and cleaned with ethanol. Finally, the catalyst was left to dry under vacuum overnight at 80 ºC. The obtained PtCu/C catalysts were named according to the

different carbon supports, such as PtCu/CNT for carbon nanotubes and PtCu/CNT-A when such carbon supports were previously activated.

3.4. Synthesis of PtNi catalysts

The PtNi catalysts were synthesised in the University of Panama by Caballero-Manrique's group. In this synthesis, the Ni/C nanoparticles were prepared by chemical reduction of Ni with $NaBH_4$ in basic medium, adapting the procedure from Hosseini et al. [115] and Zignani et al. [104].

The procedure consisted of a dispersion containing 10 mg of carbon support (Vulcan XC-72R), 1.5 mL of isopropanol and 0.5 mL of water. The mixture was then sonicated for 1 h and then 1 mL of the Ni solution (containing 10 mg of $NiCl_2$) was added and dispersed for 1 h more. Afterwards, 16.5 mg of trisodium citrate, as stabilizing agent, were added and then, 5 mL of a solution containing 33.7 mg of $NaBH_4$, the reducing agent, and 5 mg of NaOH were added followed by vigorous stirring at 75 ºC. Once the reaction was completed, the hydrosol obtained was left 24 h at 70 ºC in an open oven to remove de residual $NaBH_4$ and Ni/C dry powder was obtained. Then the galvanic replacement was performed in ethylene glycol slowly adding 10 wt.% H_2PtCl_6. It was left stirring for 4 h at 90 ºC and then the Pt(Ni)/C was collected, cleaned and left drying overnight at 80 ºC.

3.5. Structural characterization

3.5.1. X-ray diffraction

The X-ray diffraction (XRD) technique allows obtaining very important structural parameters of the catalysts, such as the degree of crystallinity, the grain size, the identification of crystalline phases (alloys) and the lattice parameter.

The crystallite size (d) of the catalyst can be determined by means of Scherrer's Eq. (34), where k is the crystallite shape factor (generally taken as 0.9), θ is the Bragg angle, B is the full width at half maximun (FWHM), and λ is the wavelength of the X-rays used. According to the equation, a large crystallite will show thin peaks on the diffractogram.

$$d = \frac{k\,\lambda}{B\,cos\theta} \qquad (34)$$

The structural analysis was performed by XRD with a PANalytical X'Pert PRO MPD θ/θ powder diffractometer, from Malvern Panalytical Ltd., Malvern, UK, (Cu anode, 45 kV, 40 mA), using a Cu Kα-filtered radiation (λ = 1.5418 Å), 2θ step size of 0.026º and a measuring time of 200 s per step. This instrument is found in the Scientific and Technological Centers of the Universitat de Barcelona (CCiTUB). The powder samples were prepared using a small amount of the catalyst powder, which was sandwiched between Mylar polyester films of 3.6 µm of thickness in a specific sample holder, as in Fig. 7.

Figure 7. Sample set up for XRD analysis.

Since the materials obtained in this work consist of bimetallic nanoparticles, the composition of the crystallites can be obtained using Vegard's law, which states that the lattice parameter of substitutional solid solution varies linearly between the lattice parameter values of the components. For the metallic system studied in this work, Vegard's law would be as in Eq. (35), where d_{PtCu} is the *d*-spacing obtained in the XRD diffractogram, X_{Pt} is the fraction of Pt and d_{Pt} is the *d*-spacing of pure Pt and finally X_{Cu} is the atomic fraction of Cu and d_{Cu} is the *d*-spacing of pure Cu.

$$d_{PtCu} = X_{Pt}d_{Pt} + X_{Cu}d_{Cu} = X_{Pt}d_{Pt} + (1 - X_{Pt})d_{Pt} \quad (35)$$

3.5.2. Transmission electron microscopy

The transmission electron microscopy (TEM) is made with an instrument that takes advantage of the physic-chemical phenomena that occur when a beam of electrons collides with a thin sample, thus allowing to obtain a magnified image of the region

observed. The electron beam is produced by the emission of electrons from a W or LaB_6 filament, which generates a uniform current density whose energy is in the range of 100 to 200 keV. The transmission electron microscope had a typical resolution ranging from 0.2 nm to 200 mm.

There are several modes of image formation in TEM. If the image is formed from the transmitted beam, which has not been scattered, then the image of the object is dark on a bright background. If, on the other hand, scattered electrons are used, the image appears bright on a dark background. Therefore, these two techniques are called bright field and dark field imaging, respectively. In addition, it is possible to analyse the signals produced by the incident electrons, the scattered electrons, and the diffracted electrons, thus allowing obtaining structural information and its elemental analysis.

The images obtained by TEM offer information about the structure of the samples, such as the distribution of the nanoparticles in the support as well as whether the material is amorphous or crystalline. In the case of observing a crystalline material, using high resolution TEM (HRTEM) the electrons diffract according to Bragg's law. In this diffractogram, different points can be obtained, which are ordered with respect to a central point, giving information about the orientation and structure of the crystals present.

A working modality in TEM is scanning transmission electron microscopy (STEM), which in essence is performed with a TEM microscope to which a system of deflector coils has been attached, which allows sweeping the electron beam on the surface of the sample. Due to having a highly focused electron probe during the scan, it is possible to couple an energy dispersive spectroscopy (EDS) detector and obtain information about the composition of the sample at high magnifications.

Sample preparation for these analyses consisted of dispersing its powder in ethanol. Subsequently, a few drops of the above dispersion were placed on a nickel grid (coated with a carbon film) and dried in argon atmosphere.

The microscope used was a Jeol JEM 2100 (Fig. 8) with a resolution of 0.24 nm coupled with an Oxford XMAX 80 cm^2 energy dispersive X-ray microanalyzer. All image processing was performed with the Gatan Microscopy Suite 2.0 software package. This instrument is also part of the electron microscopy facilities of the CCiTUB.

Figure 8. Jeol JEM 2100 transmission microscope from CCiTUB.

3.5.3. X-ray photoelectron spectroscopy

XPS consists of the irradiation of the sample with X-rays generated from a source of Mg (1253.6 eV) or Al (1486.6 eV). The photons interact with the electrons located in the orbitals of the most external atoms in the sample (up to a penetration of 5 nm), which produce the emission of photoelectrons from the atoms. The photons with which the sample is irradiated must be more energetic than the binding energy of the electrons in the atoms, which depend on the nature of the atom and its oxidation/reduction state.

During the process, electrons of different energy levels can be removed, so that a spectrum is obtained that shows all the accessible energy levels and the distribution of the kinetic energy of the photoelectrons. The photoemitted electrons from the inner layers of atoms travel a mean path of 0.5 to 4 nm and constitute the characteristic peaks of the spectrum, while those that undergo inelastic shocks and scatter generate the background of the spectrum. This technique allows elucidating the oxidation state and the chemical environment of an element (except H and He) if it is found at concentrations greater than 0.1 at.%.

For the XPS analyses of the catalysts, a Physical Electronics PHI 5500 Multitechnique System spectrometer with a monochromatic X-ray source (Al Kα line of 1486.6 eV,

powered at 350 W) was used. The energy was calibrated using the $3d_{5/2}$ line of Ag with a FWHM of 0.8 eV. The catalyst powders were disposed on a carbon tape for the analyses. The analyser was placed 20º with respect to the tape for a better detection of the composition of the external layers. After the initial survey spectrum (187.85 eV of pass energy and 0.8 eV $step^{-1}$), the high-resolution spectra (23.5 eV of pass energy and 0.1 eV $step^{-1}$) were obtained. The corresponding XPS spectra, acquired without sputtering and after Ar^+ sputtering (to remove adventitious carbon or analyse more inner layers), were deconvoluted using the MultiPak V8.2B software.

3.6. Electrochemical characterization

The electrochemical tests were carried out in a Metrohm cell with double glass wall to set the temperature at 25.0 ± 0.1 ºC using an MP-5 Julabo thermostat. The reference electrode was a RHE from Gaskatel (all potentials have been referred to the RHE unless otherwise indicated), and the auxiliary electrode was a Pt wire (Incometal). A scheme of electrochemical cell set up is shown in Fig. 9.

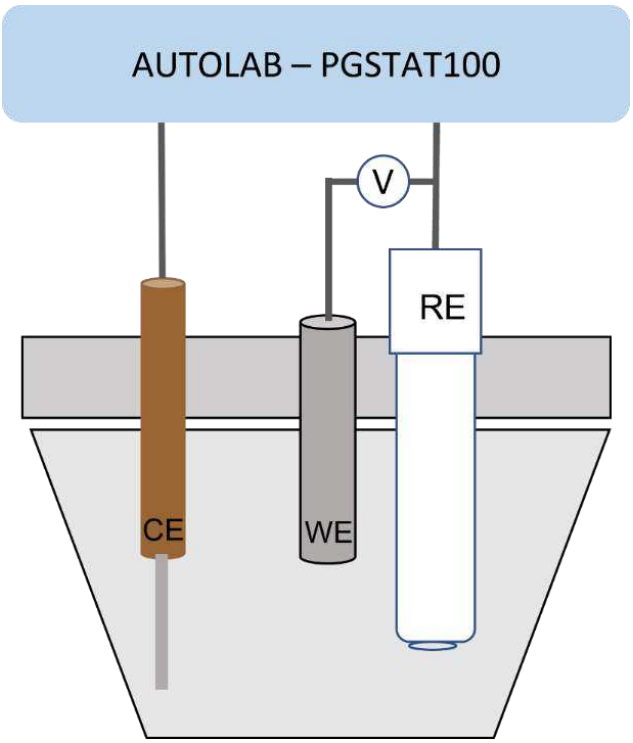

Figure 9. Cell set up for electrochemical testing.

The electrochemical tests were performed in deaerated 0.5 M H_2SO_4 as electrolyte and using an Autolab PGSTAT100 potentiostat-galvanostat commanded by the NOVA 2.1

software, both from Metrohm Autolab B.V. The electrolyte was deaerated by N_2 bubbling. Before performing any electrochemical test, the catalyst was consecutively cycled at 100 mV s^{-1} between 0.0 and 1.2 V until obtaining a steady profile to assure that it was as clean as possible.

3.6.1. Working electrode preparation

The working electrode was a GC electrode from Metrohm with a 5 mm diameter (0.196 cm^2 in section), modified by the catalyst. Before preparing the GC with the catalyst, the electrode was polished on Buehler PSA cloths impregnated with suspensions of 0.3 and 0.05 µm alumina consecutively, until achieving a specular shine. Between each polishing step it was rinsed with Milli-Q water in ultrasonic bath and dried using an IR lamp. Then, the catalyst ink was prepared by dispersing 1.0 mg of the catalyst powder in 500 µL of water. The catalyst ink was sonicated for 30 min and then it was drop casted on the surface of the GC tip until the suitable amount of the catalyst ink was deposited. Once the ink was dried under an IR lamp, the catalyst layer was coated by adding 2.5 µL of 1 wt.% Nafion®.

The GC was coupled to the rotating disk electrode (RDE), also from Metrohm, and connected to the Autolab, controlling the rotation rate (ω) between 100 and 10,000 rpm (± 1 rpm).

3.6.2. Cyclic voltammetry

Cyclic voltammetry (CV) is an electrochemical technique that allows observing the redox processes that occur at the interface formed by the working electrode and the solution, through the cyclic variation of the potential with time at a certain scanning speed between an initial and a final potential. Once the final potential is reached in a direct sweep, it is reversed to the initial one. The variation of potential generates a current between the working and the counter electrodes in the configuration of three electrodes by means of a potentiostat, which is registered as a function of the potential.

This technique can provide considerable information about the kinetics of redox processes, as well as coupled chemical reactions or adsorption processes. For this reason, cyclic voltammetry is used as an initial experiment in electroanalytical studies, since it offers a rapid location of the redox potentials of the electroactive species, the effect that

the electrolyte has on the redox process, and therefore serves to carry out a qualitative study of the processes that occur at the interface.

The CV has been used for the electrochemical characterization of the catalysts studied in this work, generally in the potential range between 0.0 V and 1.2 V vs. RHE at a scanning rate of 20 mV s^{-1}.

The profiles obtained for the cyclic voltammograms of carbons do not show any peaks but only capacitive currents. This happens because no redox reaction takes place on the carbon surface between the selected potentials. However, when the catalyst containing active metal particles with carbon is tested, the profile shows the capacitive current but also a faradaic process. For example, if we start the cyclic voltammogram in the anodic direction, it is observed that upon reaching a certain value of potential, which is the equilibrium potential for the redox reaction under study, the current begins to increase until it reaches a maximum value. This maximum value is due to the fact that the species that react on the surface of the electrode have been consumed. Once the maximum anode potential value is reached, the potential sweep is reversed. It is then that an increase in cathodic current is obtained that corresponds to the reduction of the previously oxidized species.

When the CV is performed with a Pt-based catalyst, under N_2 atmosphere, the catalytic activity of the H adsorption and desorption can be studied, using the peaks observed between 0.0 and 0.2 V. These peaks can be used to calculate the electrochemical surface area (ECSA), which measures the real area of the catalyst that is electrochemically active, and it is one of the parameters that allows determining its electrocatalytic activity.

The measurement of the ECSA is based on the charge transfer that occurs between the electrode surface and the species that are chemisorbed on it. The integration of the H anodic peak gives the amount of H desorbed and that in the cathodic sweep the amount of H adsorbed. The adsorption/desorption of H on polycrystalline Pt can be assumed to be carried out by the formation of a hydrogen monolayer, one H adsorbed on each Pt atom, and corresponds to a total charge of 210 µC cm^{-2}. In this way, as shown in Eq. (36) the value of the ECSA (cm^2 g_{Pt}^{-1}) is obtained by dividing the average charge spent in the processes of adsorption and desorption of H (Q_H, µC cm^{-2}) by the total charge of a

monolayer of H on polycrystalline Pt (210 μC cm^{-2}) and the overall Pt load on the electrode (m_{Pt}, g_{Pt} cm^{-2}).

$$ECSA_H = \frac{Q_H}{210 \cdot m_{Pt}} \quad (36)$$

The CO stripping is a special type of CV where a previously adsorbed monolayer of CO is electrochemically oxidized and thus removed from the surface of the catalyst. The CO stripping test allows also determining the ECSA of a Pt catalyst. In addition, the onset potential of the CO oxidation allows determining the tolerance of the catalyst towards CO, since a lower onset potential means that the latter is easier removed from the catalyst surface and therefore, it is less poisoned by CO.

To obtain the CO stripping curves, CO was first bubbled through the solution for 15 min, whereas a potential of 0.1 V was applied to the working electrode. The dissolved CO was removed by N_2 bubbling through the solution for 30 min and then, the adsorbed CO monolayer was oxidized by CV within the range 0.0 - 1.2 V at 20 mV s^{-1}. The calculation of the ECSA from the CO stripping is made from the charge associated with the oxidation of a CO monolayer previously adsorbed (Q_{CO}), and the value of the oxidation charge of a monolayer of CO adsorbed on polycrystalline Pt (420 μC cm^{-2}), one CO per Pt atom, by means of Eq. (37).

$$ECSA_{CO} = \frac{Q_{CO}}{420 \cdot m_{Pt}} \quad (37)$$

The MOR processes were studied in the acidic solution once the catalyst had been electrochemically cleaned and a steady cyclic voltammogram was obtained. After the catalyst cleaning, the working solution was changed. Therefore, the electrode was extracted from the cell, cleaned with Milli-Q water and carefully dried with paper in order to avoid the contamination of the new electrolyte. The electrode was then introduced in a solution of 1.0 M CH_3OH and 0.5 M H_2SO_4 to study the activity of the catalyst against the oxidation of methanol. The electrolyte was then deaerated for 30 min with N_2 and then one cyclic voltammogram was recorded in the potential range between 0.0 and 1.2 V at a scan rate of 20 mV s^{-1}. The onset potential of the MOR allows determining the catalytic activity towards methanol oxidation, since a lower onset potential means a higher activity (easy oxidation in that surface).

3.6.3. Linear sweep voltammetry

Linear sweep voltammetry (LSV) consists of recording the variation of current while the potential at the working electrode is swept linearly with time at a given sweep rate, as in CV, but the potential sweep is made from an initial potential to a final potential in a single direction.

This electrochemical test has been used to characterize the oxygen reduction reaction on the RDE modified by the different catalysts. RDE allows studying the mass transport by diffusion and convection by rotating the working electrode at different speeds (ω). The RDE is made up of a rod, GC in this case, embedded in an insulating material (Teflon) with a larger diameter than that of the GC rod. Thus, only the basal disk of the latter is exposed to the electrolyte. When the disk electrode rotates, a defined flow pattern is generated, thus acting as a pump that sucks the electrolyte towards the electrode and then expels it. The vigorous stirring of the electrolyte by means of the RDE determines the thickness of the diffusion layer that forms near the electrode, so that it is possible to reach stationary currents, with a steady concentration profile of the electroactive species (O_2) in the diffusion layer. Fig. 10 shows the simplified concentration profile for the steady conditions (model of the Nernst diffusion layer).

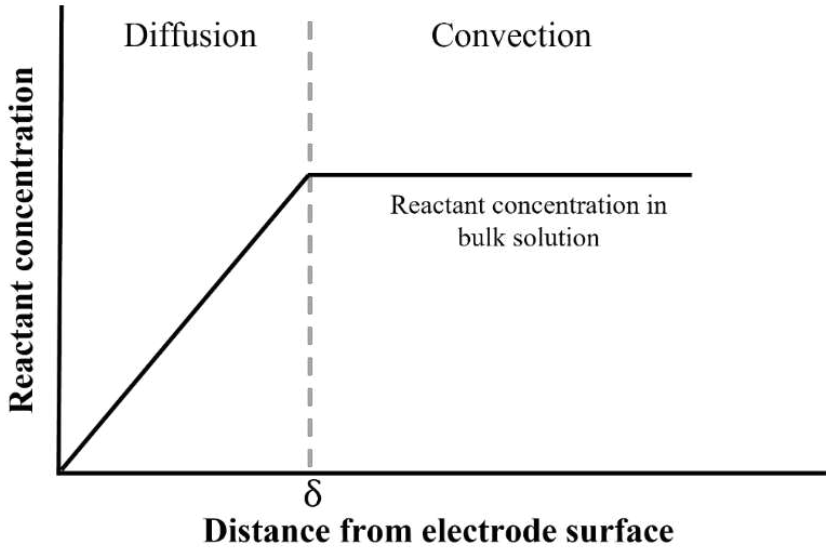

Figure 10. Representation of the Nernst diffusion layer profile model.

According to the Nernst model, the electrolyte near the electrode varies in linear form (Fig. 10). This region of thickness δ is known as the diffusion layer and the only way of

transporting the species is diffusion. The region after the diffusion layer is the bulk solution, where the concentration of all the species is constant because of the forced convection of the electrolyte [116].

The thickness of the diffusion layer δ can be estimated by means of Eq. (38), at a certain rotation speed of the electrode (ω), if the values of the diffusion coefficient (D) and kinematic viscosity (v) are known:

$$\delta = 1.61\, v^{1/6} D^{1/3} \omega^{-1/2} \quad (38)$$

This means that δ depends on the rotation velocity of the electrode, so that for a given reaction controlled by mass transport, the RDE current can be estimated according to Eq. (39), where j_l is the limiting current density, n the mols electrons involved in the electrochemical reaction per mol of reactant, F is the Faraday constant and C_o is the concentration of the species under study within the solution:

$$j_l = (nFC_oD)\delta^{-1} \quad (39)$$

The combination of Eqs. (38) and (39) yields the Levich Eq. (40). The limiting current depends on the speed of rotation, so the I vs. $\omega^{1/2}$ plot will be linear if there is no kinetic impediment to the reaction:

$$j_l = 0.62nFD^{2/3}v^{-1/6}C_o\omega^{1/2} \quad (40)$$

RDE is commonly used to measure the activity of the ORR in electrocatalysts used in low-temperature fuel cells. To evaluate the ORR, the electrolyte, 0.5 M H_2SO_4 solution in this case, was saturated with pure oxygen for 30 min. Then, a linear potential sweep was performed in a potential range from 1.0 V to 0.2 V at different rotation speeds (500, 1000, 1500, 2000 and 2500 rpm). Since it is intended to reach a steady state, the sweep rate of the LSV is usually low, 5 mV s^{-1}. All the experiments were carried out with softly bubbling pure O_2 gas in the electrolyte.

3.6.4. Accelerated degradation tests

Since the stability of PEMFCs catalysts is still a critical point, accelerated degradation tests were performed. They consisted in continuous cycling of the working electrode between 0.6 and 1.0 V at 100 mV s^{-1} in deaerated 0.5 M H_2SO_4 for a large number of

cycles. This potential range was selected because in these conditions some oxidation of carbon and Pt is expected, resulting in possible atomic restructuration of the catalyst and carbon oxidation, which can lead to mass loss of the carbon support and, therefore, aggregation of the metallic nanoparticles. The ECSA decay after a given number of cycles will be represented as $ECSA/ECSA_o$, which is the ratio between the ECSA measured after such number of cycles and the initial value ($ECSA_o$), versus the number of cycles. These ECSA values were obtained from the atomic hydrogen adsorption-desorption charges in the voltammograms performed at 20 mV s^{-1} from 0.0 to 1.2 V.

4. Results and discussion

The most important findings of this thesis are presented in this chapter. It has been divided in three sections, according to the different carbon support types that have been studied. Section 4.1 is about PtNi and PtCu nanoparticles supported on carbon blacks, Vulcan XC-72R and Vulcan XC-72 respectively. Section 4.2 deals with PtCu nanoparticles supported on carbon nanotubes and carbon nanofibers. Finally, Section 4.3, about PtCu nanoparticles supported on mesoporous carbons, where both commercial mesoporous carbons (CMK-3 and CMK-8) and mesoporous carbons obtained from chitosan have been studied.

4.1. Catalysts supported on carbon blacks

4.1.1. Synthesis and Evaluation of PtNi Electrocatalysts for CO and Methanol Oxidation in Low Temperature Fuel Cells

This work was performed in collaboration with Prof. Caballero-Manrique from the University of Panama during her stay in our lab group. As indicated in the experimental part, these catalysts were synthesised in the University of Panama, based in our collaboration project with the University of Barcelona, and the experimentation was performed in the laboratory of the University of Barcelona, thus forming part of the present thesis. The work consisted in the electroless deposition of Ni on Vulcan XC-72R followed by deposition of Pt and Ru species. The catalyst properties obtained showed significant improvements with respect to commercial Pt/C, such as a better tolerance towards CO poisoning and higher specific and mass activities of the catalyst in front of the MOR.

The catalysts studied in this work were obtained by the synthetic procedure explained in Chapter 3, Section 3.4. Different Pt(IV):Ni(II) weight ratios of the precursors were used in order to find the optimal one for the catalyst performance. The electrochemical analysis of the catalysts obtained showed that those obtained from the precursor ratios of 1:1 and 2:1 presented small current densities, while those obtained from precursor ratios of 3:1 and 8:1 presented greater current densities referred to the electrode section. This was explained by the higher amount of Pt active sites for the latter. The deposition of Ru species onto Pt(Ni)/C for the 3:1 Pt(IV):Ni(II) weight ratio, led to similar CV profile to

that of Pt(Ni)/C 3:1 but with lower current densities in the H adsorption and desorption region due to the blockage of Pt sites by Ru species.

Different structural analyses were performed in order to understand the structure and morphology of the catalysts. The XRD diffractograms showed the presence of a *fcc* Pt structure with a slightly shift to smaller values with respect to pure Pt, which was explained by the expansion of the Pt lattice due to its growth on hexagonal Ni core or because the peak is the sum of the contribution of small hexagonal Ni with the dominant Pt cubic phase. This was confirmed with the TEM using the FFT analysis, which showed the presence of both cubic Pt and hexagonal Ni, and also by the EDS analyses, where the composition of the nanoparticles showed a higher content of Pt (15-19 wt.%) compared to the Ni content (0.6-1 wt.%). The mean particle size of the nanoparticles measured using the TEM was around 3 nm, which is similar to the values obtained by calculating the crystallite size from the XRD data. The TEM images showed the good dispersion of Pt(Ni) nanoparticles on the carbon support.

The CO stripping showed that using the Pt(Ni)/C catalysts the CO oxidation takes place at lower potentials than in Pt/C, thus meaning that they present a better tolerance towards CO poisoning. In addition, the CO oxidation peak could be deconvoluted in two contributions, which indicated that the oxidation took place on two different Pt sites of different activity. The origin of this shift was attributed to the electron donor effect of Ni to Pt. This could also explain the lower onset potential for Pt(Ni)/C 3:1 in front of the CO oxidation than for Pt(Ni)/C 8:1, since the first one has higher amount of Ni. The same trend was observed in the case of the Ru-containing catalysts, with lower onset potentials than those without Ru due to bifunctional mechanism of CO oxidation when Ru is present.

The study of the methanol oxidation on the different catalysts by LSV showed that the most negative onset potentials was obtained using Pt(Ni)/C 3:1, the second more negative was Pt(Ni)/C 8:1 and finally Pt/C, which showed the highest onset potential of the catalysts studied. The different behaviour of the Pt(Ni) towards methanol oxidation was explained by their different relative amount of Ni, as it happened with the CO oxidation, since it is known that CO is an intermediate of the MOR. The onset potentials when using Pt(Ni) were comparable to those obtained with PtRu, but still higher, which was related to the different methanol mechanism on these different catalysts.

catalysts

MDPI

Article

Synthesis and Evaluation of PtNi Electrocatalysts for CO and Methanol Oxidation in Low Temperature Fuel Cells

Griselda Caballero-Manrique [1,2], Julia Garcia-Cardona [1], Enric Brillas [1], Juan A. Jaén [2], John Manuel Sánchez [1,2] and Pere L. Cabot [1,*]

[1] Laboratori d'Electroquímica dels Materials i del Medi Ambient, Secció de Química Física, Facultat de Química, Universitat de Barcelona, Martí i Franquès 1-11, 08028 Barcelona, Spain; griselda.caballero@up.ac.pa (G.C.-M.); jul.gar.95@gmail.com (J.G.-C.); brillas@ub.edu (E.B.); john5l07sanchez@hotmail.com (J.M.S.)

[2] Department of Physical Chemistry, Universidad de Panamá, Panama 69860076, Panama; juan.jaen@up.ac.pa

* Correspondence: p.cabot@ub.edu; Tel.: +34-93-403-92-36

Received: 27 April 2020; Accepted: 17 May 2020; Published: 19 May 2020

Abstract: Pt(Ni)/C and PtRu(Ni)/C catalysts were synthesized by electroless deposition of Ni on a carbon dispersion followed by sequenced Pt deposition and spontaneous deposition of Ru species. The structural analyses of the catalysts with 88:12 and 98:2 Pt:Ni atomic ratios pointed out to the formation of small hexagonal Ni crystallites covered by thin cubic Pt surface structures with no evidence about PtNi alloy formation. The onset potentials for CO oxidation on Pt(Ni)/C and PtRu(Ni)/C were about 0.10 and 0.24 V more negative than those of Pt/C, thus indicating their better CO tolerance. The surface Ru species appeared to have the major effect by facilitating the CO removal by the bifunctional mechanism. The onset potential for the methanol oxidation reaction (MOR) of Pt(Ni)/C was about 0.15 V lower than that of Pt/C. The mass and specific activities together with the exchange current densities of the Pt(Ni)/C catalysts were also higher than those of Pt/C, making in evidence their higher activity in front of the MOR. The Tafel slopes for the MOR on Pt(Ni)/C suggested different reaction mechanism than on Pt/C. The electronic (ligand) effect of Ni on Pt was considered the main reason to explain the higher activity of Pt(Ni)/C in front of the CO oxidation and the MOR.

Keywords: Pt(Ni)/C catalysts; PtRu(Ni)/C catalysts; galvanic exchange; Ru spontaneous deposition; CO oxidation; methanol oxidation reaction

1. Introduction

The shortage of fossil fuel deposits increases over time along with the energy demand, causing a negative impact on the environment. Thus, many researchers worldwide have turned their attention toward a common goal of developing alternative energy sources. After several decades, fuel cells have emerged as an alternative to other energy sources. There is considerable research on this topic, encompassing the study of aspects such as the production, storage and transportation of hydrogen; new ways of obtaining hydrogen and new catalytic materials, among others [1]. A fuel cell is an electrochemical device that converts directly the chemical energy of a reaction into electrical energy. It allows electricity to be generated by two electrodes, an anode and a cathode, separated by an electrolyte, combining hydrogen and oxygen electrochemically, in the absence of combustion reactions [2]. Very high efficiencies can be reached because they are not affected by Carnot's heat engine limitation and the absence of moving components within the device, reducing the friction losses that are present in an internal combustion engine.

The cleanest fuel is pure hydrogen. However, the cheapest H_2 is still obtained from hydrocarbon reforming and it is well known that it contains a remaining CO, which easily poisons the Pt catalyst generally used in the low temperature fuel cells such as proton exchange membrane fuel cells (PEMFCs). On the other hand, there have been significant efforts in the study of the electrochemical oxidation of alcohols and other hydrocarbons. Organic liquid fuels are characterized by a high energy density, whereas the electromotive force associated with their electrochemical oxidation to CO_2 is comparable to that of hydrogen combustion to produce water [3–5]. The anode reaction for the methanol oxidation reaction (MOR) on Pt and Pt-based alloys in direct-methanol fuel cells (DMFCs) has been explored since many years ago [3,6–9]. DMFCs, which also use proton exchange membranes as electrolyte, are fed directly by a methanol/water mixture at the anode. Methanol is oxidized to CO_2, but by-products such as formaldehyde, formic acid, and especially the intermediate carbon monoxide, which decrease the cell efficiency, are formed. The PtRu alloys are at present the best candidates for the MOR and their good performance are explained by the bifunctional mechanism and the electronic effect of the Ru alloying atom [7–19]. According to the theory of the bifunctional mechanism, the formation of hydroxylated species on Ru at low potentials favor the formation of CO_2 from adsorbed CO on Pt:

In addition, the modification of the electronic structure of Pt by Ru can decrease the adsorption strength of the poisoning species, thus contributing together with the bifunctional mechanism to increase the rate of Equation (1):

$$Pt\text{-}CO + Ru(OH) \rightarrow Pt + Ru + CO_2 + H^+ + e^- \quad (1)$$

The electrooxidation of ethanol is also of special interest because it has a high energy content, with 12 electrons per mol, low toxicity and little environmental concerns [4,5]. The ethanol oxidation reaction (EOR) is more complex than that of methanol because it requires de C-C bond breaking and the CO_2 yield is small in mild conditions of temperature and pressure [20,21]. Good performances have been reported when using PtRu, PtRh, PtPd and PtSn catalysts [20,22–26]. Conversely, Fe, Ni and Co supported on micro/nano-structured carbon did not present catalytic activity for the EOR [27]. The C-C bond breaking was favored with PtRh. However, the ethanol conversion to CO_2 is still limited.

At present, the benchmark catalysts for PEMFCs in the industrial-related applications are carbon-supported Pt and Pt-based alloys [28]. It is generally accepted that alloying Pt with other transition metals allows improving the reaction rates by tuning the d-band structure of the Pt surfaces to lower the bond strength of the Pt-adsorbates, thus leading to better resistance to poisoning [12,28–32]. Many basic research scientists are currently focusing their attention to obtain catalysts with precursors that provide good electrocatalytic activity using small amounts of noble catalytic metals to lower costs [33–36]. Thus, alloying Pt with other transition metals such as Cu, Fe, Ni and Co, has allowed obtaining catalysts with better performance due to favorable electronic effects together with decreasing the amount of precious metals [14,17,18,28,29,31,33,35,37–46].

Ni-containing Pt-based alloys have been synthesized and tested for the oxygen reduction reaction (ORR) [28,33,35,39,41,47–49], and the CO [18,38], methanol [8,31,37,41,50–53] and ethanol [8,22,29,44–46] oxidation reactions, with generally better results than using Pt/C and the same alloys in the absence of Ni. The oxidation of ethylene glycol and glycerol on one-dimensional Pt_3Ni nanowires and nanorods has been also studied [54], with the conclusion that it presented higher mass and specific activities than Pt/C. This was generally explained by geometric factors related to the Pt-Pt bond length decrease and/or the ligand effect of Ni on Pt. Thus, Zignani et al. [39] obtained carbon-supported Pt_xNi_y catalysts that showed a high electrochemically active surface area (ECSA) and good activity towards ORR in acidic medium as compared to commercial Pt/C. Similar results together with good stability were reported by Beermann et al. [28] and Choi et al. [33] with Rh-doped and halide-doped PtNi alloys, respectively. In addition, the methanol tolerance of PtNi alloy cathodes in DMFCs was better than that of Pt/C [41]. On the other hand, alloying the PtRu catalysts with Ni improved their activity for CO, methanol and ethanol oxidation reactions [18,31,38]. Thus, Park et al. [31] reported onset potentials por the MOR decreasing in the sequence: $Pt/C > Pt_1Ni_1/C > Pt_1Ru_1/C > Pt_1Ru_4Ni_1/C$. Wang et al. [45] and Ribadeneira et al. [46]

found that $Pt_{63}Ru_{32}Ni_{10}/C$ and $Pt_{75}Ru_{15}Ni_{10}/C$, respectively, performed better than Pt_1Ru_1/C for the EOR. The same was reported for the PtRh alloys used for the ethanol oxidation [29,44]. Erini et al. [44] found that the EOR activity of $Pt_{38}Rh_{57}Ni_{05}$ outperformed the benchmark $Pt_{52}Rh_{12}Sn_{36}/C$ in acidic and alkaline media, with higher specific currents per mass of precious metals than the latter. Shen et al. [29] reported for PtRh catalysts supported on graphene nanosheets that the onset potential for the EOR in $Pt_{75}Rh_{15}Ni_{10}$ was better than that of $Pt_{75}Rh_{25}$. In these papers, catalytic structures mainly consisting of alloys in the form of *fcc* Pt solid solutions have been described.

There are other research papers dealing with core-shell structures [18,37]. Serra et al. [37] used CoNi nanorods covered by a Pt shell formed by galvanic displacement for the MOR, which presented much better performance than Pt nanorods and Pt/C. Wang et al. [18] reported core-shell structures for the CO oxidation. In this case, a carbon-supported PtNi alloy core covered with a PtRu shell was prepared by impregnation and high temperature reduction, followed by galvanic displacement and annealing treatment. This structure showed higher activity than that of PtRu/C due to the synergistic effect between core and shell. In the latter core-shell structures, Ni did not appear to be in contact with the electrolyte. However, it is under discussion whether the surface Ni is being dissolved during the stability tests [28,33] and/or it is oxidized to highly conductive $Ni(OH)_2$, which may help the desorption of CO by the bifunctional mechanism [38,51]. Recently, Glüsen et al. [49], using dealloyed PtNi/C catalysts with a PtNi core and a Pt-rich shell, found that Ni was necessary in the core and detrimental in the shell for both, the activity and stability of the DMFC cathode. Recent publications show the renewed interest in studying PtNi alloys for methanol oxidation [49,51–54].

In this study, Pt(Ni)/C and PtRu(Ni)/C electrocatalysts on Vulcan XC72R carbon were synthesized using different proportions of metals by chemical reduction of a Ni precursor with $NaBH_4$ and subsequent deposition of Pt from a Pt(IV) precursor. It is then expected that the final structure was a Ni-rich core covered by a Pt-rich shell, similarly to the Pt(Cu)/C and PtRu(Cu)/C catalysts prepared earlier by the authors, which led to good onset potentials for the CO oxidation and the MOR [14,17,42,43]. The catalysts obtained were evaluated in a three-electrode cell for the oxidation reactions of CO and methanol in sulfuric acid. The characterization of the catalysts obtained was performed using the electrochemical methods of cyclic voltammetry (CV), CO stripping and linear sweep voltammetry (LSV). In addition, they were analyzed by X-ray diffraction (XRD), transmission electron microscopy (TEM), energy-dispersive X-ray spectroscopy (EDS) and high-resolution TEM (HRTEM).

2. Results and Discussion

2.1. Electrochemical Characterization by CV

Preliminary experiments showed that the cyclic voltammograms for the catalysts prepared from Pt(IV):Ni(II) ratios of the precursors of 1:1 and 2:1 in weight presented small current densities referred to the electrode section and thus, small hydrogen adsoeption/desorption charges. These values were greater for Pt(IV):Ni(II) ratios of 3:1 and 8:1. This can be explained by the different number of Pt active sites in each specimen, which were smaller in the case of 1:1 and 2:1 due to an insufficient amount of Pt to effectively cover the Ni cores. Representative cyclic voltammograms in deaerated 0.5 M H_2SO_4 in the range from −0.2 to 0.8 V of the Pt(Ni)/C catalysts with precursor ratios of 3:1 and 8:1, which will be designed in the following lines as Pt(Ni)/C 3:1 and 8:1, respectively, are depicted in Figure 1, curves *a* and *b*, respectively. As can be seen, the cyclic voltammograms of the Pt(Ni)/C catalysts presented the typical features of Pt/C (curve *c*) [7,17,55,56]: (i) the hydrogen adsorption/desorption region on the (110) and (100) Pt faces (from −0.2 to about 0.2 V), (ii) the Pt oxidation (from ca. 0.45 V) and (iii) the corresponding Pt oxide reduction peak (at about 0.6 V). Note that they have been normalized to the respective hydrogen desorption charge, which is proportional to the number of active sites of the corresponding catalyst, thus allowing a better comparison of their profiles with that of Pt/C. The Pt(Ni)/C catalysts presented cyclic voltammograms with similar profile in the hydrogen adsorption/desorption potential

region as that of commercial Pt/C, which is the expected result when a core shell Pt(Ni) catalyst structure is approached. However, the corresponding peaks in Pt(Ni)/C appear to be somewhat deformed with respect to those of Pt/C, probably due to the conditioning effect of the Ni core on the surface Pt. Some more differences appear in the potential region of Pt oxidation. Pt is oxidized from about 0.45 V in Pt(Ni)/C, whereas it is from about 0.6 V for Pt/C. In addition, the cathodic peak corresponding to Pt oxide reduction appears at about 0.6 V for Pt(Ni)/C, but it is somewhat shifted in the negative direction for Pt/C.

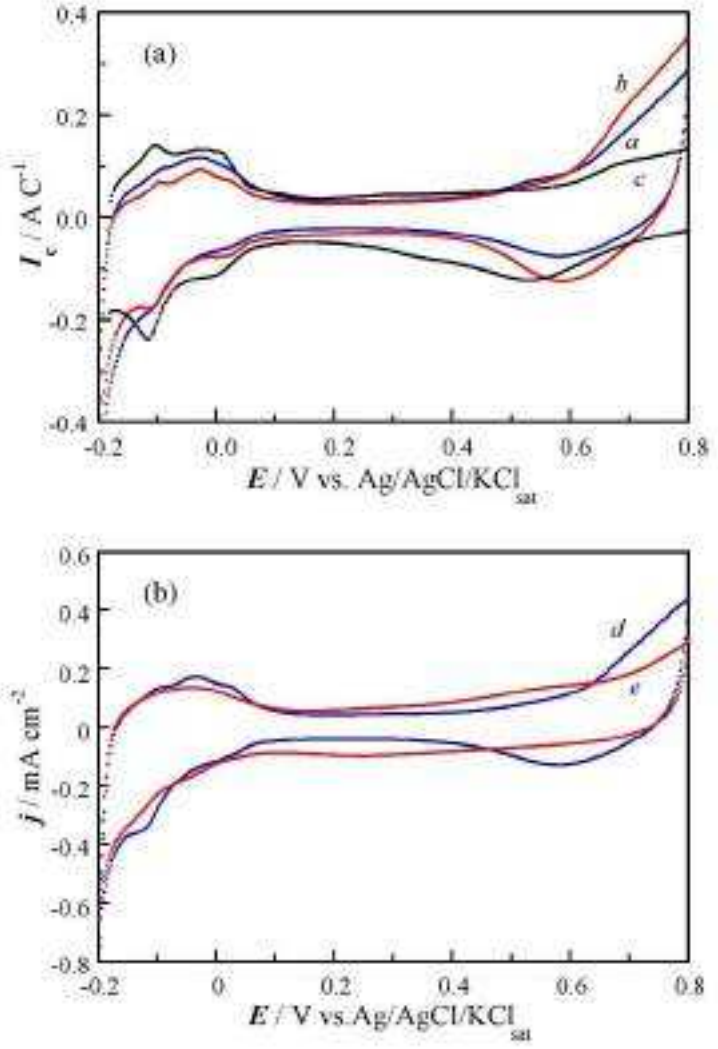

Figure 1. *Cont.*

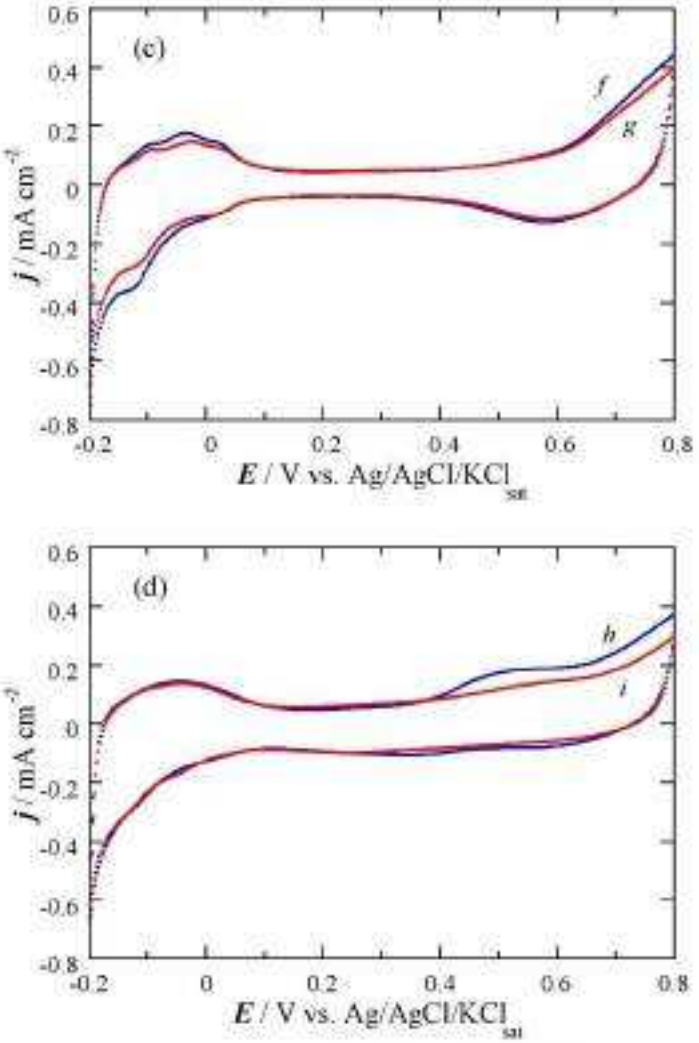

Figure 1. Cyclic voltammograms in deaerated 0.5 M H_2SO_4 of (**a**) Pt(Ni)/C 3:1 (curve *a*) and 8:1 (*b*), compared to Pt/C (*c*); (**b**) Pt(Ni)/C 3:1 (curve *d*) compared to that of PtRu(Ni)/C 3:1 (*e*); (**c**) Pt(Ni)/C 3:1, 1st cyclic voltammogram (curve *f*) compared to the 100th one (*g*); and (**d**) PtRu(Ni)/C 3:1, 1st cyclic voltammogram (curve *h*) compared to the 100th one (*i*) In (**a**) the curves are normalized to the hydrogen desorption charge. In (**b**–**d**), the current densities are relative to the electrode section. Sweep rate 20 $mV\,s^{-1}$.

The same trend was reported in our previous paper in which a Pt(Cu)/C was also synthesized by sequenced deposition of Cu and Pt [17]. The onset potential for Pt oxidation in Pt(Cu)/C under the same conditions as in this work was also 0.45 V and the Pt oxide reduction peak was also found at about 0.6 V. This can be interpreted in the same form as in the case of Pt(Cu)/C [17], assuming that the Pt(Ni) nanoparticles present Pt surface structures that are more defective than those found in the lattice of the pure Pt nanoparticle and consequently, the Pt surface atoms are more active in Pt(Ni).

The effect of the spontaneous deposition of Ru species onto Pt(Ni)/C is exemplified in Figure 1b. This figure, in which the current densities referred to the electrode section have been represented, compares the cyclic voltammograms of Pt(Ni)/C 3:1, without (curve *d*) and with deposited Ru species (*e*). As indicated in the experimental part, both specimens were prepared to have the same Pt load. Both curves show similar profiles and are the same as that of Pt (Figure 1a), but the current densities for PtRu(Ni)/C in the potential range of hydrogen adsorption/desorption region are smaller than in Pt(Ni)/C due to the blockage of Pt active sites by the deposited Ru species [11]. As the latter are inactive for hydrogen adsorption, the ECSA of PtRu(Ni)/C is smaller than that of Pt(Ni)/C. In addition, the current densities in the intermediate potential region of 0.1–0.5 V are higher for PtRu(Ni)/C because the capacitive currents increase due to the formation of hydroxylated Ru species. In the potential region of 0.6–0.8 V the current densities are again smaller due the blockage of Pt active sites, which results in a less amount of Pt exposed to oxidation. When comparing the hydrogen adsorption/desorption charges, that corresponding to PtRu(Ni)/C is 80% of Pt(Ni)/C, thus indicating that the coverage of the Pt active sites in the former is 0.20. A very similar value has been obtained for PtRu(Ni)/C 8:1, with a coverage of 0.21 by the Ru species. According to our previous work [11], these values are in the optimum range 0.2–0.3 for CO and methanol electrooxidation. It is worth to note that such small coverages lead to only 0.3 at% of Ru to the PtRu(Cu)/C nanoparticles [17], but it was sufficient to produce major effects in the methanol and the CO electrooxidation.

The cyclic voltammograms were reproducible and repetitive after the first cycle. However, in order to have a first approach to the stability of the catalysts, many consecutive cyclic voltammograms were performed. The first and the 100th cyclic voltammograms for Pt(Ni)/C and PtRu(Ni)/C 3:1 at 20 mV s^{-1} are depicted in Figure 1c,d, respectively. It is shown in these figures that the 1st and 100th cyclic voltammogram of Pt(Ni)/C (curves *f* and *g*), and of PtRu(Ni)/C (curves *h* and *i*), have the same profiles, although a slight decrease in the current densities of the latter is apparent. The hydrogen desorption charges after the consecutive cycling of Pt(Ni)/C and PtRu(Ni)/C 3:1 decreased by 8.8 and 3.0% respectively, with comparable values of 10.5 and 5.0% for 8:1. This can be due to the surface Pt restructuration because the anodic limit of the cyclic voltammograms is well in the potential range of Pt oxidation and therefore, the catalysts can be considered rather stable [43], thus suggesting that Ni is reasonably covered by a Pt shell.

2.2. *Structural Analysis*

The XRD diffractograms of the Pt(Ni)/C catalysts studied are plotted in Figure 2a, where they are compared to that of Pt/C. The diffraction angles of pure Pt have been also depicted in this figure. Four peaks for the Pt(Ni)/C specimens centered at 2θ angles of 39.8, 46.2, 67.6 and 81.4° appear, which can be related to the (111), (200), (220) and (311) planes of *fcc* Pt [57]. The diffraction angles of the Pt(Ni)/C specimens are only slightly shifted to smaller values with respect to pure Pt, with reported 2θ values of 40.04, 46.54, 67.86 and 81.51° [58], indicating that the Pt-based structures in Pt(Ni)/C are mainly composed of pure Pt. In addition, no diffraction peaks can be ascertained in relation to possible Ni-based phases, which should appear in the positions represented in Figure 2h. If present, they should be as very small crystallites or in amorphous form. Figure 2b is a magnification of the region corresponding to the (111) diffraction peak of Pt, which include the 2θ signals of the (010) and (002) planes of the Ni hexagonal structure at 39.10 and 41.53°, respectively, and also that of the (111) plane of cubic Ni, with a 2θ value of 44.37° [58].

In order to estimate the alloying degree between the involved metal atoms, the Vegard's law is normally applied. However, this law cannot be applied in our case because the Pt-based peaks of the Pt(Ni)/C catalysts are shifted to angles slightly smaller than that of pure Pt. If a *fcc* PtNi alloy was formed, 2θ should be displaced to higher angles, which would correspond to a Pt lattice contraction [18,28,35,39]. In Figure 2, the Pt diffraction peaks are shifted towards the diffraction angle of hexagonal Ni instead to the higher angles where the cubic Ni signal is located. Studies about PtNi catalysts in the literature, prepared by simultaneous reduction of the platinum and nickel

precursors [18,28,33,39,49,51,52,59], described *fcc* alloy structures with 2θ angles between those of pure cubic Pt and pure cubic Ni, then higher than those of Pt, according to a Pt lattice contraction, just the opposite found in this paper. This can be explained assuming that hexagonal Ni is spontaneously formed when depositing Ni alone in the present synthesis conditions, whereas cubic PtNi results from Pt and Ni codeposition.

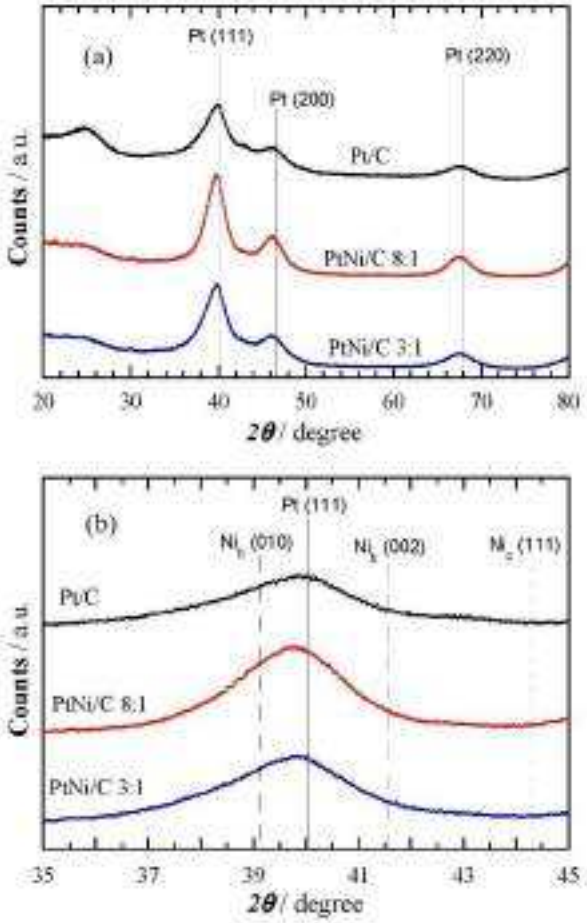

Figure 2. (a) XRD diffractograms of the catalysts studied, where that of Pt/C has been included for comparison. (b) Magnification of the XRD profiles shown in (a) in the Pt (111) 2θ region, including the diffraction angles of hexagonal and cubic Ni.

A Pt lattice contraction was found for Pt(Cu)/C catalysts prepared in the same form as in our present paper, thus indicating some alloying degree between Pt and Cu, forming a *fcc* PtCu alloy structure [43,60]. As this is not the case from the results shown in Figure 2, we may conclude that a PtNi alloy is not being formed in the present conditions. The probable structure of the synthesized Pt(Ni) nanoparticles is composed of very small Ni core with hexagonal structure covered by a Pt shell with cubic structure. We feel that the position of the Pt peaks in Figure 2 could be explained in two forms: (*i*) the Pt lattice is slightly expanded because it has grown on the hexagonal Ni core and (*ii*)

this peak is the summation of the contribution of small hexagonal Ni crystallites together with the dominant Pt cubic phase.

From the Pt diffraction angles, the crystallite sizes have been estimated using the Scherrer Equation (2) and collected in Table 1:

$$d = \frac{K\lambda}{B\cos\theta} \quad (2)$$

where $K = 0.9$, λ (nm) is the wavelength of the X-ray radiation and B (radians) is the width of the measured diffraction peak at an intensity equal to half the maximum one.

Table 1. Mean crystallite size (from XRD), mean particle size (from TEM), composition (from EDS) and ECSA of the Pt(Ni)/C catalysts, compared to commercial Pt/C.

Catalyst	Crystallite Size/nm	Particle Size/nm	Pt Content/wt%	Ni Content/wt%	Pt:Ni/at%	ECSA [a] $/m^2$ g^{-1}
Pt(Ni)/C 3:1	2.4 ± 0.4	2.7 ± 0.5	15.1 ± 2.3	0.62 ± 0.11	88:12	47.8
Pt(Ni)/C 8:1	2.7 ± 0.5	3.5 ± 0.7	19.3 ± 2.8	0.11 ± 0.03	98:2	31.5
Pt/C	2.2 ± 0.5	2.6 ± 0.5	19.0 ± 1.1	0.0	100:0	74.5

[a] Relative error about 5%.

Representative TEM images of the specimens at different magnifications are given in Figure 3. Figure 3a and c show the homogeneous dispersion of the Pt(Ni) nanoparticles on carbon, whereas Figure 3b and d depict the corresponding HRTEM images. The size distribution has been included in the insets of Figure 3a,c, with the mean values also listed in Table 1. They are somewhat higher than those estimated from XRD, but this can be due to the difficulties is ascertaining from the TEM observations the real form of the nanoparticles and their possible aggregation.

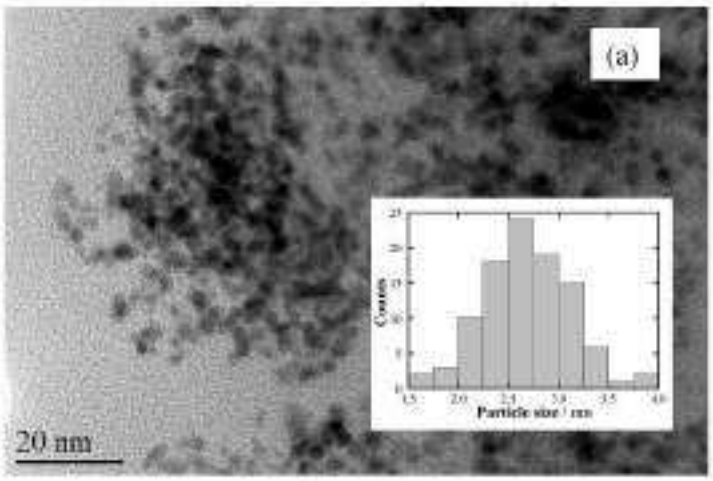

Figure 3. *Cont.*

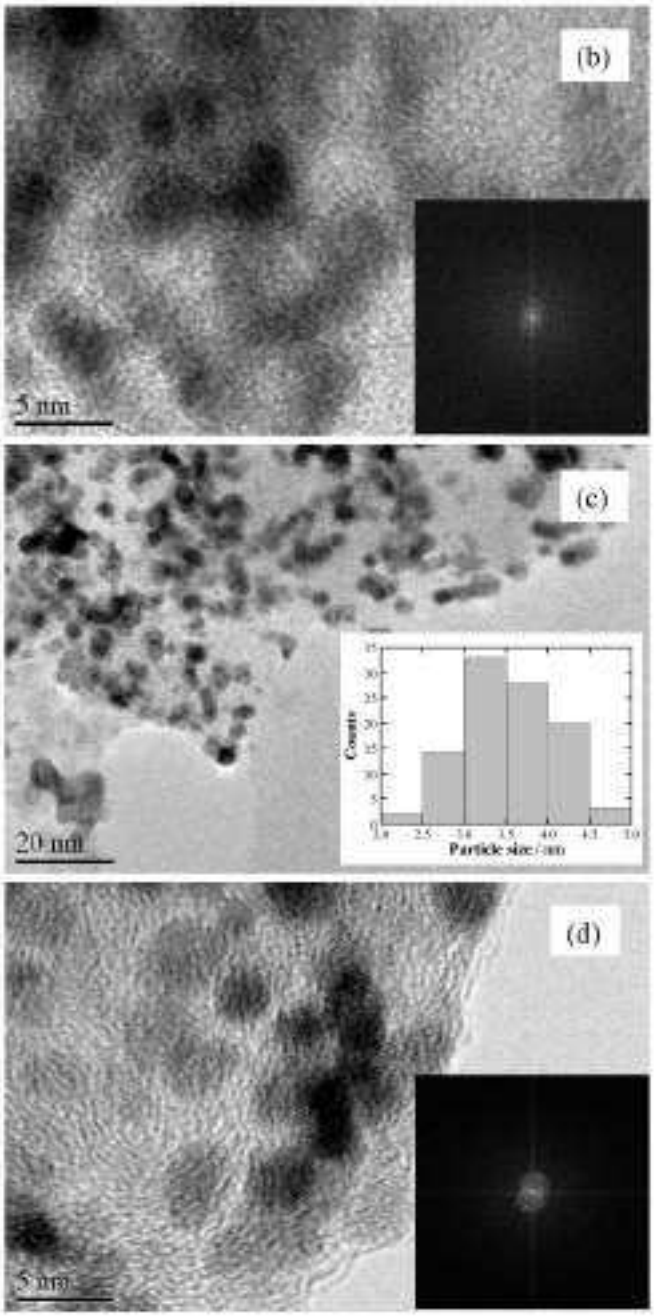

Figure 3. TEM pictures and size distribution of the nanoparticles of (**a**) Pt(Ni)/C 3:1 and (**c**) Pt(Ni)/C 8:1. The high resolution images of Pt(Ni)/C 3:1 and Pt(Ni)/C 8:1 are given in (**b**,**d**), respectively, together with the corresponding FFT pictures presented in the insets.

The Fast Fourier Transform (FFT) analyses given in the inset of Figure 3b reveal *d*-spacings of 2.32, 2.29 and 2.26 Å for the 3:1 precursor ratio, whereas that of Figure 3d, *d*-spacings of 2.35, 2.30, 2.25 and 1.96 Å for 8:1. These values are comparable to the *d*-spacings of 2.25 and 1.95 Å for cubic Pt and to 2.30, 2.17 and 2.03 Å for hexagonal Ni [58]. Cubic Ni should contribute with *d*-spacings of 2.04 and 1.77 Å and seems to be not relevant in this case, in agreement with the XRD results of Figure 2. On the other hand, the EDS analyses performed in STEM mode on different regions of the catalysts were similar, indicating a homogenous dispersion, and led to the mean values also listed in Table 1. It can be observed that the Pt contents in the Pt(Ni)/C catalysts are relatively high, with about 15 and 19 wt% for the 3:1 and 8:1 precursor ratios, respectively, and comparable to commercial Pt/C. The respective amounts of Ni were rather small, of about 0.6 and 0.1 wt%, which corresponded to relative Pt:Ni at% ratios of 88:12 and 98:2. Despite Pt clearly dominated, the TEM results also suggested the presence of small hexagonal Ni structures together with cubic Pt, in agreement with the XRD results. Due to the higher amount of Pt, the possibility that the Pt peaks in Figure 2 to be the summation of the contribution of small hexagonal Ni crystallites together with the dominant Pt cubic phase is more feasible.

2.3. CO Electrooxidation

The cyclic voltammograms corresponding to CO stripping experiments of the Pt(Ni)/C catalysts are depicted in Figure 4a. It is shown that the current-voltage profiles for both, Pt(Ni)/C 3:1 (curve *a*) and 8:1 (curve *b*) present peak potentials that are shifted to potentials more negative than that corresponding to Pt/C (curve *c*). This is related to the different onset potentials, which were about 0.38 and 0.44 V for Pt(Ni)/C 3:1 and 8:1, respectively, whereas that for Pt/C was about 0.48 V. Moreover, the CO stripping peaks in the Pt(Ni)/C catalysts can be deconvoluted into two contributions, with a shoulder at about 0.50 V and a peak at about 0.56 V, whereas only one peak at about 0.60 V appeared in the case of Pt/C. These two contributions for the Pt(Ni)/C catalysts suggest that CO oxidation takes place on two different surface Pt domains having different activity. Both show onset potentials placed at more negative values than that of Pt/C, meaning that more active structures for CO oxidation have been formed in Pt(Ni)/C. This can be explained by the formation of two different domains, one being Ni-rich, in which Ni is covered by a thin layer of Pt, and another one which is Pt-rich, consisting of a thicker layer of Pt on Ni. The peak potential of 0.6 V can be assigned to CO oxidation on Pt (100) and (111) terrace sites [55], which is consistent with the CV profile of Pt/C shown in Figure 1, curve *c*. According to this figure, the Pt(Ni) nanoparticles appeared to have Pt sites of the same type as those of pure Pt and for this reason, we may conclude that the negative shift of the onset potentials to more negative values for the Pt(Ni)/C catalysts was at least due to the electronic effect of Ni. In fact, Park et al. [31] have reported electronic effects of Ni on Pt in PtNi alloys with 1:1 and 3:1 atomic ratios, evidenced by the Pt 4*f* band shift of Pt to smaller binding energies due to the electronic donor effect of Ni. In addition, computational calculations of Jiang et al. [50] showed partial charge transfer from Ni to Pt in Pt_nNi_n alloy clusters, which was supposed to be responsible for the decreased CO poisoning. On the other hand, Corona et al. [32] reported the binding energy tuning of oxygen species with Pt for Pt(Ni) core-shell structures, thus increasing the activity for the oxygen reduction reaction. As a result, Ni in Pt(Ni) produces a positive effect in increasing the CO tolerance of Pt. It is also of interest to note that the onset potential for CO stripping in Pt(Cu)/C catalysts previously studied by us, obtained also by sequenced deposition, was about 0.4 V [17,42], a value close to that of Pt(Ni)/C, curve *a* in Figure 4a. This highlights that Ni and Cu behave in a similar manner in both catalysts. There is however, a significant difference in the onset potentials of Pt(Ni)/C 3:1 and 8:1, which can be the result of the different Pt:Ni atomic ratio in the Pt(Ni) catalysts, as found from the EDS analyses. Pt(Ni)/C 3:1 has higher amount of Ni than 8:1 and therefore, a greater quantity of Ni-rich domains is expected, thus explaining why the peak appearing at the most negative potential is more pronounced than in the latter.

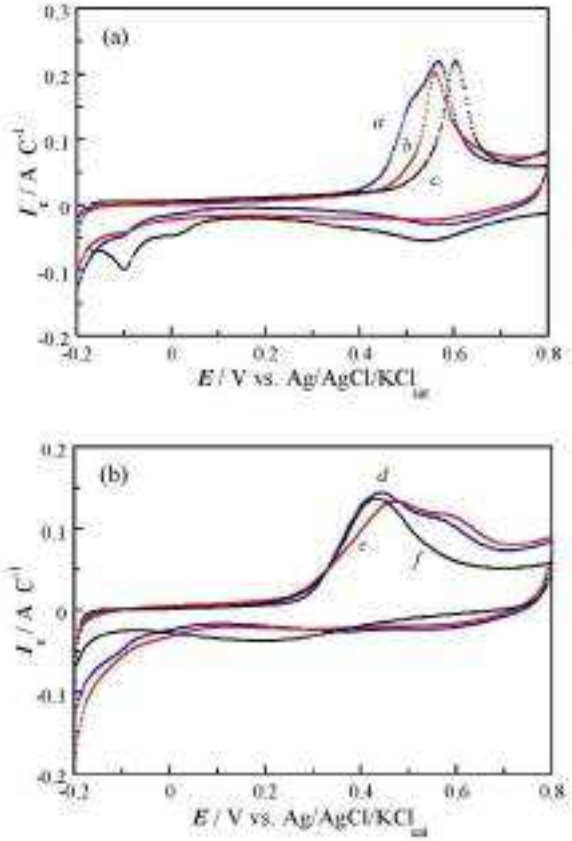

Figure 4. CO stripping experiments on the different catalysts in deaerated 0.5 M H_2SO_4. (a) Pt(Ni)/C 3:1 (curve *a*) and 8:1 (*b*), compared to Pt/C (*c*). (b) PtRu(Ni)/C 3:1 (curve *d*) and 8:1 (*e*), compared to commercial PtRu/C (*f*). Curves normalized to the CO stripping charge. Sweep rate 20 mV s^{-1}.

From all these results, the positive effect of Ni in the CO tolerance of Pt can be explained by the electronic effect of charge transfer to Pt (ligand effect), which weakens the CO adsorption strength. It is worth mentioning that oxidized Ni species have also been suggested to facilitate the CO oxidation reaction via hydrogen spillover and the enhanced oxidation of CO by nickel hydroxides [38]. No evidence about the presence of oxidized Ni species has been obtained in this paper because according to the cyclic voltammograms shown in Figure 1, it seems that Ni should be completely covered by Pt. A further discussion about this point is performed from the methanol oxidation results shown below.

It is also interesting to compare the CO stripping experiments obtained with the Pt(Ni)/C catalysts with those for PtRu(Ni)/C and PtRu/C. This is presented in Figure 4b, where the different curves have been also normalized to the CO stripping charge. It is shown that there is only one stripping peak for PtRu/C (curve *c*), with a peak potential of about 0.44 V, whereas there are two peaks at 0.44 and 0.56 V for both, Pt(Ni)/C 3:1 (curve *a*) and 8:1 (curve *b*). In the case of PtRu/C, due to the 1:1 atomic ratio, the active sites for CO oxidation have all similar structural characteristics. This appears to be different for PtRu(Ni)/C, in which two distinct structural regions seem to be present, the first one similar to that of PtRu/C (peak potential of 0.44 V) and the second one, similar to that found for Pt(Ni)/C in Figure 4a

(peak potential of 0.56 V). The most interesting result in Figure 4b is that the onset potentials for CO oxidation for both PtRu(Ni)/C catalysts are close to that of PtRu/C, of about 0.24 V. This represents a shift of about 0.14 and 0.20 V in the negative direction with respect to Pt(Ni)/C 3:1 and 8:1, and of about 0.24 V for PtRu/C with respect to Pt/C, respectively. An additional interesting feature is that this onset potential of about 0.24 V approximately coincides with that of PtRu(Cu)/C catalysts prepared by galvanic exchange of Pt with Cu [37,42].

Liang et al. [38] reported an onset potential for CO stripping in PtRuNi/C with 1:1:1 atomic ratios which was about the same as that obtained for PtRu/C. Wang et al. [18] studied the CO tolerance in PtRu/PtNi/C core shell catalysts synthesized by impregnation and high temperature reduction, followed by galvanic displacement of surface Ni by Ru species and further annealing treatment. The nominal atomic ratio of Pt to Ni was 3, and the onset potential for CO stripping in 0.1 M $HClO_4$ was about the same as that for PtRu/C, also in agreement with our results. However, the use of a PtNi core allowed saving the Pt amount and therefore, the mass specific currents (referred to the unit mass of Pt) were significantly higher. One can then conclude that Ni and Cu behave in a similar manner and that the Ru deposited species play the major role in PtRu(Ni)/C and PtRu(Cu)/C.

The Ru species expected to be deposited on Pt(Ni)/C are the same as those on Pt/C, mainly RuO_2 and hydrous oxides RuO_xH_y, as determined by XPS [61]. In this case, the formation of the hydroxylated species $RuO_xH_y(OH)$ through the following Equation (3) is expected [61,62]:

$$RuO_xH_y + H_2O \rightarrow RuO_xH_y(OH) + H^+ + e^- \quad (3)$$

then being $RuO_xH_y(OH)$ instead of Ru(OH) of Equation (1) the Ru species participating in the bifunctional Equation (4) favoring the CO removal:

$$RuO_xH_y(OH) + Pt\text{-}CO \rightarrow RuO_xH_y + Pt + CO_2 + H^+ + e^- \quad (4)$$

Due to the coverage of surface Pt by the Ru species, CO is easier removed by the bifunctional mechanism and the effect of Ni is not now detected due probably to its relatively small amount. In any case, the presence of Ni allows decreasing the cost of the catalyst because less amount of Pt is used.

2.4. Methanol Electrooxidation

The activity of the catalysts has been compared through the corresponding mass activities j_m (currents per Pt mass) and specific activities j_s (currents per squared cm of Pt), which are particularly useful to compare the catalytic activities when dealing with catalysts having different ECSAs [28,43,47]. They were determined from the catalyst loading on the GCE and the charge of the CO stripping peaks, considering that the oxidation of a CO monolayer on polycrystalline Pt needed 420 $\mu C\ cm^{-2}$ [63] leading to the ECSA results also listed in Table 1. Values in the range 50–100 $m^2\ g^{-1}$ are quite frequent in the literature and depend on the support employed and the synthesis procedure, which condition the number of nucleation centers for the metal deposition [39,40,43,59]. In our case, the Pt deposition in ethylene glycol proceeds on the previously prepared Ni/C specimens. In these conditions, apart from the Pt(IV) reduction by ethylene glycol, the galvanic exchange of Ni by Pt can also take place according to the following Euqaiton ($E^0 = 1.004$ V):

$$2\,Ni + PtCl_6^{2-} \rightarrow Pt + 2\,Ni^{2+} + 6Cl^- \quad (5)$$

It is then expected that Pt is mainly deposited on the Ni particles in Ni/C because of such a galvanic exchange and that the interaction between the metals is stronger than that with carbon. This can also explain that the ECSA of Pt(Ni)/C 8:1 is smaller than that of Pt(Ni)/C 3:1 because the smaller amount on Ni in the former can facilitate a greater Pt agglomeration. The higher mean size of the Pt(Ni)/C 8:1 nanoparticles estimated from the TEM analyses with respect to the mean values estimated from XRD is also in agreement with such a higher agglomeration in the latter.

The linear sweep voltammograms obtained for the methanol oxidation on the different catalysts studied are shown in Figure 5, the mass activities j_m in Figure 5a and the specific activities j_s in Figure 5b. It is apparent in Figure 5a,b that Pt(Ni)/C 3:1 (curves *a*) showed the most negative onset potentials of about 0.15 V, in front of those of Pt(Ni)/C 8:1 (curves *b*) and Pt/C (curves *c*), with respective onset potentials of about 0.25 and 0.30 V. The improved onset potentials for Pt(Ni)/C with respect to Pt/C correlated with their higher mass and specific activities depicted in Figure 5a,b. This cannot be assigned to the ability of Ni itself for the MOR because, at least, the most part of Ni in the Pt(Ni) nanoparticles can be supposed to be occluded by Pt shells. On the other hand, it was evidenced by Macias-Ferrer et al. [50] that carbon-supported Ni did not have catalytic activity for the MOR. These results are also in agreement with those reported in this paper for CO oxidation (Figure 4a), what is not strange because CO appears to be an intermediate in the methanol oxidation [8,64].

It is also shown in the insets of Figure 5a,b the j_m and j_s values of the catalysts at 0.4 V for a better comparison of their activity. Note the highest j_m value of 220 mA mg_{Pt}^{-1} for Pt(Ni)/C 3:1 in front of 75 and 97 mA mg_{Pt}^{-1} for Pt(Ni)/C 8:1 and Pt/C, respectively. The same trend is observed for j_s, with respective values of 0.45, 0.23 and 0.24 mA cm_{Pt}^{-2} for Pt(Ni)/C 3:1, Pt(Ni)/C 8:1 and Pt/C. The difference between both Pt(Ni)/C catalysts could be also explained by their different relative amount of Ni-rich domains, which would be more active for the methanol (and CO) oxidation, and Pt-rich ones, less active for these reactions. The Ni-rich domains should be more abundant in Pt(Ni)/C 3:1 and this correlated with its greater activity. The smaller mass activities found for Pt(Ni)/C 8:1 could be explained by its smaller Ni content, making it more similar to Pt/C. In fact, Guerrero-Ortega et al. [52] reported maximum mass activities at 20 mV s^{-1} in the same electrolyte of about 700 mA mg_{Pt}^{-1} for methanol oxidation in Ni_3Pt alloys, a value greater than that obtained in the present work of about 420 mA mg_{Pt}^{-1}. This difference can be ascribed to the different Ni content and suggests that it can be increased with the amount of Ni. It is also interesting to remark that Wang et al. [51] reported also onset potentials of about 0.1–0.2 V vs. SCE, which is about 0.15–0.25 V vs. $Ag/AgCl/KCl_{sat}$, at a sweep rate of 50 mV s^{-1} in 0.5 M methanol +0.5 M H_2SO_4, for *fcc* PtNi alloys supported on electrochemically reduced porous graphene oxide. The best onset potentials and the maximum current densities were achieved for the Pt:Ni atomic ratio of 1:1, decaying for higher Pt relative contents and also for higher Ni relative contents. The structure and electronic modification of Pt by Ni has always been invoked to explain the favorable effect of Ni in the alloy in front of the MOR, although some effect of the Ni oxidized species has also been considered [31,51,52]. These results points to that there is a scope to optimize the synthesis of the Pt(Ni)/C catalysts of the present paper to obtain better mass activities.

The onset potentials when using PtRu appeared to be better than those obtained with PtNi, as in the case of CO. Considering the potential scale of the $Ag/AgCl/KCl_{sat}$ reference electrode, onset potentials for the MOR in commercial 1:1 PtRu/C in the conditions of the present paper of about 0.10 V were reported by us [65]. Park et al. [31] gave onset potentials in 2.0 M methanol +0.5 M H_2SO_4 at 50 mV s^{-1} of 0.15, 0.07, 0.09, 0.12 and 0.06 V for pure Pt, 1:1 Pt:Ru, 1:1 Pt:Ni, 3:1 Pt:Ni, and 5:4:1 Pt:Ru:Ni alloy nanoparticle catalysts, respectively. It is then demonstrated that the onset potentials for PtNi catalysts may approach those of PtRu ones, but they are still smaller. This is probably related to the mechanism of the methanol oxidation on these different catalysts. To obtain further insight about this point, the E vs $\log j_s$ plots shown in Figure 6 were performed, from which the anodic Tafel slopes b_a and charge transfer coefficients α_a were obtained and collected in Table 2. Note that the specific current densities j_s corresponded to real current densities because they were referred to the unit area of Pt.

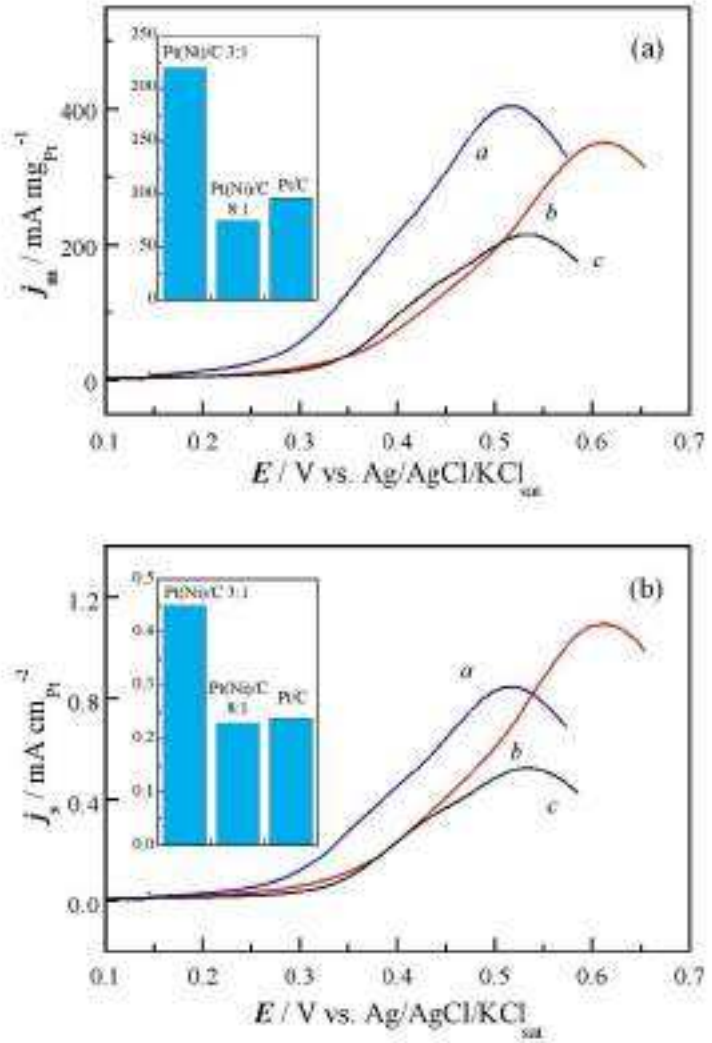

Figure 5. Linear sweep voltammograms obtained for the methanol oxidation in 1.0 M methanol +0.5 M H_2SO_4 on the Pt(Ni)/C 3:1 (curves *a*) and 8:1 (curves *b*), compared to those of Pt/C (curves *c*), corresponding to (**a**) the mass activities j_m, and to (**b**) the specific activities j_s. Sweep rate of 20 mV s^{-1}. The j_m and j_s values at 0.4 V are given in the insets.

Good correlation between E and log j_s can be observed, with squared correlation coefficients greater than 0.99. The respective exchange current densities j_{0s}, estimated by extrapolating the Tafel plots to the standard potential of the MOR of −0.153 V vs. Ag/AgCl/KCl$_{sat}$ (0.046 V vs. SHE) [65], are listed in Table 2.

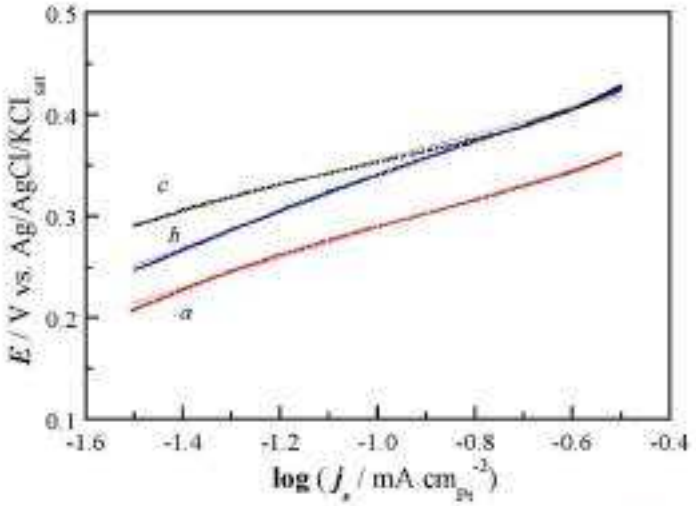

Figure 6. Tafel plots corresponding to the linear sweep voltammograms of Figure 5b. Methanol oxidation in 1.0 M methanol + 0.5 M H_2SO_4 on the Pt(Ni)/C 3:1 (*a*) and 8:1 (*b*) catalysts, compared to that of Pt/C (*c*).

Table 2. Tafel slopes b_a, anodic charge transfer coefficients α_a, and exchange current densities j_{s0} of the MOR, as determined from Figure 6.

Catalyst	b_a/V dec^{-1}	α_a	j_{s0}/mA cm^{-2}
Pt(Ni)/C 3:1	0.150	0.39	1.3×10^{-4}
Pt(Ni)/C 8:1	0.170	0.35	1.2×10^{-4}
Pt/C	0.125	0.48	1.3×10^{-5}

The j_{s0} results clearly evidence that the Pt(Ni)/C catalysts were about ten times more active than Pt/C. The different values of the Tafel slopes and of the anodic charge transfer coefficients also point out to differences in the mechanism for the methanol oxidation on Pt(Ni)/C and Pt/C. The Tafel slope of 0.125 V dec^{-1} and the charge transfer coefficient of 0.48 are close to the values of 0.119 V dec^{-1} and 0.5, respectively, predicted for one electron transfer step as the rate-determining process with the adsorbed intermediates following a Langmuir isotherm [65]. In the case of the methanol oxidation on PtRu/C, in which the hydroxylated species on Ru participated in the bifunctional mechanism, a Tafel slope of 0.199 V dec^{-1} was found, the oxidation of the intermediate CO-type species being proposed as the rate-determining step [65]. Tafel slopes in the range 0.123 to 0.230 V dec^{-1} were also reported in our previous kinetic studies of methanol oxidation on Ru-decorated Pt/C, when the coverage of the Pt sites varied from 0.0 to 0.6, which was attributed to an increase in the amount of the hydroxylated Ru species with coverage [11]. The Tafel slopes and charge transfer coefficients for the MOR on Pt(Ni)/C are intermediate between those found for Pt/C and PtRu/C and suggest that the rate-determining step of the reaction on Pt(Ni)/C is also the oxidation of the intermediate CO-type species. It has been reported in previous studies that $Ni(OH)_2$ plays a role in the CO oxidation and the MOR on PtNi alloys [31,38,51,52], which it is not easily dissolved [28], because it can be oxidized according to Equation (6) [31,38].

$$Ni(OH)_2 \rightarrow NiOOH + H^+ + e^- \quad (6)$$

and can be recovered by the following redox Equations (7) and (8):

$$NiOOH + x\ Pt\text{-}H \rightarrow Ni(OH)_2 + x\ Pt \quad (7)$$

$$2\ NiOOH + Pt\text{-}CO + H_2O \rightarrow 2\ Ni(OH)_2 + CO_2 + Pt \quad (8)$$

Coming back to the present catalysts it seems improbable that there were significant amounts of $Ni(OH)_2$, considering the cyclic voltammograms of Figure 1 and the overall amount of Ni in the catalysts, as previously discussed. There is in fact the possibility of some $Ni(OH)_2$ formation because the galvanic exchange of Equation (5) leads to Ni^{2+} and in addition, the different structure of Ni and Pt may produce defective Pt/Ni interfaces enabling some Ni oxidation during the anodic scans. However, no significant quantity is expected and the electronic effect of charge transfer (ligand effect) of Ni to Pt is considered the main reason explaining why the activity of Pt(Ni)/C in front of the CO oxidation and the MOR is higher than that of Pt/C. However, these results open the way to further studies analyzing the possible presence and role of oxidized Ni species in Pt(Ni)/C.

3. Materials and Methods

3.1. Synthesis of the Pt(Ni)/C and PtRu(Ni)/C Catalysts

The dispersion of Ni nanoparticles on carbon was prepared by chemical reduction of the Ni(II) precursor with sodium borohydride in basic medium using a procedure adapted from Hosseini et al. [59] and Zignani et al. [39]. The carbon employed was Vulcan XC72R (Cabot Corporation, Boston, MA, USA), which presents a particle size of about 30 nm and a surface area of about 250 $m^2\ g^{-1}$ [17,66], which is frequently used as a support in the literature because its low cost and sufficiently high surface area to obtain a good dispersion of the catalyst nanoparticles. Instead of Pt(IV) and Ni(II) precursors co-reduction, the Ni(II) was reduced first and afterwards, Pt was deposited from a Pt(IV) precursor in order to approach a core-shell structure [43]. First, a carbon dispersion was prepared with 10 mg of carbon, 1.5 mL of isopropyl alcohol (analytical grade, Merck KGaA, Darmstadt, Germany) and 0.5 mL of distilled water, purified by means of a Millipore Direct-Q 3UV-R system ($\rho > 18.2\ M\Omega\ cm$, Merck, Darmstadt, Germany). This mixture was sonicated for 1 h. Then a $NiCl_2$ solution prepared dissolving a given amount of $NiCl_2.6H_2O$ (99.95%, Alfa Aesar, Haverhill, MA, USA) in 1 mL of water was added and further dispersed for 1 h more. The amount of the Ni(II) precursor to prepare 1 mL of such solution was about 10 mg. Afterwards, 0.0165 g of trisodium citrate (analytical grade, Merck KGaA, Darmstadt, Germany) dissolved in 1 mL of water was added to the mixture as a stabilizing agent. Finally, a solution prepared with 0.0337 g of $NaBH_4$ (analytical grade, Merck KGaA, Darmstadt, Germany) and 0.0050 g of NaOH (analytical grade, Alfa Aesar, Haverhill, MA, USA) in 5 mL of water was added dropwise with vigorous stirring at 75 °C. The Ni hydrosol was aged for 24 h at 70 °C in open oven to decompose the residual $NaBH_4$ and obtain dry powder.

The resulting Ni/C powder was dispersed in 3.5 mL ethylene glycol (analytical grade, Alfa Aesar, Haverhill, MA, USA) for 2 h and then, the corresponding amount of 10 wt.% H_2PtCl_6 solution (3 wt.% Pt) (analytical grade, Merck KGaA, Darmstadt, Germany) was added. The amount of the Pt(IV) precursor employed depended on the catalyst to be synthesized, varying between 1:1 and 8:1 the relative content in weight of Pt to Ni in the Pt(IV):Ni(II) precursor ratios. The pH of the mixture was adjusted to a value in the range 7.0–8.0 and it was then stirred for 4 h at 90 °C. The Pt(Ni)/C electrocatalyst was collected after washing with water and then oven dried at 80 °C.

On the basis of the synthesized Pt(Ni)/C catalysts, the PtRu(Ni)/C ones were prepared by spontaneous deposition, as indicated elsewhere [17]. To obtain these catalysts, 1.0 mg mL^{-1} dispersion of Pt(Ni)/C in a 1:1 mixture by volume of isopropanol/water was prepared. Then, 40 µL of this dispersion were placed on the tip of a clean glassy carbon electrode (GCE) and dried under a lamp. Afterwards, the modified electrode was introduced into an aged 8.0 mM solution of $RuCl_3$ in 0.10 M $HClO_4$ (analytical grade Alfa Aesar, Haverhill, MA, USA and Merck, Darmstadt, Germany, respectively)

for 30 min without stirring to carry out the spontaneous deposition of Ru species [17]. This immersion time was selected because in these conditions, intermediate coverage values of the Pt sites by Ru species, suitable for CO and methanol oxidation, were obtained [10,17,67]. Accordingly, PtRu(Ni)/C is mainly Pt(Ni)/C with Ru species on the surface. After careful rinsing with water, the PtRu(Ni)/C catalyst was ready for testing.

3.2. Structural Analyses

The Pt(Ni)/C catalysts were characterized by means of XRD with a PANalytical X'Pert PRO MPD θ/θ powder diffractometer (Cu anode, 45 kV, 40 mA, Malvern Panalytical Ltd., Malvern, UK), using a Cu K_α-filtered radiation (λ = 1.5418 Å), 2θ step size of 0.026° and a measuring time of 200 s per step. The powder of the samples to be analyzed were sandwiched between 3.6-µm thick polyester films.

The samples were examined by TEM using a Hitachi H-800 MT electron microscope (Chiyoda, Tokyo, Japan), which was provided with an EDS detector for the elemental analyses, and by HRTEM with a 200 kV JEOL JEM 2100 F (Akishima, Tokyo, Japan). The elemental analyses by EDS was performed on five different representative zones, taking the average with the experimental error. The size distribution was determined from TEM by counting more than one hundred nanoparticles. The high-resolution pictures, recorded in a Gatan Multiscan 794 charge-coupled device camera, were treated by means of the Gatan Digital Micrograph 3.7.0 software (Pleasanton, CA, USA) to obtain the corresponding FFT images, from which the d-spacing values were determined. To prepare the samples for observation, small amounts of the catalysts were sonicated in 3 mL of n-hexane for 10 min and then, a drop of the dispersion was placed on a holey carbon grid, which was heated with a lamp to evaporate the solvent.

3.3. Electrochemical Testing

The electrochemical characterization was carried out in a conventional three-electrode 100 mL cell (PAR, Ametek, Berwyn, PA, USA) with double wall for thermostatization by means of a PARSTAT (PAR) 3000A potentiostat. The base electrolyte was 0.5 M H_2SO_4 (analytical grade, Merck KGaA, Darmstadt, Germany), deaerated by N_2 purging (99.999%, Praxair, Nippon Gases, Japan). The auxiliary electrode was a rolled Pt wire. The reference electrode was a double junction Ag/AgCl/KCl_{sat} (E = 0.199 V vs. SHE at 25 °C). All the potentials given in this paper have been referred to such a reference electrode. The working electrode was a GCE 5 mm in diameter (0.196 cm^2 in section) GCE (PINE Research Instrumentation, Durham, NC, USA), surface-modified by the catalyst. Prior to the modification, the GCE was polished consecutively with an alumina suspension of 0.3 and 0.05 µm in grain size using a polishing cloth (ALS Co., Ltd., Tokyo, Japan) to achieve specular gloss. Between polishing steps, the electrode was sonicated in water and dried. For the electrochemical testing, amounts of 1.0 mg mL^{-1} of the Pt(Ni)/C catalyst powders were dispersed by sonication in isopropanol/water mixture 1:1 by volume and then, 40 µL of each dispersion were dropped on the GCE, which was further dried by heating with a lamp. In the cell containing deaerated 0.5 M H_2SO_4, the catalyst was submitted to a cleaning protocol by CV consisting in consecutive cycles at 100, 50 and 20 mV s^{-1} in the potential range between −0.2 and 0.8 V up to a stationary profile. The PtRu(Ni)/C catalysts prepared by spontaneous deposition of Ru species were also submitted to the same cleaning protocol.

After the cleaning protocol, the CO electrooxidation activity was analyzed by means of CO stripping voltammograms in 0.5 M H_2SO_4 and the same potential range between −0.2 and 0.8 V at 20 mV s^{-1}. For the CO adsorption, CO gas (Linde 3.0, purity greater than 99.9%, Dublin, Ireland) was bubbled through the solution for 15 min while applying a potential of −0.100 V to the working electrode. The non-adsorbed CO remaining in solution was removed by N_2 bubbling through the solution for 30 min. The activity of the catalysts for the methanol reaction was examined by LSV at 20 mV s^{-1}, starting the scan from −0.2 V. The corresponding tests were performed using deaerated 1.0 M solutions of each alcohol (analytical grade, Panreac Química, Barcelona, Spain) in 0.5 M H_2SO_4. The experiments were repeated three times to test the reproducibility. The corresponding results were

compared to those obtained from commercial 20 wt% Pt/C and 20 wt% 1:1 PtRu/C (Premetek, Cherry Hill, NJ, USA) catalysts.

4. Conclusions

In this paper, the electrochemical performance of Pt(Ni)/C and PtRu(Ni)/C catalysts, synthesized by sequenced deposition of Ni, Pt and Ru to approach core-shell structures, in front of the CO and methanol oxidation reactions has been studied. The best hydrogen desorption charges were obtained for the Pt(Ni)/C alloys with relative amounts in weight of Pt to Ni of 3:1 and 8:1. The EDS analyses indicated 88:12 and 98:2 Pt:Ni atomic ratios in these alloys, respectively, the corresponding ECSAs being of 47.8 and 31.5 $m^2\ g_{Pt}^{-1}$. The XRD, HRTEM and FFT analyses pointed out to the formation of small hexagonal Ni crystallites covered by cubic Pt surface structures with no evidence about PtNi alloy formation. Two anodic peaks were found in the CO oxidation on Pt(Ni)/C alloys, thus suggesting the presence of two distinct structural domains in the catalyst surface, probably Pt on hexagonal Ni-rich domains and on cubic Pt-rich ones. The potential shift in the negative direction of about 0.10 V for the onset of CO oxidation in Pt(Ni)/C with respect to Pt/C was explained by the charge transfer of Ni to Pt (ligand effect), which resulted in an easier removal of adsorbed CO, thus increasing the CO tolerance of the catalyst. The onset potential for CO oxidation and tolerance was improved with PtRu(Ni)/C. The effect of surface Ru species spontaneously deposited on Pt appeared to present the major effect by facilitating the CO removal by the bifunctional mechanism. The onset potentials of Pt(Ni)/C 3:1 and 8:1 for the methanol oxidation, which were about 0.15 and 0.05 V lower than that of Pt/C, respectively, depending on the Ni content, also indicated the positive effect of Ni. The mass and specific activities of the Pt(Ni)/C catalysts were also higher than those of Pt/C, with exchange current densities one order of magnitude greater than that of the latter. The experimental Tafel slopes for the MOR on Pt(Ni)/C were higher, and the charge transfer coefficients smaller, than those of Pt/C, thus suggesting different rate-determining steps in the mechanism. The ligand effect of Ni on Pt was also considered the main reason why the activity of Pt(Ni)/C in front of the MOR was higher than that of Pt/C.

Author Contributions: G.C.-M. and P.L.C. conceived and designed the experiments; G.C.-M., J.M.S. and J.G.-C. performed the experiments; G.C.-M., E.B., and P.L.C. analyzed the data; J.A.J. and J.G.-C. contributed reagents/materials/analysis tools; G.C.-M., J.A.J., P.L.C. and E.B. wrote the paper. All authors have read and agreed to the published version of the manuscript.

Funding: The authors thank the financial support from the National Secretariat for Science, Technology, and Innovation of Panama (SENACYT) through the Project FID-16-035 and National Research System (SNI).

Acknowledgments: The authors thank the Scientific and Technological Centers of the University de Barcelona (CCIT-UB) for the TEM and XRD analysis facilities.

Conflicts of Interest: The authors declare no conflict of interest. The funding sponsors had no role in the design of the study; in the collection, analyses, or interpretation of data; in the writing of the manuscript, and in the decision to publish the results.

References

1. Serov, A.; Zenyuk, I.; Arges, C.; Chatenet, M. Hot topics in alkaline exchange membrane fuel cells. *J. Power Sources* **2017**, *375*, 149–157. [CrossRef]
2. Alcaide, F.; Cabot, P.L.; Brillas, E. Fuel Cell for chemicals and energy cogeneration. *J. Power Sources* **2006**, *153*, 47–60. [CrossRef]
3. Cohen, J.; Volpe, D.; Abruña, H. Electrochemical determination of activation energies for methanol oxidation on polycrystalline platinum in acidic and alkaline electrolytes. *Phys. Chem. Chem. Phys.* **2007**, *9*, 49–77. [CrossRef] [PubMed]
4. Demirci, U.B. Direct liquid-feed fuel cells: Thermodynamic and environmental concerns. *J. Power Sources* **2007**, *169*, 239–246. [CrossRef]
5. Ong, B.C.; Kamaruddin, S.K.; Basri, S. Direct liquid fuel cells: A review. *Int. J. Hydrogen Energy* **2017**, *42*, 10142–10157. [CrossRef]

6. Apanel, G.; Johnson, E. Direct methanol fuel cells—Ready to go commercial? *Fuel Cells* **2004**, *11*, 12–17. [CrossRef]
7. Vassiliev, Y.B.; Bagotsky, V.S.; Osetrova, N.V.; Khasova, O.A.; Mayorova, N.A. Electroreduction of carbon dioxide: Part I. The mechanism and kinetics of electroreduction of CO_2 in aqueous solutions on metals with high and moderate hydrogen overvoltages. *J. Electroanal. Chem. Interfacial Electrochem.* **1985**, *189*, 271–294. [CrossRef]
8. Puthiyapura, V.K.; Lin, W.F.; Russell, A.E.; Brett, D.J.L.; Hardacre, C. Effect of Mass Transport on the Electrochemical Oxidation of Alcohols Over Electrodeposited Film and Carbon-Supported Pt Electrodes. *Top. Catal.* **2018**, *61*, 240–253. [CrossRef]
9. Spendelow, J.S.; Wieckowski, A. Electrocatalysis of oxygen reduction and small alcohol oxidation in alkaline media. *Phys. Chem. Chem. Phys.* **2007**, *9*, 2654–2675. [CrossRef]
10. Ruth, K.; Vogt, M.; Zuber, R. Development of CO-Tolerant Catalysts. In *Handbook of Fuel Cells–Fundamentals, Technology and Applications*; Vielstich, W., Gasteiger, H.A., Lamm, A., Eds.; John Wiley & Sons: New York, NY, USA, 2003; Volume 3, pp. 489–496.
11. Velázquez-Palenzuela, A.; Brillas, E.; Arias, C.; Centellas, F.; Garrido, J.A.; Rodríguez, R.M.; Cabot, P.L. Carbon monoxide, methanol and ethanol electro-oxidation on Ru decorated carbon-supported Pt nanoparticles prepared by spontaneous deposition. *J. Power Sources* **2013**, *225*, 163–171. [CrossRef]
12. Antolini, E. Effect of the structural characteristics of binary Pt-Ru and ternary Pt-Ru-M fuel cell catalysts on the activity of ethanol electrooxidation in acid medium. *ChemSusChem* **2013**, *6*, 966–973. [CrossRef] [PubMed]
13. Rigsby, M.A.; Zhou, W.P.; Lewera, A.; Duong, H.T.; Bagus, P.S.; Jaegermann, W.; Hunger, R.; Wieckowski, A. Experiment and theory of fuel cell catalysis: Methanol and formic acid decomposition on nanoparticle Pt/Ru. *J. Phys. Chem. C* **2008**, *112*, 15595–15601. [CrossRef]
14. Caballero-Manrique, G.; Brillas, E.; Centellas, F.; Garrido, J.A.; Rodríguez, R.M.; Cabot, P.L. Electrochemical oxidation of the carbon support to synthesize Pt(Cu) and Pt-Ru(Cu) core-shell electrocatalysts for low-temperature fuel cells. *Catalysts* **2015**, *5*, 815–837. [CrossRef]
15. Watanabe, M.; Motoo, S. Electrocatalysis by ad-atoms: Part III. Enhancement of the oxidation of carbon monoxide on platinum by ruthenium ad-atoms. *J. Electroanal. Chem. Interfacial Electrochem.* **1975**, *60*, 275–283. [CrossRef]
16. Brankovic, S.R.; Wang, J.X.; Adzic, R.R. Pt Submonolayers on Ru Nanoparticles: A Novel Low Pt Loading, High CO Tolerance Fuel Cell Electrocatalyst. *Electrochem. Solid-State Lett.* **2001**, *4*, 217–220. [CrossRef]
17. Caballero-Manrique, G.; Velázquez-Palenzuela, A.; Centellas, F.; Garrido, J.A.; Arias, C.; Rodríguez, R.M.; Brillas, E.; Cabot, P.L. Electrochemical synthesis and characterization of carbon-supported Pt and Pt-Ru nanoparticles with Cu cores for CO and methanol oxidation in polymer electrolyte fuel cells. *Int. J. Hydrogen Energy* **2014**, *39*, 12859–12869. [CrossRef]
18. Wang, Q.; Wang, G.; Tao, H.; Li, Z.; Han, L. Highly CO tolerant PtRu/PtNi/C catalyst for polymer electrolyte membrane fuel cell. *RSC Adv.* **2017**, *7*, 8453–8459. [CrossRef]
19. Dinh, H.; Ren, X.; Garzon, F.; Zelenay, P.; Gottesfeld, S. Electrocatalysis in direct methanol fuel cells: In-situ probing of PtRu anode catalyst surfaces. *J. Electroanal. Chem.* **2000**, *491*, 222–233. [CrossRef]
20. Alcaide, F.; Álvarez, G.; Cabot, P.L.; Genova-Koleva, R.V.; Grande, H.J.; Martínez-Huerta, M.; Miguel, O. Supporting PtRh alloy nanoparticle catalysts by electrodeposition on carbon paper for the ethanol electrooxidation in acidic medium. *J. Electroanal. Chem.* **2020**, *861*, 113960. [CrossRef]
21. Iwasita, T.; Pastor, E. A DEMS and FTIR spectroscopic investigation of adsorbed ethanol on polycrystalline platinum. *Electrochim. Acta* **1994**, *39*, 531–537. [CrossRef]
22. Zhou, W.; Zhou, Z.; Song, S.; Li, W.; Sun, G.; Tsiakaras, P.; Xin, Q. Pt based anode catalysts for direct ethanol fuel cells. *Appl. Catal. B* **2003**, *46*, 273–285. [CrossRef]
23. Zignani, S.C.; Baglio, V.; Sebastián, D.; Siracusano, S.; Aricò, A.S. Enhancing ethanol oxidation rate at PtRu electro-catalysts using metal-oxide additives. *Electrochim. Acta* **2016**, *191*, 183–191. [CrossRef]
24. Zhou, W.K.; Zhou, B.; Li, W.Z.; Zhou, Z.H.; Song, S.Q.; Sun, G.Q.; Xin, Q.; Douvartzides, S.; Goula, M.; Tsiakaras, P. Performance comparison of low-temperature direct alcohol fuel cells with different anode catalysts. *J. Power Sources* **2004**, *126*, 16–22. [CrossRef]
25. Zhou, W.J.; Li, W.Z.; Song, S.Q.; Zhou, Z.H.; Jiang, L.H.; Sun, G.Q.; Xin, Q.; Poulianitis, K.; Kontou, S.; Tsiakaras, P. Bi- and tri-metallic Pt-based anode catalysts for direct ethanol fuel cells. *J. Power Sources* **2004**, *131*, 217–223. [CrossRef]

26. Spinacé, E.V.; Dias, R.R.; Brandalise, M.; Linardi, M.; Neto, A.O. Electro-oxidation of ethanol using PtSnRh/C electrocatalysts prepared by an alcohol-reduction process. *Ionics* **2010**, *16*, 91–95. [CrossRef]
27. Macias-Ferrer, D.; Melo, J.A.; Páramo, U.; Silva, R.; Lam-Maldonado, M.; Meraz-Melo, M.A.; Verde-Gómez, J.Y.; Díaz-Zavala, N.P. Pt, Co, Fe and Ni Nanoparticles on Micro/Nano-Structured Carbon for the Methanol Electro-Oxidation in Acid Medium. *AJER* **2018**, *7*, 344–356. [CrossRef]
28. Beermann, V.; Gocyla, M.; Willinger, E.; Rudi, S.; Heggen, M.; Dunin-Borkowski, R.E.; Willinger, M.G.; Strasser, P. Rh-doped Pt-Ni octahedral nanoparticles: Understanding the correlation between elemental distribution, ORR and shape stability. *Nano Lett.* **2016**, *16*, 1719–1725. [CrossRef]
29. Shen, Y.; Zhang, M.Z.; Xiao, K.; Xi, J. Synthesis of Pt, PtRh, and PtRhNi alloys supported by pristine graphene nanosheets for ethanol oxidation. *ChemCatChem* **2014**, *6*, 3254–3261. [CrossRef]
30. Stamenkovic, V.R.; Mun, B.S.; Arenz, M.; Mayrhofer, K.J.J.; Lucas, C.A.; Wang, G.F.; Ross, P.N.; Markovic, N.M. Trends in electrocatalysis on extended and nanoscale Pt-bimetallic alloy surfaces. *Nat. Mater.* **2007**, *6*, 241–247. [CrossRef]
31. Park, K.W.; Choi, J.H.; Kwon, B.K.; Lee, S.A.; Sung, Y.E.; Ha, H.Y.; Hong, S.A.; Kim, H.; Wieckowski, A. Chemical and Electronic Effects of Ni in Pt/Ni and Pt/Ru/Ni Alloy Nanoparticles in Methanol Electrooxidation. *J. Phys. Chem. B* **2002**, *106*, 1869–1877. [CrossRef]
32. Cerqua, B.; Howard, M.; Zhang, L.; Henkelman, G. Computational screening of core@shell nanoparticles for the hydrogen evolution and oxygen reduction reactions. *J. Chem. Phys.* **2016**, *145*, 244708. [CrossRef] [PubMed]
33. Choi, J.; Lee, Y.; Kim, J.; Lee, H. Enhancing stability of octahedral PtNi nanoparticles for oxygen reduction reaction by halide treatment. *J. Power Sources* **2016**, *307*, 883–890. [CrossRef]
34. Wu, F.; Liu, Y.; Wu, C. Preparation of Pt/C Nanocatalysts by Ethylene Glycol Method in Weakly Acidic Solutions. *J. Mater. Sci. Technol.* **2010**, *26*, 705–710. [CrossRef]
35. Mohanraju, K.; Cindrella, L. One-pot surfactant-free synthesis of high surface area ternary alloys, PtMCo/C (M ½ Cr, Mn, Fe, Ni, Cu) with enhanced electrocatalytic activity and durability for PEM fuel cell application. *Int. J. Hydrogen Energy* **2016**, *41*, 9320–9331. [CrossRef]
36. Stephen, A.; Ross, N.; Mikheenko, I.; Macaskie, L. Platinum and Palladium Bio-Synthesized Nanoparticles as Sustainable Fuel Cell Catalysts. *Front. Energy Res.* **2019**, *7*, 1–13. [CrossRef]
37. Serra, A.; Gómez, E.; Vallés, E. Novel electrodeposition media to synthesize CoNi-Pt Core@Shell stable mesoporous nanorods with very high active surface for methanol electro-oxidation. *Electrochim. Acta* **2015**, *174*, 630–639. [CrossRef]
38. Liang, Y.; Zhang, H.; Tian, Z.; Zhu, X.; Wang, X.; Yi, B. Synthesis and Structure-Activity Relationship Exploration of Carbon-Supported PtRuNi Nanocomposite as a CO-Tolerant Electrocatalyst for Proton Exchange Membrane Fuel Cells. *J. Phys. Chem. B* **2006**, *110*, 7828–7834. [CrossRef]
39. Zignani, S.; Baglio, V.; Sebastián, D.; Rochi, T.; Gonzalez, E.; Arico, A. Investigation of PtNi/C as methanol tolerant electrocatalyst for the oxygen reduction reaction. *J. Electroanal. Chem.* **2016**, *763*, 10–17. [CrossRef]
40. Mershchikov, V.; Alekseenko, A.; Guterman, V.; Nechitailov, A.; Glebova, N.; Tomasov, A.; Spiridonova, O.; Belenov, S.; Zelenina, N.; Safronenko, O. Effective Platinum-Copper Catalysts for Methanol Oxidation and Oxygen Reduction in proton-Exchange membrane Fuel Cell. *Nanomaterials* **2020**, *10*, 742. [CrossRef]
41. Antolini, E.; Salgado, J.R.C.; Gonzalez, E.R. Carbon supported Pt75M25 (M = Co, Ni) alloys as anode and cathode electrocatalysts for direct methanol fuel cells. *J. Electroanal. Chem.* **2005**, *580*, 145–154. [CrossRef]
42. Caballero-Manrique, G.; Nadeem, I.; Brillas, E.; Centellas, F.; Garrido, J.A.; Rodriguez, R.M.; Cabot, P.L. Effects of the Electrodeposition Time in the Synthesis of Carbon-Supported Pt(Cu) and Pt-Ru(Cu) Core-Shell Electrocatalysts for Polymer Electrolyte Fuel Cells. *Catalysts* **2016**, *6*, 125. [CrossRef]
43. García-Cardona, J.; Sirés, I.; Alcaide, F.; Brillas, E.; Centellas, F.; Cabot, P.L. Electrochemical performance of carbon-supported Pt(Cu) electrocatalysts for low-temperature fuel cells. *Int. J. Hydrogen Energy* **2020**, in press. [CrossRef]
44. Erini, N.; Rudi, S.; Beermann, V.; Krause, P.; Yang, R.; Huang, Y.; Strasser, P. Exceptional Activity of a Pt–Rh–Ni Ternary Nanostructured Catalyst for the Electrochemical Oxidation of Ethanol. *ChemElectroChem* **2015**, *2*, 903–908. [CrossRef]
45. Wang, Z.B.; Zuo, P.J.; Wang, G.J.; Du, C.Y.; Yin, G.P. Effect of Ni on PtRu/C Catalyst Performance for Ethanol Electrooxidation in Acidic Medium. *J. Phys. Chem. C* **2008**, *112*, 6682–6687. [CrossRef]

46. Ribadeneira, E.; Hoyos, B.A. Evaluation of Pt–Ru–Ni and Pt–Sn–Ni catalysts as anodes in direct ethanol fuel cells. *J. Power Sources* **2008**, *180*, 238–242. [CrossRef]
47. Cui, C.; Gan, L.; Li, H.H.; Yu, S.H.; Heggen, M.; Strasser, P. Octahedral PtNi nanoparticle catalysts: Exceptional oxygen reduction activity by tuning the alloy particle surface composition. *Nano Lett.* **2012**, *12*, 5885–5889. [CrossRef]
48. Stamenkovic, V.R.; Fowler, B.; Mun, B.S.; Wang, G.; Ross, P.N.; Lucas, C.A.; Markovic, N.M. Improved Oxygen Reduction Activity on $Pt_3Ni(111)$ via Increased Surface Site. *Science* **2007**, *315*, 493–497. [CrossRef]
49. Glüsen, A.; Dionigi, F.; Paciok, P.; Heggen, M.; Müller, M.; Gan, L.; Strasser, P.; Durán-Botkowski, R.E.; Stolten, D. Dealloyed PtNi-Core-Shell Nanocatalysts Enable Significant Lowering of Pt Electrode Content in Direct Methanol fuel Cells. *ACS Catal.* **2019**, *9*, 3764–3772. [CrossRef]
50. Jiang, Q.; Jiang, L.; Hou, H.; Qi, J.; Wang, S.; Sun, G. Promoting Effect of Ni in PtNi Bimetallic Electrocatalysts for the Methanol Oxidation Reaction in Alkaline Media Experimental and Density Functional Theory Studies. *J. Phys. Chem. C* **2010**, *114*, 19714–19722. [CrossRef]
51. Wang, Y.; Yang, J.; Sun, S.; Wang, L.; Cao, T.; Zhang, D.; Xue, Z.; Zhou, X. PtNi nanoparticles supported on electrochemically reduced porous graphene oxide for methanol oxidation reaction. *Chem. Phys. Lett.* **2019**, *730*, 575–581. [CrossRef]
52. Guerrero-Ortega, L.P.A.; Manzo-Robledo, A.; Ramírez-Meneses, E.; Mateos-Santiago, J.; Lartundo-Rojas, L.; Caribay-Febles, V. Methanol electrooxidation reaction at the interface of (bi)-metallic (PtNi) synthesized nanoparticles supported on carbon Vulcan. *Int. J. Hydrogen Energy* **2018**, *43*, 6117–6130. [CrossRef]
53. Wang, C.; Zhang, Y.; Zhang, Y.; Xu, P.; Feng, C.; Chen, T.; Guo, T.; Yang, F.; Wang, Q.; Wang, J.; et al. Highly Ordered Hierarchical Pt and PtNi Nanowire Arrays for Enhanced Electrocatalytic Activity toward Methanol Oxidation. *ACS Appl. Mater. Interfaces* **2018**, *10*, 9444–9459. [CrossRef] [PubMed]
54. Gao, F.; Zhang, Y.; Song, P.; Wang, J.; Yan, B.; Sun, Q.; Li, L.; Zhu, X.; Du, Y. Shape-control of one-dimensional PtNi nanostructures as efficient electrocatalysts for alcohol electrooxidation. *Nanoscale* **2019**, *11*, 4831–4836. [CrossRef]
55. Solla-Gullón, J.; Vidal-Iglesias, F.J.; Herrero, E.; Feliu, J.M.; Aldaz, A. CO monolayer oxidation on semi-spherical and preferentially oriented (100) and (111) platinum nanoparticles. *Electrochem. Commun.* **2006**, *8*, 189–194. [CrossRef]
56. Esparbé, I.; Brillas, E.; Centellas, F.; Garrido, J.A.; Rodríguez, R.M.; Arias, C.; Cabot, P.L. Structure and electrocatalytic performance of carbon-supported platinum nanoparticles. *J. Power Sources* **2008**, *190*, 201–209. [CrossRef]
57. Rizo, R.; Sebastián, D.; Lázaro, M.J.; Pastor, E. On the design of Pt-Sn efficient catalyst for carbon monoxide and ethanol oxidation in acid and alkaline media. *Appl. Catal. B Environ.* **2017**, *200*, 246–254. [CrossRef]
58. Powder Diffraction File (2018). International Centre for Diffraction Data (ICDD). 12 Campus Boulevard. Newton Square, PA, USA. 2018. Available online: http://www.icdd.com (accessed on 30 March 2020).
59. Hosseini, M.G.; Mahmoodi, R. Preparation method of NaBPt/C nanocatalyst affects the performance of direct borohydride-hydrogen peroxide fuel cell: Improved power density and increased catalytic oxidation of borohydride. *J. Colloid Interface Sci.* **2017**, *500*, 264–275. [CrossRef]
60. Maya-Cornejo, J.; Carrera-Cerritos, R.; Sebastián, D.; Ledesma-García, J.; Arriaga, L.G.; Arico, A.S.; Baglio, V. PtCu catalyst for the electro-oxidation of ethanol in an alkaline direct alcohol fuel cell. *Int. J. Hydrogen Energy* **2017**, *42*, 27919–27928. [CrossRef]
61. Velázquez-Palenzuela, A.; Centellas, F.; Garrido, J.A.; Arias, C.; Rodríguez, R.M.; Brillas, E.; Cabot, P.L. Structural characterization of Ru-modified carbon-supported Pt nanoparticles using spontaneous deposition with CO oxidation activity. *J. Phys. Chem. C* **2012**, *116*, 18469–18478. [CrossRef]
62. Sugimoto, W.; Yokoshima, K.; Murakami, Y.; Takasu, Y. Charge storage mechanism of nanostructured anhydrous and hydrous ruthenium-based oxides. *Electrochim. Acta* **2006**, *52*, 1742–1748. [CrossRef]
63. Dos Santos, L.; Colinati, F.; González, E.R. Preparation and characterization of supported Pt-Ru catalysts with a high Ru content. *J. Power Sources* **2006**, *158*, 869–877. [CrossRef]
64. Wang, H.; Baltruschat, H. DEMS Study on Methanol Oxidation at Poly- and Monocrystalline Platinum Electrodes: The Effect of Anion, Temperature, Surface Structure, Ru Adatom, and Potential. *J. Phys. Chem.* **2007**, *111*, 7038–7048. [CrossRef]

65. Velázquez-Palenzuela, A.; Centellas, F.; Garrido, J.A.; Arias, C.; Rodríguez, R.M.; Brillas, E.; Cabot, P.L. Kinetic analysis of carbon monoxide and methanol oxidation on high performance carbon-supported Pt-Ru electrocatalyst for direct methanol fuel cells. *J. Power Sources* **2011**, *196*, 3503–3512. [CrossRef]
66. Antolini, E. Carbon supports for low-temperature fuel cell catalysts. *Appl. Catal. B Environ.* **2009**, *88*, 1–24. [CrossRef]
67. Velázquez-Palenzuela, A.; Brillas, E.; Arias, C.; Centellas, F.; Garrido, J.A.; Rodríguez, R.M.; Cabot, P.L. Structural analysis of carbon-supported Ru-decorated Pt nanoparticles synthesized using forced deposition and catalytic performance towards CO, methanol, and ethanol electro-oxidation. *J. Catal.* **2013**, *298*, 112–121. [CrossRef]

4.1.2. Nanostructuring Determines Poisoning: Tailoring CO Adsorption on PtCu Bimetallic Nanoparticles

This work was performed in collaboration with the computational research group led by Prof. Viñes from the University of Barcelona. The work consisted in the analyses and interpretation of the CO tolerance of different Pt(Cu)/C catalysts obtained from the electroless deposition of Cu and further galvanic exchange with Pt. All the experimental part of this paper corresponds to the present thesis, which includes the synthesis and characterization of the different catalysts by means of electrochemical (CV) and structural techniques (HRTEM and XRD), together with a strong participation in the fruitful discussion with the computational results obtained by our colleagues.

Different synthetic methods were performed in order to obtain Pt(Cu) core-shell nanoparticles supported on Vulcan XC-72. The different synthetic methods consisted in the electroless deposition of Cu both, in aqueous alkaline medium, using formaldehyde (**S1**) or $NaBH_4$ (**S2**) as the reducing agent, and in water-in-oil microemulsion (**S3**), using $NaBH_4$ as the reducing agent. The catalysts obtained were compared to the commercial ones Pt/C and PtCu/C.

The nanoparticles obtained were observed by TEM, which showed spherical and aggregated nanoparticles in all of the synthesised catalysts, making difficult to identify single crystals. The XPS analyses showed a decrease in the Pt content when the samples were sputtered for different times, thus revealing a Pt surface enrichment. Therefore, the nanoparticles consist of a PtCu alloy core with a shell composed mainly by Pt. The XRD allowed the identification of Pt metal in the catalysts, with Pt diffraction peaks slightly shifted to higher angles compared to pure Pt, which was explained by the alloy formation with Cu. The crystallite sizes were estimated from the XRD data, which were around 2 nm for PtCu/C_S1, PtCu/C_S2 and Pt/C and about 3.5 nm for PtCu/C_S3 and PtCu/C. The structural characterization also showed a decrease in the particle size as the Cu content increased.

The CO stripping voltammograms of all the catalysts showed the typical shape for Pt catalysts, where the CO oxidation peak appears in the potential range between 0.5 and 0.8 V. The onset potential for the CO oxidation on the catalysts is related to their CO adsorption strength, the onset potential being shifted to more negative values when the

CO adsorption is weaker. This shift in the onset potential is known to occur in Pt(M) core-shell nanoparticles, in which the electronic interaction of the core metal with the Pt-rich shell modifies the electroactivity of the latter. The effect of the core metal usually results in the decrease of the onset potential, making the catalyst more tolerant to CO.

For the PtCu/C catalyst and PtCu/C_S2 and PtCu/C_S3, the results obtained were as expected, since the onset potential was shifted to more negative values when compared to Pt/C, thus revealing a weaker bond between the CO and the catalyst surface. However, the PtCu/C_S1 CO stripping showed a higher onset potential compared to Pt/C, indicating a stronger CO adsorption, not previously described in the literature. Since CO adsorption is a surface phenomenon, the explanation of this exception was found when studying the different possible surface structures of the synthesised nanoparticles. From the experimental point of view, since the nanoparticles were very small (ca 1.5 nm), it is very difficult to perform the structural analysis needed to obtain this information using experimental means. However, the computational calculations allowed evaluating the dependence between the CO adsorption strength and the structure and composition of the nanoparticle surface. The explanation found by the computational group for this phenomenon was that certain defects present in the nanoparticle surface can lead to a higher CO adsorption energy, which would be seen in the CO stripping analysis as a higher onset potential value, thus meaning that the surface with more defects are easier poisoned by CO.

Volume 3
Number 10
21 May 2022
Pages 4041–4390

Materials Advances

rsc.li/materials-advances

ISSN 2633-5409

ROYAL SOCIETY OF CHEMISTRY

PAPER
Francesc Viñes, Pere L. Cabot et al.
Nanostructuring determines poisoning: tailoring CO adsorption on PtCu bimetallic nanoparticles

Materials Advances

ROYAL SOCIETY OF CHEMISTRY

PAPER

View Article Online
View Journal | View Issue

Cite this: Mater. Adv., 2022, 3, 4159

Nanostructuring determines poisoning: tailoring CO adsorption on PtCu bimetallic nanoparticles†

Lorena Vega, ‡[a] Julia Garcia-Cardona, ‡[b] Francesc Viñes, *[a] Pere L. Cabot *[a] and Konstantin M. Neyman [a,c]

Here we show, combining CO stripping voltammograms on different PtCu nanoparticle (NP) low-temperature fuel cell electrocatalysts and density functional calculations, that surface chemical ordering and the presence of certain defects explain the CO tolerance vs. poisoning of such systems. The CO withdrawal for these dueling CO-slingers depends on whether they are well-shaped core@shell Cu@Pt NPs, more CO-tolerant, or having Cu-surrounded surface Pt atoms or adatoms/vacancies surface defects, less CO-tolerant. The latter sites are critical on nm-sized PtCu NPs, displaying stronger CO adsorption compared to pure Pt NPs. Avoiding such sites is key when designing less expensive and CO-poisoned Cu@Pt NP-based electrocatalysts.

Received 21st February 2022,
Accepted 11th March 2022

DOI: 10.1039/d2ma00196a

rsc.li/materials-advances

1 Introduction

Fuel cells are regarded as a forefront, efficient way to transform chemical energy into electricity involving low pollutant emissions,[1] highly appealing, *e.g.*, to provide power for small residential areas, even when remote. Aside, fuel cells are attractive to the automotive sector and portable electronic devices, to mention a few applications of technological interest.[2,3] In this context, proton exchange membrane fuel cells (PEMFCs) have arisen as one of the most promising technologies contributing to meeting the growing global energy demands while keeping sustainable zero carbon emissions, particularly thanks to their high energy density and efficiency, with demonstrated durability.[4]

Platinum is the main electrocatalyst for PEMFCs, long regarded as the best material to carry out the hydrogen oxidation reaction (HOR) and the oxygen reduction reaction (ORR). However, Pt scarcity translates into prohibitive costs, plus it gets readily poisoned when the industrial grade hydrogen (H_2) source contains carbon monoxide (CO) impurities,[5] given the strong bond of CO to Pt surfaces.[6] The CO tolerance can be improved, *e.g.*, using PtRu alloy electrocatalysts, but at the expense of decreasing the fuel cell efficiency and yet introducing another expensive metal.[7]

An appealing way of decreasing the costs is to employ core@shell M@Pt nanoparticles (NPs), in which a more abundant and cheaper metal constitutes the NP core not directly participating in the catalytic process. In addition, the NP shaping aids at increasing the surface-to-mass ratio. Note that such solutions may imply a modulation of the Pt shell electronic structure by the core M metal,[8] affecting the catalytic power, the CO affinity, and even the core@shell NP stability.[9] Thus, the core@shell NPs composition, size, and shape are envisaged as controllable features to maximize the H_2 activation while reducing the CO poisoning.

Along this line, diverse experiments have been performed with a plethora of cheaper sacrificial metal cores, M = Co, Ni, Fe, Sn, Mn, Zn, or Pb.[10–16] Among them, the Cu@Pt formulation has attracted great attention[10,17,18] given the availability of Cu, a common catalyst, *e.g.* for the reverse water gas shift reaction,[19] and used as an electrocatalyst for the carbon dioxide reduction reaction.[20] There exists a number of methodologies to prepare Cu@Pt NPs supported on porous carbon, including direct current,[21] and chemical reduction of Cu ions by sodium borohydride or formaldehyde,[22–25] generally followed by galvanic exchange with Pt. The galvanic exchange has been previously used as a simple and cost-effective method to synthesize catalysts for different important electrochemical applications.[26] Thus, as some examples of pioneering works, Pt submonolayers on Ru NPs,[27] Pt layers on Au surfaces,[28,29] Pt monolayers on core–shell NPs (by displacing Cu monolayers),[10] and Pt shells covering Cu, Ni, and Co deposits on glassy carbon substrates[13] were prepared in this form.

[a] Department de Ciència de Materials i Química Física, Universitat de Barcelona, c/Martí i Franquès 1-11, 08028 Barcelona, Spain. E-mail: francesc.vines@ub.edu, p.cabot@ub.edu
[b] Institut de Química Teòrica i Computacional (IQTCUB), Universitat de Barcelona, c/Martí i Franquès 1-11, 08028 Barcelona, Spain
[c] ICREA (Institució Catalana de Recerca i Estudis Avançats), Pg. Lluís Companys 23, 08010 Barcelona, Spain

† Electronic supplementary information (ESI) available: Adsorption sites and energies on bridge, hollow, and O-connected top sites. Bader charges on motifs and discussion on them. See DOI: 10.1039/d2ma00196a

‡ L. V. and J. G.-C. equally contributed.

It is known that Cu@Pt NPs are excellent catalysts for NO_x reduction.[32] Their thermodynamic stability, rationalized by density functional theory (DFT) simulations on NP models,[33] revealed a significant cohesion and commensurability of Cu and Pt phases. The improved catalytic activity was assigned to a Cu → Pt electron transfer and a lowering of the Pt d-band centre. This mechanism was invoked as well to explain the weaker CO binding on Cu@Pt systems using slab-model DFT simulations of Pt monolayers on Cu support.[34] Note that on extended systems the effect is maintained, although less expressed, even in case of a surface Pt single atom alloy (SAA) as follows from the observations of improved CO poisoning tolerance of PtCu SAA.[35]

However, *not all that glitters is gold*, and the manufacturing of Cu@Pt NPs is not exempt from adverse effects in terms of CO poisoning, which may be enhanced by particular NP size, shape, or synthesis procedures. We show this here by decreasing the size limits to *circa* 1.5 nm for Cu@Pt particles obtained by galvanic exchange and Cu selective oxidation, thus prompting the possibility of having a diversity of abundant defects at the NP surface. The CO stripping voltammograms on a series of synthesized and commercially available Cu@Pt NPs with different particle sizes and Pt:Cu ratios reveal that the CO adsorption is, in general terms, weakened compared to pure Pt NPs, but, in the smallest size limit, it may be remarkably strengthened. An atomistic insight gained by DFT simulations on Cu@Pt NP models reveals that certain surface defects, including Cu-surrounded Pt atoms, Pt adatoms, and Pt vacancies, may decrease the tolerance towards CO poisoning.

2 Experimental details

2.1 PtCu bimetallic nanoparticles synthesis

The PtCu catalysts studied in this work were synthesized by different procedures. They all consisted in a two-step synthesis where carbon-supported Cu NPs (Cu/C) were firstly obtained by different deposition methods. Later, once the Cu/C was formed, a partial galvanic replacement took place when the powder was suspended in a 5 mM H_2PtCl_6 + 0.1 M $HClO_4$ solution with vigorous stirring for 45 min, proceeded according to the following reaction:

$$2Cu + PtCl_6^{2-} \rightarrow 2Cu^{2+} + Pt + 6Cl^- \quad (1)$$

The resulting carbon-supported Cu@Pt core@shell NPs were separated, cleaned, and dried. Carbon XC72 from Cabot Corp. was used as the support in all cases. All the solutions were prepared from Milli-Q water (Merck) and the analytical-grade reagents from Merck GmbH ($NaBH_4$, H_2PtCl_6, Na_2-EDTA, *n*-heptane, Brij-30, acetone, ethanol) and Panreac Applichem GmbH ($CuSO_4{\cdot}5H_2O$, formaldehyde, NaOH, polyvinylpyrrolidone).

The electroless deposition to obtain Cu NPs was performed in basic aqueous media, using formaldehyde or $NaBH_4$ as reducing agents, and in water in oil microemulsion, using $NaBH_4$. Synthesis 1, **S1**, consists in the preparation of the Cu/C catalyst precursor following the work of Georgieva *et al.*[23] The carbon powder was dispersed in 100 mL of a solution containing 10 mM $CuSO_4{\cdot}5H_2O$ as the Cu precursor, 30 mL L^{-1} CH_2O as the reducing agent, 50 mM Na_2-EDTA as the complexing agent, and as the surfactant 0.0005 mM polyvinylpyrrolidone (PVP). The pH was raised up to 12.5–13.0 with NaOH and then the suspension was kept at 45 °C in a water bath under stirring for 30 min. The suspended solid was centrifuged at 9500 rpm for 15 min and then re-suspended in ultrapure ethanol and centrifuged again several times to remove the surfactant. The Cu/C NPs were left to dry under vacuum overnight. Synthesis 2, **S2**, was performed from a sonicated suspension containing given amounts of $CuSO_4{\cdot}5H_2O$ and the carbon support in 1.0 M NaOH. Then, $NaBH_4$ was slowly added during 15 min for the copper deposition, the sonication continued for 30 min more and then, the suspension was filtered.[25] In Synthesis 3, **S3**, the catalysts were prepared by a water-in-oil method,[30] which consists in a microemulsion containing *n*-heptane, Brij-30 as the surfactant, and an aqueous solution of $CuSO_4$, with a water-to-surfactant molar ratio of 7. An excess of $NaBH_4$ was added to form Cu NPs, further sonicating the microemulsion for 2 h. Finally, 21 mg of the carbon support were added to the microemulsion, which was further kept stirred for 1 h and then, the phase separation was produced by acetone addition. Once the organic phase was separated from aqueous phase and cleaned, the resulting powder was filtered.

2.2 CO stripping experiments

The electrochemical experiments were done in a three-electrode electrochemical cell using an $Ag|AgCl|KCl_{sat}$ reference electrode, a Pt stick auxiliary electrode, and a 5 mm-diameter glassy carbon electrode (GCE) as the working one (all from Metrohm). The GCE was polished to mirror finish as described elsewhere.[25] The electrolyte was 0.5 M H_2SO_4 (Merck, analytical grade) and the experiments were performed using an Ecochemie Autolab PGSTAT100 commanded by the Autolab Nova 2.1.4 software. The GCE was coated with 20 μL of the catalyst ink, prepared by sonicating 1 mg of the catalyst powder dispersed in 0.5 cm^3 of a water : isopropanol (analytical grade, Panreac) mixture (1 : 1 in volume), and left to dry at room temperature. Despite not using the Nafion binder, the particulate films were found to be stable during the present measurements. Prior to the CO stripping experiments, the ink-modified electrode was cleaned by repetitive cycling between −0.2 and 0.8 V at 100, 50 and 20 mV s^{-1} up to a steady profile. It is worth mentioning that this is a normal procedure to obtain clean Pt surfaces also for PtCu NPs (activation process). To this respect, it is important to note that the steady profiles were rapidly obtained, with no extra peaks apart from those typical of pure Pt, and that the difference between the first and the steady curves was only a slight increase in the peak currents (also observed for Pt/C). Therefore, the surface restructuration, being possible, should be minimum. To obtain the CO stripping curves, CO gas (99.9% Linde) was bubbled through the 0.5 M H_2SO_4 solution for 15 min keeping the electrode potential at −0.1 V. Dissolved CO was removed by N_2 bubbling (99.9995% Linde) through the solution for 30 min and then, the monolayer of CO adsorbed on the surface was

oxidized by cyclic voltammetry (CV) between −0.2 and 1.0 V at 20 mV s^{-1} without stirring. The experimental results were compared with those obtained using commercial 20 wt% Pt/C and 20 wt% PtCu/C (1 : 1 at. ratio), both from Premetek, after preparing the corresponding working electrodes in the same way as indicated above.

2.3 NP size, morphology, and composition characterization

Transmission electron microscopy (TEM) by means of a 200 kV JEOL JEM 2100 microscope was used for the sample observation. The X-ray diffraction (XRD) analyses were performed sandwiching the powders between 3.6 μm-thick polyester films using a PANalytical XPert PRO MPD (θ/θ powder diffractometer (Cu anode, 45 kV, 40 mA). The measurements were conducted with a Cu K_α-filtered radiation (λ = 1.5418 Å), 2θ step size of 0.026° and 200 s per step of measuring time. The TEM observation of the specimens studied showed the presence of small nanoparticles, dispersed on the supporting carbon. Representative examples are shown in Fig. 1a and b for **S1** and commercial PtCu/C, respectively. NPs about 1–2 nm in diameter can be observed in the picture of the former and of about 3–4 nm in that of the latter, also presenting, as expected, some size distribution.

As shown in this Fig. 1, the NPs were rather spherical, and some aggregation could also be observed. It is then difficult to identify whether all the dark spots are single crystals (crystallites). Different analytical techniques such as XRD, X-ray photoelectron spectroscopy (XPS), energy-dispersive spectroscopy (EDS) and inductively coupled plasma have been used to analyse the composition of the samples.[10,17,18,22,24,25] It should be noted, however, that the analytical results obtained from all these techniques would coincide only when the NPs were composed of the zero-valent elements and were completely crystalline and homogeneous. It was shown by XPS that Pt and Cu oxidized states appeared for PtCu NPs supported on different carbons, which could not be integrated into the crystallites.[55,56] In addition, the Pt(0):Cu(0) at% ratios obtained by the XPS analyses performed with different sputtering time approached those of XRD. It was also shown that the overall composition given by EDS significantly differed from the composition of the crystallites ascertained by XRD and XPS, which was then explained by the presence of the significant amounts of the identified Pt and Cu oxidized species. Considering that the metallic PtCu solid solution—Pt(0):Cu(0)—is the main structure involved in CO oxidation, since the oxidized species are not expected to work for this reaction, and that XRD allows identifying such Pt(0):Cu(0) single crystals, the studied catalysts were accordingly analyzed by means of the XRD technique.

The XRD patterns of the synthesized catalysts are shown in Fig. 2, where they are compared to commercial Pt/C and PtCu/C samples. The focus on the 35 to 55° region allows one comparing the peaks to the expected signals for Pt and Cu(111) and (200) surfaces, and thus confirming the Pt phase of Pt/C reference, as well as Pt-like and Cu-like phases of different composition on

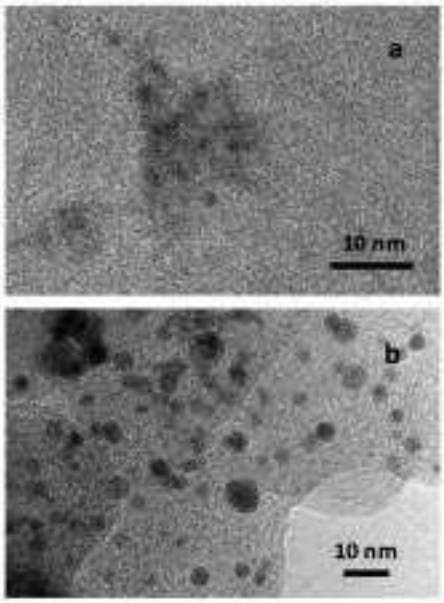

Fig. 1 Representative TEM pictures of the PtCu catalysts studied: (a) **S1** and (b) commercial PtCu/C.

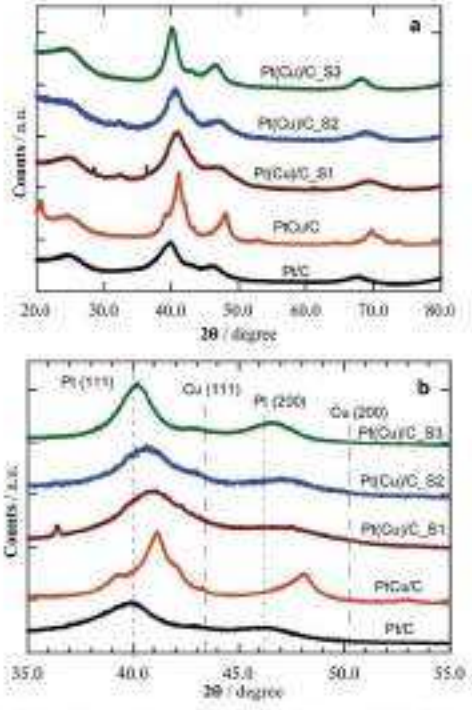

Fig. 2 XRD patterns of the studied Pt and PtCu catalysts. (a) Extended XRD diffractograms and (b) magnification of the peaks with higher intensity. The diffraction angles of pure Pt and Cu crystallites have been marked for comparison.

Table 1 Structural data of the catalysts obtained from the XRD analyses. The mean crystallite sizes have been determined by Scherrer's equation and the Pt:Cu at% ratios have been obtained from Vegard's law

Catalyst	Crystallite size/nm	Pt:Cu ratio/at%	Lattice parameter (a)/nm
PtCu/C_S1	1.5	64:36	0.3814
PtCu/C_S2	2.0	73:27	0.3838
PtCu/C_S3	3.3	91:9	0.3883
PtCu/C	3.4	57:43	0.3805
Pt/C	2.6	100:0	0.3911

commercial PtCu/C and samples **S1** to **S3**. It is worth mentioning that the XRD results show the mean composition of the crystallites through the peak displacements from those corresponding to the pure metals. The peak diffraction angles of the PtCu NPs shown in Table 1 are between those of pure Pt and pure Cu, but closer to the former, thus indicating that Pt is dominant in the crystallites.

Table 1 summarizes the XRD results, *i.e.* the average NP size (from Scherrer's equation) and the Pt:Cu ratios (Vegard's law). Note that commercial PtCu/C and Pt/C samples have mean NP sizes of 3.4 and 2.6 nm, the former with a Pt:Cu at% ratio of 57:43. Samples **S1** to **S3** featured increasing size, from 1.5 to 3.5 nm, and decreasing of the Cu content, from Pt:Cu 64:36 in **S1** to 91:9 for **S3**, in line with a Cu@Pt core@shell structure, since the surface Cu atoms were removed and replaced by Pt atoms during the galvanic exchange.[25] The samples offer cases of similar size, around 2 (**S1**, **S2**, and Pt reference) or 3.5 (**S3** and PtCu) nm, with variable composition, and also cases with similar composition and different size, *e.g.* **S3** and Pt reference, or **S1** and PtCu, enabling a discussion of size and composition effects.

Aside, the lattice parameters, a, determined from the XRD diffractograms, go along with the Cu content, *i.e.* the larger the Cu content, the smaller is a, thus resulting in a concomitant lattice strain increase while reducing the NP size.[33] Table 1 shows that an increase in the Cu content in **S1**–**S3** is paired with a NP size decrease. This is an expected result when the number of the overall atoms in the NPs are the same. However, this is difficult to control in the synthesis, also because of the distribution of NP sizes and compositions achieved, which makes their analysis only viable through mean values. The final NPs were the result of the galvanic replacement of Cu by Pt, which means that the initial Cu NPs were partially destroyed together with an alloy formation, with the final composition and size as indicated in Table 1. Therefore, the NP size has to be mainly related to the different synthesis methods, which also conditioned the NPs composition. Note the different NP composition of commercial PtCu/C, resulting from another synthesis procedure, involving the simultaneous chemical reduction of Pt and Cu precursors with the alloy formation to a given NP size.

3 Methods and models

3.1 Computational details

The present DFT calculations were carried out using the plane-wave based Vienna *ab initio* simulation package (VASP) code.[37,38] The Perdew–Burke–Ernzerhof (PBE)[39] exchange–correlation functional was used in the description of the valence electrons, combined with the projector augmented wave (PAW) representation of core electrons.[40,41] Given the strong adsorption of CO on Pt, the inclusion of dispersive forces just slightly increases the adsorption strength, as shown on Pt(111), by ~0.3 eV.[42] Thus, the poisoning by CO due to its strong chemical bonding to Pt is reasonably well accounted at the PBE level. Metal NPs were modeled within a 2.5 × 2.5 × 2.5 nm large periodically repeated cells with at least 0.75 nm separation between adjacent particles, with negligibly weak interactions of metal NPs at such distances.[43] Only the Γ Brillouin zone k-point was sampled for the single NPs. The kinetic energy cut-off for the plane-waves basis set was set to 415 eV, a value large enough to acquire adsorption energies converged within chemical accuracy, *i.e.* below ~0.04 eV. For the electron density calculation, a cut-off value of 450 eV provided properly converged Bader charges. One-electron levels were smeared by 0.2 eV through a Gaussian function, yet finally the converged energies were extrapolated to zero smearing. All atoms were fully relaxed accomplishing a maximum forces criterion of 0.02 eV Å^{-1}. Charges were evaluated through a Bader atoms-in-molecules analysis, and charge density difference (CDD) plots gained as the electron density difference of the system containing the NP with the adsorbed CO, and the electron densities of the isolated NP and CO at fixed geometry of the adsorption system.[44]

3.2 Employed nanoparticles models

The PtCu NPs models were constructed mimicking the experimental ca. 60 at% Pt and 40 at% Cu composition of sample **S1**, while using as template 201-atoms truncated octahedrons, following the Wulff construction shape minimizing the NP overall surface tension,[45] which resulted in an average NPs diameter of ~1.5 nm, explicitly meeting the sample **S1** NPs size, although the models are suited to simulate the CO adsorption on larger NPs, such as those of samples **S2** and **S3**, being the CO adsorption of local character, *vide infra*, while such NPs being within the so-called scalable regime,[33,43] where adsorption results are converged with the NP model size. The model NPs already feature a metallic band structure, at variance with the discrete energy levels featured by smaller metal clusters.[33] The models created to simulate different present active sites in experiments are as follows: (i) an immaculate (regular) Cu@Pt core@shell NP, $Cu_{79}@Pt_{122}$—**model 3**—which obeys the topological stability preference;[46] (ii) a $Cu_{79}Pt@Pt_{121}Cu$ model derived from **model 3** exchanging one surface Pt atom with one core Cu atom—**model 5**—; (iii) NPs with single surface Pt atoms surrounded by surface and subsurface Cu neighbors—**model 6**—; (iv) NPs with single surface Pt atoms surrounded by surface Cu neighbors—**model 7**—, (v) models derived from **model 7** removing surface Cu atoms and optimizing the resulting structure—**model 8**—; and (vi) models with surface defects created on the immaculate $Cu_{79}@Pt_{122}$ model—adatom and vacancy models—.

Except for the $Cu_{79}@Pt_{122}$ NP, different models had to be built to duly represent the variety of surface defects. Notice that models 5–7 represent situations with a marginal surface Cu

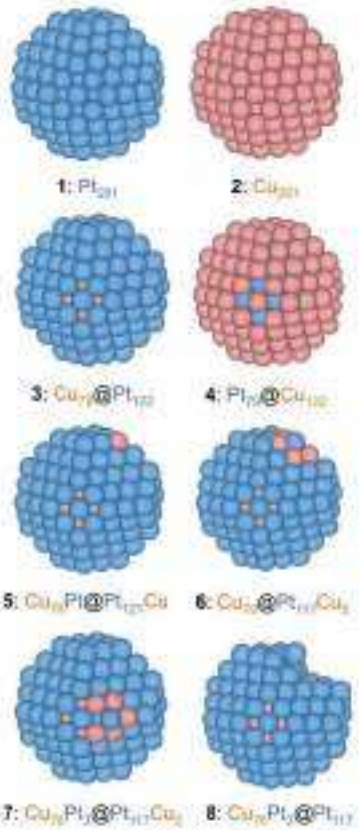

Fig. 3 Eagle-eye views of the different employed NP models: 1: pure Pt_{201}; 2: pure Cu_{201}; 3: $Cu_{79}@Pt_{122}$—perfect Cu-core@Pt-shell; 4: $Pt_{79}@Cu_{122}$—perfect Pt-core@Cu-shell; 5: $Cu_{78}Pt@Pt_{121}Cu$—an example of exchanging a core Cu atom with a surface Pt atom (a corner site in the example); 6: $Cu_{78}@Pt_{121}Cu_2$—with a surface Pt atom (a corner site in the example) surrounded by Cu atoms; 7: $Cu_{78}Pt_2@Pt_{121}Cu_2$—as in 6, but with the Pt atom surrounded by 5 surface Cu atoms and one subsurface Pt atom; 8: $Cu_{78}Pt_2@Pt_{117}$—resulted from 7 by removing 5 surface Cu atoms and subsequent geometry optimization. Pt and Cu atoms are shown as blue and brown spheres.

content, which cannot be completely ruled out neither from the synthesis procedure, nor the XRD analysis, nor the Cu surface segregation under working conditions. However, **model 8** and adatoms and vacancies mimic situations where such surface Cu has been selectively oxidized and removed during the voltammogram cycles. Finally, apart from the just mentioned PtCu model NPs, the following reference systems were also calculated: Pristine Pt_{201}—**model 1**—and Cu_{201} NPs—**model 2**—, inverse $Pt_{79}@Cu_{122}$—**model 4**—, and pure Pt_{201} NPs with generated surface defects, see Fig. 3.

3.3 CO adsorption assessment

CO molecule adsorption was systematically studied on the aforementioned NP models. Numerous positions were considered, see Fig. S1 of the ESI,† including top, bridge, and face-centred cubic (fcc) hollows, regarded to be more stable than hexagonal close packed (hcp) hollows.[55] In addition, CO adsorption was investigated on the surface vacancy defected models with one, three, or seven atoms missing on the (001) and (111) facets. CO adsorption energy, E_{ads}, was calculated from the energies of the optimized CO molecule, E_{CO}, clean NP, E_{NP}, CO adsorbed on the NP model, $E_{CO/NP}$, as follows:

$$E_{ads} = E_{CO/NP} - E_{NP} - E_{CO} \quad [2]$$

Within this definition, the more negative the E_{ads} is, the stronger is the CO adsorption. Aside from testing hcp from fcc sites, our calculations revealed a clear trend towards the perpendicular CO adsorption *via* its C atom, even when starting from a parallel CO adsorption mode with both C and O atoms interacting with the NP. Aside, a very weak O-connected CO perpendicular adsorption is found, with E_{ads} of at most of −0.05 eV, see Table S1 of the ESI.† Thus, the latter adsorption mode has been discarded in the oncoming discussion, considering only the much stronger C-connected CO perpendicular adsorption, see Table 2.

Table 2 Adsorption energies, E_{ads}, in eV, for CO adsorbed in different top positions, see Fig. 3 for different models, and sites in Fig. S1 of the ESI

Model/Site	A	B	C	D	E	F
1	−2.08	−2.01	−1.77	−1.52	−1.68	−2.05
2	−0.98	−0.90	−0.79	−0.60	−0.62	−0.86
3	−1.74	−1.54	−1.40	−0.61	−1.03	−1.65
4	−1.33	−1.15	−1.09	−0.97	−0.97	−1.33
5	−0.95	−0.82	−0.60	−0.53	−0.45	−0.88
6	−1.88	−1.83	−1.81	−1.21	−1.44	−1.76
7	−2.24	−2.27	−2.22	−1.67	−1.94	−2.07
8	−2.07	−2.21	−2.61	−2.29	−1.58	−1.81

4 Results and discussion

4.1 CO stripping voltammograms on reference Pt and PtCu bimetallic nanoparticles

The CO stripping studies have been carried out for three PtCu bimetallic NP systems synthesized on a carbonaceous support, named **S1**, **S2**, and **S3**, and compared with Pt/C and PtCu/C commercial catalysts, see Fig. 4. The general shape of these curves is typical for Pt.[47] The main peak appears in these curves during the anodic sweep, in the potential range 0.5–0.8 V, which corresponds to the oxidation of adsorbed CO. This peak is preceded by a suppression of H adsorption/desorption due to CO adsorption at Pt active sites. After the CO stripping, Pt is oxidized to surface PtO, which is reduced again to Pt in the cathodic sweep, leading to the peak located at about 0.6 V. Afterwards, the hydrogen adsorption profile, also typical for Pt, appears in the potential range from 0.1 to −0.2 V. It is also apparent that the carbon powder substrates show high capacitive currents in that region, thus obscuring the H adsorption picture.

Note that the currents have been referred to the CO stripping charge of each specimen. When normalizing in this form, the

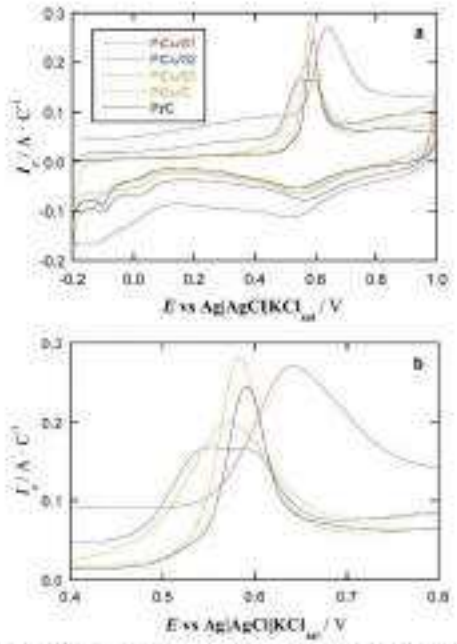

Fig. 4 (a) CO stripping curves of PtCu and reference Pt samples in deaerated 0.5 mol dm^{-3} H_2SO_4 at a scan rate of 20 mV s^{-1}. (b) Magnification of the curves to better visualise the onset potential for CO oxidation.

Pt loading is not relevant, since the stripping charges are proportional to the number of active sites, and then, the onset potentials for CO oxidation, which indicate the relative catalytic activities, can be easily compared. Importantly, no Cu oxidation is perceived in the CV curves of Fig. 4. In the case that some free Cu remained on the surface, it should be oxidized at 0.0–0.2 V potentials[48] and no peaks can be observed in this potential region.

In the case of the S1, S2, and S3 samples, this can happen because (i) during the galvanic replacement, Pt atoms remove the surface Cu atoms of the previously deposited Cu NPs and (ii) after the repetitive cycling to reach the steady profile, the possible remaining surface Cu atoms are removed. NPs of the commercial PtCu/C catalyst should also undergo a surface Pt enrichment according to the point (ii). However, it is important to note that no extra peaks apart from those typical of pure Pt appeared in the cleaning protocol (repetitive cyclic voltammograms), and, therefore, any Cu oxidation peak was not detected in any case, including the first voltammogram. This points out to a minimum Cu surface removal by the Pt shell protection of the underlying Cu, the CO stripping voltammograms showing the effect of Cu on Pt through shifting the onset of the CO oxidation potential. Besides, the size of the NPs studied in this paper was too small to detect Pt and Cu concentration gradients along the NP diameter (line profile) by energy-dispersive X-ray spectroscopy (EDS) because of insufficient spatial resolution of the technique.[35,49–52] For small PtCu NPs (2–5 nm), obtained also by galvanic displacement of Cu by Pt on different carbon supports, X-ray photoelectron spectroscopy (XPS) analyses with different Ar$^+$ sputtering times were performed.[35,49–52] Interestingly, the XPS results showed that the Pt(0)/Cu(0) ratio decreased when increasing the sputtering time, thus strongly indicating a Pt surface enrichment. Thus, the NPs can be described as having core@shell structures with a PtCu alloy core and a shell mainly composed of Pt atoms.

The profiles of the cyclic voltammograms in Fig. 4 are then the same as that of Pt/C, although with different potential shifts of the CO stripping peaks. The onset potential of these peaks indicates the strength of CO adsorption, being smaller as the onset potential is shifted in the negative direction. According to literature, many PtCu samples feature more negative onset potential for CO oxidation than pure Pt, seen e.g. in Cu@Pt core@shell NPs produced by electrochemical reduction of Cu followed by a partial galvanic replacement with Pt,[35] NPs with a Cu-core to Pt-shell gradient structure,[53] Pt NPs with a small content of dissolved Cu,[54] even PtCu alloy NPs prepared using a reducing agent in basic media followed by a partial galvanic replacement with Pt.[23] This is indeed observed in the CO stripping plots in Fig. 4 for commercial PtCu, PtCu_S2, and PtCu_S3 samples, revealing a weaker CO adsorption when compared to commercial Pt/C, and so, such samples duly accomplish the sought mission of performing similarly or even better than reference Pt/C, but with a lower Pt mass content.

The adsorbed OH necessary to generate CO_2 (and water) during the oxidation process appears to play a minor role, a point quantified by DFT calculations. The calculated hydroxyl adsorption energy below −0.5 eV on pure Pt NPs[34] suggests its easy displacement by CO molecules adsorbed at least 1 eV stronger; *vide infra*. Regarding the deviations with respect to pure Pt, commercial PtCu/C is the closest to Pt/C, with a peak potential shift of merely −10 mV, even when a Pt : Cu ratio is close to 60 : 40, see Table 1. The PtCu_S3 shows a peak shift of *circa* −50 mV; its similar size to commercial PtCu/C implies that the extra shift comes from the Pt : Cu composition of *ca.* 90 : 10, indicating that some effect is achieved at small contents of Cu, as observed for PtCu NPs with decreasing Cu content,[55] even in solid solution limits containing just *ca.* 1 at% Cu.[56] The PtCu_S2 sample has a particle size close to that of Pt/C, but with a ~70 : 30 Pt : Cu ratio, also revealing a weaker CO adsorption.

Note that in this latter sample, a broad band appears in which one can discern two features at 0.54 and 0.58 V, which could be well related to well-faceted (111) and (100) Pt domains reported in the literature.[56] Another possibility could be the coexistence of different orientations of the CO adsorbed molecule (horizontal and vertical), with different Pt-CO binding energies. However, the vertical orientation is normally considered due to the strong adsorption of CO on Pt. Related to this point, it is worth noting that the H desorption (the same as adsorption) charges in other PtCu/C alloys explored by us were half of the CO stripping charges,[23] thus suggesting only one H atom (one electron for desorption) and only one CO molecule (two electrons for stripping) per Pt active atom and indicating the vertical adsorption of CO on the latter.

The most striking feature is that PtCu_S1 sample with Pt : Cu ratio 60 : 40 and 1.5 nm large particles features a CO oxidation peak shifted by ~50 mV to more positive potentials compared to Pt/C sample, indicating a stronger CO poisoning of PtCu_S1. To the best of our knowledge, this is the first observation of CO poisoning enhancement for nanostructured PtCu samples. This is in strong contrast with the results obtained for commercial PtCu/C sample featuring not very different Pt:Cu composition, but significantly different NP size (3.4 nm). Note, however, that the negative onset potential shift for CO oxidation for commercial PtCu/C is smaller than those for PtCu_S2 and PtCu_S3 samples, thus suggesting that decreasing the amount of Cu in the PtCu alloy can facilitate the CO removal. However, probably there is not only a mere size effect. The synthesized NPs are the result of a galvanic exchange of Cu by Pt. If the initially deposited Cu NPs have significantly different sizes and surface structures in the applied preparation protocols the galvanic exchange may lead to PtCu NPs varying both sizes and surface defectiveness.

Since CO adsorption is a surface phenomenon, it is expected to strongly depend on the surface structure, being sensitive to the surface defects presence. To the best of the authors' knowledge, it is, *a priori*, not yet possible to observe from experimental surface analyses the existence of surface defects in an about monolayer shell thickness. Indeed, the computational calculations performed for a wide set of possible models bridges this gap identifying defective and non-defective surface positions with different CO adsorption energies. We started with the simplest models, having in mind the complexity of the experimental NPs (and also of the calculations), with a complete coverage of the surface Pt sites by CO molecules, the solvent and electrolyte, and the carbon support.

4.2 Computational CO adsorptive landscapes on Pt and PtCu nanoparticles

In order to explain the aforementioned experimental findings, a systematic DFT study of the CO adsorption on realistic NP models has been carried out. Truncated octahedron shapes have been considered, in line to the equilibrium Wulff shape minimizing the NP surface tension.[85] The basic NPs contain 201 atoms, corresponding to ~1.5 nm size, comparable to the particles size in the PtCu_S1 sample. Pure Pt_{201} was used as a reference, and an immaculate Cu_{79}@Pt_{122} core@shell NP with ~40 at% Cu and ~60 at% Pt has been studied, which may serve as explicit models the experimentally synthesized PtCu_S1 NPs, but are suited models for local adsorption simulations of larger NPs. Other references, such as pure Cu_{201} and an inverse Pt_{79}@Cu_{122} NP, have been studied as well, *vide supra*. Pt adatoms on Pt_{201} and Cu_{79}@Pt_{122} template NPs were inspected, as an ultimate expression of Pt low-coordination. Also, surface Pt vacancies were generated, mimicking situations in which surface Cu atoms have been selectively oxidized (removed). Furthermore, partially surface oxidized models, still containing Cu surface atoms, were investigated, *e.g.* exchanging core Cu and surface Pt exchange positions—$Cu_{78}Pt$@$Pt_{121}Cu$—, in line with previous studies suggesting that such surface Cu atoms could be beneficial for the CO oxidation, serving as vicinal OH adsorbing centres.[34] Finally, we explored models with a surface Pt atom surrounded by Cu neighbors, see Fig. 3, since such structures have been appointed to bind CO stronger than Pt(111) surfaces, where the CO adsorption may favor the surface segregation of the subsurface Cu and increase the stability of surface alloys.[77]

A thorough DFT study on all the plethora of adsorption sites and CO connection ways was carried out employing the above-mentioned NP models. Notice that the goal here is to find particular surface sites or structures that, because of their nature, favor or disfavor the CO bond strength, which is regarded as the key factor determining the CO bias in the experimental CO stripping curves. However, one should refrain from direct comparing the adsorption energies changes with the observed peak shifts, as the latter are also affected by factors other than the specific NP surface structure, *e.g.* coverage, solvation, and presence of electrolytes, to name a few.[38] In addition, the samples feature a distribution of sizes and compositions, with a diversity of active sites. Thus, the aim is to find particular surface active sites responsible of the weakening or strengthening of the CO bond.

With that in mind, let us focus on the E_{ads}. Not unexpectedly, DFT results show stable M–CO adsorption through C atom. Note that horizontal CO adsorption was also systematically tested, although in all cases the molecule raised to adopt a minimum with a vertical configuration, in line with experiments.[27] The top positions were found to be the most preferred, and even though bridge and hollow positions feature CO adsorption minima, the CO tends to displace from many of them upon relaxation, decreasing its coordination, i.e. hollow → bridge and bridge → top, see Tables S2 and S3 of the ESI.† Thus, for a due comparison, only top adsorption sites are discussed in the following, see Table 2, present on all of the employed PtCu NP models and the Cu_{201} and Pt_{201} references.

Overall results on pure Cu and Pt@Cu NPs, as well as on isolated surface Cu atoms—$Cu_{78}Pt$@$Pt_{121}Cu$ NP model—reveal weaker CO adsorption compared to Pt_{201}, with E_{ads} ranging from −0.35 eV—on $Cu_{78}Pt$@$Pt_{121}Cu$—to −1.25 eV—on Pt@Cu NP—, in line with data from $Pt_{116}Cu$ NP models,[74] and clearly smaller in magnitude than on the corresponding sites of Pt_{201} NP, from −1.51 to −2.09 eV. As far as Cu@Pt NPs are concerned, the presence of surface Cu atoms would not prevent CO occupying exposed more strongly adsorbing surface Pt sites. So, surface Cu atoms would only lower the number of available Pt surface active sites per NP. Thus, only weaker CO bonding would be observed on pure Cu or Pt@Cu NPs. However, the Cu phase is not a viable substitute to the Pt phase in PEMFCs, plus the Pt@Cu NPs feature instability issues.[12,13] If any, as aforementioned, such surface Cu atoms could be beneficial for a somewhat stronger OH adsorption, which could tune the CO oxidation performance towards CO_2.[34]

Focusing on the CO adsorption on surface Pt atoms, a comparison is made between reference Pt_{201} NP, pristine Cu_{79}@Pt_{122}, and other Cu@Pt models where a Pt surface atom is fully surrounded by Cu atoms—having both surface and subsurface Cu neighbors—or superficially surrounded—having

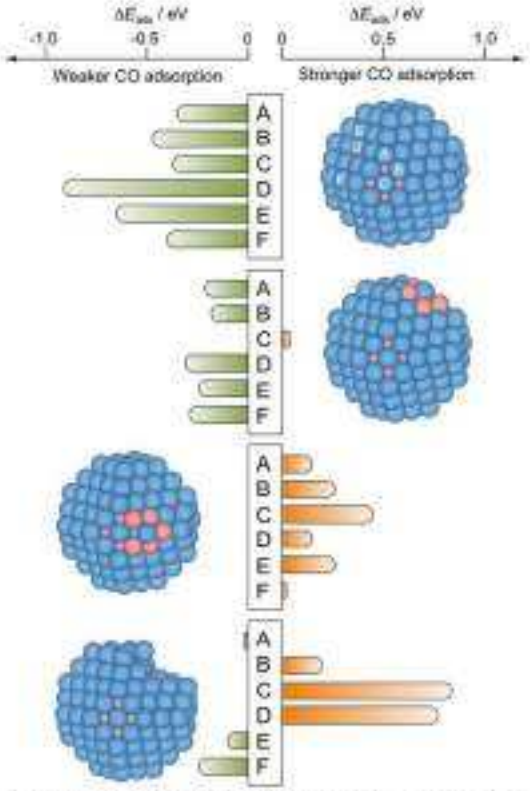

Fig. 5 Differences in CO adsorption energies, ΔE_{ads}, on PtCu NPs with respect to reference Pt_{201} NP, calculated for all topologically different top sites, see Fig. S1 of the ESI,† from top to bottom, perfect Cu@Pt core@shell NP—**model 5**, see Fig. 4—with a surface Pt atom fully coordinated to Cu atoms—**model 6**—, with a surface Pt atom coordinated to surface Cu atoms—**model 7**—, and **model 8** resulting from removal of five surface Cu atoms from **model 7** and subsequent optimization. Sites A–D are shown in model 1 but are the same for the rest of **models 5–8**.

only surface Cu neighbors—. In the latter case, models were relaxed and analyzed, in which the surface Cu atoms were removed, mimicking the aforementioned Cu selective oxidation used to prepare the PtCu **S1–S3** samples.[35] Fig. 5 shows the difference of CO adsorption energy, ΔE_{ads}, for these four models with respect to the Pt_{201} NP reference and reveals that the perfect Cu@Pt NP consistently features CO adsorption by 0.35 to 0.91 eV weaker, in line with the potential reductions shown in Fig. 3, and as a result of Cu → Pt charge transfer and lowering of the d-band centre.[33]

4.3 Effect of surface Cu

However, the exposure of surface Cu may disrupt this better performance, e.g. as a result of a partial selective Cu oxidation, a preference of Cu atoms to be located around surface corner sites at 50 : 50 Cu : Pt compositions,[46] or due to the formation of a surface alloy.[57] Indeed, the NP model exposing surface Pt atoms fully surrounded by Cu atoms features still negative, yet more moderate ΔE_{ads} values, with E_{ads} reduced by 0.21 eV. The presence of Cu atoms around single Pt atoms may even lead to sites with a slightly stronger CO E_{ads} when compared to Pt_{201} NP, as calculated on terrace (001) sites; see Fig. 5 and Table 2. Such a CO bond strengthening is aggravated when the surface Pt atom is just superficially surrounded by Cu atoms; thus, the presence of subsurface Pt atoms makes the exposed surface Pt atom a highly active site, strengthening the CO adsorption by up to 0.44 eV, in line with findings for PtCu surface alloy surfaces.[57] This clearly shows that the Pt surface isolation by Cu atoms is detrimental for resistance of PtCu nanoalloys to CO poisoning, and is a plausible explanation for the larger potential observed on PtCu_**S1** sample.

However, the above results have to be taken with caution, as such surface Cu may well be oxidized and dissolved in the course of several cycles of the CO stripping as that shown in Fig. 4. Still, the CO affinity can as well be counteracted or accentuated by this selective oxidation of the surface Cu, see Fig. 5. Whenever surface Cu atoms surrounding the surface Pt active center are removed, the resulting relaxed structure becomes distorted, featuring highly undercoordinated Pt atoms, shown on **model 8**. The adsorption on such sites is quite similar to that on the Pt_{201} reference NP, although in some cases with a strengthened CO adsorption —Pt atom at **C**, see Section S2 of the ESI,†— or a weakened CO adsorption—Pt atom at **F** in Fig. 5.

4.4 Effect of surface undercoordinated Pt atoms and vacancies

Indeed, undercoordinated Pt atoms after the surface Cu removal display E_{ads} values larger in magnitude than the most stable **A** site on Pt_{201} model with E_{ads} = −2.07 eV; particularly, E_{ads} for the (001) and (111) facets on **model 8** are −2.61 and −2.29 eV respectively, see Table 2. Other types of sites featuring stronger CO adsorption are Pt atoms of the **model 7** surrounded by surface Cu atoms, yet having subsurface Pt neighbors, displaying E_{ads} of −2.22, −2.24, and −2.27 eV for **C**, **A**, and **B** sites, respectively. Clearly, Pt isolation, either Cu-surrounded, or as adatoms after Cu oxidation, seems to be a key factor in the CO bond strengthening explaining the peculiarity of the observed CO stripping curve of PtCu_**S1** sample with its peak at larger bias than for pure Pt. Note, that such sites with a stronger CO binding may well be present in other PtCu samples, however, their effect might be hidden for larger NPs exposing a

Table 3 CO adsorption energies, E_{ads}, calculated on a Pt adatom or Pt_n vacancies defects in core@shell $Cu_{79}@Pt_{123}$, as well as on reference Pt_{201} model NPs. Values are given in eV

Facet	Site	$Cu_{79}@Pt_{123}$	Pt_{201}
(001)	Pt adatom	−1.96	−1.95
	Pt vacancy	−1.88	−2.02
(111)	Pt adatom	−2.53	−2.25
	Pt_1 vacancy	−1.70	−0.69
	Pt_2 vacancy	−2.43	−1.23
	Pt_7 vacancy	−0.73	−1.69

majority of sites binding CO in a weaker fashion. Thus, the effect of the stronger binding sites may be relevant and observable for their statistically sound amount, as appears to be the case for smaller PtCu NPs.

To further substantiate this finding, we examined CO adsorption propensity of a Pt adatom on (001) and (111) facets of Pt_{201} *vs.* the Cu@Pt NP, and of Pt vacancies on the same facet for the same models, see Table 1, both as models of low-coordinated Pt atoms resulting from a surface Cu removal. In particular, Pt adatom on (111) facets of the Cu@Pt model stabilizes the CO attachment by 0.18 eV. The vacancies of one and three missing Pt atoms strengthen the CO adsorption by 1.01 and 1.23 eV, respectively, due to a surface reconstruction leading to a distorted, and so, a priori, more active (111) facet. Indeed, CO adsorption on two sites of the Cu@Pt NP—the Pt adatom and the three-Pt atom (Pt_3) vacancy on the (111) facet—is stronger than on the most stable regular site of the Pt_{201} NP.

4.5 Electronic structure assessment of CO adsorption

The seemingly counterintuitive CO adsorption strengthening can be understood though a Bader charge analysis and charge density difference (CDD) plots, see Fig. 6. Briefly, the stronger CO bonding is mainly due to the more negative charge of the surface Pt atom when it is Cu-surrounded compared to a pure Pt NP case. Such accentuated negatively charge site favors attraction to it of the $C^{\delta+}$ CO atom, see Bader charges in Tables S3 and S4 of the ESI,† and their corresponding discussion. Aside, CDD plots in Fig. 6 reveal a donation/back-donation mechanism, where the aforementioned excess charge is back-donated from Pt 5d states to the $2\pi^*$ CO orbital, contributing to a stronger binding. This electron transfer is a common feature observed on Pt_3 vacancies and Pt adatoms attaching CO stronger to PtCu NPs than to pure Pt one.

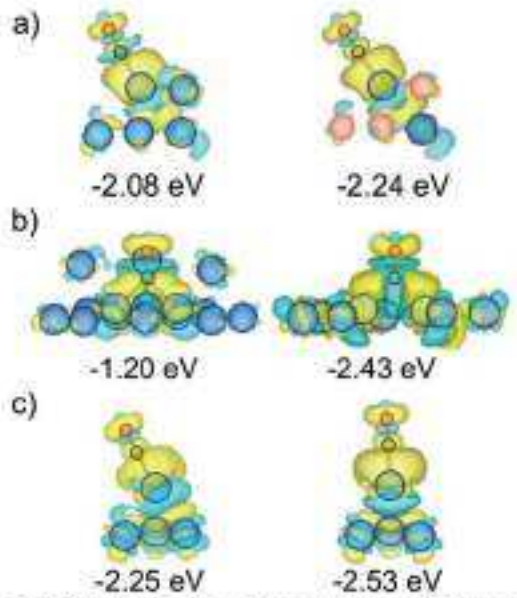

Fig. 6 CDD plots of PtCu NPs (right images) with stronger CO adsorption than on the corresponding sites of purely Pt NPs (left images): (a) A site on Pt_{201} *vs.* it superficially Cu-surrounded, and having subsurface Pt neighbors; (b) CO Adsorption on the centre of 3 Pt atom terrace (111) vacancy of Pt_{201} and on 3 Pt atom terrace (111) vacancy restructured surface of core@shell $Cu_{55}@Pt_{123}$; (c) CO Adsorption on terrace (111) Pt adatom of Pt_{201} and core@shell $Cu_{55}@Pt_{123}$. Cyan and yellow contours denote electron density depletion and accumulation regions, displayed for values of ±0.001 e Bohr^{-3}.

5 Conclusions

To conclude, the CO stripping studies of differently synthesized and commercial PtCu NPs compared to pure Pt NPs reveal notably different CO adsorption behavior. The latter depends on the synthesis method, which defines the size and structure of PtCu NPs indicating that well-shaped particles larger than 2 nm with low Cu content are more resilient towards CO poisoning. However, this CO resistance is compromised for core@shell PtCu NPs of *ca.* 1.5 nm with a relatively low Pt : Cu content of ~60 : 40. Rationalizing these observations, the present DFT simulations on diverse PtCu models show, as expected, a weakening of the CO adsorption on regular sites exposed by the Cu@Pt NPs. Interestingly, this effect is calculated to disappear on such sites as single Pt atoms surrounded by surface Cu ones or under-coordinated Pt atoms resulting, *e.g.*, from the selective oxidation of surface Cu atoms. Indeed, Pt adatoms and few-atom Pt vacancies in Cu@Pt NPs may even strengthen the CO binding, implying an easier poisoning. The effect of these surface defects may get hidden in the presence of a majority of the regular sites, explaining the peak shifts and broadenings detected in the CO stripping voltammograms for differently prepared Cu@Pt NPs. Nevertheless, the effect can become critical for relatively small NPs, highlighting the importance of synthesis procedures in which the appearance of such defects is minimized and setting a size threshold for the employment of PtCu samples as electrocatalysts in PEMFCs. Aside, in order to avoid such CO poisoning enhancement by the surface presence of Cu, or the formation of Pt defects, the PtCu NP synthesis should be driven towards forming a complete and uniform Pt shell, probably favored by a slow cationic exchange and working temperatures enabling the atomic rearrangement within the NPs.

Conflicts of interest

There are no conflicts to declare.

Acknowledgements

The work has been supported by the *Ministerio de Ciencia y Universidades* (MCIUN) RTI2018-095460-B-I00, PGC2018-093863-B-C22, and CTQ2016-78616-R research grants, and by the Spanish Structures of Excellence *María de Maeztu* program

through grant MDM-2017-0767. The research was also funded by the *Agencia Estatal de Investigación* (AEI, Spain) under project number PID2019-109291RB-I00 and the *Generalitat de Catalunya* (AGAUR, Spain) through the FI-SDUR PhD scholarship received by J. G. C. (2020 FISDU 00005). The authors are grateful to the CCiT-UB (Scientific and Technological Centers of the Universitat de Barcelona) for their support with the XRD and TEM analyses. The authors are also grateful to *Generalitat de Catalunya* for the pre-doctoral grant 2018FI-B-00384 for L. V. and partial support through grants 2017SGR13 and XRQTC. F. V. is thankful to *Ministerio de Economía y Competitividad* (MEC) for his *Ramón y Cajal* (RYC-2012-10129) research contract. The authors are thankful to *Red Española de Supercomputación* (RES) for the granted computing time (QS-2020-1-0002 and QS-2020-2-0006).

Notes and references

1 D. Thompsett, *Pt Alloys as Oxygen Reduction Catalysts. Handbook of Fuel Cells. Fundamentals, Technology and Applications*, John Wiley & Sons, 2003, New York.
2 M. K. Mahapatra and P. Singh, *Fuel Cells: Energy Conversion Technology. Future Energy: Improved, Sustainable and Clean Options for our Planet*, Elsevier, 2014, London.
3 M. K. Debe, *Nature*, 2012, **486**, 43–51.
4 S. Sui, X. Wang, X. Zhou, Y. Su, S. Riffat and C.-J. Liu, *J. Mater. Chem. A*, 2017, **5**, 1808–1825.
5 K. Ruth, M. Vogt and R. Zuber, *Development of CO-Tolerant Catalysts on Pt/Ru Catalysts*, John Wiley & Sons, 2010, New York.
6 P. Janthon, F. Viñes, J. Sirijaraensre, J. Limtrakul and F. Illas, *J. Phys. Chem. C*, 2017, **121**, 3970–3977.
7 A. Velázquez-Palenzuela, E. Brillas, C. Arias, F. Centellas, J. A. Garrido, R. M. Rodríguez and P. L. Cabot, *J. Catal.*, 2013, **298**, 112–121.
8 V. R. Stamenkovic, B. S. Mun, M. Arenz, K. J. J. Mayrhofer, C. A. Lucas, G. Wang, P. N. Ross and N. M. Markovic, *Nat. Mater.*, 2007, **6**, 241–247.
9 Y. Shao, G. Yin and Y. Gao, *J. Power Sources*, 2007, **171**, 558–566.
10 M. Gatalo, M. Bele, F. Ruiz-Zepeda, E. Šest, M. Šala, A. R. Kamšek, N. Maselj, T. Gakun, P. Jovanović, N. Hodnik and M. Gaberšček, *Angew. Chem., Int. Ed.*, 2019, **58**, 13266–13270.
11 N. Kristian, Y. Yu, J.-M. Lee, X. Liu and X. Wang, *Electrochim. Acta*, 2010, **56**, 1000–1007.
12 V. V. Pham, V.-T. Tu and C. Sunglae, *Int. J. Hydrogen Energy*, 2017, **42**, 13192–13197.
13 B. B. Bokhonov and D. V. Dudina, *J. Alloys Compd.*, 2017, **707**, 233–237.
14 M. M. S. Pupo, F. E. López-Suárez, A. Bueno-López, C. T. Menses, K. I. B. Eguiluz and G. R. Salazar-Banda, *J. Appl. Electrochem.*, 2015, **45**, 139–150.
15 K. M. El-Khatib, R. M. Abdel Hameed, R. S. Amin and A. E. Fetohi, *Microchem. J.*, 2019, **145**, 566–577.
16 S. Wojtysiak, M. Kamiński, J. Krajczewski, P. Dłużewski and A. Kudelski, *Vib. Spectrosc.*, 2014, **75**, 11–18.
17 A. Sarkar and A. Manthiram, *J. Phys. Chem. C*, 2010, **114**, 4725–4732.
18 S. Baek, K. H. Kim, M. J. Kim and J. J. Kim, *Appl. Catal., B*, 2017, **217**, 313–321.
19 A. A. Gokhale, J. A. Dumesic and M. Mavrikakis, *J. Am. Chem. Soc.*, 2008, **130**, 1402–1414.
20 Y. Hori, A. Murata, R. Takahashi and S. Suzuki, *J. Am. Chem. Soc.*, 1987, **109**, 5022–5023.
21 G. Caballero-Manrique, A. Velázquez-Palenzuela, E. Brillas, F. Centellas, J. A. Garrido, R. M. Rodríguez and P. L. Cabot, *Int. J. Hydrogen Energy*, 2014, **39**, 12859–12869.
22 I. Mintsouli, J. Georgieva, S. Armyanov, E. Valova, G. Avdeev, A. Hubin, O. Steenhaut, J. Dille, D. Tsiplakides, S. Balomenou and S. Sotiropoulos, *Appl. Catal., B*, 2013, **136–137**, 160–167.
23 J. Georgieva, E. Valova, I. Mintsouli, S. Sotiropoulos, S. Armyanov, A. Kakaroglou, A. Hubin, O. Steenhaut and J. Dille, *J. Appl. Electrochem.*, 2014, **44**, 215–224.
24 V. V. Pryadchenko, V. V. Srabionyan, A. A. Kurzin, N. V. Bulat, D. B. Shemet, L. A. Avakyan, S. V. Belenov, V. A. Volochaev, I. Zizak, V. E. Guterman and L. A. Bugaev, *Appl. Catal., A*, 2016, **525**, 226–236.
25 J. García-Cardona, I. Sirés, F. Alcaide, E. Brillas, F. Centellas and P. L. Cabot, *Int. J. Hydrogen Energy*, 2020, **45**, 20582–20593.
26 A. Papaderakis, I. Mintsouli, J. Georgieva and S. Sotiropoulos, *Catalysts*, 2017, **7**, 80.
27 S. R. Brankovic, J. X. Wang and R. R. Adzic, *Electrochem. Solid-State Lett.*, 2001, **4**, A217–A220.
28 S. Ambrosio and N. Dimitrov, *Electrochim. Acta*, 2015, **160**, 248–255.
29 Y.-G. Kim, J. K. Kim, D. Vairavapandian and J. L. Stickney, *J. Phys. Chem. B*, 2006, **110**, 17998–18006.
30 R. R. Adzic, J. Zhang, K. Sasaki, M. B. Vukmirovic, M. Shao, J. X. Wang, A. U. Nilekar, M. Mavrikakis, J. A. Valerio and F. Uribe, *Top. Catal.*, 2007, **46**, 249–262.
31 S. Papadimitriou, S. Armyanov, E. Valova, A. Hubin, O. Steenhaut, E. Pavlidou, G. Kokkinidis and S. Sotiropoulos, *J. Phys. Chem. C*, 2010, **114**, 5217–5223.
32 S. Zhou, B. Varughese, B. Eichhorn, G. Jackson and K. McIlwrath, *Angew. Chem., Int. Ed.*, 2005, **44**, 4539–4543.
33 F. Viñes and A. Görling, *Chem. – Eur. J.*, 2020, **26**, 11478–11491.
34 Z.-J. Zhao, R. Mu, X. Wang and J. Gong, *Langmuir*, 2017, **33**, 8700–8706.
35 G. Giannakakis, M. Flytzani-Stephanopoulos and E. C. H. Sykes, *Acc. Chem. Res.*, 2019, **52**, 237–247.
36 J. Solla-Gullón, V. Montiel, A. Aldaz and J. Clavilier, *J. Electrochem. Soc.*, 2003, **150**, E104–E109.
37 G. Kresse and J. Furthmüller, *Phys. Rev. B: Condens. Matter Mater. Phys.*, 1996, **54**, 11169–11186.
38 G. Kresse and J. Hafner, *Phys. Rev. B: Condens. Matter Mater. Phys.*, 1994, **49**, 14251–14269.
39 J. P. Perdew, K. Burke and M. Ernzerhof, *Phys. Rev. Lett.*, 1996, **77**, 3865–3868.
40 P. E. Blöchl, *Phys. Rev. B: Condens. Matter Mater. Phys.*, 1994, **50**, 17953–17979.
41 G. Kresse and D. Joubert, *Phys. Rev. B: Condens. Matter Mater. Phys.*, 1999, **59**, 1758–1775.

42 P. Janthon, F. Viñes, J. Sirijaraensre, J. Limtrakul and F. Illas, *J. Phys. Chem. C*, 2017, **121**, 3970–3977.
43 F. Viñes, F. Illas and K. M. Neyman, *Angew. Chem., Int. Ed.*, 2007, **46**, 7094–7097.
44 M. Happel, N. Luckas, F. Viñes, M. Sobota, M. Laurin, A. Göling and J. Libuda, *J. Phys. Chem. C*, 2011, **15**, 479–491.
45 J. Rovirets, L. Vega and F. Viñes, *Surf. Sci.*, 2017, **664**, 45–49.
46 L. Vega, H. A. Aleksandrov, R. Farris, A. Bruix, F. Viñes and K. M. Neyman, *Mater. Adv.*, 2021, **2**, 6457–6734.
47 H. A. Gasteiger, N. M. Markovic and P. N. Ross Jr., *J. Phys. Chem.*, 1995, **99**, 8290–8298.
48 G. Caballero-Manrique, E. Brillas, F. Centellas, J. A. Garrido, R. M. Rodríguez and P. L. Cabot, *Catalysts*, 2015, **5**, 815–837.
49 J. García-Cardona, F. Alcaide, E. Brillas, I. Sirés and P. L. Cabot, *Catalysts*, 2021, **11**, 724.
50 V. V. Pryadchenko, S. V. Belenov, D. B. Shemet, V. V. Srabionyan, L. A. Avakyan, V. V. Volochaev, A. S. Mikheykin, K. E. Bdoyan, I. Zizak, V. V. Guterman and L. A. Bugaev, *J. Phys. Chem. C*, 2018, **122**, 17199–17210.
51 V. E. Guterman, S. V. Belenov, A. A. Alekseenko, R. Lin, N. Y. Tabachkova and O. I. Safronenko, *Electrocatalysis*, 2018, **9**, 350–362.
52 J. Maya-Cornejo, R. Carrera-Cerritos, D. Sebastián, J. Ledesma-García, L. G. Arriaga, A. S. Aricò and V. Baglio, *Int. J. Hydrogen Energy*, 2017, **42**, 27919–27928.
53 A. A. Alekseenko, V. E. Guterman, S. V. Belenov, V. S. Menshikov, N. Y. Tabachkova, O. I. Safronenko and E. A. Moguchikh, *Int. J. Hydrogen Energy*, 2018, **43**, 3676–3687.
54 L. Luo, L. Zhang, Z. Duan, A. S. Lapp, G. Henkelman and R. M. Crooks, *ACS Nano*, 2016, **10**, 8760–8769.
55 R. M. Castagna, J. M. Sieben, A. E. Alvarez and M. M. E. Duarte, *Int. J. Hydrogen Energy*, 2019, **44**, 5976–5982.
56 M. R. Zamanzad Ghavidel, A. H. A. Monteverde Videla, S. Specchia and E. Bradley Easton, *Electrochim. Acta*, 2017, **230**, 58–72.
57 K. J. Andersson and I. Chorkendorff, *Surf. Sci.*, 2010, **604**, 1733–1736.
58 E. V. Carino, H. Y. Kim, G. Henkelman and R. M. Crooks, *J. Am. Chem. Soc.*, 2012, **134**, 4153–4162.

Electronic Supplementary Material (ESI) for Materials Advances.

Electronic Supplementary Information

Nanostructuring Determines Poisoning: Tailoring CO Adsorption on PtCu Bimetallic Nanoparticles

Lorena Vega,[a,b,†] Julia Garcia-Cardona,[a,†] Francesc Viñes,[a,b*] Pere L. Cabot[a,*] and Konstantin M. Neyman[a,b,c]

[a]*Departament de Ciència de Materials i Química Física, Universitat de Barcelona, c/ Martí i Franquès 1-11, 08028 Barcelona, Spain*

[b]*Institut de Química Teòrica i Computacional (IQTCUB), Universitat de Barcelona, c/ Martí i Franquès 1-11, 08028 Barcelona, Spain*

[c]*ICREA (Institució Catalana de Recerca i Estudis Avançats), Pg. Lluís Companys 23, 08010 Barcelona, Spain*

* Corresponding authors: Pere L. Cabot (p.cabot@ub.edu), Francesc Viñes (francesc.vines@ub.edu)

† L. V. and J. G.-C. equally contributed.

Fig. S1 Different studied CO adsorption sites exemplified on the Pt_{201} nanoparticle.

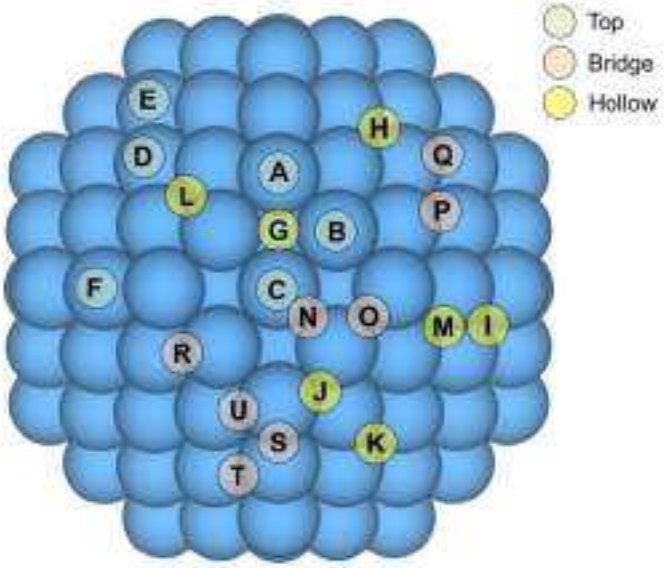

Table S1 Calculated adsorption energies, E_{ads}, given in eV, of CO molecule adsorbed through its O atom in various top positions of the nanoparticulate models **1**, **2**, **3**, and **5**. The adsorption sites and models are specified in Figs. S1 and Figure 2 of the main text. In model **5**, the O-end CO adsorption is explored on the exposed Cu atom.

Model / Site	A	B	C	D	F
1	~0	~0	~0	~0	~0
2	-0.01	-0.01	-0.01	~0	-0.01
3	-0.05	-0.05	-0.05	-0.04	-0.05
5	-0.03	-0.02	-0.01	-0.01	-0.02

Table S2 Adsorption energies, E_{ads}, in eV, for CO adsorbed in different bridge positions, see Fig. S1, of different models, see Fig. 2 in the main text.

Model / Site	N	O	P	Q	R	S	T	U
1	-1.97	-2.07	-1.94	-1.86	-1.73	-1.97	-1.75	-1.76
2	-0.77	→A	-0.60	→D	→I	→A	→I	→R
3	-1.67	-1.94	-1.15	-1.09	-1.22	-1.82	-1.40	-1.41
5	→P[a]	→B[a]	→E[a]	→E[a]	→U[b]	→A[a]	→A[a]	→R

[a] on Pt atom
[b] bridge between two Pt

Table S3 Adsorption energies, E_{ads}, in eV, for CO adsorbed in different hollow positions, see Fig. S1, of different models, see Fig. 2 in the main text.

Model / Site	G	H	I	J	K	L	M
1	-1.54	-1.78	→P	→P	-1.89	→T	→P
2	-0.80	-0.83	-0.69	-0.73	-0.68	→B	-0.67
3	-1.50	→S	→P	-1.23	-1.25	→O	-1.31
5	-1.64	→P[a]	→S[a]	→R[b]	→P[a]	→O[a]	→T[b]

[a] on Pt atom
[b] bridge between two Pt

S1 Electronic effects

The discussed seemingly counterintuitive CO adsorption strengthening can be understood using charge density difference (CDD) plots, see Fig. 5 of the main text, evaluating the donation/back-donation bonding mechanism, plus the corresponding Bader charge[1] data, see Tables S4 and S5. According to the Bader charges, the Pt corner atom completely surrounded at the surface by Cu atoms and having all subsurface Pt neighbours is negatively charged by -0.43 *e* due a charge transfer from its surface Cu neighbours, which contrasts with a significantly smaller negative charge of -0.11 *e* of the corner Pt atom in the Pt_{201} NP. Such accentuated negatively charged site favours attraction to it of the $C^{\delta+}$ CO atom. Figure 5 of the main text clearly shows a donation/back-donation mechanism on all Pt adsorption sites, and so, this excess charge is back-donated from Pt 5*d* states to the $2\pi^*$ CO orbital, contributing to a stronger binding. Finally, despite this charge transfer, the remaining charge of the corner Pt atom is still -0.13 *e*, serving as a Coulombic anchor to the $C^{\delta+}$ atom of the adsorbed CO molecule.

In the Pt_3 vacancy, CO bridges two rearranged surface Pt atoms, each with a negative charge of -0.15 *e*, different from a slightly positive charge of 0.07 *e* found in the Pt_3 vacancy in Pt_{201}. The conjunction of under-coordination and accumulation of electron charge is thus again the main origin of a stronger back-donation, resulting as well in a larger magnitude of the adsorption energy. Finally, the most undercoordinated Pt adatom on a (111) facet bears larger positive charge on the Pt_{201} NP, 0.26 *e*, than on the Cu@Pt NP, 0.18 *e*, thus weakening the CO adsorption in the former case.

Table S4 Bader charges, Q, in *e*, on metal atoms of **A** sites, see Fig. S1, of different models, see Fig. 2 of the main text, prior or after to CO adsorption, as well as on the adsorbed CO molecule. Surface (Sur) and subsurface (Sub) types of atoms are indicated. A distinction is made for surface, Q_{Sur}, and subsurface, Q_{Sub}, charges. CO adsorption energies E_{ads} (in eV) are also listed for convenience.

				Prior		After		
Model	E_{ads}	M_{Sur}	M_{Sub}	Q_{Sur}	Q_{Sub}	Q_{Sur}	Q_{Sub}	Q_{CO}
1	-2.08	Pt	Pt	-0.10	0.11	0.16	0.04	-0.16
2	-0.98	Cu	Cu	-0.06	0.06	0.20	0.02	-0.17
3	-1.67	Pt	Cu	-0.14	0.30	0.14	0.28	-0.16
5	-0.95	Cu	Cu	0.29	0.29	0.47	0.28	-0.13
6	-1.87	Pt	Cu	-0.54	0.21	-0.22	0.15	-0.18
7	-2.24	Pt	Pt	-0.44	-0.43	-0.13	-0.49	-0.19
8	-2.07	Pt	Cu	-0.09	0.29	0.18	-0.31	-0.17

Table S5. Bader charges, Q, in *e*, on Pt adatoms or Pt_3 vacancy sites of Pt_{201} (**model 1**) and $Cu_{79}@Pt_{119}$ (**model 3**) NPs prior and after CO adsorption, as well as on the CO molecule. Surface (Sur) and subsurface (Sub) types of atoms are indicated. A distinction is made for surface, Q_{Sur}, and subsurface, Q_{Sub}, charges. CO adsorption energies E_{ads} (in eV) are also listed for convenience.

Model	E_{ads}	M_{Sur}	M_{Sub}	Q_{Sur}	Q_{Sub}	Q_{Sur}	Q_{Sub}	Q_{CO}
1: Pt_3 vacancy	-1.20	Pt	Pt	0.07	-0.06	0.20	-0.05	-0.34
1: Pt adatom	-2.25	Pt	Pt	-0.01	-0.02	0.26	−0	-0.19
3: Pt_3 vacancy	-2.43	Pt	Cu	-0.15	0.22	0.06	0.12	-0.26
3: Pt adatom	-2.53	Pt	Pt	-0.02	-0.10	0.18	-0.14	-0.21

References

1 Bader, R. F. W. *Atoms in Molecules: a Quantum Theory*, Oxford University Press New York, 1990.

4.2. Electrochemical Performance of Carbon-Supported Pt(Cu) Electrocatalysts for Low-Temperature Fuel Cells

The most used carbon support for PEMFCs catalysts are CBs, since they are cheap and easily obtained. However, they present some disadvantages, as they present impurities that can poison the catalyst, deep micropores that limit the access of reactants to the catalyst and have low thermochemical stability. Since Pt catalysts supported on CNTs and CNFs have shown increased stability and catalytic activity compared to Pt catalysts supported on CBs, these carbonaceous materials have been studied in this work as alternative supports for PtCu.

The catalysts were prepared by electroless deposition of Cu in aqueous basic media using $NaBH_4$ as reducing agent, as explained in Chapter 3, Section 3.3, followed by a partial galvanic replacement of Cu by Pt. The carbon supports were MWCNTs and CNFs, which were used as received and also after a mild chemical activation with HNO_3 (identified by an "-A" at the end of the carbon support designation). The catalysts obtained were compared to commercial Pt/C and PtCu/C and also to synthesised PtCu supported on carbon XC-72.

The catalysts obtained were analysed by XRD in order to ascertain their structure. There was the evidence of a carbon diffraction peak in the samples containing both MWCNTs and CNFs, which was not previously found in the catalysts obtained with Vulcan XC-72. This peak suggests a greater crystallinity of these carbon materials. The other part of the diffractogram was consistent with the shape of pure Pt, although the peaks were slightly shifted to higher values, which was explained by the lattice contraction as a consequence of the PtCu alloy formation. The composition of the crystal structure and the crystallite size were obtained by using Scherrer's and Vegard's laws, Eqs. (34) and (35), respectively. The Pt content of the crystallite, 2-4 nm in size, was higher than that of Cu. The particle sizes were consistent with those observed by TEM and, although nanoparticle agglomeration was observed, there was evidence of their good attachment to the carbon support.

The EDS analyses showed similar weight percentage of Pt and Cu, thus indicating a Pt reduction by 50% of the catalysts. Using the XPS a further understanding of the nanoparticle composition was obtained, since all the samples showed a decrease in the

Pt(0):Cu(0) ratio after Ar^+ sputtering for 60s. This result indicated that the nanoparticles presented a core containing PtCu alloy and a Pt-rich shell.

The ECSAs of the catalysts were all similar, around 70-80 $m^2\ g_{Pt}^{-1}$ for all the catalysts except for the MWCNTs and those using the activated carbons, which presented larger agglomeration of nanoparticles as compared to the non-activated ones, thus making the catalytic surface less accessible to reactants. The CO stripping showed a significant onset potential shift for CO oxidation, from ca. 0.7 V for PtCu/C and Pt/C to ca. 0.65 V for PtCu/CNF and PtCu/XC-72, being that of Pt/C the most positive one. These results confirm the weakening of the Pt-CO bond and the consequent increase in the CO oxidation rate, which could be related to the Cu alloying effect.

The highest catalytic activities in front of the ORR were obtained using Pt(Cu)/CNF, followed by the commercial PtCu/C catalyst, with limiting current values of about 260 and 180 mA mg_{Pt}^{-1}, respectively. The onset potential for Pt(Cu)/MWCNT was more positive than those of the other catalysts, followed by Pt(Cu)/XC-72 and Pt(Cu)/CNF, which would mean a greater catalytic activity if it was not for its low ECSA value. Therefore, Pt(Cu)/CNF possessed higher mass activities than the others, but Pt(Cu)/MWCNT yielded greater specific activity.

Since one of the interests of using these materials as support for PEMFCs catalysts was to increase their stability, the relative stability of the catalysts was studied by accelerated degradation tests, knowing that the occurrence of atomic restructuration because of the oxidation/reduction of Pt species and carbon oxidation could lead to nanoparticle aggregation. The results showed ECSA losses of about 25% for Pt(Cu)/CNF, 11% for Pt(Cu)/MWCNT and 42% for Pt(Cu)/XC-72, proving the higher stability obtained by using the alternative carbon supports presented in this work.

INTERNATIONAL JOURNAL OF HYDROGEN ENERGY 45 (2020) 10581–10593

Available online at www.sciencedirect.com

ScienceDirect

journal homepage: www.elsevier.com/locate/he

Electrochemical performance of carbon-supported Pt(Cu) electrocatalysts for low-temperature fuel cells

Julia Garcia-Cardona [a], Ignasi Sirés [a], Francisco Alcaide [a,b], Enric Brillas [a], Francesc Centellas [a], Pere L. Cabot [a,*]

[a] Laboratori d'Electroquímica Dels Materials I Del Medi Ambient, Departament de Química Física, Facultat de Química, Universitat de Barcelona, Martí I Franquès 1-11, 08028, Barcelona, Spain
[b] CIDETEC, Paseo Miramón, 196, 20014 Donostia-San Sebastián, Spain

HIGHLIGHTS

- The Pt(Cu) nanoparticles exhibited PtCu alloying with external Pt-rich shell.
- The supported Pt(Cu) catalysts had higher CO tolerance than commercial Pt/C and PtCu/C.
- The Pt(Cu) nanostructures of about 3 nm allowed saving the Pt amount by about 50 wt%.
- Pt(Cu)/CNF and Pt(Cu)/MWCNT had respectively the best mass and specific activity for ORR.
- Pt(Cu)/CNF and Pt(Cu)/MWCNT presented better relative stability than Pt(Cu)/XC72.

GRAPHICAL ABSTRACT

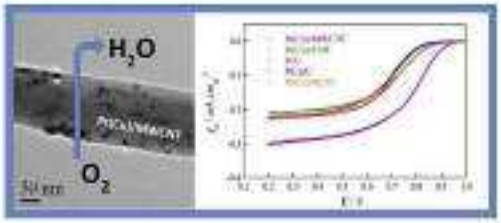

ARTICLE INFO

Article history:
Received 5 October 2019
Received in revised form
3 February 2020
Accepted 7 February 2020
Available online 28 February 2020

Keywords:
CO oxidation
Galvanic exchange
Low-temperature fuel cells

ABSTRACT

Pt(Cu) nanoparticles supported on carbon nanofibers (CNFs), multi-walled carbon nanotubes (MWCNTs) and Vulcan carbon XC72, have been synthesized by electroless deposition and galvanic exchange. The structural analyses show contracted Pt fcc lattices due to the formation of a PtCu alloy core covered by a Pt-rich shell, mean crystallite sizes of about 3 nm, as well as good dispersion and carbon attachment. The electrochemical surface areas (ECSAs) of Pt(Cu)/CNF and Pt(Cu)/XC72 are comparable to those of commercial Pt/C and PtCu/C. The Pt(Cu) electrocatalysts show more negative onset potentials for CO oxidation than Pt/C and PtCu/C, thus indicating their greater CO tolerance. Pt(Cu)/CNF and Pt(Cu)/MWCNT present the highest mass activity and specific activity for the O_2 reduction, respectively, both with better relative stability than Pt(Cu)/XC72. Pt(Cu)/CNF and Pt(Cu)/

* Corresponding author.
E-mail address: p.cabot@ub.edu (P.L. Cabot).
https://doi.org/10.1016/j.ijhydene.2020.02.038

Oxygen reduction reaction
Pt(Cu) electrocatalysts

MWCNT are then considered good cathode catalysts, yielding estimated savings of about 50 wt% Pt, when applied to low-temperature fuel cells.

Introduction

The energy demand has increased considerably in recent years and the needs have been mainly fulfilled by using fossil fuels, which are rapidly depleting and cause a huge impact on the environment because of the emission of greenhouse gases and pollutants, thereby contributing to the climate change, health problems and acid rain [1–3]. Therefore, it is mandatory to increase the use and development of renewable energy. Fuel cells are one of the most promising green alternatives because they can operate more efficiently than other energy sources, being only dependent on an unlimited renewable source of reactants and approaching zero carbon emissions [4].

It is well known that a large part of the greenhouse gas emissions and release of atmospheric pollutants arises from the use of fossil fuels for transportation. The proton exchange membrane fuel cells (PEMFCs) represent a big advantage over internal combustion engines in automotive vehicles, as they produce zero emissions when using hydrogen as the fuel and oxygen from the air as the oxidant [2,5]. In PEMFCs, the catalysts are generally based on Pt, which is the best material to promote the hydrogen oxidation reaction (HOR) and the oxygen reduction reaction (ORR). However, this metal is too expensive and scarce on the Earth and, moreover, when used at the anode in PEMFCs, it can be easily poisoned by the CO impurities contained in the H_2 gas of industrial grade [6]. To counteract this problem, the use of PtRu electrocatalysts has been proposed [7–9], but the high price of Ru is still a major drawback.

As a strategy to economize Pt, the synthesis of carbon-supported multi-metallic catalysts may allow the reduction of the Pt content. Core-shell nanoparticles, in which a Pt shell coats the surface of a sacrificial metal core that is cheaper and/or more abundant [10–12], are particularly interesting among such materials. The structural properties of the noble catalyst undergo significant changes due to its interactions with the core. The surface stress and changes in the electronic properties of the noble coating can eventually lead to a remarkable improvement of its catalytic properties.

The Pt–Cu bimetallic system is the object of recent interest [11–36]. Cu covered by noble metals without carbon support [11,12] and PtCu alloys, Pt(Cu) core-shells and Cu-dealloyed PtCu supported on carbon blacks [13–30] have been studied to determine their structure and activity in front of CO and methanol oxidation, ethanol oxidation and the oxygen reduction reaction (ORR). Promising results regarding the reduction of Pt amount and CO poisoning have been obtained. These catalysts have been mainly supported on Vulcan carbon XC72 and XC72R using different procedures [14–28]. In aqueous media, the Pt(Cu) core-shell electrocatalysts have been prepared either by direct current deposition [18,23,24] or electroless deposition of Cu using $NaBH_4$ [19,25], formaldehyde [20] and water-ethylene glycol mixtures with $NaBH_4$ and ascorbic acid [20,27–31], both methods followed by a galvanic exchange of Cu by Pt.

Most of the Pt-based nanoparticle catalysts for PEMFCs are supported on porous materials with high specific surface area because this allows using a small amount of Pt and obtaining a high dispersion and narrow size distribution of Pt nanoparticles, an important requirement for their high catalytic performance [37]. Carbon blacks are the most employed supports due to their high surface area, electrical conductivity, porosity and low cost [23]. However, they have several disadvantages [37,38] such as the presence of impurities, mainly organo-sulphur groups (that can poison the catalyst) and the existence of deep micropores that can trap the catalyst nanoparticles (thus making them inaccessible to reactants). In addition, carbon blacks are thermochemically unstable and therefore, they can suffer corrosion with the consequent disintegration of the catalyst layer.

Multi-walled carbon nanotubes (MWCNTs) and carbon nanofibers (CNFs) present some advantages as compared to carbon blacks. They exhibit a unique structure and properties that provide high electrical performance and a specific metal-support interaction (between the delocalized π-electrons of the carbon support and Pt d-electrons) [38,39]. In addition, CNTs and CNFs have few impurities, they do not show deep cracks and can enhance the cell performance with their ordered structure, thereby favoring the mass transport and the electron conductivity. The carbon support may be oxidized in the PEMFC cathode, due to the O_2 feed, especially under standby conditions, thus causing the detachment of the Pt nanoparticles with the corresponding activity loss. CNTs have shown to improve the durability of catalysts as compared with Vulcan XC72 [22,39–41]. An accelerated degradation test in diluted acidic solution at high potential (1.2 V vs RHE) has been made to study de durability of both, the support and the supported catalysts. It was observed that the oxygen content in Vulcan XC72 was much higher than that in CNTs, whereas the degradation of the surface area of the Pt nanoparticles was greatly suppressed when supported on the latter, which was attributed to their larger resistance to corrosion. Previous works have studied the synthesis and characterization of Cu-dealloyed PtCu alloys supported on CNTs and multi-walled carbon nanotubes (MWCNTs), showing an enhancement of both, the catalytic activity related to the ORR and the electrochemical surface area [42–44].

Considering all this, the main objective of this work is to synthesize and test Pt(Cu) electrocatalysts, supported on CNFs and MWCNTs, for CO oxidation and ORR. The Pt(Cu)/CNF and Pt(Cu)/MWCNT catalysts have been prepared by electroless

deposition of copper on the CNFs and the MWCNTs followed by galvanic exchange with Pt. They have been characterized by means of structural and electrochemical techniques and the corresponding results were compared (i) to those obtained with synthesized Pt(Cu) catalysts supported on carbon XC72 [Pt(Cu)/XC72], prepared in the same manner as Pt(Cu)/CNF and Pt(Cu)/MWCNT, and (ii) to commercial Pt/C and PtCu/C.

Materials and methods

Reagents

All the reagents were of analytical grade: HNO_3, NaOH, H_2SO_4 (98 wt%), $CuSO_4{\cdot}5H_2O$, ethanol (96 wt%) and 2-propanol (dry) were from Panreac. The H_2PtCl_6 aqueous solution (10 wt%) was from Merck. $NaBH_4$ and the Nafion® solution (5 wt%) were from Sigma-Aldrich. The solutions were prepared using Millipore Milli-Q high-purity water (resistivity >18.2 MΩ cm at 25 °C). The carbon supports were Vulcan carbon XC72 from Cabot Corporation and CNFs and MWCNTs from Sigma-Aldrich. The catalysts obtained were compared to Pt/C (20 wt%) and PtCu/C (1:1, 20 wt%) commercial catalysts from Premetek, which employ Vulcan XC72 as the carbonaceous support. N_2 and CO gases were Linde 3.0 (purity ≥ 99.9%).

Synthesis of the carbon-supported Pt(Cu) catalysts

The catalysts were prepared following a similar procedure to the two-step synthesis reported by Mintsouli et al. [13], consisting of an electroless deposition of copper ions on the carbon supports followed by partial galvanic replacement of Cu by Pt. The XC72, CNF and MWCNT supports were used as received and also after activation in 2.0 M HNO_3 for 30 min at boiling temperature, the activated specimens being denoted as XC72-A, CNF-A and MWCNT-A, respectively.

First, weighted amounts of $CuSO_4{\cdot}5H_2O$ and the carbon support were dispersed in 1.0 M NaOH using an ultrasonic bath. Then, a determined amount of $NaBH_4$ was slowly added to stimulate the copper deposition. The sonication was prolonged for 30 min and then, the suspension was filtered. The powder obtained was resuspended in 0.1 M HCl + 1.5 mM H_2PtCl_6 using the ultrasonic bath for 45 min to ensure the galvanic replacement according to reaction (1):

$$2Cu + PtCl_6^{2-} \rightarrow 2Cu^{2+} + Pt + 6Cl^- \quad (1)$$

which has a standard redox potential of $E^o = 0.404$ V. Finally, the suspension was filtered and the powder was dried at 80 °C. The catalysts thus synthesized were Pt(Cu)/XC72, Pt(Cu)/XC72-A, Pt(Cu)/CNF, Pt(Cu)/CNF-A, Pt(Cu)/MWCNT and Pt(Cu)/MWCNT-A.

Structural characterization

The X-ray diffraction (XRD) of the supports and the catalysts was performed by means of a PANalytical X'Pert PRO MPD θ/θ powder diffractometer (Cu anode, 45 kV, 40 mA), using a Cu K_α-filtered radiation (λ = 1.5418 Å), 2θ step size of 0.026° and a measuring time of 200 s per step. The powder samples were sandwiched between films of polyester of 3.6 μm in thickness.

The catalysts were examined by means of transmission electron microscopy (TEM) using a 200 kV JEOL JEM 2100, which also allowed obtaining the corresponding energy-dispersive X-ray spectroscopy (EDS) analyses. In this case, the catalyst powder was sonicated in 3 mL of ethanol for 10 min. A drop of suspension was placed over a holey-carbon Ni grid and then, the solvent was evaporated until total drying using a 40 W lamp for 5 min. For the EDS analyses, about ten different regions of the same sample were examined, taking the corresponding result in composition as the mean value of all of them.

The X-ray photoelectron spectroscopy (XPS) analyses were performed by means of a Physical Electronics PHI 5500 Multitechnique System spectrometer with a monochromatic X-ray source (Al Kα line of 1486.6 eV, powered at 350 W). The energy was calibrated using the $3d_{5/2}$ line of Ag with a full width at half maximum (FWHM) of 0.8 eV. The catalyst powders were disposed on a carbon tape for the analyses. The analyzer was placed 20° with respect to the tape for a better detection of the composition of the external layers. After the initial survey spectrum (187.85 eV of Pass Energy and 0.8 eV/step), the high-resolution spectra (23.5 eV of Pass Energy and 0.1 eV/step) was obtained. The corresponding XPS spectra, acquired without sputtering and after Ar^+ sputtering for 60 s, were analyzed using the MultiPak V8.2B software.

Electrochemical tests

The electrochemical characterization of the catalysts was performed in a 200 mL conventional three-electrode cell from Metrohm, provided with a double wall to keep a constant temperature of 25.0 ± 0.1 °C with the help of a Julabo MP-5 thermostat. The reference and auxiliary electrodes were a reversible hydrogen electrode (RHE) from Gaskatel GmbH and a Pt wire, respectively. All the potentials reported in this work are referred to the RHE. The working electrode for the electrochemical tests was a Metrohm glassy carbon (GC) tip (5 mm in diameter, section of 0.196 cm^2) for Autolab rotating disk electrode (RDE). It was polished with Micropolish II deagglomerated alumina of 0.3 and 0.05 μm on a PSA-backed White Felt cloth from Buehler. After each polishing step, the GC was sonicated in water. Suitable amounts of the catalysts were deposited onto the tip of the GC. The catalyst inks were prepared from 1 mg of the catalyst powder, sonicated in 500 μL of a mixture of isopropanol and water (1:1 in volume) for 30 min. Volumes of 20 μL of the ink were dropped onto the GC tip and, after being dried at room temperature, a thin Nafion® film was applied on the catalyst ink. For the cyclic voltammetry (CV) trials, the catalyst was coated with 2.5 μL of 5 wt% Nafion® solution, whereas to study the ORR, it was coated with 5 μL of 0.1 wt% Nafion® solution.

The electrochemical experiments were performed in 0.50 M H_2SO_4 using a Solartron SI 1287 potentiostat-galvanostat, commanded by a CorrWare software, version 2.6b. Before the CV tests, N_2 was bubbled for 30 min through the solution in order to remove the dissolved O_2 and it was kept over the liquid surface during these measurements. After

the O_2 removal, the working electrode was scanned repeatedly at a scan rate of 100 mV s^{-1} within the potential range from 0.0 to 1.2 V until reaching a stationary profile to ensure the removal of any adsorbed impurity. Afterwards, steady cyclic voltammograms were recorded at 20 mV s^{-1} within the same potential range. To obtain the CO stripping curves, CO was first bubbled through the solution for 15 min, whereas a potential of 0.1 V was applied to the working electrode. The dissolved CO was removed by N_2 bubbling through the solution for 30 min and then, the adsorbed CO monolayer was oxidized by CV within the range 0.0–1.2 V at 20 mV s^{-1}. The ORR was studied using the RDE with the catalyst-coated GC employing a 0.50 M H_2SO_4 solution, after bubbling pure O_2 through it. The potential was scanned linearly from 0.8 to 0.0 V at 5 mV s^{-1} and at different rotational speeds between 500 and 2500 rpm.

Results and discussion

Structural characterization

The XRD diffractograms of the different carbon supports are shown in Fig. 1a, where the diffraction lines corresponding to different carbon planes have been highlighted. It is evident that the carbon peak corresponding to the (002) plane at about 26° was much thinner for MWCNTs and CNFs than for Vulcan XC72, suggesting a greater crystallinity of the two former carbons. Although it is not a very relevant factor for the catalyst deposition, the crystallite sizes of the MWCNTs and the CNFs were estimated from that peak using the Scherrer equation:

$$d = \frac{K\lambda}{B\cos\theta} \quad (2)$$

where K = 0.9, λ is the wavelength of the X-ray radiation, and B is the width (in radians) of the measured diffraction peak at an intensity equal to half the maximum intensity. The sizes were thus estimated to be 9.3 and 12 nm for CNFs and MWCNTs, respectively. Considering the C(100) peak, a crystallite size value of 1.3 nm was obtained for XC72. According to the furnishers, the diameter of the CNFs and the MWCNTs was about 100 nm, whereas their lengths were in the range 20–200 and 5–9 μm, respectively. The diameter of the XC72 nearly spherical particles was about 50 nm. The small values of the crystallite sizes with respect to the dimensions of the carbonaceous structures indicate their small range of crystallinity.

The XRD diffractograms of the different catalysts studied are depicted in Fig. 1b and c. Fig. 1b shows those corresponding to the carbon-supported Pt(Cu) ones, which are compared to those obtained for commercial Pt/C and PtCu/C. The diffractograms of the synthesized ones have all similar shape and Pt appears to predominate. The Cu structure is not clearly identified and no XRD peaks corresponding to copper oxides can be observed. The XRD peaks of these carbon-supported Pt(Cu) catalysts can be related to fcc Pt (111), (200) and (220) planes and they are located at 2θ values of 40.8°, 47.2° and 69.2°, respectively (PDF #00-001-1194) [35]. As shown in Fig. 1b, the Pt peaks corresponding to commercial Pt/C are located at 40.0°, 46.3° and 67.5°. The shift of the Pt peaks in the synthesized Pt(Cu) samples indicates that a PtCu alloy is probably formed. Shifting to higher angles with respect to pure Pt can be explained by a lattice contraction as a consequence of the formation of the PtCu alloy, because the atomic radius of Cu (145 pm) is smaller than that of Pt (177 pm). The XRD diffractogram of commercial PtCu/C also included in Fig. 1b and c shows diffraction peaks related to those of the three mentioned planes of Pt at 41.1°, 48.1° and 69.6°,

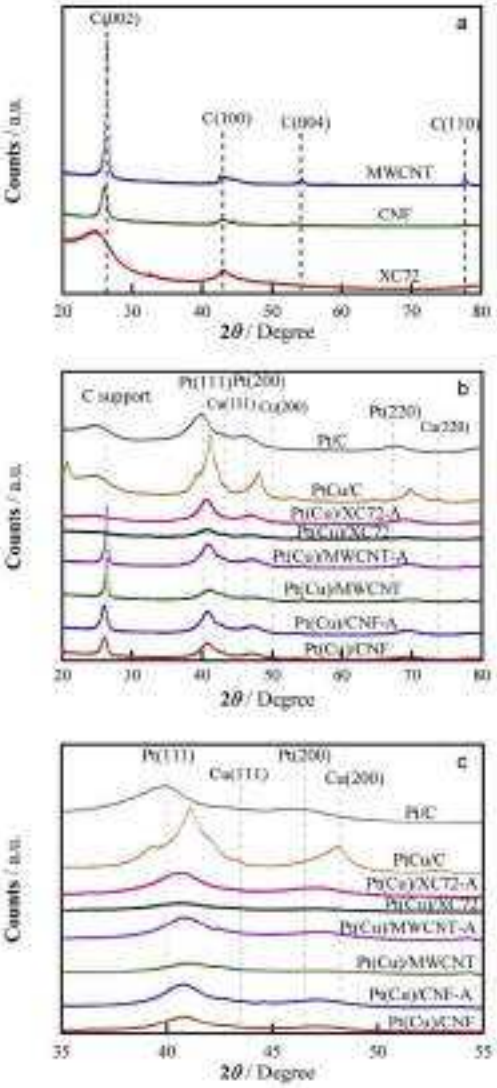

Fig. 1 – XRD diffractograms of (a) carbon supports and (b) supported catalysts under study. (c) Magnification of the main peaks of plot (b), which correspond to (111) and (200) Pt and Cu planes.

respectively. The diffraction angles of the synthesized carbon-supported Pt(Cu) catalysts are between those of pure Pt and PtCu. Accepting that the Pt signal shift is due to Cu alloying, the Cu content in commercial PtCu should be higher. The composition of the PtCu alloys in the samples studied can be estimated from Vegard's law, which relates the lattice parameter a_{PtCu} of the PtCu alloy with the atomic fraction of Cu (x):

$$a_{PtCu} = (1 - x)\, a_{Pt} + x\, a_{Cu} \quad (3)$$

where a_{Pt} and a_{Cu} are the lattice parameter of Pt (0.3916 nm) and Cu (0.3608 nm) [45]. The corresponding results are shown in Table 1. As shown in this table, the amount of Pt in the PtCu alloy lattice of the Pt(Cu) catalysts is in the range 1.6–2.7 times greater than that of Cu, whereas that of the commercial one approaches the Pt:Cu 1:1 ratio. This indicates that in the galvanic exchange of Cu by Pt, the external Cu atoms are oxidized and replaced by Pt and that some lattice reordering takes place to form a PtCu alloy, in agreement with previous results in the literature [30,31,32]. If residual Cu oxidized species remained on the catalyst surface, they should be amorphous or in rather small amounts, since no Cu(II) crystalline phases were found in the diffractograms.

As shown in Fig. 1b and c, the Pt diffraction peaks are broad. This peak broadening could be caused, apart from the small size of the nanoparticles, by their non-uniform composition and therefore, the superposition of the peaks of different phases, as previously reported by Guterman et al. [30]. In spite of not being pure metals, the crystallite size of the nanoparticles was estimated from Scherrer's equation (2), with the values also listed in Table 1. Note that these values are around 3 nm, which is considered a suitable size for PEMFCs application.

Fig. 2 shows TEM images of the synthesized catalysts, where the Pt(Cu) nanoparticles can be seen as black spots. These images also show the morphology of the carbonaceous supports, displaying the shape of fibers for Pt(Cu)/CNF and Pt(Cu)/CNF-A (Fig. 1a and b, respectively), nanotubes for Pt(Cu)/MWCNT and Pt(Cu)/MWCNT-A (Fig. 1c and d), and spherules for Pt(Cu)/XC72 and Pt(Cu)/XC72-A (Fig. 1e and f). As shown in these figures, the diameter of the carbonaceous materials and their length in the case of the nanofibers and nanotubes correspond to the values provided by the furnishers, mentioned in the experimental part. The Pt(Cu) nanoparticles appear to be organized in a variety of sizes, with relative dispersion over the supports and some aggregation.

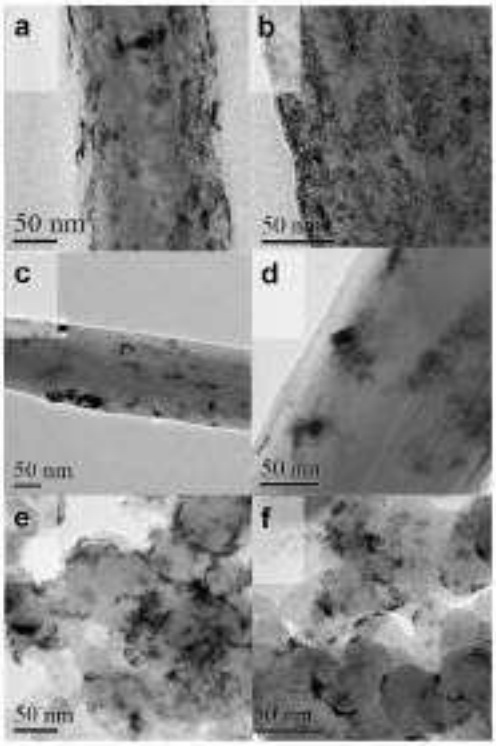

Fig. 2 – TEM images of (a) Pt(Cu)/CNF, (b) Pt(Cu)/CNF-A, (c) Pt(Cu)/MWCNT, (d) Pt(Cu)/MWCNT-A, (e) Pt(Cu)/XC72 and (f) Pt(Cu)/XC72-A.

Table 1 – Crystallite sizes of the catalyst nanoparticles and PtCu alloying obtained from the XRD diffractograms of Fig. 1 and catalyst composition from EDS analyses.

Catalyst	Crystallite size/nm	PtCu at% ratio[a]	Metal content[b]/ wt%		Pt:Cu at% ratio[c]
			Pt	Cu	
Pt(Cu)/CNF	2.9	71:29	5.1	4.1	29:71
Pt(Cu)/CNF-A	2.3	66:34	5.9	6.2	24:76
Pt(Cu)/MWCNT	3.0	62:38	7.4	5.9	29:71
Pt(Cu)/MWCNT-A	2.8	68:34	8.1	6.2	30:70
Pt(Cu)/XC72	2.0	73:27	7.4	7.3	25:75
Pt(Cu)/XC72-A	4.7	70:30	5.7	4.2	31:69
PtCu/C (commercial)	3.4	57:43	15.1	4.9	50:50
Pt/C (commercial)	2.6	100:0	20.0	0.0	100:0

[a] Pt:Cu atomic ratio of the PtCu alloy from XRD (Vegard's law).
[b] Overall content in the catalyst from EDS (mean standard deviation of 1.5 wt %).
[c] Pt:Cu atomic ratio in the catalyst from EDS.

There is a clear evidence in these images of the successful attachment of Pt(Cu) nanoparticles to the carbon support both, using the carbonaceous material as received and after activation. It can also be observed in these figures that the deposited Pt(Cu) crystallites have elongated forms, developed over the support, with little vertical growth. The composition of the supported Pt(Cu) nanoparticles was semiquantitatively determined by EDS, obtaining the values summarized in Table 1. These values are the result of the synthesis history, and it is expected that they strongly depend on the support properties. Accordingly, they will also depend on the crystallite size of the previously deposited Cu nanoparticles.

It is interesting to note that the weights of Pt and Cu are in the same order of magnitude, thus indicating that the amount of Pt has been reduced by about 50 wt%. However, these weights correspond to different atomic amounts of Pt and Cu, the latter being dominant by 2–3 folds. The difference with respect to the PtCu alloy composition obtained from Vegard's law is significant, thus indicating that there many Cu species (oxidized or not) without Pt bonding.

EDS line profiles to ascertain the Cu and Pt distribution in the nanoparticles were attempted. However, the resolution was no sufficient because of their small size. For this reason, XPS surface analyses were performed, as suggested by Mayo-Cornejo et al. [31]. In our case, the spectra were acquired with the analyzer placed 20° with respect to the plane of the samples to obtain a better approach of the composition of the most external layers. No mild sputtering was carried out to avoid the removal of Pt and Cu surface species apart from adventitious carbon. These analyses were performed then without sputtering and with Ar^+ sputtering for 60 s. The Pt and Cu high resolution spectra measured for Pt(Cu)/CNF are shown in Fig. 3. Fig. 3a and c correspond to the Cu binding energy (BE) region, before sputtering and after sputtering, respectively, and Fig. 3b and d, to the Pt BE region, before sputtering and after sputtering, also respectively. The deconvolution of the spectra revealed the presence of Cu and Pt oxidized species. The atomic percentages of the metallic form with respect to the other forms of the element together with the overall Pt:Cu atomic ratios are listed in Table 2. From these data, the Pt(0):Cu(0) atomic ratio has been derived and also given in the table.

Table 2 – Relative atomic composition of the different oxidation states of Cu and Pt species in different catalysts. The atomic ratio of the overall forms and of the metallic forms of Pt and Cu is also given.

Species	Ar⁺	Pt(Cu)/CNF	Pt(Cu)/MWCNT	Commercial PtCu/C
Pt(0):Pt(II):Pt(IV)	N	62:10:28	61:17:22	66:11:23
Cu(0):Cu(II)	N	30:70	25:75	43:57
Pt(0):Pt(II):Pt(IV)	Y	66:11:23	50:40:10	43:31:26
Cu(0):Cu(II)	Y	81:19	77:23	72:28
Overall Pt:Cu	N	66:34	57:43	85:15
Overall Pt:Cu	Y	70:30	58:42	76:24
Pt(0):Cu(0)	N	81:19	77:23	90:10
Pt(0):Cu(0)	Y	65:35	48:52	65:35

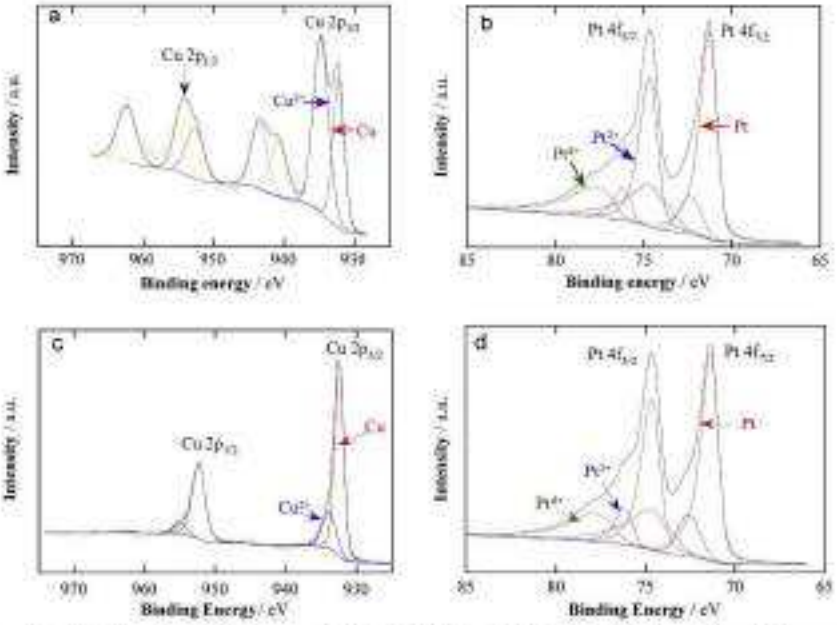

Fig. 3 – Deconvoluted high-resolution XPS spectra of the Pt(Cu)/CNF catalyst in the BE region of Cu: a) before and c) after sputtering; and in the BE region of Pt: b) before and d) after sputtering.

The data given in Table 2 show for non-sputtered samples the presence of some significant amounts of oxidized Pt and also of big amounts of oxidized copper. It is also shown that oxidized copper largely disappears after Ar^+ sputtering and therefore, it is essentially a residual oxidized copper on the surface. On the other hand, the overall Pt:Cu ratio of the Pt(Cu) catalysts does not significantly vary upon sputtering, whereas the Pt(0):Cu(0) ratio, related to the alloy formation, changes significantly, with a marked decrease of the Pt content in this ratio upon sputtering. This strongly suggests that the surface of the catalyst nanoparticles are Pt-enriched and that they can be visualized as a PtCu alloy core covered by a Pt shell or at least by a Pt-rich shell.

Electrochemical characterization

Representative steady cyclic voltammograms of the catalysts under study, using the mass activities j_m (current values referred to the Pt load), at 20 mV s^{-1} in deaerated 0.50 M H_2SO_4, are shown in Fig. 4. The j_m vs E curves in Fig. 4a correspond to Pt(Cu)/CNF, Pt(Cu)/MWCNT and Pt(Cu)/XC72. The same catalysts prepared from the activated carbonaceous supports had the same shape as those without activation, but they presented smaller current density values. The shape of these cyclic voltammograms were the same as that of Pt and there was no evidence about Cu dissolution because no additional peaks appeared. This indicates that the Pt-rich shell may avoid the oxidation of the internal Cu. The potential region within the range 0.0–0.3 V corresponded to desorption (anodic sweep) and adsorption (cathodic sweep) of atomic hydrogen. These peaks are not as well defined as in the case of a perfect crystal faceting because the Pt structure appears to be conditioned by the Cu alloying [18,46,47]. The Pt oxidation can be identified from potentials around 0.65 V in the anodic sweep, with the corresponding reduction peak in the cathodic sweep at about 0.8 V. The cyclic voltammogram of PtCu/C (Fig. 4b, curve d), presents also the same features as that of Pt/C (Fig. 4b, curve e), without additional peaks for Cu dissolution, thus being in agreement with the existence of a Pt-rich shell (Table 2). Note that the currents per mass of the cyclic voltammogram of Pt(Cu)/CNF (Fig. 4a, curve a) are close to those of the curves shown in Fig. 4b. Overlapping of these three curves indicates that they have comparable electrochemical surface areas (ECSAs).

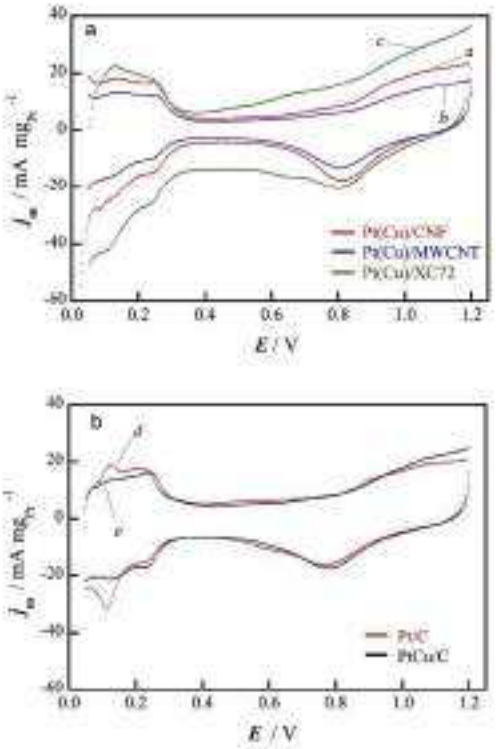

Fig. 4 – Cyclic voltammograms of the carbon-supported catalysts in deaerated 0.50 M H_2SO_4 at a scan rate of 20 mV s^{-1}. (a) Synthesized Pt(Cu)/CNF (a), Pt(Cu)/MWCNT (b) and Pt(Cu)/XC72 (c). (b) Commercial PtCu/C (d) and Pt/C (e).

The ECSAs of the catalysts were estimated from the hydrogen potential region of the corresponding cyclic voltammograms. The overall charge of hydrogen desorption ($Q_{H,\,des}$, in μC) for a given Pt load (m_{Pt}, in μg_{Pt}, cm^{-2}) was determined, and considering that the charge associated with the formation or stripping of an atomic hydrogen monolayer is 210 μC cm^{-2} [46], the ECSAs were obtained using equation (4):

$$ECSA = \frac{Q_{H,\,des}}{210\, m_{Pt}} \quad (4)$$

The obtained values, collected in Table 3, are about 70–80 $m^2\, g_{Pt}^{-1}$ for all the catalysts except for the MWCNTs and those using the activated carbons. Activation is typically performed to increase the number of nucleation centers for the nanoparticles. However, in this case, it did not yield a larger ECSA, probably because there is a larger agglomeration as compared to the non-activated ones and they are then less accessible.

The cyclic voltammograms corresponding to CO stripping, using also the mass activities j_m, are shown in Fig. 5. The oxidation peak between about 0.6 and 1.0 V corresponds in all

Table 3 – ECSAs of the studied catalysts, estimated from desorption of atomic hydrogen and from CO stripping. The corresponding Pt loadings are also indicated.

Catalyst	Pt loading/μg cm^{-2}	$ECSA_{H,\,des}$/ $m^2\, g_{Pt}^{-1}$	$ECSA_{CO,\,des}$/ $m^2\, g_{Pt}^{-1}$
Pt(Cu)/CNF	10.4	70.1	70.7
Pt(Cu)/CNF-A	12.0	19.6	20.8
Pt(Cu)/MWCNT	15.1	44.6	44.6
Pt(Cu)/MWCNT-A	16.5	10.7	11.3
Pt(Cu)/XC72	15.1	78.4	78.6
Pt(Cu)/XC72-A	17.6	40.8	41.3
PtCu/C (commercial)	18.5	86.4	87.2
Pt/C (commercial)	20.4	73.3	74.5

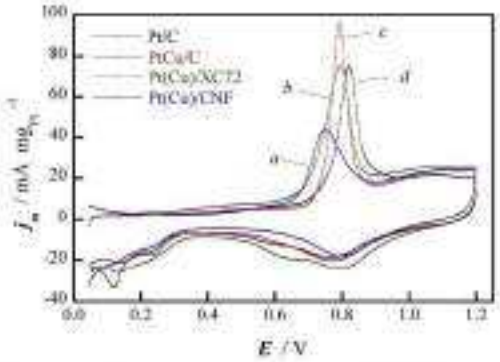

Fig. 5 – CO stripping curves in deaerated 0.50 M H_2SO_4 at scan rate of 20 mV s^{-1} corresponding to Pt(Cu)/CNF (a), Pt(Cu)/XC72 (b), PtCu/C (c) and Pt/C (d).

cases to the oxidative stripping of the pre-adsorbed CO monolayer. Note, however, that there is a significant shift of the onset potential for CO oxidation to more negative potentials, from ca. 0.7 V for PtCu/C (curve c) and Pt/C (curve d) to ca. 0.65V for Pt(Cu)/CNF (curve a) and Pt(Cu)/XC72 (curve b). This is in agreement with previous work of the authors using Pt(Cu) catalysts prepared by electrodeposition of Cu nanoparticles on Vulcan carbon XC72R and further galvanic exchange with Pt [18,23,24], in which the same shift with respect to Pt/C was found. This can be explained by the Pt–CO bond weakening due to the effect of the Cu alloying, with the consequent increase in the CO oxidation rate [18,26,48]. The Pt-rich shell in these Pt(Cu) catalysts is then more active for CO oxidation, thus meaning that they are more tolerant to CO. Note that the onset potential for CO oxidation on PtCu/C (Fig. 5, curve c) is practically the same as that using Pt/C (curve d). The main difference as compared to the carbon-supported Pt(Cu) catalysts is that PtCu appears to have more Pt in the external part (see Table 2), being less effective on the Pt–CO bond. The ECSAs of the catalysts were also determined from the CO stripping curves, considering the charge for the CO desorption (Q_{CO-des}) and that the oxidation of a monolayer of adsorbed CO on polycrystalline Pt requires 420 μC cm^{-2} [18,46]. The corresponding results are also listed in Table 3, which shows the excellent agreement with the ECSAs obtained from atomic hydrogen desorption.

The catalytic activity of the catalysts in front of the ORR was studied by linear sweep voltammetry in O_2-saturated 0.50 M H_2SO_4, using the RDE. The polarization curves using the mass activities j_m obtained at a rotational speed of 1500 rpm are shown in Fig. 6a. It is shown that in all cases, the current approaches a limiting value at large overpotentials. The highest j_m values were obtained using the Pt(Cu)/CNF (curve a), followed by the commercial PtCu/C catalyst (curve d). According to Fig. 6a, the respective limiting values were about 260 and 180 mA mg_{Pt}^{-1}. Note that the latter is comparable to that obtained for Cu-dealloyed PtCu supported on synthesized CNTs, of about 250 mA mg_{Pt}^{-1}, under the same conditions [44]. There were no significant differences between Pt(Cu)/MWCNT

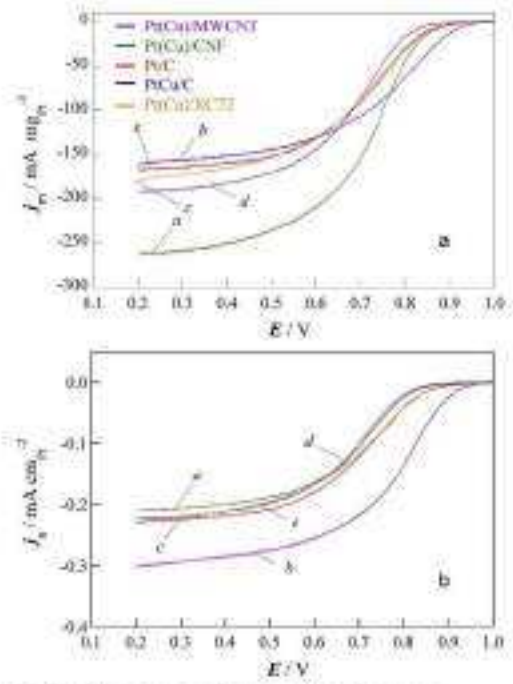

Fig. 6 – Linear sweep voltammograms for oxygen reduction in O_2-saturated 0.50 M H_2SO_4, (a) considering the current per mass j_m and (b) the current per ECSA j_s, corresponding to Pt(Cu)/CNF (a), Pt(Cu)/MWCNT (b), Pt(Cu)/XC72 (c), PtCu/C (d) and Pt/C (e). Sweep rate: 5 mV s^{-1}. RDE rotation rate of 1500 rpm.

(curve b), Pt(Cu)/XC72 (curve c) and the commercial Pt/C (curve e). Note however, that the onset potential for Pt(Cu)/MWCNT (and also for Pt(Cu)/MWCNT-A) were more positive than those of the other catalysts. This should entail a greater activity, which is not reflected in the limiting currents per mass, probably because its ECSA is smaller (Table 3).

This behavior, which is very probably related to the catalyst-support interaction, merits to be further explored in depth. In fact, the specific activities j_s (currents referred to the ECSA) are more indicative of the electrocatalyst activity than the mass activities and current densities relative to the electrode section [49,50]. This is of particular interest when comparing electrocatalysts with nanoparticles having quite different size, as in our case. When the metal load and nanoparticle size are the same for different catalysts, it is expected that the surface specific activity at a given potential keeps the same order of magnitude as that of the current densities referred to the electrode section [50]. Then, both indicate their different electrocatalytic activity. For this reason, the j_s vs E plots, obtained dividing j_m by the corresponding ECSAs, have been depicted in Fig. 6b. As shown in this figure, Pt(Cu)/MWCNT not only presented the most positive onset potential but also the highest surface specific

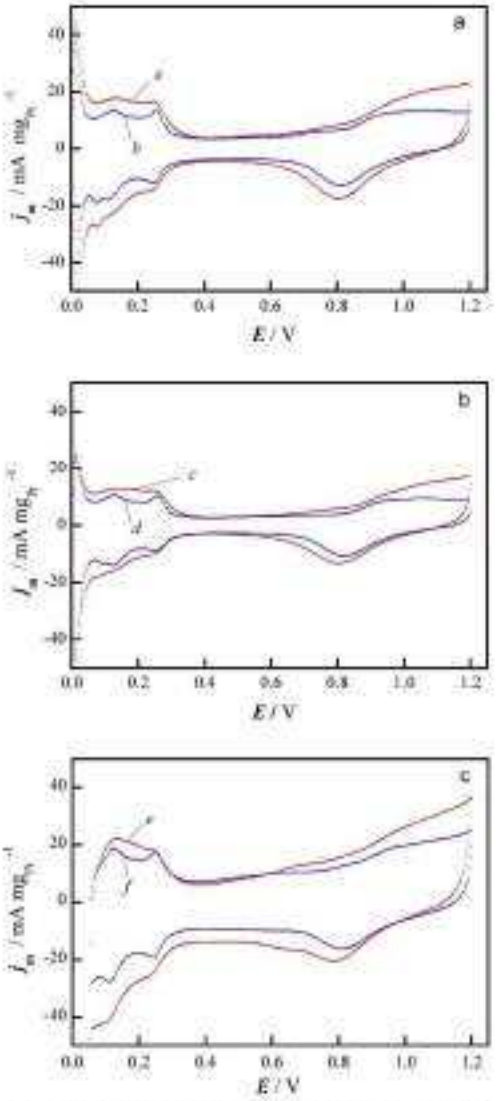

Fig. 7 – Cyclic voltammograms of (a) Pt(Cu)/CNF, (b) Pt(Cu)/MWCNT and (c) Pt(Cu)/XC72 in deaerated 0.50 M H_2SO_4 at 20 mV s^{-1}, before the stability test (curves a, c, e) and after 1000 cycles within the same potential region at 200 mV s^{-1} (curves b, d, f).

currents, being correlated to a greater electrocatalytic activity. Then, according to Fig. 6a and b, Pt(Cu)/CNF possessed higher mass activities than the others, but Pt(Cu)/MWCNT yielded greater specific activity. As the Pt(Cu) nanoparticles were prepared in the same manner, there must be a notable effect of the support on their behavior.

It is also of interest to analyze the relative stability of the synthesized catalysts. This can be done by continuously cycling the specimens between 0.0 and 1.2 V, from hydrogen adsorption to Pt and carbon oxidation [24], in deaerated 0.50 M H_2SO_4, employing a large number of cycles. The curves depicted in Fig. 7a, b and c show the initial cyclic voltammogram (curve *a*, *c*, *e*) using Pt(Cu)/CNF, Pt(Cu)/MWCNT and Pt(Cu)/XC72, respectively, in deaerated 0.5 M H_2SO_4 at 20 mVs^{-1} and the corresponding final cyclic voltammogram (curve *b*, *d*, *f*) at the same scan rate, obtained after 1000 cycles at 200 mV s^{-1}. The occurrence of certain atomic restructuration can be inferred, which may result from the carbon and Pt oxidation with further Pt oxide reduction together with the local restructuration and possible aggregation of the nanoparticles. After these tests, the final ECSAs were 53.1, 39.7 and 45.5 m^2 g$_{Pt}^{-1}$, respectively, accounting for by ECSA losses of about 25%, 11% and 42%, respectively. These values are comparable to previous ones reported in the literature for somewhat different systems and protocols [40,41]. Thus, ECSA losses of 22% and 46% were reported for Pt nanoparticles deposited on MWCNTs (Pt/MWCNTs) and commercial Pt/C, respectively [41]. This confirms the much greater stability of the CNFs and the MWCNTs as compared to XC72. The greater loss in the case of Pt(Cu)/XC72 could then be related to its poorer corrosion resistance when compared with the CNFs and MWCNTs. The ECSA decrease for XC72 could be particularly enhanced by the rather spherical shape of the carbon particles (see Fig. 3e), which may stimulate the nanoparticle aggregation during carbon oxidation. In spite of undergoing an intermediate ECSA loss, the Pt(Cu)/CNF catalysts eventually exhibited the greatest ECSA.

Then, Pt(Cu)/CNF and Pt(Cu)/MWCNT, apart from presenting relatively good stability and contributing with high mass and specific activities, respectively, allow saving about 50% of Pt. These results suggest that they could be good candidates as cathodes for the ORR in low-temperature fuels cells.

Conclusions

Pt(Cu) nanoparticle electrocatalysts, supported on CNFs, MWCNTs and Vulcan carbon XC72, were synthesized by electroless deposition of Cu and further galvanic exchange with $PtCl_4^{2-}$. The XRD analyses of Pt(Cu)/CNF, Pt(Cu)/MWCNT and Pt(Cu)/XC72 catalysts revealed Pt-like fcc structures with diffraction peaks between those corresponding to pure Pt and Cu, thus indicating the formation of a PtCu alloy. The mean crystallite sizes of the Pt(Cu) nanoparticles were about 3 nm. TEM observations revealed the carbon morphology of nanofibers, nanotubes and spherules along with a good dispersion and carbon attachment of the Pt(Cu) nanoparticles. The XPS analyses showed that the Pt(Cu) nanoparticles consisted of a PtCu alloy covered by a Pt-rich shell.

The ECSAs were determined from desorption of atomic hydrogen and also from CO stripping, yielding values of 70.5 and 78.5 m^2 g$_{Pt}^{-1}$ for Pt(Cu)/CNF and Pt(Cu)/XC72, respectively, which were comparable to those of commercial Pt/C and PtCu/C. A smaller value of 41.0 m^2 g$_{Pt}^{-1}$ was obtained for Pt(Cu)/MWCNT. The activation of the carbonaceous materials did not

allow obtaining greater ECSAs. The carbon-supported Pt(Cu) catalysts showed onset potentials for CO oxidation about 50 mV more negative that those corresponding to Pt/C and PtCu/C, thus indicating the electronic effect of the Cu on Pt. This resulted in an easier CO oxidation and higher CO tolerance as compared to pure Pt.

The ORR curves obtained in O_2-saturated 0.50 M H_2SO_4 using the RDE showed that the mass activity of Pt(Cu)/CNF was higher than that of commercial Pt/C and of PtCu/C, whereas those of Pt(Cu)/MWCNT and Pt(Cu)/XC72 were comparable to that of Pt/C. On the other hand, Pt(Cu)/MWCNT possessed higher specific activity than the others. According to the relative stability tests, Pt(Cu)/CNF and Pt(Cu)/MWCNT were more resistant to corrosion and presented much smaller ECSA loss than Pt(Cu)/XC72. These results suggest that Pt(Cu)/CNF and Pt(Cu)/MWCNT could be suitable candidates for the ORR in the low-temperature fuel cells, eventually allowing a significant electrocatalyst cost decrease thanks to the 50 wt% reduction in the amount of Pt employed.

Acknowledgments

The authors thank the financial support from project CTQ2016-78616-R (AEI/FEDER, EU). The authors also thank the CCIT-UB (Scientific and Technological Centers of the Universitat de Barcelona) for the facilities in the electron microscope observations and the XRD and XPS analyses.

REFERENCES

[1] Li W, Liu J, Zhao D. Mesoporous materials for energy conversion and storage devices. Nat Rev Mater 2016;1:16023. https://doi.org/10.1038/natrevmats.2016.23.

[2] Daud WRW, Rosli RE, Majlan EH, Hamid SAA, Mohamed R, Husaini T. PEM fuel cell system control: a review. Renew Energy 2017;113:620–38. https://doi.org/10.1016/j.renene.2017.06.027.

[3] Kamat PV. Meeting the clean energy demand: nanostructure architectures for solar energy conversion. J Phys Chem C 2007;111:2834–60. https://doi.org/10.1021/jp066952u.

[4] Sui S, Wang X, Zhou X, Su Y. A comprehensive review of Pt electrocatalysts for the oxygen reduction reaction: nanostructure, activity, mechanism and carbon support in PEM fuel. J Mater Chem 2017;5:1808–25. https://doi.org/10.1039/c6ta08807f.

[5] Wang Y, Chen KS, Mishler J, Cho SC, Adroher XC. A review of polymer electrolyte membrane fuel cells: technology, applications, and needs on fundamental research. Appl Energy 2011;88:981–1007. https://doi.org/10.1016/j.apenergy.2010.09.030.

[6] Ruth K, Vogt M, Zuber R. Development of CO-tolerant catalysts on Pt/Ru catalysis. In: Vielstich W, Gasteiger HA, Lamm A, editors. Handb Fuel cells - fundam Technol Appl. New York: John Wiley & Sons; 2010. p. 489–96.

[7] Velázquez-Palenzuela A, Brillas E, Arias C, Centellas F, Garrido JA, Rodríguez RM, Cabot PL. Structural analysis of carbon-supported Ru-decorated Pt nanoparticles synthesized using forced deposition and catalytic performance toward CO, methanol, and ethanol electrooxidation. J Catal 2013;298:112–21. https://doi.org/10.1016/j.jcat.2012.11.006.

[8] Antolini E. Formation of carbon-supported PtM alloys for low temperature fuel cells: a review. Mater Chem Phys 2003;78:563–73. https://doi.org/10.1016/S0254-0584(02)00389-9.

[9] Liu Z, Ling XY, Su X, Lee JY. Carbon-supported Pt and PtRu nanoparticles as catalysts for a direct methanol fuel cell. J Phys Chem B 2004;108:8234–40. https://doi.org/10.1021/jp049422h.

[10] Shao M, Sasaki K, Nebojsa MS, Zhang L, Adzic RR. Synthesis and characterization of platinum monolayer oxygen-reduction electrocatalysts with Co–Pd core–shell nanoparticle supports. Electrochem Commun 2007;9:2848–53. https://doi.org/10.1016/j.elecom.2007.10.009.

[11] Papadimitriou S, Tegou A, Pavlidou E, Armyanov S, Valova E, Kokkinidis G, Sotiropoulos S. Preparation and characterisation of platinum- and gold-coated copper, iron, cobalt and nickel deposits on glassy carbon substrates. Electrochim Acta 2008;53:6559–67. https://doi.org/10.1016/j.electacta.2008.04.015.

[12] Mohl M, Dobo D, Kukovecz A, Konya Z, Kordas K, Wei J, Vajtai R, Ajayan PM. Formation of CuPd and CuPt bimetallic nanotubes by galvanic replacement reaction. J Phys Chem C 2011;115:9403–9. https://doi.org/10.1021/jp113128g.

[13] Xia BY, Wu H Bin, Wang X, Wen X, Lou D. One-pot synthesis of cubic $PtCu_3$ nanocages with enhanced electrocatalytic activity for the methanol oxidation reaction. J Am Chem Soc 2012;134:13934–7. https://doi.org/10.1021/ja3051662.

[14] Xiong L, Manthiram A. Effect of atomic ordering on the catalytic activity of carbon supported PtM (M = Fe , Co , Ni , and Cu) alloys for oxygen reduction in PEMFCs 2005. J Electrochem Soc 2005;152:A697–703. https://doi.org/10.1149/1.1862256.

[15] Oezaslan M, Strasser P. Activity of dealloyed $PtCo_3$ and $PtCu_3$ nanoparticle electrocatalyst for oxygen reduction reaction in polymer electrolyte membrane fuel cell. J Power Sources 2011;196:5240–9. https://doi.org/10.1016/j.jpowsour.2010.11.016.

[16] Oezaslan M, Strasser P. $PtCo_3$, PtCu and Pt_3Cu alloy nanoparticle electrocatalysts for oxygen reduction reaction in alkaline and acidic medium. J Electrochem Soc 2012;159:B444–54. https://doi.org/10.1149/2.105204jes.

[17] Jayasayee K, Rob van Veen JA, Manivasagam TG, Celebi S, Hensen EJM, de Bruijn FA. Oxygen reduction reaction (ORR) activity and durability of carbon supported PtM (Co, Ni, Cu) alloys: influence of particle size and non-noble metals. Appl Catal B Environ 2012;111–112:515–26. https://doi.org/10.1016/j.apcatb.2011.11.003.

[18] Caballero-Manrique G, Velázquez-Palenzuela A, Brillas E, Centellas F, Garrido JA, Rodríguez RM, Cabot PL. Electrochemical synthesis and characterization of carbon-supported Pt and Pt-Ru nanoparticles with Cu cores for CO and methanol oxidation in polymer electrolyte fuel cells. Int J Hydrogen Energy 2014;39:12859–69. https://doi.org/10.1016/j.ijhydene.2014.06.089.

[19] Mintsouli I, Georgieva J, Armyanov S, Valova E, Avdeev G, Hubin A, Steenhaut O, Dille J, Tsiplakides D, Balomenou S, Sotiropoulos S. Pt-Cu electrocatalysts for methanol oxidation prepared by partial galvanic replacement of Cu/carbon powder precursors. Appl Catal B Environ 2013;136–137:160–7. https://doi.org/10.1016/j.apcatb.2013.01.053.

[20] Guterman VE, Belenov SV, Alekseenko AA, Lin R, Tabachkova NY, Safronenko OI. Activity and stability of Pt/C and Pt–Cu/C electrocatalysts. Electrocatalysis 2018;9:550–62.

[21] Sarkar A, Manthiram A. Synthesis of Pt@Cu core-shell nanoparticles by galvanic displacement of Cu by Pt^{4+} ions

and their application as electrocatalysts for oxygen reduction reaction in fuel cells. J Phys Chem C 2010;114:4725–32. https://doi.org/10.1021/jp908931r.
[22] Podlovchenko BI, Gladysheva TD, Filatov AY, Yashina LV. The use of galvanic displacement in synthesizing Pt(Cu) catalysts with the core-shell structure. Russ J Electrochem 2010;46:1189–97. https://doi.org/10.1134/S1023193510100150.
[23] Caballero-Manrique G, Nadeem I, Brillas E, Centellas F, Garrido J, Rodríguez RM, Cabot PL. Effects of the electrodeposition time in the synthesis of carbon-supported Pt(Cu) and Pt-Ru(Cu) core-shell electrocatalysts for polymer electrolyte fuel cells. Catalysts 2016;6:125–42. https://doi.org/10.3390/catal6080125.
[24] Caballero-Manrique G, Brillas E, Centellas F, Garrido JA, Rodríguez RM, Cabot PL. Electrochemical oxidation of the carbon support to synthesize Pt(Cu) and Pt-Ru(Cu) core-shell electrocatalysts for low-temperature fuel cells. Catalysts 2015;5:815–37. https://doi.org/10.3390/catal5020815.
[25] Geboes B, Mintsouli I, Wouters B, Georgieva J, Kakaroglou A, Sotiropoulos S, Valova E, Armyanov S, Hubin A, Breugelmans T. Surface and electrochemical characterisation of a Pt-Cu/C nano-structured electrocatalyst, prepared by galvanic displacement. Appl Catal B Environ 2014;150–151:249–56. https://doi.org/10.1016/j.apcatb.2013.12.020.
[26] Georgieva J, Valova E, Mintsouli I, Sotiropoulos S, Armyanov S, Kakaroglou A, Hubin A, Steenhaut O, Dille J. Carbon-supported Pt(Cu) electrocatalysts for methanol oxidation prepared by Cu electroless deposition and its galvanic replacement by Pt. J Appl Electrochem 2014;44:215–24. https://doi.org/10.1007/s10800-013-0618-2.
[27] Pryadchenko VV, Srabionyan VV, Kurzin AA, Bulat NV, Shemet DB, Avakyan LA, Belenov SV, Volochaev VA, Zizak I, Guterman VE, Bugaev LA. Bimetallic PtCu core-shell nanoparticles in PtCu/C electrocatalysts: structural and electrochemical characterization. Appl Catal Gen 2016;525:226–36. https://doi.org/10.1016/j.apcata.2016.08.008.
[28] Alekseenko AA, Belenov SV, Menshikov VS, Guterman VE. Pt(Cu)/C Electrocatalysts with low platinum content. Russ J Electrochem 2018;54:415–25. https://doi.org/10.1134/S1023193518050026.
[29] Alekseenko AA, Guterman VE, Belenov SV, Menshikov VS, Tabachkova NY, Safronenko OI, Moguchikh EA. Pt/C electrocatalysts based on the nanoparticles with the gradient structure. Int J Hydrogen Energy 2018;43:3676–87. https://doi.org/10.1016/j.ijhydene.2017.12.143.
[31] Maya-Cornejo J, Carrera-Cerritos R, Sebastian D, Ledesma-García J, Arriaga LG, Aricò AS, Baglio V. PtCu catalyst for the electro-oxidation of ethanol in an alkaline direct alcohol fuel cell. Int J Hydrogen Energy 2017;42:27919–28. https://doi.org/10.1016/j.ijhydene.2017.07.226.
[32] Pryadchenko VV, Belenov SV, Shemet DB, Srebionyan VV, Avakyan LA, Volochaev VA, Mikheykin AS, Bdoyan KE, Zizak I, Guterman VE, Bugaev LA. Effect of thermal treatment on the atomic structure and electrochemical characteristics of bimetallic PtCu Core–Shell nanoparticles in Pt/C electrocatalysts. J Phys Chem C 2018;122:17199–210. https://doi.org/10.1021/acs.jpcc.8b03606.
[33] Sung Y, Hwang J, Shik J. Characterization and activity correlations of Pt bimetallic catalysts for low temperature fuel cells. Int J Hydrogen Energy 2011;36:4007–14. https://doi.org/10.1016/j.ijhydene.2010.12.058.
[34] Xu Z, Zhang H, Liu S, Zhang B, Zhong H. Facile synthesis of supported Pt-Cu nanoparticles with surface enriched Pt as highly active cathode catalyst for proton exchange membrane fuel cells. Int J Hydrogen Energy 2012;37:17976–83. https://doi.org/10.1016/j.ijhydene.2012.09.090.
[35] Yang L, Ding Y, Chen L, Luo S. Hierarchical reduced graphene oxide supported dealloyed platinum e copper nanoparticles for highly efficient methanol electrooxidation. Int J Hydrogen Energy 2017;42:5705–12. https://doi.org/10.1016/j.ijhydene.2017.01.133.
[36] Hosseini SJ, Bahrami M, Samadi Z, Hashemi SF, Koushani M, Habib B. Designing of some platinum or palladium-based nanoalloys as effective electrocatalysts for methanol oxidation reaction. Int J Hydrogen Energy 2018;43:15095–111. https://doi.org/10.1016/j.ijhydene.2018.06.062.
[30] Guterman VE, Lastovina TA, Belenov SV, Tabachkova NY, Vlasenko VG, Khodos II, Balakshina EN. Pt/C [M–Ni, Cu, or Ag] electrocatalysts: effects of alloying components on morphology and electrochemically active surface areas. J Solid State Electrochem 2014;18:1307–17. https://doi.org/10.1007/s10008-013-2314-x.
[37] Sharma S, Pollet BG. Support materials for PEMFC and DMFC electrocatalysts - a review. J Power Sources 2012;208:96–119. https://doi.org/10.1016/j.jpowsour.2012.02.011.
[38] Shao Y, Liu J, Wang Y, Lin Y. Novel catalyst support materials for PEM fuel cells: current status and future prospects. J Mater Chem 2009;19:46–59. https://doi.org/10.1039/b813070c.
[39] Stobinski L, Lesiak B, Kövér L, Tóth J, Biniak S, Trykowski G, Judek J. Multiwall carbon nanotubes purification and oxidation by nitric acid studied by the FTIR and electron spectroscopy methods. J Alloys Compd 2010;501:77–84. https://doi.org/10.1016/j.jallcom.2010.04.102.
[40] Shao Y, Yin G, Gao Y, Shi P. Durability Study of Pt/C and Pt/CNTs catalysts under simulated PEM fuel cell conditions. J Electrochem Soc 2006;153:A1093–7. https://doi.org/10.1149/1.2191147.
[41] Devrim Y, Arica ED. Multi-walled carbon nanotubes decorated by platinum catalyst for high temperature PEM fuel cell. Int J Hydrogen Energy 2019;44:18951–86. https://doi.org/10.1016/j.ijhydene.2019.01.051.
[42] El-Deeb H, Bron M. Microwave-assisted polyol synthesis of PtCu/carbon nanotube catalysts for electrocatalytic oxygen reduction. J Power Sources 2015;275:893–900. https://doi.org/10.1016/j.jpowsour.2014.11.060.
[43] El-Deeb H, Bron M. Electrochemical dealloying of PtCu/CNT electrocatalysts synthesized by $NaBH_4$-assisted polyol-reduction: influence of preparation parameters on oxygen reduction activity. Electrochim Acta 2015;164:315–22. https://doi.org/10.1016/j.electacta.2015.02.137.
[44] Rivera-Lugo YY, Salazar-Gastelum MI, López-Rosas DM, Reynoso-Soto EA, Pérez-Sicairos S, Velraj S, Flores-Hernández JR, Félix-Navarro RM. Effect of template , reaction time and platinum concentration in the synthesis of PtCu/CNT catalyst for PEMFC applications. Energy 2018;148:561–70. https://doi.org/10.1016/j.energy.2018.01.069.
[45] Powder Diffraction File. International centre for diffraction data (ICDD), 12 campus boulevard. Newton Square, Pennsylvania 2018. 19073-3273, USA. n.d. http://www.icdd.com. [Accessed September 2019].
[46] Esparbé I, Brillas E, Centellas F, Garrido JA, Rodríguez RM, Arias C, Cabot PL. Structure and electrocatalytic performance of carbon-supported platinum nanoparticles. J Power Sources 2009;190:201–9. https://doi.org/10.1016/j.jpowsour.2009.01.075.
[47] Serrano-Ruiz JC, López-Cudero A, Solla-Gullón J, Sepúlveda-Escribano A, Aldaz A, Rodríguez-Reinoso F. Hydrogenation of α,β unsaturated aldehydes over polycrystalline, (111) and (100) preferentially oriented Pt nanoparticles supported on carbon. J Catal 2008;253:159–66. https://doi.org/10.1016/j.jcat.2007.10.010.

[48] Kitchin JR, Barteau MA. Modification of the surface electronic and chemical properties of Pt (111) by subsurface 3d transition metals. J Chem Phys 2004;120:10240–6. https://doi.org/10.1063/1.1737365.

[49] Cui C, Gan L, Li HH, Yu SH, Heggen M, Strasser P. Octahedral PtNi nanoparticle catalysts: exceptional oxygen reduction activity by tuning the alloy particle surface composition. Nano Lett 2012;12:5885–9. https://doi.org/10.1021/nl3033709.

[50] Beermann V, Gocyla M, Willinger E, Rudi S, Heggen M, Dunin-Borkowski RE, Willinger MG, Strasser P. Rh-doped Pt-Ni octahedral nanoparticles: understanding the correlation between elemental distribution, ORR and shape stability. Nano Lett 2016;16:1719–25. https://doi.org/10.1021/acs.nanolett.5b04636.

4.3. PtCu supported on mesoporous carbons

4.3.1. Testing PtCu Nanoparticles Supported on Highly Ordered Mesoporous Carbons CMK3 and CMK8 as Catalysts for Low-Temperature Fuel Cells

Aiming to find alternative materials to CBs and considering the optimum properties for energy storage and conversion applications that have been described in the literature about OMCs, two different types of MCs have been studied as carbon supports for PtCu nanoparticles. There are also several studies that suggest a higher stability of the catalysts obtained when supporting Pt nanoparticles on these carbonaceous materials, as compared to those using carbon blacks. Among the many types of MCs, CMK-3 and CMK-8 have been widely studied as supports for different types of catalyst applications, since their mesoporous structure play a key role.

Using CMK-3 and CMK-8, PtCu catalysts were prepared, as explained in Chapter 3, Section 3.3, using $NaBH_4$ to reduce Cu in alkaline medium, prior to a partial galvanic replacement of Cu by Pt. The carbon supports used were CMK-3 and CMK-8 both, as received and activated (the latter identified with an "-A" at the end). The structural and electrochemical properties of the synthesised catalysts were compared to PtCu supported on XC-72 and XC-72-A and also to commercial Pt/C.

The structural characterization of the catalysts obtained was performed using XRD, TEM and XPS analyses. The XRD results of the supports showed wide peaks related to a short-range graphitic structure. The diffractograms of the catalysts had a similar profile, corresponding to the Pt *fcc* structure and no peaks corresponding to possible Cu species were observed. The shift of the peaks compared to those of pure Pt was explained by the lattice contraction due to the formation of PtCu, in agreement with the FFT results from TEM. The amount of Pt in the PtCu alloy was between 2.7 and 4.5 times higher than that of Cu, thus indicating some lattice reordering during the galvanic replacement and resulting in a PtCu alloy. However, the EDS analyses showed a lower Pt:Cu ratio in Pt(Cu). Consequently, there was some amount of pure and/or oxidized Cu in the catalysts, too small or amorphous to provide any signals.

The mean crystallite sizes were in the range of 4-5 nm compared to the value of 2.6 nm of the Pt/C used as the reference, which is in correspondence to the mean particle sizes measured with TEM. The nanoparticles of the catalyst obtained appeared to be rather spherical on CMK-3, while they had a more elongated and zigzag shape on CMK-8, which could be explained by their different structure, since CMK-3 presents 2D channels while CMK-8 cubic ones. The Pt-rich shell of Pt(Cu) was confirmed bythe XPS analyses, since a decrease in the Pt content was observed after argon sputtering.

The electrochemical properties of the catalysts showed ECSA values around 70 $m^2\ g_{Pt}^{-1}$ for catalysts with non-activated carbon supports, while 50 $m^2\ g_{Pt}^{-1}$ for catalysts with activated carbon supports, all of them somewhat smaller than in the case of Pt/C. The studies of CO stripping revealed a 50 mV shift of the onset potential towards negative potentials of the PtCu catalysts than that of Pt/C, which is in agreement with our previous work. The relative stability of the catalysts could be also evaluated electrochemically by measuring the ECSA loss after 5000 cycles and the lowest ECSA losses were obtained with Pt(Cu)/CMK3 and Pt(Cu)/CMK8, which were 25% and 32% respectively. Therefore, non-activated CMK-3 and CMK-8 appeared to have a higher resistance towards degradation than XC-72.

Considering the stability results, the catalytic activity towards ORR was studied for Pt(Cu)/CMK3 and Pt(Cu)/CMK8, which showed a more positive onset potential for ORR than that obtained with Pt/C, although their limiting current densities were lower. It should be taken into count that the limiting current densities cannot be directly compared, because they depend on the catalyst loading, the nanoparticle size, the carbon support, and the thickness of the prepared thin-film electrode, and this was not possible to control all together for the catalysts available. Another explanation for the lower current densities could be that the mesoporous channels of these MCs can also have a role in the limiting current densities, as it has been previously reported in other studies.

catalysts

MDPI

Article

Testing PtCu Nanoparticles Supported on Highly Ordered Mesoporous Carbons CMK3 and CMK8 as Catalysts for Low-Temperature Fuel Cells

Julia García-Cardona, Francisco Alcaide, Enric Brillas, Ignasi Sirés and Pere L. Cabot *

Laboratori d'Electroquímica dels Materials i del Medi Ambient, Secció de Química Física, Facultat de Química, Universitat de Barcelona, Martí i Franquès 1-11, 08028 Barcelona, Spain; jul.gar.956@gmail.com (J.G.-C.); francisco.alcaide@ub.edu (F.A.); brillas@ub.edu (E.B.); i.sires@ub.edu (I.S.)

* Correspondence: p.cabot@ub.edu

Abstract: Pt(Cu) nanoparticles supported on CMK3 and CMK8 ordered mesoporous carbons (OMCs) have been synthesized by electroless deposition of Cu followed by galvanic exchange with Pt. The structural characterization by high-resolution transmission electron microscopy and X-ray diffraction showed the formation of Pt(Cu) nanoparticles of 4–5 nm, in which PtCu alloys with contracted *fcc* Pt lattice and 70–80 at.% Pt was identified. The X-ray photoelectron spectroscopy analyses indicated that the Pt(Cu) nanoparticles were mainly composed of a PtCu alloy core covered by a Pt-rich shell, in agreement with the steady cyclic voltammograms, which did not show any Cu oxidation peaks. Electroactive surface areas up to about 70 m^2 g_{Pt}^{-1} were obtained. The onset potentials for CO oxidation and the oxygen reduction reaction were more negative and positive, respectively, as compared to Pt/C, thus indicating higher activity of these Pt(Cu) catalysts with respect to the latter. Based on the corresponding binding energies, these better activities were attributed to the favorable geometric and ligand effects of Cu on Pt, which were able to reduce the adsorption energy of the intermediates on Pt. Pt(Cu)/CMK3 showed competitive mass and specific activities, as well as better stability than Pt/C.

Keywords: PtCu electrocatalysts; galvanic exchange; ordered mesoporous carbon; CO tolerance; oxygen reduction reaction

check for updates

Citation: García-Cardona, J.; Alcaide, F.; Brillas, E.; Sirés, I.; Cabot, P.L. Testing PtCu Nanoparticles Supported on Highly Ordered Mesoporous Carbons CMK3 and CMK8 as Catalysts for Low-Temperature Fuel Cells. *Catalysts* **2021**, *11*, 724. https://doi.org/10.3390/catal11060724

Academic Editors: Vladimir Certoman, Sergey Belenov and Anastasia Alekseenko

Received: 18 May 2021
Accepted: 4 June 2021
Published: 10 June 2021

1. Introduction

The present energy demand is still mostly satisfied by fossil fuels that have a huge negative impact on the environment. For this reason, the development of cleaner energy sources to avoid the emission of hazardous substances is needed [1–5]. Considering that a great percentage of CO_2 emissions is directly linked to transportation based on combustion engines, electric vehicles moved by proton exchange membrane fuel cells (PEMFCs) appear to be a greener alternative. PEMFCs can operate with an unlimited source of reactants (H_2 and O_2, which can be obtained by water splitting using renewable energies), near zero carbon emissions (only water is produced by the H_2 cold combustion) and efficiencies (not limited by the Second Law of Thermodynamics) significantly higher than those of combustion engines [6–13].

The catalysts currently used in PEMFCs are based on Pt or Pt alloys, since this metal is at present the best for the hydrogen oxidation reaction (HOR) and the oxygen reduction reaction (ORR). However, the main drawbacks of Pt are that it is scarce and expensive, which has a big impact on the PEMFCs cost. Pt is also easily poisoned by CO impurities present in the H_2 gas obtained from hydrocarbon reforming. The use of PtRu catalysts reduces this problem [14–20], but Ru is also scarce and expensive. For this reason, Pt is usually supported as nanoparticles on porous carbonaceous materials, aiming to reduce the total amount of metal used and maximize its surface area. The cost of the catalyst,

which is a great obstacle for PEMFCs commercialization [18], is considerably reduced by following this strategy.

A more recent approach to cutting expenses is to synthesize carbon-supported multimetallic catalysts, which can further reduce the Pt content. The use of sacrificial metals such as Cu or Ni that are cheaper and much more abundant than Pt, is particularly interesting because of their additional electronic effect on Pt. It has been proved that the structural properties of the noble catalyst present significant changes due to its interactions with other metals, leading to a remarkable improvement in its catalytic activity [14–21]. Pt-based catalysts alloyed with Ni, Co, Fe, Pd, and others showed specific activities for the ORR at 0.9 V vs. the reversible hydrogen electrode (RHE) 1.5–3 times higher than commercial Pt/C [22–25], due mainly to the electronic modification of the 5*d* orbitals of Pt [23] and/or the Pt lattice contraction [24]. Thus, dealloyed $Pt_{75}Co_{25}$ showed a specific activity of 0.55 mA cm_{Pt}^{-2} in front of 0.18 mA cm_{Pt}^{-2} for 30 wt.% Pt/C [25].

The PtCu bimetallic system has attracted interest in recent years [26–36], with several studies focused on PtCu alloys, Pt(Cu) core-shell structures and Cu-dealloyed PtCu nanoparticles supported on carbon blacks, mainly Vulcan® XC72 and XC72R. In most cases, Cu was first deposited and afterwards, it was partially displaced by galvanic exchange with Pt(IV). Copper nanoparticles were generated either by: (i) constant-potential deposition [26,35,36] or (ii) electroless deposition using reducing agents such as $NaBH_4$ [37,38], formaldehyde [39], and $NaBH_4$ or ascorbic acid in water-ethylene glycol mixtures [40–44]. These catalysts were studied to determine their CO tolerance and activity toward the methanol and ethanol oxidation reactions [26,38,39,42,44,45] and the ORR [33,34,40,41,46–49]. The PtCu/C catalysts provided ORR specific activities 2–3 times higher than those of Pt/C [47]. Thus, Guterman et al. [49] reported kinetic currents of 0.49 mA cm_{Pt}^{-2} at 0.9 vs. RHE for the ORR on $Pt_{65}Cu_{35}$, whereas it was of 0.19 mA cm_{Pt}^{-2} on Pt/C. The results were promising regarding the reduction of the amount of Pt used and the increase in the activity of the catalysts in such reactions.

The role of the catalyst support on the catalyst performance also needs to be studied. Most of the catalysts assessed for PEMFCs were supported on porous carbonaceous materials. They have high specific surface area, can present many different structures with tailorable surface chemistry, and facilitate the catalyst recovery [50–54]. This allowed the obtaining of high dispersion and narrow size distribution of Pt nanoparticles, the use of the noble metal then being more efficient. Carbon blacks such as XC72R have been the most used supports for energy conversion applications. They are cheap materials with a high surface area, electrical conductivity, and porosity [55–59]. However, the presence of organo-sulphur impurities (which can poison the metal catalyst) and deep micropores (which can trap the metal nanoparticles, making them inaccessible to the ionomer and reactants) can limit the catalyst performance. In addition, carbon blacks are unstable at high temperatures, so they can suffer corrosion while the cell is working [60–63]. For all these reasons, carbon blacks may not be the best supports and therefore, novel alternatives have been tested.

Different papers on the use of graphene [64,65], carbon nanotubes (CNTs) [66–69], and carbon nanofibers (CNFs) [54,70–74] have reported some of their advantages as supports because these highly graphitic carbons exhibit high specific surface areas, a wide potential window, and high chemical stability. Both CNTs and CNFs improved the durability of the catalysts when compared to Vulcan XC72 [67–74]. Promising results have also been reported for PtCu alloy structures when supported on CNTs and CNFs [48,75,76].

More recently, optimum properties for energy storage and conversion applications have been described for ordered mesoporous carbons (OMCs) synthesized by replication from silica templates [77–81]. It was reported that they presented monodispersed three-dimensionally attached mesospheres with large surface areas, thus facilitating the diffusion of reactants and by-products [51,53]. OMCs such as CMK3 yielded uniform distribution of small Pt clusters with high specific surface area and improved catalytic activities [82–85]. Gupta et al. [86] reported a high stability of PtCu catalysts supported on mesoporous

carbon, with electrochemical active surface area (ECSA) and catalytic activity losses <2% after 1000 cycles, in contrast to the 70% loss determined for commercial carbon. The interaction between the carbon support and Pt plays a decisive role in its electrocatalytic activity when applied to PEMFCs. Thus, Liu et al. described the assembly of small Pt nanoclusters of about 1.4 nm on OMCs to 10 wt.% load, thus gaining in specific activity with respect to Pt(20 wt.%)-Vulcan, from 0.19 mA cm^{-2} at 0.9 V vs. RHE of the latter to 0.216 mA cm^{-2} [88]. Phan et al. [81] showed the excellent properties of mesoporous CMK3 and CMK8 for application in non-aqueous electrochemical double layer capacitors, in which the mesopores and the mesopore structures played the main role. Other strategies consisted of doping mesoporous carbons with other elements such as nitrogen [89,90], which was shown to favor the ORR through shifting the half-wave potential $E_{1/2}$ toward the positive direction by about 40 mV and an increase by 2.5 times in the specific activity, from 0.29 to 0.71 mA cm^{-2} at 0.9 V vs. RHE with respect to commercial Pt/C. In this case, this ORR enhancement was assigned to the favorable interaction between Pt and N.

To gain better knowledge of the application of mesoporous carbon supports to PEMFCs, we present in this study the preparation of Pt(Cu) nanoparticles on CMK3 and CMK8 carbons, as received and also submitted to an activation process, with respective specific surface areas over 900 and 500 $m^2\ g^{-1}$ [91], by direct Cu electroless deposition and further galvanic displacement with Pt. The structure and composition of the obtained catalysts have been characterized by means of X-ray diffraction (XRD), scanning electron microscopy (SEM), transmission electron microscopy (TEM), high-resolution TEM (HRTEM), energy-dispersive spectroscopy (EDS) and X-ray photoelectron spectroscopy (XPS). The ECSA of the catalysts was determined using cyclic voltammetry (CV) and CO stripping measurements. The ORR catalytic activity was tested by linear sweep voltammetry (LSV) using the rotating-disk electrode (RDE) technique. It is shown that the synthesized Pt(Cu)/OMCs presented better activity and stability than commercial Pt/C.

2. Results and Discussion

2.1. Structural Characterization

The XRD analyses of the supports and catalysts studied in this paper led to the diffractograms depicted in Figure 1a–c. Those corresponding to the carbon supports (Figure 1a) show wide peaks related to a short-range graphitic structure, with diffraction angles of the (002) and (100) planes at about 26° and 43°, respectively [92].

The XRD diffractograms of the Pt(Cu) catalysts supported on CMK3 and CMK8 and on the activated carbons CMK3-A and CMK8-A are shown in Figure 1b, where they are compared to commercial Pt/C. All these diffractograms have a similar profile, revealing the predominance of the Pt *fcc* structure. However, the Pt peaks in Pt(Cu) were slightly shifted with respect to those of Pt/C. Figure 1c is a magnification of Figure 1b to better highlight the shift of the Pt peaks in the Pt(Cu) catalysts. No XRD peaks corresponding to Cu species could be found, thus meaning that, if present, pure Cu and Cu oxides should be very small crystallites or in amorphous form. The Pt peaks of Pt/C at 2θ values of 40.0°, 46.3°, and 67.5° corresponded to *fcc* Pt (111), (200), and (220) planes, respectively [92]. The *fcc* peaks of Cu (111) and (200), which corresponded to 2θ angles of 43.3° and 50.5°, have also been marked in Figure 1c, whereas those of Pt(Cu) fell between those of pure Pt and pure Cu. The small shift in the Pt peaks of the Pt(Cu) samples with respect to the pure Pt can then be related to the Pt lattice contraction because of the formation of a PtCu alloy [22,93]. The atomic radius of Cu (145 pm) is smaller than that of Pt (177 pm), resulting in a decrease in the lattice parameter, which can be estimated using Vegard's law [92]:

$$a_{PtCu} = (1 - x)\, a_{Pt} + x\, a_{Cu} \quad (1)$$

where (a_{PtCu}) is the lattice parameter of the PtCu alloy with a Cu atomic fraction x, and a_{Pt} and a_{Cu} the lattice parameters of pure Pt (0.3916 nm) and Cu (0.2608 nm), respectively.

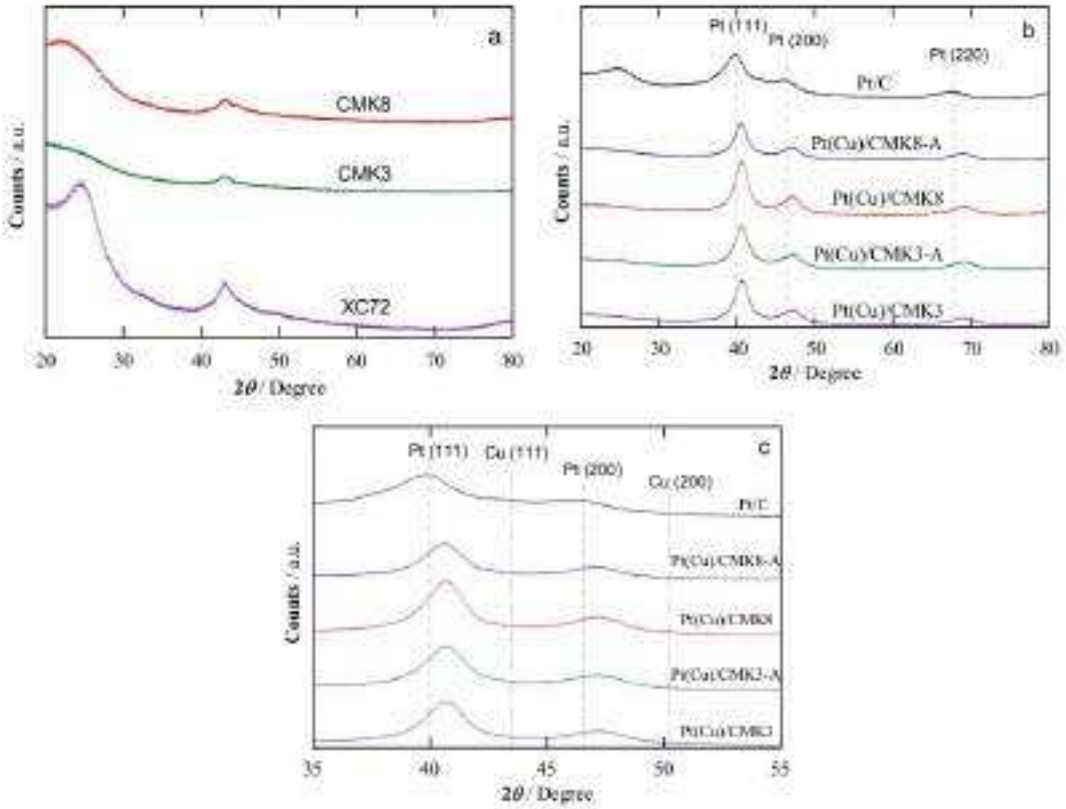

Figure 1. (**a**) XRD analyses of the supports and (**b**) of the supported Pt(Cu) catalysts. The region corresponding to Pt and Cu peaks (111) and (200) shown in plot (**b**) has been magnified in (**c**) to better show the peak location. The acronyms indicated refer to carbon black XC72, mesoporous carbons CMK3 and CMK8, and the activated mesoporous carbons CMK3-A and CMK8-A.

The results obtained are summarized in Table 1, where the amount of Pt in the PtCu alloy is 2.7–4.5 times higher than that of Cu. This indicates that in the galvanic replacement, Pt oxidizes and replaces Cu with some lattice reordering that results in a PtCu alloy, which is in agreement with previous literature [44,94]. However, the Pt:Cu ratio in Pt(Cu) by EDS is lower than that in the PtCu alloy. This means that there was some amount of pure and/or oxidized Cu species in the catalysts, either amorphous or at least as nanocrystals too small to provide any signals.

The broadness of the peaks can be associated with the small size of the crystallites as well as to their possible non-uniform composition, which could result from the superposition of peaks corresponding to different phases [42]. Despite not being pure metals, Scherrer's Equation (2) allowed the estimation of the crystallite size of the PtCu nanoparticles:

$$d = \frac{K\lambda}{B\cos\theta} \quad (2)$$

where λ is the X-ray wavelength used, B is the width (in radians) of the diffraction peak at half the maximum, and $K = 0.9$. As shown in Table 1, the mean crystallite sizes were in the range of 4–5 nm, somewhat greater than that of Pt nanoparticles in the commercial Pt/C

used as the reference, which was 2.6 nm. The synthesis of the catalysts could probably be tuned to further reduce the particle size. It is also shown in Table 1 that the nanoparticle size was slightly decreased by about 0.5 nm when the OMCs were previously activated. This agrees with the formation of more active centers for nanoparticle nucleation when activating [87].

Table 1. Particle size and compositional characteristics of the supported Pt(Cu) catalysts obtained from XRD and EDS analyses and TEM observations.

Catalyst	Crystallite Size [a]/nm	Pt:Cu Ratio [b]/at.%	Metal Content [c]/wt.%		Pt:Cu Ratio [d]/at.%	Particle Size [e]/nm
			Pt	Cu		
Pt(Cu)/CMK3	4.4	83:17	26	9	48:52	4.8
Pt(Cu)/CMK3-A	4.0	72:28	19	14	30:70	4.8
Pt(Cu)/CMK8	5.1	80:20	32	6	64:36	5.1
Pt(Cu)/CMK8-A	4.5	83:17	38	6	68:32	4.9
Pt/C	2.6	100:0	19	0	100:0	2.5

[a] Mean crystallite size from XRD. [b] Atomic composition of the PtCu alloy by XRD. [c] Overall metal loading from EDS (standard deviation of 1.5 wt.%). [d] Pt to Cu atomic ratio by EDS. [e] Mean particle size from TEM measurements (standard deviation of 0.8).

The HRTEM images given in Figure S1a,b of the Supporting Information (SI) show the textural properties of the carbon supports. As can be seen in Figure S1a, CMK3 presented long ordered parallel channels, in agreement with the 2D hexagonal structure of the mesoporous SBA-15 template. In contrast, CMK8 presented the cubic channels typical of the mesoporous KIT-6 template. These observations agree with previous work in the literature [81,87,95].

The TEM micrographs of the different carbon-supported Pt(Cu) catalysts are collected in Figure S1c–f (SI). The black spots shown in this figure can be related to the Pt(Cu) nanoparticles, which appear to be successfully attached onto the OMCs either when these were used as received or upon activation. The nanoparticles appear to be rather spherical on CMK3, whereas they have a more elongated and zigzag shape on CMK8. This can be explained by the different form of the channels, 2D in CMK3 and cubic in CMK8, respectively [81]. The corresponding size distribution histograms obtained after counting more than 100 nanoparticles are shown as insets in the corresponding TEM micrographs. The mean values were about 4–5 nm (see Table 1) and presented a good agreement with those obtained from XRD.

The HRTEM micrographs of all the samples and their corresponding FFT analyses are presented in Figure S2 (SI). The representative spots are also included, with the corresponding d-spacings. It is interesting to observe that there were d-spacing values close to pure Pt of 0.227 and 0.140 nm [96], related to the Pt (111) and (220) planes, respectively, as shown in Figure S2a (SI). However, there were also smaller values, such as 0.223 and 0.220 nm, as depicted in Figure S2d,f (SI), respectively, which are consistent with a Pt lattice contraction due to Cu incorporation in the formation of the PtCu alloy, in agreement with the XRD analyses. This would also suggest that there was a surface Pt-rich structure on the nanoparticles.

The average compositions of the Pt(Cu) catalysts supported on the OMCs measured by EDS are also summarized in Table 1. The values are strongly dependent on the support since there is a significant difference between the amount of Pt and Cu in CMK3 and CMK8. The overall metal contents in the catalysts were in the range 35–44 wt.%. However, the amount of Pt in CMK8 was about 30 wt.%, higher than that of CMK3, which was about 20 wt.%. Conversely, the amount of Cu was only 6 wt.% in CMK8, whereas it was about 10 wt.% in CMK3. Converted to at.%, the Pt:Cu atomic ratios were about 2:1 on CMK8, although the at.% Cu exceeded that of Pt on CMK3. These differences may arise from the different availability of the active centers for the nucleation of the Cu nanoparticles and also by their availability by the Pt(IV) species when they have been formed. This is

not surprising because CMK3 and CMK8 have different channel textures and thus, can condition the transport of the reactants [14,53,63,81].

If one looks at the at.% composition corresponding to the PtCu alloy as measured by XRD, the Pt:Cu ratios were in the range 3:1 to 5:1, values very different from those measured by EDS. A possible explanation could be that there was a significant amount of Cu occluded in a Pt-rich shell, higher in CMK3 than in CMK8. However, this does not seem very probable because the mean particle sizes estimated from XRD and TEM measurements are very similar, all around 4–5 nm, regardless of the support and, in addition, the PtCu alloy composition obtained from XRD was not so different in all the catalysts. Therefore, apart from the possibility of the nanoparticles having an inner, Cu-rich core, Cu was probably present in oxidized form outside the PtCu alloy structure, i.e., not bonded to Pt. For this reason, the EDS line profile of the section of the nanoparticles was attempted. Unfortunately, their size was too small, and the resolution was insufficient to determine the Pt and Cu distribution. Additional information about this point is discussed below from XPS analyses, which are able to provide compositional information of the most external part of the nanoparticles [44,48].

As described in the experimental part, the XPS spectra were acquired at 20° with respect to the plane on which the samples were deposited, thus aiming to better ascertain the composition of their most external layers. Compositional differences before any sputtering and after an Ar^+ sputtering for 60 s were expected. It is worth mentioning that the mild initial sputtering normally performed to clean the surface from adventitious carbon was not carried out to avoid the Pt and Cu surface species removal. Figure 2a-d shows the Pt and Cu high-resolution spectra of Pt(Cu) /CMK3, measured before and after sputtering, together with the corresponding deconvolution considering the different possible oxidation states. The XPS spectra of all the samples obtained in this work were similar, thus indicating that the catalyst nanoparticles had similar compositional properties. It is worth mentioning that the measured Pt 4f7/2 and Pt 4f5/2 binding energies (BEs) before sputtering were 71.4 and 74.7 eV, respectively (see Figure 2a), and 71.5 and 74.8 after sputtering (Figure 2b). The Pt high-resolution spectra of all the specimens are depicted together in Figure 2e,f, where it is clearly shown that the BEs of the peaks are coincident, thus indicating the same Pt 4f7/2 and Pt 4f5/2 BE values for all the catalysts studied, which is confirmed by the corresponding peak deconvolution. They approach very well those reported previously for PtCu alloys also obtained from galvanic displacement (71.4 and 74.8 eV [44]), and for PtCu alloys obtained from the one-pot hydrothermal method (71.5 and 74.8 eV [97]). These values also strongly agree with those obtained for pure Pt supported on graphene nanosheets (71.4 and 74.8 eV [93]), pure Pt electrodeposited on a microporous carbon layer (71.5 and 74.8 eV [98]), and pure Pt on XC72 carbon (71.47 and 74.77 eV [99]). Values of 71.2 and 74.8 eV were reported for platinized carbon electrodes [100]. The higher Pt 4f7/2 binding energy could be due to the interaction with the support and the particle size [93].

It is worth mentioning here that the shift of the Pt peaks found in the XRD analyses of Figure 1b,c when forming the PtCu alloy as compared to pure Pt is in contrast with the absence of any peak shifts in the XPS Pt 4f peaks. Cu in Pt(Cu) in fact produces a Pt lattice contraction, and if the compressive strain were the only effect of Cu on Pt, a shift of the Pt 4f BEs to higher values would be expected [95,101]. As this was not observed in the Pt high-resolution spectra of Pt(Cu), we can also appreciate here the effect of charge transfer from Cu to Pt (ligand effect), which would produce a shift in the Pt BEs toward the opposite direction. In fact, the electronegativity of Cu (1.90) is smaller than that of Pt (2.28). The combination of both effects, compressive strain of the Pt lattice together with charge transfer from Cu to Pt, could explain that the BEs of Pt 4f peaks did not significantly move from the values corresponding to pure Pt.

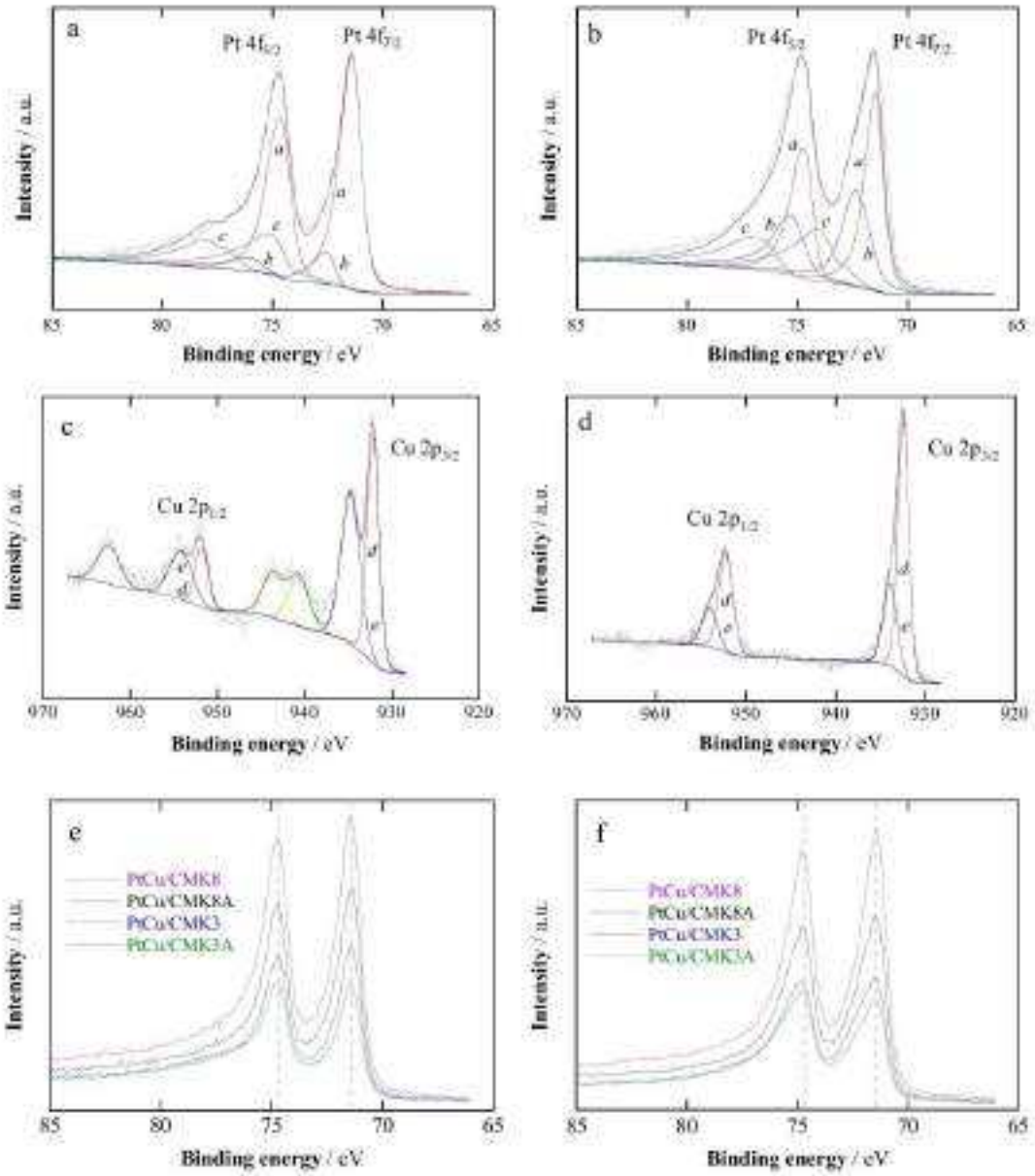

Figure 2. High-resolution XPS spectra of Pt(Cu)/CMK3 in the (**a**) Pt 4f BE region before and (**b**) after sputtering; and in the (**c**) Cu 2p BE region before and (**d**) after sputtering. The Pt 4f peaks in all the specimens are compared (**e**) before and (**f**) after sputtering. Curves *a*, *b* and *c* in (**a**,**b**) correspond to the doublets of Pt(0), Pt(II), and Pt(IV) species, respectively, whereas *d* and *e* in (**c**,**d**) account for the doublets of Cu(I) and Cu(II), respectively.

The BE values corresponding to the Pt(II) species were 72.6 and 76.2 eV before sputtering (Figure 2a) and 72.4 and 75.3 eV after sputtering (see Figure 2b), which reasonably matched with those reported previously for PtCu (72.7 and 76.0 eV [44], or 72.3 and 75.7 eV [97]), and pure Pt (72.4 and 75.7 eV [99]). The BEs of the Pt(IV) species were probably less accurate due to its amount and to the deconvolution approach, with values of 75.2 and 78.1 eV before sputtering and 74.1 and 77.1 eV after sputtering. However, the latter reasonably matched with those reported for PtCu (73.9 and 77.2 eV [44]) and for pure Pt (73.6 and 76.9 eV [99]).

It is also worth mentioning the BEs of metallic Cu 2p3/2 and 2p1/2, with respective values of 932.1 and 951.8 eV before sputtering (see Figure 2c) and 932.5 and 952.3 eV after sputtering (see Figure 2d). They reasonably agreed with 932.0 and 951.9 eV [44] and 932.1 and 951.8 eV [97] given for PtCu. A BE value of 932.6 eV has been reported for metallic Cu 2p3/2 measured in pure Cu [102]. The values corresponding to Cu(II) species were 934.8 and 954.3 eV before sputtering (see Figure 2c) and 934.9 and 954.1 eV after sputtering (see Figure 2d). In addition, satellite peaks of Cu oxide for BEs in the range 938–948 eV and over 959 eV are shown in Figure 2c, which did not appear after sputtering (see Figure 2d) due to the significant amount of Cu oxide [44,97].

The relative atomic composition of the Pt(Cu) nanoparticles was obtained from these analyses and the corresponding results are collected in Table 2. As shown, the relative Pt:Cu overall surface composition was dominated by Pt, in amounts in the range of 58–90 at.% without sputtering, which slightly decreased to 50–83 at.% after sputtering. These values were higher than the relative Pt:Cu overall composition obtained from EDS (see Table 1), in which Pt is in the range of 30–68 at.%. Note that XPS is a surface technique and Ar^+ sputtering removes the external layers of the catalyst surface, whereas the EDS analyses showed the overall composition of the nanoparticles. Pt, if mainly present in the external part of the nanoparticles, should be the first to be removed and therefore, its relative amount should be reduced by sputtering, as found here. This is then a strong indication that the external part of the nanoparticles was Pt-rich, with its relative amount being smaller in their internal part.

Table 2. Overall Pt:Cu:C and Pt:Cu composition (at.%) for the different catalysts, before (N) and after (Y) Ar^+ sputtering.

Species	Ar^+	Pt(Cu) /CMK3	Pt(Cu) /CMK3-A	Pt(Cu) /CMK8	Pt(Cu) /CMK8-A
Pt:Cu:C	N	5:1:94	4:3:93	14:2:84	9:1:90
Pt:Cu:C	Y	6:3:91	6:6:88	17:3:80	13:2:85
Pt:Cu	N	77:23	58:42	86:14	90:10
Pt:Cu	Y	70:30	50:50	83:17	83:17
Pt(0):Pt(II):Pt(IV) [a]	N	66:10:24	60:3:37	43:45:12	68:10:22
Pt(0):Pt(II):Pt(IV) [a]	Y	43:32:25	46:30:24	74:10:16	63:13:24
Cu(0):Cu(II) [b]	N	48:52	44:56	52:64	38:62
Cu(0):Cu(II) [b]	Y	71:29	73:27	78:22	70:30
Pt(0):Cu(0) [c]	N	82:18	65:35	84:16	94:6
Pt(0):Cu(0) [c]	Y	64:36	40:60	83:17	81:19

[a] Relative composition of the Pt oxidation states. [b] Relative composition of the Cu oxidation states. [c] Pt(0):Cu(0) ratio of the metallic forms.

The Pt and Cu high-resolution spectra of the different specimens studied, exemplified in Figure 2, show a significant contribution of Pt and Cu oxidized species. Thus, 43–68 at.% of Pt was in the form of Pt(0) before sputtering and varied to 43–74 at.% after sputtering. Although there was some increase in the oxidized Pt species in CMK3 and CMK3-A after sputtering, this cannot be considered relevant in front of the nanoparticle composition. Conversely, 38–52 at.% of Cu was in the form of Cu(0) before sputtering and 70–78 at.% after sputtering. This means that the Cu(II) species were mainly located on surface positions, later being removed in great part by Ar^+ sputtering. Perhaps oxidized Cu was produced during the galvanic replacement by the Pt(IV) species. In any case, the oxidized Pt and

Cu forms did not appear to be in crystalline form (or they were too small), or was in such small amounts as to be undetectable by XRD (see Figure 1) or HRTEM (see Figure S2 of SI).

The most indicative result is the Pt(0):Cu(0) relative ratio because it is considered to be the responsible for the catalyst activity. According to its relative composition before sputtering, the amount of Pt(0) was in the range of 65–94 at.%, whereas it was in the range of 40–83 at.% after sputtering. The clear decrease of the relative Pt content after sputtering strongly indicates that the surface of the PtCu alloy nanoparticles was rich in Pt and that the Pt relative amount was smaller in the core.

On the other hand, the PtCu alloy compositions resulting from the XRD spectra yielded 72–83 at.% Pt (see Table 1). This should be considered a mean alloy composition value, being reasonably comparable with those of the Pt(0):Cu(0) ratio from XPS analysis before sputtering (see Table 2), in the 65–94 at.% range. Apart from this, no evidence about a significant amount of pure crystalline Cu was obtained in the XRD spectra of Figure 1c and therefore, the structure of the Pt(Cu) nanoparticles could be described as mainly composed of a PtCu alloy core covered by a Pt-rich shell.

2.2. Electrochemical Characterization

Quasistationary cyclic voltammograms of the Pt(Cu) samples supported on CMK3 (curves *a* and *b*) and CMK8 (curves *d* and *e*) in deaerated 0.5 mol dm^{-3} H_2SO_4 solution at 20 mV s^{-1} are shown in Figure 3a,b, respectively, where they are compared to commercial Pt/C (curve *c*).

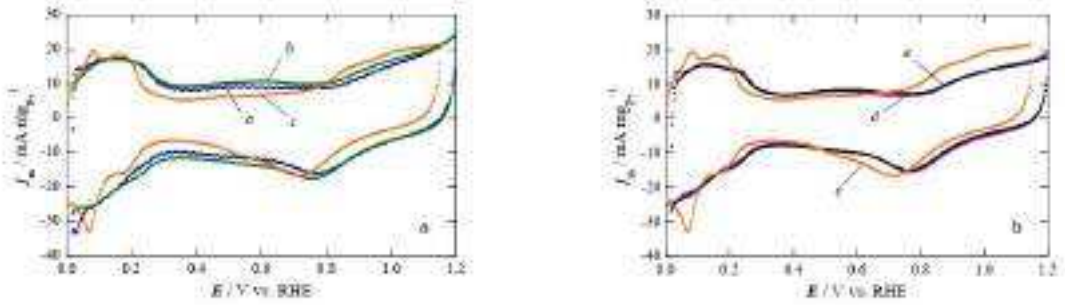

Figure 3. Cyclic voltammograms in deaerated 0.5 mol dm^{-3} H_2SO_4 solution at a scan rate of 20 mV s^{-1}: (**a**) Pt(Cu)/CMK3 (curve *a*), Pt(Cu)/CMK3-A (*b*), and Pt/C (*c*); (**b**) Pt(Cu)/CMK8 (curve *d*), Pt(Cu)/CMK8-A (*e*), and Pt/C (*c*).

These curves represent the mass activities (j_m), currents referred to the Pt load on the glassy carbon electrode (GCE) modified with the catalyst (see Table 3). As can be observed in this figure, the cyclic voltammograms of Pt(Cu) supported on the OMCs have a similar shape to those of Pt/C. The adsorption and desorption peaks of atomic H were displayed in the cathodic and anodic sweep in the range from 0.0 to 0.3 V, the Pt oxidation started at about 0.7 V in the anodic sweep, and the Pt oxide reduction was initiated at about 0.9 V in the cathodic sweep, in agreement with previous results in the literature [103]. Using our Pt(Cu) catalysts, the hydrogen adsorption/desorption peaks were not as well defined as those found for a perfect crystal faceting of Pt, thus suggesting that the Pt structure was conditioned by Cu alloying, as previously suggested for similar catalysts [26,48]. It is also apparent that Cu is not being dissolved from the Pt(Cu) nanoparticles because no additional peaks were displayed and the consecutive cyclic voltammograms achieved a steady state, thus indicating that a Pt-rich shell avoided the oxidation of the internal Cu.

Table 3. Pt loadings for electrochemical testing, ECSAs measured from hydrogen desorption (H-des) and CO stripping (CO-des) and onset potentials for CO oxidation (E_{CO}) in the corresponding cyclic voltammograms.

Catalyst	Pt Loading /μg cm^{-2}	$ECSA_{H\text{-}des}$ /m^2 g$_{Pt}^{-1}$	$ECSA_{CO\text{-}des}$ /m^2 g$_{Pt}^{-1}$	E_{CO} /V
Pt(Cu)/CMK3	26.5	68.5	68.7	0.65
Pt(Cu)/CMK3-A	19.4	56.3	57.7	0.65
Pt(Cu)/CMK8	19.6	72.8	73.2	0.66
Pt(Cu)/CMK8-A	23.3	44.6	45.2	0.64
Pt/C (commercial)	20.4	84.3	85.2	0.70

The ECSAs of the different catalysts studied were estimated from Equation (3):

$$ECSA = \frac{Q_{H-des}}{210\ m_{Pt}} \quad (3)$$

where $Q_{H\text{-}des}$ is the charge of hydrogen desorption (μC), m_{Pt} is the Pt load (g) on the GCE and 210 (μC cm^{-2}) is the charge associated with the stripping (or formation) of a monolayer of atomic hydrogen [104]. The ECSA values are summarized in Table 3.

As shown in this table, the ECSA values were about 70 m^2 g$_{Pt}^{-1}$ for the non-activated supports, which are somewhat smaller values than in the case of Pt/C, whereas they were about 50 m^2 g$_{Pt}^{-1}$ for the activated supports. With activation, we expected an increase in the number of active centers for the nucleation of the nanoparticles. In fact, the particle sizes on the activated supports, according to the XRD results, were about 0.5 nm smaller than for the non-activated ones (see Table 1). However, this did not lead to the expected ECSA increase. The ECSA decrease for the activated supports could then be explained by a larger agglomeration of the deposited Pt(Cu) nanoparticles, which would result in a reduction of accessible Pt active centers [53,55,62].

The CO stripping voltammograms as j_{ox} vs. potential are depicted in Figure 4a,b for the CMK3-type (curves *a* and *b*) and CMK8-type (curves *d* and *e*) supports, respectively, being compared to Pt/C (curve *c* in both plots). The peak observed in the anodic sweep, between 0.6 and 1.0 V, corresponded to the oxidative stripping of the previously adsorbed CO monolayer. It is worth mentioning the more negative onset potential for CO oxidation E_{CO} of the Pt(Cu)/OMC catalysts as compared to that of Pt (see Table 3). The E_{CO} values were about 0.65 V for all the Pt(Cu) catalysts, which were about 50 mV more negative than that of Pt/C. This negative shift with respect to Pt/C has also been found for other Pt(Cu) catalysts synthesized by potentiostatic [26] and electroless deposition of Cu [48], thus indicating that the Pt(Cu) catalysts were more tolerant to CO.

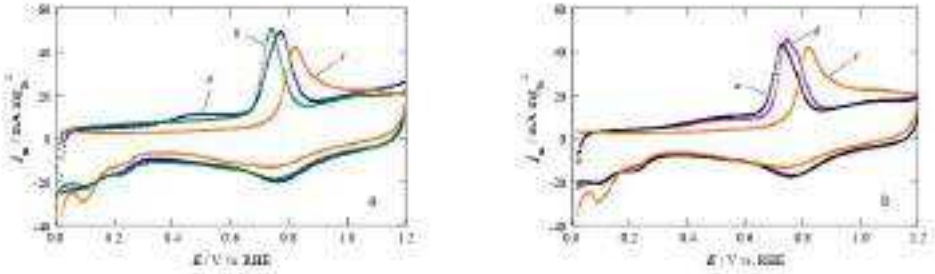

Figure 4. CO stripping curves in deaerated 0.5 mol dm^{-3} H_2SO_4 solution at a scan rate of 20 mV s^{-1}. (**a**) Pt(Cu)/CMK3 (curve *a*), Pt(Cu)/CMK3-A (*b*), and Pt/C (*c*); (**b**) Pt(Cu)/CMK8 (curve *d*), Pt(Cu)/CMK8-A (*e*), and Pt/C (*c*).

The CO stripping curves also allowed the obtaining of the ECSAs of the studied Pt(Cu) catalysts. These were determined from the CO desorption charge ($Q_{CO\text{-}des}$), taking the value of 420 $\mu C\,cm^{-2}$ as the charge needed for the removal of a CO monolayer [104]. The corresponding results match very well with those measured from the hydrogen adsorption profile (see Table 3).

The relative stability of the catalysts was also studied since there is evidence that it can be improved when OMCs are used as supports [5,105]. This can be done by means of the accelerated degradation tests, consisting of continuously cycling the test samples up to a large number of cycles, taking an anodic limit in which the carbon support and Pt oxidation may occur, which may result in some atomic restructuration on the catalyst surface and possible aggregation of the nanoparticles [48]. In this case, the cyclic voltammograms were recorded between 0.6 and 1.0 V in deaerated 0.5 mol dm^{-3} H_2SO_4 solution at a scanning rate of 100 mV s^{-1}. The decrease of the ECSA after the indicated number of cycles is represented in Figure 5, where the ECSA/$ECSA_0$ is the ratio between the ECSA at the given cycle and that obtained in the initial cycle, both measured using the $Q_{H\text{-}des}$ of the cyclic voltammograms performed at 20 mV s^{-1} from 0.0 to 1.2 V.

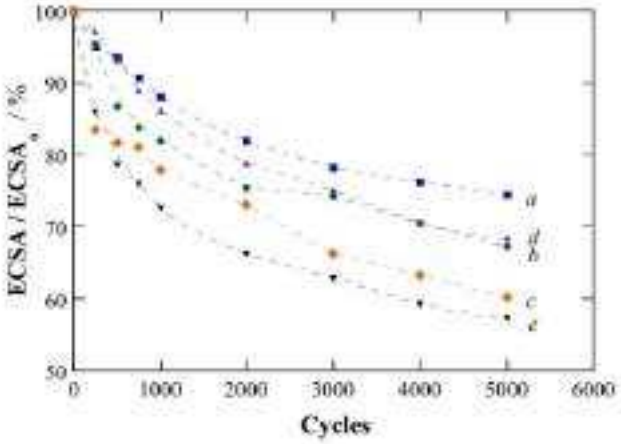

Figure 5. ECSA loss for each catalyst after cycling within the potential range between 0.6 and 1.0 V at 100 mV s^{-1} in 0.5 mol dm^{-3} H_2SO_4 solution. Curves *a*–*e* correspond to the same catalysts indicated in Figures 3 and 4.

Figure 5 highlights that Pt(Cu)/CMK3 and Pt(Cu)/CMK8 presented the smallest ECSA loss of 25% and 32%, respectively, after 5000 cycles, whereas the reference Pt/C showed a value of 40%. The ECSA losses of Pt(Cu)/CMK3-A and Pt(Cu)/CMK8-A, corresponding to 33% and 43%, respectively, were worse than those of non-activated supports. These values can be compared to previous results given in the literature for Pt(Cu)/CNF, Pt(Cu)/MWCNT, Pt(Cu)/XC72 [48] and Pt/C [68], with corresponding ECSA losses of 25%, 11%, 42%, and 46%. Non-activated CMK3 and CMK8 then appeared to be more resistant to degradation than XC72. This could be due to the particular structure of the OMCs being more resistant to structural change than the spherical carbonaceous particles in XC72. In fact, when the OMCs are activated, some structural changes should occur, thus leading to a less resistant support and therefore, to higher ECSA losses.

Considering the previous results of ECSA and stability, the activity of Pt(Cu)/CMK3 and Pt(Cu)/CMK8 in front of the ORR was studied by LSV using the RDE in O_2-saturated 0.5 mol dm^{-3} H_2SO_4 solution at 1500 rpm by scanning the potential at 5 mV s^{-1} from 1.2 to 0.2 V. The linear sweep voltammograms are plotted in Figure 6a,b, using the j_m values, which are a measure of the efficiency of the catalyst and the specific activities (j_{sp}, currents

referred to the ECSAs), indicating the activity of the corresponding catalyst surface. The same trend can be observed in both plots since the catalysts presented similar Pt loads and ECSAs. An exponential current density increase appeared at the beginning with limiting values at large overpotentials.

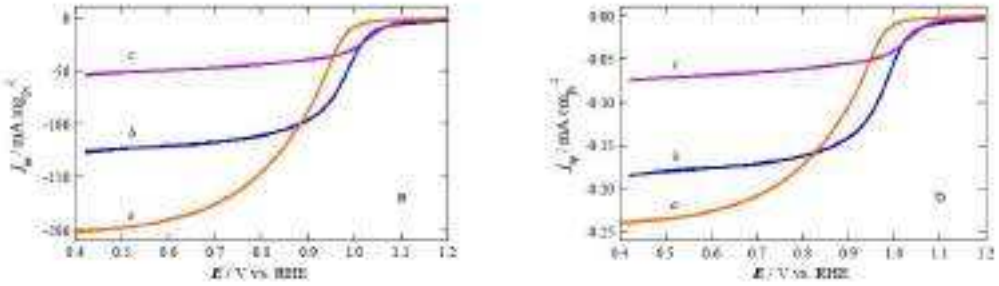

(a) (b)

Figure 6. Linear sweep voltammograms for the ORR in O_2-saturated 0.5 mol dm^{-3} H_2SO_4 solution at 5 mV s^{-1} and an RDE rotation rate of 1500 rpm. (**a**) Current per mass (j_m) and (**b**) specific current (j_{sp}) vs. potential. In both plots, the catalysts are Pt/C (*a*), Pt(Cu)/CMK3 (*b*), and Pt(Cu)/CMK8 (*c*).

Figure 6a,b shows that the ORR started at about the same potential for Pt(Cu)/CMK3 and Pt(Cu)/CMK8 and that this potential was more positive than that of Pt/C. As the onset potential of the former moved in the positive direction toward $E^0(O_2/H_2O)$, the reaction overpotential decreased, thus indicating that the supported Pt(Cu) catalysts were more active than Pt/C [49,106]. The catalytic activity is generally given by the specific current densities measured at a given potential in the kinetic region [106]. However, the limiting current densities cannot be directly compared because they depend on the catalyst loading, the nanoparticle size, the carbon support, and the thickness of the prepared thin-film electrode. Thus, limiting j_m values of about 270 mA mg_{Pt}^{-1} were obtained for Pt(Cu)/CNF, in which the Pt(Cu) catalyst was prepared according to the same procedure employed here, with mean particle size and ECSA values of 2.9 nm and 71 m^2 g_{Pt}^{-1}, respectively [48]. In the same paper, we reported j_m values of 180 mA mg_{Pt}^{-1} for Pt(Cu)/XC72 with mean particle size and ECSA values of 2.0 nm and 78 m^2 g_{Pt}^{-1}, respectively. They compare to the j_m values in the range of 190–220 mA mg_{Pt}^{-1} measured using a disk rotating speed of 1600 rpm reported by Guterman et al. for different PtCu/XC72 catalysts synthesized by stepped borohydride reduction of copper and platinum precursors [49]. The textural properties of the carbons could also play a role, since a great specific surface area of the carbons such as those used here could lead to rather isolated particles with limited connectivity. In addition, the low graphitization degree of these carbons, as shown in Figure 1a, can limit their carbon conductivity and even their stability [107], thus affecting the ORR activity. The different morphology of the mesoporous channels of CMK3 and CMK8, long ordered parallel and cubic, respectively, could also have a role in the limiting current densities. This would be in agreement with the previous work of Phan et al. [81], who explained the better performance of organic supercapacitors based on CMK3 with respect to those based on CMK8 due to their different mesoporous structure, more suitable in CMK3 to improve the transport of the involved species in the charge-discharge cycles. This merits a detailed study when the mechanistic study of the reaction is pursued. However, this point is outside the scope of the present paper.

From these electrochemical tests, it is clear that the Pt(Cu) catalysts are more active in front of the CO oxidation and the ORR. The explanation should be found in the change of the electronic environment due to the charge transfer between the transition metal and Pt and the compressive strain in the Pt lattice caused by the alloy formation [93,108–110]. As

obtained by our XRD results (Figure 1), there is an evident lattice strain when forming the PtCu alloy and, in addition, a charge transfer component from Cu to Pt can be suggested from the XPS results (Figure 2), as discussed above. Both effects can account for the greater activity of Pt(Cu) with respect to Pt/C in front of such reactions because they are able to reduce the adsorption energy of the intermediates on Pt [108]. In the case of the ORR, there is also an important effect of the Pt-Pt bonding length, in this case modulated by the compressive strain due to Cu alloying since it is a structure sensitive reaction [110].

The above results allow inferring the good performance of Pt(Cu)/CMK3 as catalyst, which merits further work to tune the nanoparticle deposition to increase the catalytic performance in front of the ORR and testing in real PEMFCs.

3. Materials and Methods

3.1. Reagents

Analytical-grade reagents and high-purity water (resistivity > 18.2 MΩ cm at 25 °C) obtained from a Milli-Q water purification system (Merck KGaA, Darmstadt, Germany) have been used along this paper to prepare all the solutions. The carbon supports for the catalysts were CMK3 and CMK8 ordered mesoporous carbons purchased from ACS Chemical Inc., Pleasant, MJ, USA, and obtained from mesoporous SBA-15 and cubic Ia3d KIT-6 silica templates, respectively [91]. CMK3 was type B, with pore diameters of about 3.8–4.0 nm, total pore volumes of 1.2–1.5 $cm^3\ g^{-1}$, and a specific surface area of over 900 $m^2\ g^{-1}$. CMK8 presented pore diameters in the range of 3.2–6.6 nm, total pore volumes of 0.7–1.1 $cm^3\ g^{-1}$, and a specific surface area of over 500 $m^2\ g^{-1}$. For the electroless deposition of copper, $CuSO_4{\cdot}5H_2O$ supplied by Panreac AppliChem GmbH, Darmstadt, Germany and $NaBH_4$ supplied by Merck KGaA were used. The solution pH was adjusted using pure NaOH pellets purchased from Panreac AppliChem GmbH. Cleaning of the catalysts was performed with ethanol (96 wt.%) purchased from Panreac AppliChem GmbH. The galvanic exchange of Cu by Pt was made with Merck KGaA 10 wt.% aqueous solution of H_2PtCl_6. For the electrochemical tests, Nafion® (5 wt.%) supplied by Merck KGaA was used as an agglomerating agent. The catalyst ink was prepared with dry 2-propanol purchased from Merck KGaA. The corresponding results were compared to those obtained for the commercial 20 wt.% Pt/C from Premetek, Cherry Hill, NJ, USA (in which XC72 was the carbon support). N_2 (≥ 99.9995%) and CO (≥ 99.9%) gases supplied by Linde, Dublin, Ireland, were employed for deaeration and the CO stripping experiments.

3.2. Synthesis of the Catalysts

The catalysts were synthesized by a two-step synthesis, by an initial electroless deposition of Cu and a further partial galvanic displacement by Pt [48]. The PtCu catalysts thus obtained were denoted as Pt(Cu) because of the two-step deposition procedure. The carbonaceous supports, CMK3 and CMK8, were used either as received or after a mild activation in 2.0 mol dm^{-3} HNO_3 solution for 30 min at boiling temperature [87]. With activation, an increase in the number of active centers for the nucleation of the nanoparticles (through the surface carbon oxidation) was attempted. The resulting activated supports are identified as CMK3-A and CMK8-A, respectively.

For the preparation of the catalysts, the carbon support and $CuSO_4{\cdot}5H_2O$ were both introduced in 1.0 mol dm^{-3} NaOH and submitted to bath sonication (2000 W, Julabo GmbH, Seelbach, Germany), at room temperature. Once the carbon was dispersed, $NaBH_4$ powder was slowly added for 10 min until reaching a $CuSO_4{\cdot}5H_2O$:$NaBH_4$ weight ratio of 1.2. After 30 min of stirring, the dispersion was filtered and cleaned. The resulting carbon-supported Cu powder was resuspended by bath sonication at room temperature in 0.1 mol dm^{-3} $HClO_4$ + 5 mmol dm^{-3} H_2PtCl_6 solution for 45 min, to promote the following galvanic exchange reaction:

$$2Cu + PtCl_6^{2-} \rightarrow 2Cu^{2+} + Pt + 6Cl^- \quad (4)$$

which has a standard potential of E° = 0.404 V vs. SHE. Finally, the suspension was vacuum-filtered through 0.2 µm-porosity paper (Sartorius, Göttingen, Germany), and the collected powder was cleaned with ethanol and dried at 80 °C in an oven. The catalysts thus synthesized were identified as Pt(Cu)/CMK3, Pt(Cu)/CMK3-A, Pt(Cu)/CMK8, and Pt(Cu)/CMK8-A.

3.3. Structural Characterization

The structural analysis was performed by XRD with a PANalytical X'Pert PRO MPD θ/θ powder diffractometer from Malvern Panalytical Ltd., Malvern, UK, using the conditions described elsewhere [48] and sandwiching the powders between polyester films.

The mass and atomic compositions of the catalysts were determined from SEM observations using a scanning electron JSM5910-LV JEOL microscope furnished with an INCA-300 EDS analyzer (JEOL Ltd., Akishima, Tokyo, Japan). The corresponding measurements were taken from at least five different representative areas, the mean values and the error estimation being thus obtained. The nanoparticle morphology, size distribution, and composition were studied by means of TEM and HRTEM using a 200 kV JEOL JEM 2100 high-resolution transmission electron microscope from JEOL Ltd., Akishima, Tokyo, Japan. The samples were prepared from the powder dispersion, which was obtained by sonication in ethanol, placing a drop of it on a holey nickel grid and evaporating the solvent under the heat of a lamp. The HRTEM images were recorded with a Gatan MultiScan 794 CCD camera (Pleasanton, CA, USA). For the digital treatment of the images and analysis of selected areas of interest by Fast Fourier Transform (FFT), Gatan Digital Micrograph 3.7.0 software was used.

The samples were disposed on a carbon tape in order to perform the XPS analyses, which were conducted in a Physical Electronics PHI 5500 Multitechnique System spectrometer (Chanhassen, MN, USA) using the conditions described elsewhere [48], placing the analyzer 20° with respect to the plane of the samples to better appreciate the composition of the surface layers of the catalyst. The data acquisition was performed without sputtering and after Ar^{+} sputtering for 60 s. The XPS spectra were analyzed by means of a MultiPak V8.2B software from Physical Electronics.

3.4. Electrochemical Characterization

The working electrode was a modified 5 mm-diameter GCE tip coupled with an RDE purchased from Metrohm Autolab B.V., Utrecht, The Netherlands. The GCE tip was polished with deagglomerated alumina of 0.3 and 0.05 µm supplied by Buehler on a polishing cloth, using ethanol and water to remove the smut and cleaning by bath sonication. For the electrode modification, a catalyst ink was prepared with the suspension of the catalyst powder in 300 µL of a H_2O-isopropanol (3:1) mixture, which was sonicated for 30 min. About 20 µL of this ink was dropped onto the GCE tip to achieve Pt loadings of about 20 $\mu g_{Pt}\,cm^{-2}$, dried at room temperature, and coated with 2.5 µL of 1 wt.% Nafion® solution.

The experiments were performed in a three-electrode cell purchased from Metrohm Autolab B.V., equipped with a double wall to maintain a constant temperature of 25.0 ± 0.1 °C using a MP-5 thermostat from Julabo GmbH, Seelbach, Germany. The reference electrode was an RHE from Gaskatel GmbH, Kassel, Germany and the auxiliary electrode was a Pt wire (Incometal, Madrid, Spain). All the potentials have been referred to the RHE.

The experiments were performed in deaerated 0.5 M H_2SO_4 as electrolyte and using an Autolab PGSTAT100 potentiostat-galvanostat commanded by a NOVA 2.10 software, both from Metrohm Autolab B.V., Utrecht, The Netherlands. The solutions were deaerated by N_2 bubbling. To clean the catalysts surface, the electrode was continuously cycled at 100 mV s^{-1} between 0.0 and 1.2 V until reaching a steady profile. Afterwards, the cyclic voltammograms at 20 mV s^{-1} in the same potential range were obtained. The steady profile was already reached after the second cycle.

The CO stripping tests were performed by bubbling CO for 15 min while a potential of 0.1 V was applied. Then, N_2 was bubbled to remove the CO excess of the solution and the CO monolayer adsorbed on the catalysts was oxidized by CV at 20 mV s^{-1} between 0.0 and 1.2 V.

The activity in front of the ORR was determined by LSV in O_2-saturated (pure O_2 at 1 atm) 0.5 mol dm^{-3} H_2SO_4 by scanning the potential from 1.2 to 0.2 V at a sweep rate of 5 mV s^{-1} and 1500 rpm. Ohmic drop correction was not applied to these curves.

To test the stability of the catalysts, an accelerated degradation test, consisting of continuous cycling of the prepared electrodes between 0.6 and 1.0 V at 100 mV s^{-1} in deaerated 0.5 M H_2SO_4 for a large number of cycles was performed. The potential range was selected because in these conditions some oxidation of carbon and Pt is expected, resulting in possible atomic restructuration of the catalyst and aggregation of the nanoparticles. The ECSA decay after a given number of cycles is represented as $ECSA/ECSA_0$, which is the ratio between the ECSA measured after such number of cycles and the initial value ($ECSA_0$), versus the number of cycles. These ECSA values were obtained from the atomic hydrogen desorption charges in the voltammograms performed at 20 mV s^{-1} from 0.0 to 1.2 V.

4. Conclusions

Pt(Cu) nanoparticles with a diameter of about 4–5 nm were successfully deposited on highly ordered CMK3 and CMK8 mesoporous carbons via electroless deposition of Cu followed by galvanic exchange with Pt. XRD showed that PtCu alloys with about 70–80 at.% Pt were formed, being identified as contracted *fcc* Pt lattice, with the absence of other crystalline structures. According to the HRTEM observations, the nanoparticles were well dispersed, being spherical on CMK3 and more elongated with a zigzag shape on CMK8. This was related to the different form of the mesoporous channels, long ordered parallel in the former and cubic in the latter. The FFT analysis of the high-resolution images showed *d*-spacings corresponding to pure Pt and contracted Pt lattices, in agreement with the PtCu alloy formation. The XPS analyses of Pt in the Pt(Cu) nanoparticles before and after argon sputtering indicated that the Pt(Cu) nanoparticles were mainly composed of a PtCu alloy core covered by a Pt-rich shell. The profiles of the steady cyclic voltammograms of the Pt(Cu)/OMCs catalysts were coincident with that of pure Pt, without Cu oxidation signal due to the protective Pt-rich shell. The quality of the hydrogen adsorption/desorption peaks was lower in the case of the Pt(Cu)/OMCs, which was explained by their poorer crystal faceting. Good ECSAs of about 70 m^2 g_{Pt}^{-1} for the Pt(Cu) catalysts supported on the non-activated CMK3 and CMK8 were achieved, whereas they were significantly smaller for the activated ones, as a result of nanoparticle aggregation. The onset potentials for CO oxidation and the ORR in the Pt(Cu) catalysts were shifted to more negative and to more positive potentials, respectively, with respect to Pt/C, thus indicating the higher catalytic activity of the former. The increased CO tolerance and the higher activity in front of the ORR of the Pt(Cu) alloys with respect to Pt/C were assigned to the geometric and ligand effects of Cu on Pt, arising from the Pt lattice compressive strain and the charge transfer from Cu to Pt when alloying Cu with Pt, which modified the electronic environment of Pt to reduce the adsorption energy of the adsorbed intermediates. Pt(Cu)/CMK3 showed competitive results regarding the CO oxidation and the ORR. This material presented reasonably good mass and specific activities and exhibited much better stability than Pt/C in the accelerated degradation tests. The activation of CMK3 and CMK8 reduced the stability of the catalysts, probably due to a textural modification of the mesoporous channels.

Supplementary Materials: The following are available online at https://www.mdpi.com/article/10.3390/catal11060724/s1, Figure S1: TEM micrographs of (**a**) the CMK3 carbon support, (**b**) CMK8 carbon support, (**c**) Pt(Cu)/CMK3, (**d**) Pt(Cu)/CMK3-A, (**e**) Pt(Cu)/CMK8 and (**f**) Pt(Cu)/CMK8-A. The insets of micrographs (**c**)–(**f**) show the corresponding size distribution of the nanoparticles. Figure S2: High-resolution TEM images of (**a**) Pt(Cu)/CMK3, (**c**) Pt(Cu)/CMK3-A, (**e**) Pt(Cu)/CMK8 and (**g**) Pt(Cu)/CMK8-A. Their respective FFT analysis is shown in figures (**b**), (**d**), (**f**) and (**h**), where the *d*-spacings corresponding to the selected spots are indicated. These results have to be

compared with the d-spacings of pure Pt, which are 0.227 and 0.140 nm for (111) and (220) planes, respectively [36].

Author Contributions: Conceptualization, F.A.; methodology, P.L.C.; validation, J.G.-C.; formal analysis, P.L.C.; investigation, J.G.-C.; resources, I.S.; data curation, E.B.; writing–original draft preparation, J.G.-C.; writing–review and editing, E.B., I.S., and P.L.C.; supervision, P.L.C.; project administration, I.S.; funding acquisition, E.B. and I.S. F.A.'s contribution to this work has been made exclusively within the framework of his relationship as an external collaborator with LEMMA's group of the UB. All authors have read and agreed to the published version of the manuscript.

Funding: This research was funded by the Agencia Estatal de Investigación (AEI, Spain) under project number PID2019-109291RB-I00 and the Generalitat de Catalunya (AGAUR, Spain) through the FI-SDUR PhD scholarship received by J.G.-C. (2020 FISDU 00005).

Acknowledgments: The authors are grateful to the CCIT-UB (Scientific and Technological Centers of the Universitat de Barcelona) for their support with the surface analysis techniques.

Conflicts of Interest: The authors declare no conflict of interest. The funders had no role in the design of the study; in the collection, analyses, or interpretation of data; in the writing of the manuscript; or in the decision to publish the results.

References

1. Onat, N.; Bayar, H. The sustainability indicators of power production systems. Renew. Sustain. *Energy Rev.* **2010**, *14*, 3108–3115. [CrossRef]
2. Tie, S.F.; Tan, C.W. A review of energy sources and energy management system in electric vehicles. *Renew. Sustain. Energy Rev.* **2013**, *20*, 82–102. [CrossRef]
3. Larcher, D.; Tarascon, J.M. Towards greener and more sustainable batteries for electrical energy storage. *Nat. Chem.* **2015**, *7*, 19–29. [CrossRef] [PubMed]
4. Chu, S.; Majumdar, A. Opportunities and challenges for a sustainable energy future. *Nature* **2012**, *488*, 294–303. [CrossRef] [PubMed]
5. Li, W.; Liu, J.; Zhao, D. Mesoporous materials for energy conversion and storage devices. *Nat. Rev. Mater.* **2016**, *1*, 16023. [CrossRef]
6. Stambouli, A.B.; Traversa, E. Fuel cells, an alternative to standard sources of energy. *Renew. Sustain. Energy Rev.* **2002**, *6*, 295–304. [CrossRef]
7. Jouin, M.; Gouriveau, R.; Hissel, D.; Péra, M.C.; Zerhouni, N. Prognostics and health management of PEMFC-State of the art and remaining challenges. *Int. J. Hydrog. Energy* **2013**, *38*, 15307–15317. [CrossRef]
8. Alves, H.J.; Bley, C., Jr.; Niklevicz, R.R.; Frigo, E.P.; Frigo, M.S.; Coimbra-Araújo, C.H. Overview of hydrogen production technologies from biogas and the applications in fuel cells. *Int. J. Hydrog. Energy* **2013**, *38*, 5215–5225. [CrossRef]
9. Sulaiman, N.; Hannan, M.A.; Mohamed, A.; Majlan, E.H.; Wan Daud, W.R. A review on energy management system for fuel cell hybrid electric vehicle: Issues and challenges. *Renew. Sustain. Energy Rev.* **2015**, *52*, 802–814. [CrossRef]
10. Daud, W.R.W.; Rosli, R.E.; Majlan, E.H.; Hamid, S.A.A.; Mohamed, R.; Husaini, T. PEM fuel cell system control: A review. *Renew. Energy* **2017**, *113*, 620–638. [CrossRef]
11. Kamat, P.V. Meeting the clean energy demand: Nanostructure architectures for solar energy conversion. *J. Phys. Chem. C* **2007**, *111*, 2834–2860. [CrossRef]
12. Wang, Y.; Chen, K.S.; Mishler, J.; Cho, S.C.; Adroher, X.C. A review of polymer electrolyte membrane fuel cells: Technology, applications, and needs on fundamental research. *Appl. Energy* **2011**, *88*, 981–1007. [CrossRef]
13. Alcaide, F.; Cabot, P.L.; Brillas, E. Fuel cells for chemicals and energy cogeneration. *J. Power Sources* **2006**, *153*, 47–60. [CrossRef]
14. Antolini, E. Formation of carbon-supported PtM alloys for low temperature fuel cells: A review. *Mater. Chem. Phys.* **2003**, *78*, 563–573. [CrossRef]
15. Liu, Z.; Ling, X.Y.; Su, X.; Lee, J.Y. Carbon-supported Pt and PtRu nanoparticles as catalysts for a direct methanol fuel cell. *J. Phys. Chem. B* **2004**, *108*, 8234–8240. [CrossRef]
16. Ruth, K.; Vogt, M.; Zuber, R. Development of CO-tolerant catalysts. In *Handbook of Fuel Cells–Fundamentals, Technology and Applications*; Vielstich, W., Gasteiger, H.A., Lamm, A., Eds.; John Wiley & Sons: New York, NY, USA, 2010; Volume 3, pp. 489–496. [CrossRef]
17. Velázquez-Palenzuela, A.; Brillas, E.; Arias, C.; Centellas, F.; Garrido, J.A.; Rodríguez, R.M.; Cabot, P.L. Structural analysis of carbon-supported Ru-decorated Pt nanoparticles synthesized using forced deposition and catalytic performance toward CO, methanol, and ethanol electro-oxidation. *J. Catal.* **2013**, *298*, 112–121. [CrossRef]
18. Acres, G.J.K.; Hards, G.A. Electrocatalysts for fuel cells. Catal. Today **1997**, *38*, 393–400. [CrossRef]
19. Li, F.; Chan, K.Y.; Yung, H.; Yang, C.; Ting, S.W. Uniform dispersion of 1:1 PtRu nanoparticles in ordered mesoporous carbon for improved methanol oxidation. *Phys. Chem. Chem. Phys.* **2013**, *15*, 13570–13577. [CrossRef]

20. Nilekar, A.U.; Alayoglu, S.; Eichhorn, B.; Mavrikakis, M. Preferential CO oxidation in hydrogen: Reactivity of core-shell nanoparticles. *J. Am. Chem. Soc.* **2010**, *132*, 7418–7428. [CrossRef] [PubMed]
21. Sung, Y.; Hwang, J.; Chung, J.S. Characterization and activity correlations of Pt bimetallic catalysts for low temperature fuel cells. *Int. J. Hydrog. Energy* **2011**, *36*, 4007–4014. [CrossRef]
22. Ignaszak, A.; Teo, C.; Ye, S.; Gyenge, E. Pt-SnO_2-Pd/C electrocatalyst with enhanced activity and durability for the oxygen reduction reaction at low Pt loading: The effect of carbon support type and activation. *J. Phys. Chem. C* **2010**, *114*, 16488–16504. [CrossRef]
23. Stamenkovic, V.; Mun, B.S.; Mayrhofer, K.J.J.; Ross, P.N.; Markovic, N.M.; Rossmeisl, J.; Greeley, J.; Norskov, K. Changing the activity of electrocatalysts for oxygen reduction by tuning the surface electronic structure. *Angew. Chem. Int. Ed.* **2006**, *45*, 2897–2901. [CrossRef] [PubMed]
24. Mukerjee, S.; Srinivasan, S.J. Enhanced electrocatalysis of oxygen reduction on platinum alloys in proton exchange membrane fuel cells. *J. Electroanal. Chem.* **1993**, *357*, 201–224. [CrossRef]
25. Srivastava, R.; Mani, P.; Hahn, Strasser, P. Efficient oxygen reduction fuel cell electrocatalysis on voltammetrically dealloyed Pt–Cu–Co nanoparticles. *Angew. Chem. Int. Ed.* **2007**, *46*, 8988–8991. [CrossRef]
26. Caballero-Manrique, G.; Velázquez-Palenzuela, A.; Brillas, E.; Centellas, F.; Garrido, J.A.; Rodriguez, R.M.; Cabot, P.L. Electrochemical synthesis and characterization of carbon-supported Pt and Pt-Ru nanoparticles with Cu cores for CO and methanol oxidation in polymer electrolyte fuel cells. *Int. J. Hydrog. Energy* **2014**, *39*, 12859–12869. [CrossRef]
27. Xiong, L.; Kannan, A.M.; Manthiram, A. Pt-M (M = Fe, Co, Ni and Cu) electrocatalysts synthesized by an aqueous route for proton exchange membrane fuel cells. *Electrochem. Commun.* **2002**, *4*, 898–903. [CrossRef]
28. Xiong, L.; Manthiram, A. Effect of atomic ordering on the catalytic activity of carbon supported PtM (M = Fe, Co, Ni, and Cu) alloys for oxygen reduction in PEMFCs. *J. Electrochem. Soc.* **2005**, *152*, A697–A703. [CrossRef]
29. Podlovchenko, B.I.; Krivchenko, V.A.; Maksimov, Y.M.; Gladysheva, T.D.; Yashina, L.V.; Evlashin, S.A.; Pilevsky, A.A. Specific features of the formation of Pt(Cu) catalysts by galvanic displacement with carbon nanowalls used as support. *Electrochim. Acta* **2012**, *76*, 137–144. [CrossRef]
30. Mohl, M.; Dobo, D.; Kukovecz, A.; Konya, Z.; Kordas, K.; Wei, J.; Vajtai, R.; Ajayan, P.M. Formation of CuPd and CuPt bimetallic nanotubes by galvanic replacement reaction. *J. Phys. Chem. C* **2011**, *115*, 9403–9409. [CrossRef]
31. Mani, P.; Srivastava, R.; Strasser, P. Dealloyed binary PtM3(M = Cu, Co, Ni) and ternary $PtNi_3M$ (M = Cu, Co, Fe, Cr) electrocatalysts for the oxygen reduction reaction: Performance in polymer electrolyte membrane fuel cells. *J. Power Sources* **2011**, *196*, 666–673. [CrossRef]
32. Ding, L.X.; Wang, A.L.; Li, G.R.; Liu, Z.Q.; Zhao, W.X.; Su, C.Y.; Tong, Y.X. Porous Pt-Ni-P composite nanotube arrays: Highly electroactive and durable catalysts for methanol electrooxidation. *J. Am. Chem. Soc.* **2012**, *134*, 5730–5733. [CrossRef]
33. Ozaslan, M.; Strasser, P. Activity of dealloyed PtCo3 and PtCu3 nanoparticle electrocatalyst for oxygen reduction reaction in polymer electrolyte membrane fuel cell. *J. Power Sources* **2011**, *196*, 5240–5249. [CrossRef]
34. Jayasayee, K.; Van Veen, J.A.R.; Manivasagam, T.G.; Celebi, S.; Hensen, E.J.M.; de Bruijn, F.A. Oxygen reduction reaction (ORR) activity and durability of carbon supported PtM (Co, Ni, Cu) alloys: Influence of particle size and non-noble metals. *Appl. Catal. B Environ.* **2012**, *111–112*, 515–526. [CrossRef]
35. Caballero-Manrique, G.; Nadeem, I.; Brillas, E.; Centellas, F.; Garrido, J.A.; Rodriguez, R.M.; Cabot, P.L. Effects of the electrodeposition time in the synthesis of carbon-supported Pt(Cu) and Pt-Ru(Cu) core-shell electrocatalysts for polymer electrolyte fuel cells. *Catalysts* **2016**, *6*, 125. [CrossRef]
36. Caballero-Manrique, G.; Brillas, E.; Centellas, F.; Garrido, J.A.; Rodriguez, R.M.; Cabot, P.L. Electrochemical oxidation of the carbon support to synthesize Pt(Cu) and Pt-Ru(Cu) core-shell electrocatalysts for low-temperature fuel cells. *Catalysts* **2015**, *5*, 815–837. [CrossRef]
37. Geboes, B.; Mintsouli, I.; Wouters, B.; Georgieva, J.; Kakaroglou, A.; Sotiropoulos, S.; Valova, E.; Armyanov, S.; Hubin, A.; Breugelmans, T. Surface and electrochemical characterisation of a Pt-Cu/C nano-structured electrocatalyst, prepared by galvanic displacement. *Appl. Catal. B Environ.* **2014**, *150–151*, 249–256. [CrossRef]
38. Mintsouli, I.; Georgieva, J.; Armyanov, S.; Valova, E.; Avdeev, G.; Hubin, A.; Steenhaut, O.; Dille, J.; Tsiplakides, D.; Balomenou, S.; et al. Pt-Cu electrocatalysts for methanol oxidation prepared by partial galvanic replacement of Cu/carbon powder precursors. *Appl. Catal. B Environ.* **2013**, *136–137*, 160–167. [CrossRef]
39. Georgieva, J.; Valova, E.; Mintsouli, I.; Sotiropoulos, S.; Armyanov, S.; Kakaroglou, A.; Hubin, A.; Steenhaut, O.; Dille, J. Carbon-supported Pt(Cu) electrocatalysts for methanol oxidation prepared by Cu electroless deposition and its galvanic replacement by Pt. *J. Appl. Electrochem.* **2014**, *44*, 215–224. [CrossRef]
40. Guterman, V.E.; Belenov, S.V.; Alekseenko, A.A.; Lin, R.; Tabachkova, N.Y.; Safronenko, O.I. Activity and stability of Pt/C and Pt-Cu/C electrocatalysts. *Electrocatalysis* **2018**, *9*, 550–562. [CrossRef]
41. Priyadchenko, V.V.; Sealbunyan, Y.V.; Kurzin, A.A.; Bulat, N.V.; Shemet, D.B.; Avakyan, L.A.; Belenov, S.V.; Volochaev, V.A.; Zizak, I.; Guterman, V.E.; et al. Bimetallic PtCu core-shell nanoparticles in PtCu/C electrocatalysts: Structural and electrochemical characterization. *Appl. Catal. A Gen.* **2016**, *525*, 226–236. [CrossRef]
42. Alekseenko, A.A.; Belenov, S.V.; Menshikov, V.S.; Guterman, V.E. Pt(Cu)/C electrocatalysts with low platinum content. *Russ. J. Electrochem.* **2018**, *54*, 415–425. [CrossRef]

43. Alekseenko, A.A.; Guterman, V.E.; Belenov, S.V.; Menshikov, V.S.; Tabachkova, N.Y.; Safronenko, O.I.; Moguchikh, E.A. Pt/C electrocatalysts based on the nanoparticles with the gradient structure. *Int. J. Hydrog. Energy* **2018**, *43*, 3676–3687. [CrossRef]
44. Maya-Cornejo, J.; Carrera-Cerritos, R.; Sebastián, D.; Ledesma-García, J.; Arriaga, L.G.; Aricò, A.S.; Baglio, V. PtCu catalyst for the electro-oxidation of ethanol in an alkaline direct alcohol fuel cell. *Int. J. Hydrog. Energy* **2017**, *42*, 27919–27928. [CrossRef]
45. Hoseini, S.J.; Bahrami, M.; Fard, Z.S.; Fard, S.F.H.; Roushani, M.; Agahi, B.H.; Fath, R.H.; Sarmoor, S.S. Designing of some platinum or palladium-based nanoalloys as effective electrocatalysts for methanol oxidation reaction. *Int. J. Hydrog. Energy* **2018**, *43*, 15095–15111. [CrossRef]
46. Sarkar, A.; Manthiram, A. Synthesis of Pt@Cu Core–shell nanoparticles by galvanic displacement of Cu by Pt4+ ions and their application as electrocatalysts for oxygen reduction reaction in fuel cells. *J. Phys. Chem. C* **2010**, *114*, 4725–4732. [CrossRef]
47. Coleman, E.J.; Chowdhury, M.H.; Co, A.C. Insights into the oxygen reduction reaction activity of Pt/C and PtCu/C catalysts. *ACS Catal.* **2015**, *5*, 1245–1253. [CrossRef]
48. García-Cardona, J.; Sirés, I.; Alcaide, F.; Brillas, E.; Centellas, F.; Cabot, P.L. Electrochemical performance of carbon-supported Pt(Cu) electrocatalysts for low-temperature fuel cells. *Int. J. Hydrog. Energy* **2020**, *45*, 20582–20593. [CrossRef]
49. Menshchikov, V.; Alekseenko, A.; Guterman, V.E.; Nechitailov, A.; Glebova, N.; Tomasov, A.; Spiridonova, O.; Belenov, S.; Zelenina, N.; Safronenko, O. Effective platinum-copper catalysts for methanol oxidation and oxygen reduction in proton-exchange membrane fuel cell. *Nanomaterials* **2020**, *10*, 742. [CrossRef]
50. Samad, S.; Loh, K.S.; Wong, W.Y.; Lee, T.K.; Sunarso, J.; Chong, S.T.; Daud, W.R.W. Carbon and non-carbon support materials for platinum-based catalysts in fuel cells. *Int. J. Hydrog. Energy* **2018**, *43*, 7823–7854. [CrossRef]
51. Antolini, E. Carbon supports for low-temperature fuel cell catalysts. *Appl. Catal. B Environ.* **2009**, *88*, 1–24. [CrossRef]
52. Rodríguez-Reinoso, F. The role of carbon materials in heterogeneous catalysis. *Carbon* **1998**, *36*, 159–175. [CrossRef]
53. Sharma, S.; Pollet, B.G. Support materials for PEMFC and DMFC electrocatalysts-A review. *J. Power Sources* **2012**, *208*, 96–119. [CrossRef]
54. Elangovan, A.; Xu, J.; Brown, E.; Liu, B.; Li, J. Fundamental electrochemical insights of vertically aligned carbon nanofiber architecture as a catalyst support for ORR. *J. Electrochem. Soc.* **2020**, *167*, 066523. [CrossRef]
55. Majlan, E.H.; Rohendi, D.; Daud, W.R.W.; Husaini, T.; Haque, M.A. Electrode for proton exchange membrane fuel cells: A review. *Renew. Sustain. Energy Rev.* **2018**, *89*, 117–134. [CrossRef]
56. Shao, Y.; Liu, J.; Wang, Y.; Lin, Y. Novel catalyst support materials for PEM fuel cells: Current status and future prospects. *J. Mater. Chem.* **2009**, *19*, 46–59. [CrossRef]
57. Dicks, A.L. The role of carbon in fuel cells. *J. Power Sources* **2006**, *156*, 128–141. [CrossRef]
58. Yu, X.; Ye, S. Recent advances in activity and durability enhancement of Pt/C catalytic cathode in PEMFC. Part I. Physico-chemical and electronic interaction between Pt and carbon support, and activity enhancement of Pt/C catalyst. *J. Power Sources* **2007**, *172*, 133–144. [CrossRef]
59. Yu, X.; Ye, S. Recent advances in activity and durability enhancement of Pt/C catalytic cathode in PEMFC. Part II: Degradation mechanism and durability enhancement of carbon supported platinum catalyst. *J. Power Sources* **2007**, *172*, 145–154. [CrossRef]
60. Roen, L.M.; Paik, C.H.; Jarvi, T.D. Electrocatalytic corrosion of carbon support in PEMFC cathodes. *Electrochem. Solid State Lett.* **2004**, *7*, 8–12. [CrossRef]
61. Shao, Y.; Yin, G.; Gao, Y. Understanding and approaches for the durability issues of Pt-based catalysts for PEM fuel cell. *J. Power Sources* **2007**, *171*, 558–566. [CrossRef]
62. Zhang, S.; Yuan, X.Z.; Hin, J.N.C.; Wang, H.; Friedrich, K.A.; Schulze, M. A review of platinum-based catalyst layer degradation in proton exchange membrane fuel cells. *J. Power Sources* **2009**, *194*, 588–600. [CrossRef]
63. Shahgaldi, S.; Hamelin, J. Improved carbon nanostructures as a novel catalyst support in the cathode side of PEMFC: A critical review. *Carbon* **2015**, *94*, 705–728. [CrossRef]
64. Seo, M.H.; Choi, S.M.; Kim, H.J.; Kim, W.B. The graphene-supported Pd and Pt catalysts for highly active oxygen reduction reaction in an alkaline condition. *Electrochem. Commun.* **2011**, *13*, 182–185. [CrossRef]
65. Zhu, C.; Dong, S. Recent progress in graphene-based nanomaterials as advanced electrocatalysts towards oxygen reduction reaction. *Nanoscale* **2013**, *5*, 1753–1767. [CrossRef] [PubMed]
66. Jha, N.; Reddy, A.L.M.; Shaijumon, M.M.; Rajalakshmi, N.; Ramaprabhu, S. Pt-Ru/multi-walled carbon nanotubes as electrocatalysts for direct methanol fuel cell. *Int. J. Hydrog. Energy* **2008**, *33*, 427–433. [CrossRef]
67. Shao, Y.; Yin, G.; Gao, Y.; Shi, P. Durability study of PtC and PtCNTs catalysts under simulated PEM fuel cell conditions. *J. Electrochem. Soc.* **2006**, *153*, 1093–1097. [CrossRef]
68. Devrim, Y.; Arica, E.D. Multi-walled carbon nanotubes decorated by platinum catalyst for high temperature PEM fuel cell. *Int. J. Hydrog. Energy* **2019**, *44*, 18951–18966. [CrossRef]
69. Alexeyeva, N.; Tammeveski, K.T.; López-Cudero, A.; Solla-Gullón, J.; Feliu, J.M. Electroreduction of oxygen on Pt nanoparticle/carbon nanotube nanocomposites in acid and alkaline solutions. *Electrochim. Acta* **2010**, *55*, 794–803. [CrossRef]
70. Alvarez, G.; Alcaide, F.; Miguel, O.; Cabot, P.L.; Martínez-Huerta, M.V.; Fierro, J.L.G. Electrochemical stability of carbon nanofibers in proton exchange membrane fuel cells. *Electrochim. Acta* **2011**, *56*, 9370–9377. [CrossRef]
71. Sebastián, D.; Ruiz, A.G.; Suelves, I.; Moliner, R.; Lázaro, M.J.; Baglio, V.; Stassi, A.; Aricò, A.S. Enhanced oxygen reduction activity and durability of Pt catalysts supported on carbon nanofibers. *Appl. Catal. B Environ.* **2012**, *115–116*, 269–275. [CrossRef]

72. Jung, J.H.; Park, B.I.; Kim, J. Durability test with fuel starvation using a Pt/CNF catalyst in PEMFC. *Nanoscale Res. Lett.* **2012**, *7*, 21–25. [CrossRef]
73. Zaragoza-Martín, F.; Sopeña-Escario, D.; Morallón, E.; de Lecea, C.S.M. Pt/carbon nanofibers electrocatalysts for fuel cells. Effect of the support oxidizing treatment. *J. Power Sources* **2007**, *171*, 302–309. [CrossRef]
74. Guo, J.; Sun, G.; Wang, Q.; Wang, G.; Zhou, Z.; Tang, S.; Jiang, L.; Zhou, B.; Xin, Q. Carbon nanofibers supported Pt-Ru electrocatalysts for direct methanol fuel cells. *Carbon* **2006**, *44*, 152–157. [CrossRef]
75. El-Deeb, H.; Bron, M. Microwave-assisted polyol synthesis of PtCu/carbon nanotube catalysts for electrocatalytic oxygen reduction. *J. Power Sources* **2015**, *275*, 893–900. [CrossRef]
76. El-Deeb, H.; Bron, M. Electrochemical dealloying of PtCu/CNT electrocatalysts synthesized by NaBH4-assisted polyol-reduction: Influence of preparation parameters on oxygen reduction activity. *Electrochim. Acta* **2015**, *164*, 315–322. [CrossRef]
77. Xia, K.; Gao, Q.; Wu, C.; Song, S.; Ruan, M. Activation, characterization and hydrogen storage properties of the mesoporous carbon CMK-3. *Carbon* **2007**, *43*, 1989–1996. [CrossRef]
78. Ma, T.Y.; Liu, L.; Yuan, Z.Y. Direct synthesis of ordered mesoporous carbons. *Chem. Soc. Rev.* **2013**, *42*, 3977–4003. [CrossRef] [PubMed]
79. Eftekhari, A.; Fan, Z. Ordered mesoporous carbon and its applications for electrochemical energy storage and conversion. *Mater. Chem. Front.* **2017**, *1*, 1001–1027. [CrossRef]
80. Ambrosio, E.P.; Dumitrescu, M.A.; Francia, C.; Gerbaldi, C.; Spinelli, P. Ordered mesoporous carbons as catalyst support for PEM fuel cells. *Fuel Cells* **2009**, *9*, 197–203. [CrossRef]
81. Phan, T.N.; Gong, M.K.; Thangavel, R.; Lee, Y.S.; Ko, C.H. Enhanced electrochemical performance for EDLC using ordered mesoporous carbons (CMK-3 and CMK-8): Role of mesopores and mesopore structures. *J. Alloy Compd.* **2019**, *780*, 90–97. [CrossRef]
82. Güneş, S.; Güldür, F.Ç. Synthesis of OMC supported Pt catalysts and the effect of the metal loading technique on their PEM fuel cell performances. *Chem. Eng. Commun.* **2020**, *207*, 961–971. [CrossRef]
83. Álvarez, G.; Alcaide, F.; Miguel, O.; Calvillo, L.; Lázaro, M.J.; Quintana, J.J.; Calderón, J.C.; Pastor, E. Technical electrodes catalyzed with PtRu on mesoporous ordered carbons for liquid direct methanol fuel cells. *J. Solid State Electrochem.* **2010**, *14*, 1027–1034. [CrossRef]
84. Calvillo, L.; Gangeri, M.; Perathoner, S.; Centi, G.; Moliner, R.; Lázaro, M.J. Synthesis and performance of platinum supported on ordered mesoporous carbons as catalyst for PEM fuel cells: Effect of the surface chemistry of the support. *Int. J. Hydrog. Energy* **2011**, *36*, 9805–9814. [CrossRef]
85. Salgado, J.R.C.; Alcaide, F.; Álvarez, G.; Calvillo, L.; Lázaro, M.J.; Pastor, E. Pt-Ru electrocatalysts supported on ordered mesoporous carbon for direct methanol fuel cell. *J. Power Sources* **2010**, *195*, 4022–4029. [CrossRef]
86. Gupta, G.; Slanac, D.A.; Kumar, P.; Wiggins-Camacho, J.D.; Wang, X.; Swinnea, S.; More, K.L.; Dai, S.; Stevenson, K.J.; Johnston, K.P. Highly stable and active Pt-Cu oxygen reduction electrocatalysts based on mesoporous graphitic carbon supports. *Chem. Mater.* **2009**, *21*, 4515–4526. [CrossRef]
87. Calvillo, L.; Lázaro, M.J.; García-Bordejé, E.; Moliner, R.; Cabot, P.L.; Esparbé, I.; Pastor, E.; Quintana, J.J. Platinum supported on functionalized ordered mesoporous carbon as electrocatalyst for direct methanol fuel cells. *J. Power Sources* **2007**, *169*, 59–64. [CrossRef]
88. Liu, J.; Wu, X.; Yang, L.; Wang, F.; Yin, J. Unprotected Pt nanoclusters anchored on ordered mesoporous carbon as an efficient and stable catalyst for oxygen reduction reaction. *Electrochim. Acta* **2019**, *297*, 539–544. [CrossRef]
89. Brandiele, R.; Durante, C.; Zerbetto, M.; Vicentini, N.; Kosmala, T.; Badocco, D.; Pastore, P.; Rizzi, G.A.; Isse, A.A.; Gennaro, A. Probing the correlation between Pt-support interaction and oxygen reduction reaction activity in mesoporous carbon materials modified with Pt-N active sites. *Electrochim. Acta* **2018**, *277*, 287–300. [CrossRef]
90. Perini, L.; Durante, C.; Favaro, M.; Perazzolo, V.; Agnoli, S.; Schneider, O.; Granozzi, G.; Gennaro, A. Metal-support interaction in platinum and palladium nanoparticles loaded on nitrogen-doped mesoporous carbon for oxygen reduction reaction. *ACS Appl. Mater. Interfaces* **2015**, *7*, 1170–1179. [CrossRef] [PubMed]
91. Available online: https://www.acsmaterial.com/materials/carbon-series.html (accessed on 22 February 2021).
92. Powder Diffraction File, International Centre for Diffraction Data (ICDD), 12 Campus Boulevard Newton Square, Pennsylvania, 19073-3273, USA, 2018. Available online: http://www.icdd.com (accessed on 22 February 2021).
93. Shen, Y.; Zhang, Z.; Xiao, K.; Xi, J. Synthesis of Pt, PtRh, and PtRhNi alloys supported by pristine graphene nanosheets for ethanol electrooxidation. *ChemCatChem* **2014**, *6*, 3254–3261. [CrossRef]
94. Pryadchenko, V.V.; Belenov, S.V.; Shunnet, D.B.; Srabionyan, V.V.; Avakyan, L.A.; Volochaev, V.A.; Mikheykin, A.S.; Bdoyan, K.E.; Zizak, I.; Guterman, V.E.; et al. Effect of thermal treatment on the atomic structure and electrochemical characteristics of trimetallic PtCu core-shell nanoparticles in PtCu/C electrocatalysts. *J. Phys. Chem. C* **2018**, *122*, 17199–17210. [CrossRef]
95. Calvillo, L.; Celorrio, V.; Moliner, R.; Cabot, P.L.; Esparbé, I.; Lázaro, M.J. Control of textural properties of ordered mesoporous materials. *Microporous Mesoporous Mater.* **2008**, *116*, 292–298. [CrossRef]
96. Available online: http://database.iem.ac.ru/mincryst/ (accessed on 22 February 2021).
97. Du, X.; Luo, S.; Du, H.; Tang, M.; Huang, X.; Shen, P.K. Monodisperse and self-assembled Pt-Cu nanoparticles as an efficient electrocatalyst for the methanol oxidation reaction. *J. Mater. Chem. A* **2016**, *4*, 1579–1586. [CrossRef]

98. Alcaide, F.; Álvarez, G.; Cabot, P.L.; Genova-Koleva, R.V.; Grande, H.J.; Martínez-Huerta, M.V.; Miguel, O. Supporting PtRh alloy nanoparticle catalysts by electrodeposition on carbon paper for the ethanol electrooxidation in acidic medium. *J. Electroanal. Chem.* **2020**, *862*, 113960. [CrossRef]
99. Long, G.; Li, X.; Wan, K.; Liang, A.; Piao, J.; Tsiakaras, P. Pt/CN-doped electrocatalysts: Superior electrocatalytic activity for methanol oxidation reaction and mechanistic insight into interfacial enhancement. *Appl. Catal. B Environ.* **2017**, *203*, 541–548. [CrossRef]
100. Goodenough, J.B.; Hamnett, A.; Kennedy, B.J.; Weeks, S.A. XPS investigation of platinized carbon electrodes for the direct methanol air fuel cell. *Electrochim. Acta* **1987**, *32*, 1233–1238. [CrossRef]
101. Rigsby, M.A.; Zhou, W.P.; Lewera, A.; Duong, H.T.; Bagus, P.S.; Jaegermann, W.; Hunger, R.; Wieckowski, A. Experiment and theory of fuel cell catalysis: Methanol and formic acid decomposition on nanoparticle Pt/Ru. *J. Phys. Chem. C* **2008**, *112*, 15595–15601. [CrossRef]
102. Biesinger, M.C. Advanced analysis of copper X-ray photoelectron spectra. *Surf. Interface Anal.* **2017**, *49*, 1325–1334. [CrossRef]
103. Serrano-Ruiz, J.C.; López-Cudero, A.; Solla-Gullón, J.; Sepúlveda-Escribano, A.; Aldaz, A. Hydrogeration of α, β unsaturated aldehydes over polycrystalline, (111) and (100) preferentially oriented Pt nanoparticles supported on carbon. *J. Catal.* **2008**, *253*, 159–166. [CrossRef]
104. Ioroi, T.; Fujiwara, N.; Siroma, Z.; Yasuda, K.; Miyazaki, Y. Platinum and molybdenum oxide deposited carbon electrocatalyst for oxidation of hydrogen containing carbon monoxide. *Electrochem. Commun.* **2002**, *4*, 442–446. [CrossRef]
105. Enterría, M.; Figueiredo, J.L. Nanostructured mesoporous carbons: Tuning texture and surface chemistry. *Carbon* **2016**, *108*, 29–102. [CrossRef]
106. Mayrhofer, K.J.J.; Strmcnik, D.; Blizanac, B.B.; Stamenkovic, V.; Arenz, M.; Markovic, N.M. Measurement of oxygen reduction activities via the rotating disc electrode method: From Pt model surfaces to carbon-supported high surface area catalysts. *Electrochim. Acta* **2008**, *53*, 3181–3188. [CrossRef]
107. Shanahan, P.V.; Xu, L.; Liang, C.; Waje, M.; Dai, S.; Yan, Y.S. Graphitic mesoporous carbon as a durable fuel cell catalyst support. *J. Power Sources* **2008**, *185*, 423–427. [CrossRef]
108. Kitchin, J.R.; Nørskov, J.K.; Barteau, M.A.; Chen, J.G. Modification of the surface electronic and chemical properties of Pt(111) by subsurface 3d transition metals. *J. Chem. Phys.* **2004**, *120*, 10240–10246. [CrossRef]
109. Corona, B.; Howard, M.; Zhang, L.; Henkelman, G. Computational screening of core@shell nanoparticles for the hydrogen evolution and oxygen reduction reactions. *J. Chem. Phys.* **2016**, *145*, 244708. [CrossRef] [PubMed]
110. Beermann, V.; Gocyla, M.; Willinger, E.; Rudi, S.; Heggen, M.; Dunin-Borkowski, R.E.; Willinger, M.G.; Strasser, P. Rh-doped Pt-Ni octahedral nanoparticles: Understanding the correlation between elemental distribution, oxygen reduction reaction, and shape stability. *Nano Lett.* **2016**, *16*, 1719–1725. [CrossRef]

SUPPORTING INFORMATION

Testing PtCu nanoparticles supported on highly ordered mesoporous carbons CMK3 and CMK8 as catalysts for low-temperature fuel cells

Julia García-Cardona, Francisco Alcaide, Enric Brillas, Ignasi Sirés and Pere L. Cabot *

Laboratori d'Electroquímica dels Materials i del Medi Ambient, Secció de Química Física, Facultat de Química, Universitat de Barcelona, Martí i Franquès 1-11, 08028 Barcelona, Spain
* Correspondence: pcabot@ub.edu

In this section, the examination by SEM and HRTEM of the nanoparticulated catalysts are shown, Figs. S1 and S2.

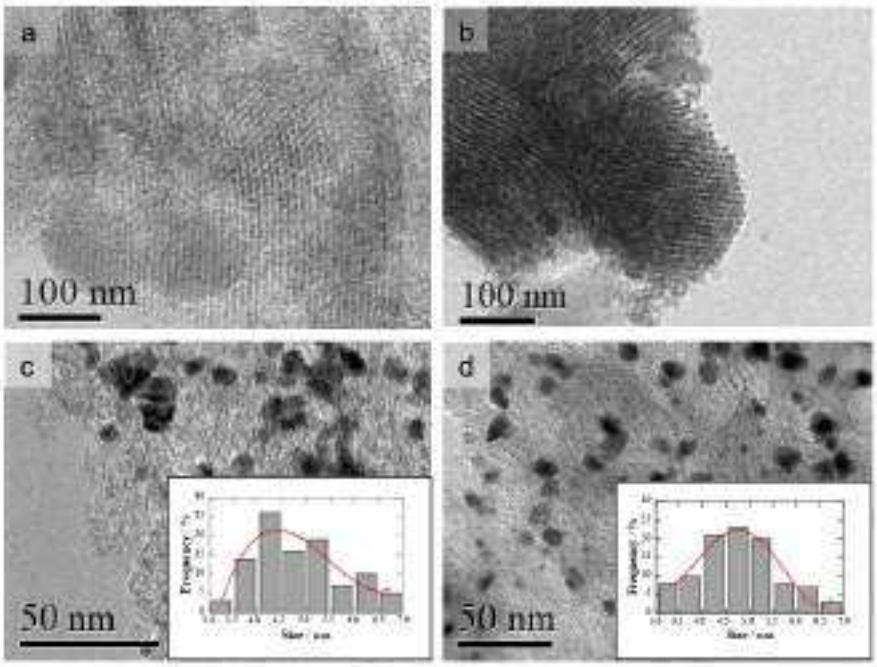

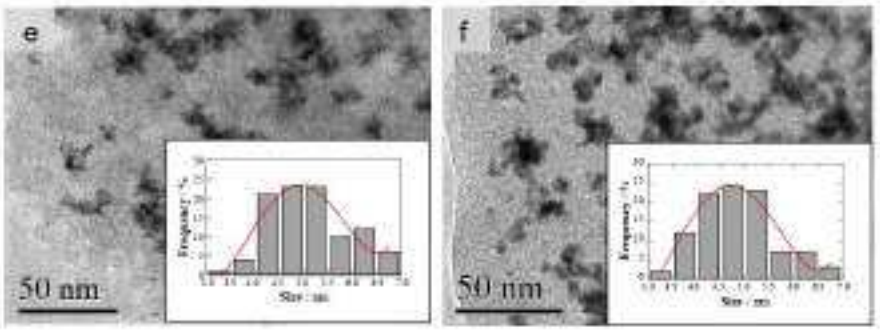

Figure S1. TEM micrographs of (**a**) the CMK3 carbon support, (**b**) CMK8 carbon support, (**c**) Pt(Cu)/CMK3, (**d**) Pt(Cu)/CMK3-A, (**e**) Pt(Cu)/CMK8 and (**f**) Pt(Cu)/CMK8-A. The insets of micrographs (c)-(f) show the corresponding size distribution of the nanoparticles.

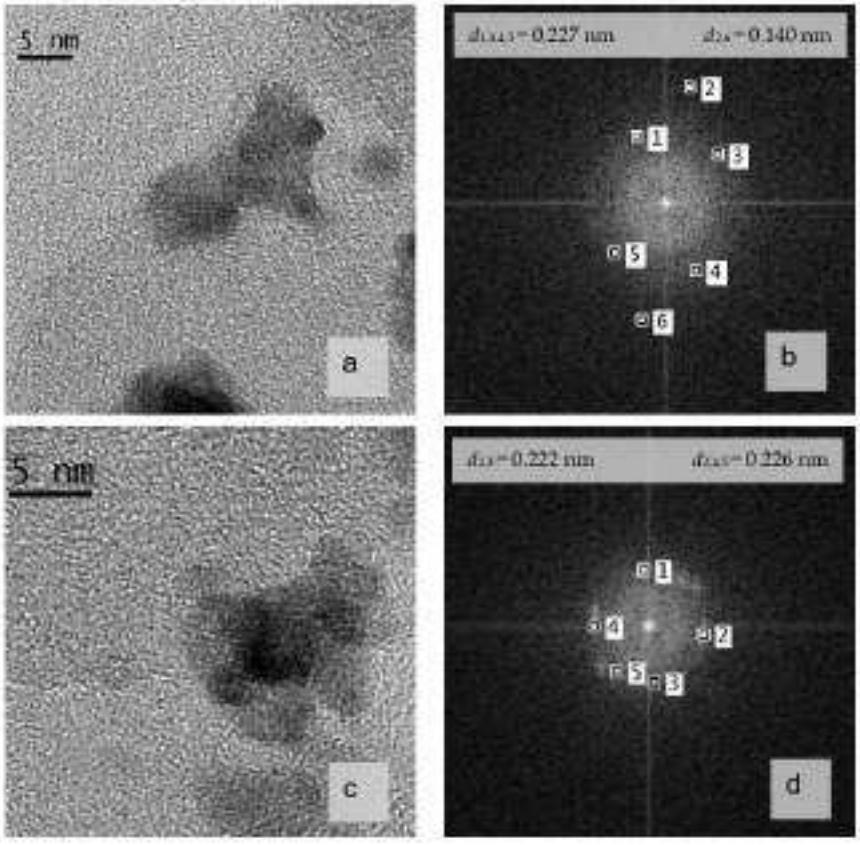

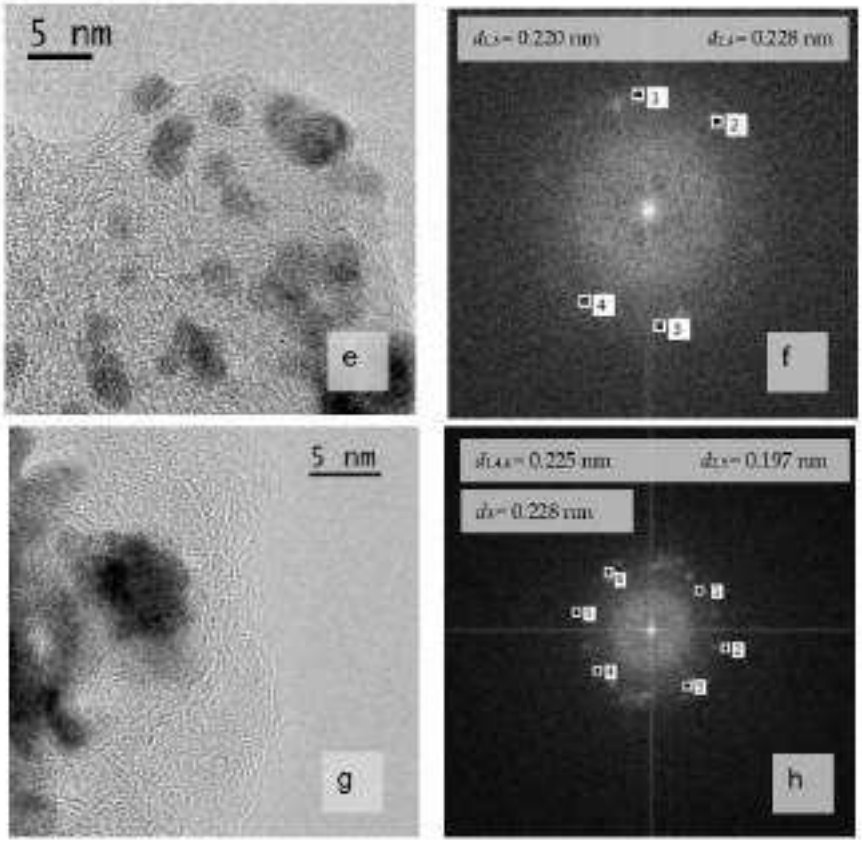

Figure S2. High-resolution TEM images of (a) Pt(Cu)/CMK3, (c) Pt(Cu)/CMK3-A, (e) Pt(Cu)/CMK8 and (g) Pt(Cu)/CMK8-A. Their respective FFT analysis is shown in figures (b), (d), (f) and (h), where the *d*-spacings corresponding to the selected spots are indicated. These results have to be compared with the *d*-spacings of pure Pt, which are 0.227 and 0.140 nm for (111) and (220) planes, respectively [96].

4.3.2. On the Viability of Chitosan-Derived Mesoporous Carbons as Supports for PtCu Electrocatalysts in PEMFC

The interesting results obtained using commercial MCs, which resulted in an improvement of the electrochemical and transport properties compared to catalysts obtained with traditional carbon materials, led us to test other mesoporous carbons. Considering previous work of some co-authors of the paper, chitosan, a polysaccharide containing amine and hydroxyl groups, was used as a precursor to synthesize N-doped mesoporous carbons (NMCs) as supports for the PtCu catalysts. Chitosan is one of the most abundant natural organic compounds, which can be easily obtained from disposable biomass, for example from crustacean shells, and consequently, its use in material production gives chitosan an added value.

The NMCs were synthesised by Durante's group from the University of Padova from chitosan and using different types of acid for prompting its dissolution and a cheap P20 silica template. They were named as CH1, CH2, CH3 and CH4 depending on the different acidic conditions. The PtCu supported catalysts were obtained by a water-in-oil method, as explained in Chapter 3, Section 3.3, using the previously mentioned NMCs derived from chitosan as well as commercial CMK-3, in order to compare the performance of all these catalysts to commercial Pt/C.

The structural characterization of carbon supports is important in order to analyse and understand the different performance of the catalysts. CH carbons presented a highly porous nature, as shown by TEM, where the presence of carbon flakes with round shape mesopores was observed. The BET surface area of the NMCs was bigger than those obtained with commercial CMK-3 and Vulcan XC-72. The graphitization degree of the CH-derived carbonaceous materials, estimated by Raman spectroscopy, was not significantly different between the different CHs and presented a relative disordered graphitic lattice. The XPS analyses showed the presence of other elements. In particular, pyridinic and/or pyrrolic N in these carbons is of additional interest, since a strong interaction between N and Pt may result in excellent catalytic activity toward the ORR. A higher amount of C sp2 and pyrrolic N in CH2, CH3 and CH4 was found when compared to CH1.

The XRD showed a dominant *fcc* Pt structure, with shifted peaks because of the presence of Cu in the Pt lattice, which allowed to determine a PtCu crystallite composition, in the range of 83-90 at.%. In addition, the broadness of the peaks allowed to determine the mean crystallite size, which was between 3 and 5 nm. The particle sizes of the spherical nanoparticles observed by TEM were in accordance to these results and, although some aggregation was observed, there was evidence of successful attachment of the nanoparticles to the carbon supports. The composition of the catalysts was obtained by EDS analyses, which showed a Pt content around 20-30 wt.%, comparable to 20 wt.% Pt/C, and Cu content around 14-21 wt.%.

The ECSA values of the catalysts were in the range 10–20 m^2 g_{Pt}^{-1}, which is 4 times smaller than of Pt/C, explained by the larger PtCu nanoparticle sizes obtained and their higher agglomeration, as both factors can reduce the number of Pt accessible active sites. The lower values for CH3 and CH4 are in agreement to the particle agglomeration observed by TEM. Therefore, the lower microporosity in CH1 and CH2 allows a better dispersion of the nanoparticles over the surface at the same time that makes nanoparticles more accessible to reactants.

The catalytic activity toward CO oxidation was higher for PtCu/NMC since the oxidation peaks were shifted about 50 mV to more negative potentials than that of Pt/C. The ORR performance of the different catalysts, according to their specific activities, were higher than that of Pt/C. The PtCu/CH3 presented the higher specific activity toward the ORR, since its onset potential for this reaction was more positive (45 mV) and also the specific activity at 0.9 V was also the highest when comparing all these catalysts. The ORR activity when using the NMCs as supports was better than that of commercial CMK-3. When studying the catalytic activity for the MOR, the PtCu/CH3 was again the better catalyst, presenting an onset potential 56 mV more negative than that of Pt/C and the highest specific current density, 1.2 mA cm^{-2} at 0.9 V. The corresponding results show that the PtCu catalysts are more active against MOR than commercial Pt/C, and that there is an effect of the different surface structures of the PtCu nanoparticles produced in the different support textures.

Electrochimica Acta 442 (2023) 141911

Contents lists available at ScienceDirect

Electrochimica Acta

journal homepage: www.journals.elsevier.com/electrochimica-acta

On the viability of chitosan-derived mesoporous carbons as supports for PtCu electrocatalysts in PEMFC☆

Julia García-Cardona [a], Ignasi Sirés [a], Marco Mazzucato [b], Riccardo Brandiele [b], Enric Brillas [a], Francisco Alcaide [a,c], Christian Durante [b,*], Pere L. Cabot [a,*]

[a] Laboratori d'Electroquímica dels Materials i del Medi Ambient, Departament de Química Física, Facultat de Química, Universitat de Barcelona, Martí i Franquès 1-11, Barcelona 08028, Spain
[b] Department of Chemical Sciences, University of Padua, Via Marzolo 1, Padova 35131, Italy

ARTICLE INFO

Keywords:
Chitosan
Mesoporous carbon
PtCu electrocatalysts
Methanol oxidation reaction
Oxygen reduction reaction

ABSTRACT

Chitosan is an abundant and non-toxic natural polysaccharide rich in nitrogen, which is used here to obtain N-doped mesoporous carbons (NMCs) as supports for Pt-saving PtCu alloy electrocatalysts, which can be of interest for low-temperature fuels cells. NMCs with different textural properties were synthesized from cheap silica templates. They presented relative dominance of disordered graphitic lattice and comparable amounts of pyrrolic and pyridinic N, with different specific BET surface areas (715–1040 $m^2 g^{-1}$) and mesopore (1.3–2.4 $cm^3 g^{-1}$) and micropore volumes (0.1–0.6 $cm^3 g^{-1}$). PtCu nanoparticles were deposited by Cu electroless deposition and further galvanic exchange with Pt, with overall Pt loadings about 20 wt.%. Pt-rich PtCu alloy crystallites with contracted Pt *fcc* lattices and sizes of 3.1–4.7 nm were formed. The synthesized PtCu/NMCs catalysts presented better specific current densities for the oxygen reduction and better CO tolerance and specific current densities for the methanol oxidation reaction than those of commercial Pt/C and PtCu/CMK-3. The PtCu/NMC prepared with the H_2SO_4-activated NMC was the most active catalyst. The different textural properties of the carbonaceous materials appeared to determine the surface structure of the PtCu nanoparticles.

1. Introduction

Platinum and Pt-based alloys, dispersed on a carbon support, are to date the best and most applied catalysts in proton exchange membrane (PEMFCs) and direct methanol fuel cells (DMFCs), which appear as promising power sources for electric vehicles and small instrumentation [1–3]. Catalyst and carbon support play together significant roles in the catalyst performance through their synergistic effects [4–7]. However, reducing their cost is necessary to plain the way to commercialization.

On one hand, Pt is expensive and scarce. Alloying with transition metals is interesting, not only in terms of cost (the Pt amount can thus be reduced), but also because of their electronic effect on Pt, which can improve its catalytic activity [8]. Thus, a wide variety of PtCu catalysts were synthesized in the past, mainly supported on carbon blacks Vulcan® XC-72 and XC-72R, which allowed increasing the catalytic activity toward the oxygen reduction, and the CO, methanol, and ethanol oxidation reactions [9–19].

On the other hand, the carbons supports should have high specific surface area, good conductivity, stability, and suitable porous structure facilitating the approach of the reactants and the products removal, as well as a good interaction between the support and the metallic nanoparticles (NPs) [7,20–25]. A wide variety of carbonaceous materials with different textures and surface structures, depending on the synthesis procedure, can be obtained. The most used and studied supports for fuel cell catalysts are carbon blacks such as Vulcan® XC-72 and XC-72R [9, 13,19,21], due to their low cost, high surface area, and good electrical conductivity. Nonetheless, they present some drawbacks such as deep micropores, which limit the accessibility of Nafion® and reactants to active sites, contain organo-sulphur impurities that can poison the catalyst, and can undergo corrosion while the cell operates [26,27]. For these reasons, alternative carbonaceous materials have been proposed [18,28–37]. It was shown that mesoporous carbons with high surface areas, adjustable pore structure and size, mechanical stability, and good conductivity, led to superior electrochemical and transport properties

☆ Paper to be considered for publication in Electrochimica Acta
* Corresponding authors.
E-mail addresses: christian.durante@unipd.it (C. Durante), pcabot@ub.edu (P.L. Cabot).
[1] Permanent address: CIDETEC, Basque Research and Technology Alliance (BRTA), Po. Miramón, 196, 20,014 Donostia-San Sebastián, Spain

https://doi.org/10.1016/j.electacta.2023.141911
Received 20 October 2022; Received in revised form 21 December 2022; Accepted 15 January 2023
Available online 17 January 2023

when compared to the traditional carbon materials [28,29,36,38]. Thus, improved catalytic activities of Pt and Pt-based NPs supported on ordered mesoporous carbons (OMCs) such as CMK-3 were achieved [30–33,35]. Note however, that it is very difficult to synthesize mesoporous silica hard templates to promote carbon replicas with suitable pore size (> 10 nm) and, consequently, they are expensive [38–40]. For this reason, the authors used in the past very cheap silica P20 (SiO_2 NPs 10–20 nm in size), usually employed for chromatographic separation, as the template (porogen agent) to obtain supercapacitors from different carbon precursors [41]. On the other hand, the authors took profit from chitosan [42,43], a polysaccharide containing amine and hydroxyl groups, which is one of the most abundant natural organic compounds, present in crustacean shells [44]. It was used as precursor to synthesize N-doped mesoporous carbon (NMC) for H_2O_2 generation in water decontamination [42] and Fe-N_x catalysts for the 4-electron O_2 reduction [41], thus making chitosan a chemical with added value from disposable biomass.

The object of this work was to synthesize novel carbon-supported Pt-saving PtCu catalysts by deposition of PtCu NPs on cheap mesoporous carbons, as a further step to the preparation of eco-friendly electrocatalysts, which can be of interest for low-temperature fuel cells. The strategy was to prepare carbons of different textural properties from chitosan as precursor, using different acid-treatments to dissolve chitosan and P20 as silica template. Accordingly, the prepared carbons and supported PtCu were characterized by means of structural techniques, additionally testing the catalysts for the CO and methanol oxidation, and the oxygen reduction. The activity of the different catalysts against the reactions studied was compared to that obtained using commercial Pt/C and PtCu NPs dispersed on commercial ordered mesoporous carbon CMK-3.

2. Materials and methods

2.1. Chemicals

In the synthesis of the carbons, the following reagent grade chemicals were used: chitosan (CH), CH_3COONH_4, HCl (40 wt.%), ethylene glycol, CH_3COOH (glacial) and Nafion® (5 wt.% in a mixture of lower aliphatic alcohols and water), were from Sigma Aldrich; H_2SO_4 (96 wt. %), ethanol, and acetone, from Fluka; and isopropanol from Merck. Alpha Gaz O_2 and Ar were supplied by Air Liquid (>99.999%). The textural properties of the synthesized carbons were compared to those of CMK-3 mesoporous carbon from ACS Materials and to Vulcan® XC-72 carbon from Cabot Corp. For the electrochemical characterization, all the solutions were prepared using high-purity Milli-Q water (Merck purification system, resistivity > 18.2 MΩ cm at 25 °C) and analytical-grade reagents. H_2SO_4 (96 wt.%) and $CuSO_4{\bullet}5H_2O$ were supplied by Panreac-Applichem and n-heptane, poly(ethyleneglycol)-dodecyl ether (surfactant Brij-30) and $NaBH_4$, by Sigma-Aldrich. Catalyst cleaning solvents were ethanol (96 wt.%) and acetone (99.5 wt.%) purchased from Panreac. The Pt precursor was 8 wt.% aqueous solution of H_2PtCl_6 from Merck. For the electrochemical tests, Nafion® (5 wt.%) and dry isopropanol from Sigma-Aldrich were used for the ink preparation. The catalysts obtained were compared to commercial 20 wt.% Pt/C from Prometek, with XC-72 as the carbon support.

2.2. Synthesis of the carbon supports

The NMCs were synthesized using CH as the carbon precursor and silica P20 as the inorganic template. The same silica was utilized in previous work of the authors, although for different carbon precursors to be applied in supercapacitors [41]. As additional novelty, the effect of four different types of acids, H_2SO_4, CH_3COOH, HCl and CH_3COONH_4, was evaluated for prompting the chitosan dissolution in water, and the resulting carbons were accordingly named from CH1 to CH4. Note that HNO_3 was not used to avoid the formation of excessive oxygenated functional groups. In a typical synthesis, 3 g of CH were mixed with 1.5 g of silica P20 in 150 mL of water, then the solution was heated at 80 °C for 3 h, and finally, after the addition of acid to the solution, the temperature was increased to 90 °C and kept for 12 h while stirring at a rotation speed of 500 rpm. Afterwards, the precursors powder was dried for 24 h and then placed in a tubular furnace and pyrolyzed using a two-step procedure. After the typical atmosphere conditioning, the powder was first heated in the furnace with a 75 sccm (standard cm^3 min^{-1}) N_2 flow at 100 °C for 1 h and, subsequently, the temperature was raised up to 750 °C at a rate of 5 °C min^{-1} and kept at that temperature for 2 h. The template was etched by treatment in a solution containing ethanol and NaOH at a concentration of 2 M in both sonicator for 3 days, keeping the temperature under 35 °C. The carbon was then separated by vacuum filtration on a nylon nanometric filter and dried overnight.

2.3. Synthesis of the supported catalysts

The catalysts were synthesized by a water-in-oil method. The microemulsion consisted of n-heptane, Brij-30 and an aqueous solution of $CuSO_4$ with a water-to-surfactant molar ratio of 7:1 [45]. The reducing agent, $NaBH_4$, was slowly added to the magnetically stirred microemulsion to form the Cu nanoparticles, with a reductant-to-metal molar ratio of 9:1 and a total stirring time of 2 h. After the reductant removal, 0.5 mL of the 8 wt.% H_2PtCl_6 solution was slowly added to perform the galvanic exchange, keeping the magnetic stirring for 1 h. Finally, 21 mg of the carbon support were added to the microemulsion, also stirring for 1 h and then, acetone was added for the phase separation. Once the organic phase was clean, it was separated from the aqueous phase and the powder was filtered. Then, the powder was added to a 5 mM H_2PtCl_6 + 0.1 M $HClO_4$ solution to improve the galvanic replacement, sonicating the suspension in bath for 1 h. Finally, the suspension was filtered, and the catalyst powder cleaned with ethanol. The resulting powder was left to dry overnight at 80 °C. The corresponding PtCu carbon-supported catalysts were then identified as PtCu/CH1, PtCu/CH2, PtCu/CH3, PtCu/CH4, and PtCu/CMK-3.

2.4. Structural characterization

The textural and physicochemical characteristics of the synthesized carbons were studied by transmission electron microscopy (TEM), elemental analyses (EA), N_2 absorption/desorption, Raman spectroscopy and X-ray photoelectron spectroscopy (XPS). TEM observations were performed using a FEI Tecnai G2 transmission electron microscope operating at 100 kV. EA was carried out using a Thermo Scientific Flash 2000 analyser. N_2 desorption/desorption isotherms were recorded at 77.3 K using a Micromeritics ASAP 2020 Plus instrument. The specific surface areas of the samples were calculated by multipoint Brunauer–Emmett–Teller (BET) analysis; the total pore volume was obtained by applying Gurvich law at $p/p^0 \sim 0.98$–1, whereas the t-plot method was used to measure the micropore volume. Pore size distribution curves were derived using density functional theory (DFT) methods and, finally, the number of mesopores was calculated as the difference between the total number of pores and the number of micropores. The Raman spectra were obtained using a DXR Raman microscope system from Thermo Fischer Scientific. The photoexcitation was performed using a laser of $\lambda = 532$ nm, a spot size on the sample ~25 μm and a power at the sample in the range 0.1–1.0 mW. The XPS measurements were performed at room temperature in an ultra-high vacuum (UHV) chamber (base pressure < 5×10^{-9} mbar), equipped with a double anode X-ray source (omicron DAR-400) and a hemispherical electron analyser (omicron EIS-125). A non-monochromatized Mg-K_α radiation ($h\nu = 1253.6$ eV) and pass energies of 50 and 20 eV for the survey and the single spectral windows, respectively, were used. The calibration of the binding energy (BE) scale was carried out using Au $4f^{7/2}$ as a reference (BE Au $4f^{7/2} = 84.0$ eV). The XPS peaks of carbon, oxygen and nitrogen were separated into single components by using symmetrical

Voigt functions.

The catalysts prepared using the indicated supports were analysed using X-ray diffraction (XRD) and TEM. For the XRD analyses, the samples were sandwiched between films of 3.6 μm – thick polyester (Mylar®), using a PANalytical X'Pert PRO MPD θ/θ powder diffractometer, with a Cu anode, 45 kV and 40 mA, Cu K_α-filtered radiation (λ = 1.5418 Å), step size of 0.026° and measuring time of 200 s per step. The morphologies and overall composition of the catalysts were examined by means of 200 kV JEOL JEM 2100 transmission electrode microscope furnished with the energy-dispersive X-ray spectroscopy (EDS) technique. For the EDS analyses, different representative domains of the sample were analysed, and the mean values were taken as the corresponding overall compositions.

2.5. Electrochemical tests

The electrochemical activity measurements were carried out by cyclic voltammetry (CV) and linear sweep voltammetry (LSV) in a cell with a double wall for the temperature regulation (25 ± 0.1 °C) by means of Julabo MP-5 thermostat and a three-electrode setup, with a glassy carbon electrode (GCE) from Metrohm (0.196 cm^2 area) as the working one, a Pt wire as the auxiliary electrode and a reversible hydrogen electrode (RHE) from Gaskatel GmbH as the reference. All the potentials mentioned in this paper are referred to the latter. The GCE tip was coupled to a rotating disk electrode (RDE) from Metrohm Autolab B.V. The GCE was polished using a PSA-backed white felt cloth from Buehler containing Micropolish II deagglomerated alumina of 0.3 and 0.05 μm. The catalysts inks were prepared by dispersing 2 mg of the catalysts in 0.5 mL of ultrapure water by sonication for 30 min. Then, suitable amounts of the catalyst inks were deposited on the GCE tip using a micropipette and once dried at room temperature, the catalyst layer was coated with 2.5 μL of 1 wt.% Nafion®.

The electrolyte used for the experiments was deaerated 0.5 M H_2SO_4 and the measurements were performed using an Autolab PGSTAT100 potentiostat-galvanostat controlled by NOVA 2.1.4 software. The solution deaeration was performed before the electrochemical experiments by bubbling N_2 through the solution and during the measurements it was maintained over the liquid phase. The freshly prepared working electrodes were repetitively cycled at 100 mV s^{-1} in the potential range from 0.0 to 1.2 V to attain steady voltammograms. The successive voltammograms obtained during this repetitive cycling presented a slight increase in the hydrogen adsorption/desorption currents, which was related to the electrochemical cleaning. Once stabilized, the representative cyclic voltammograms were acquired at 20 mV s^{-1}.

The CO tolerance of the catalysts was tested by CO stripping. In this case, CO was bubbled for 15 min while keeping the electrode potential at 0.1 V and, afterwards, the CO dissolved was removed using N_2. Then the monolayer of preadsorbed CO was oxidized by CV at 20 mV s^{-1} between 0.0 and 1.2 V. The activity test towards the ORR was performed by LSV in an O_2-saturated (atmospheric pressure) 0.5 M H_2SO_4, scanning the potential from the open circuit potential to 0.2 V at a scan rate of 5 mV s^{-1}, rotating the GCE tip of the RDE at 1500 rpm. The activity towards the MOR was examined by CV at 20 mV s^{-1}, between 0.0 to 1.2 V, using deaerated 1.0 M solutions of the alcohol in 0.5 M H_2SO_4. The Pt loading in these ORR and MOR studies was set close to 20 μg_{Pt} cm^{-2}.

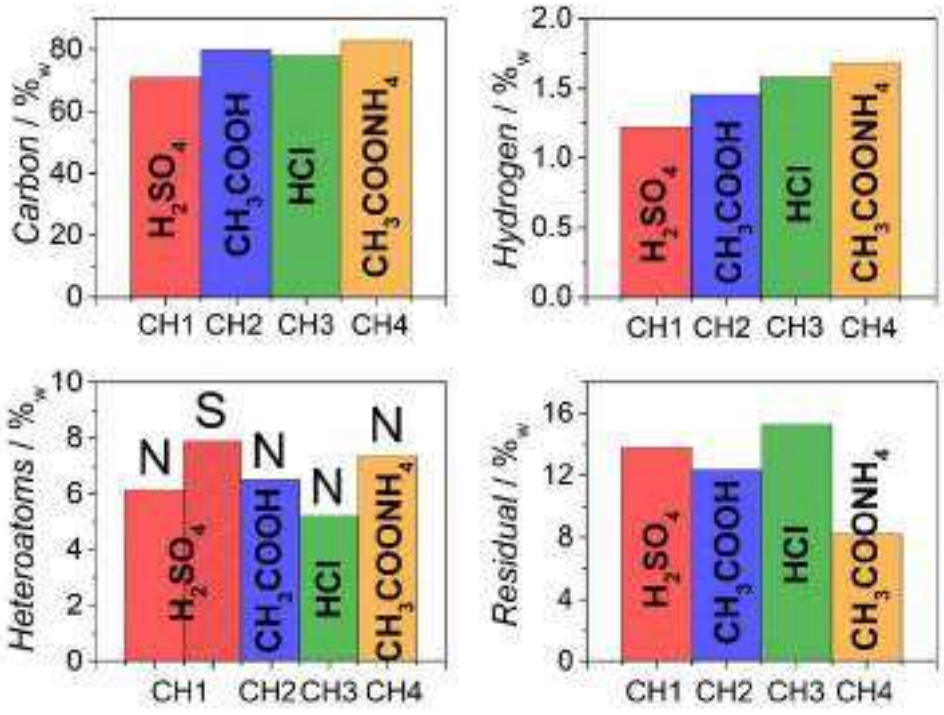

Fig. 1. Elemental analysis histograms.

3. Results and discussion

3.1. Characterization of the mesoporous carbons

The heteroatoms concentration in the four samples was evaluated by elemental analysis. Fig. 1 shows the results obtained for the synthesized NMCs. All the samples from CH1 to CH4 show an important nitrogen content ranging from 5.2 to 7.4 wt.%, the latter obtained when CH_3COONH_4 was employed for promoting the chitosan solubilization in water. The CH1 sample shows nitrogen-sulfur co-doping, where the sulfur source is the H_2SO_4 used for increasing the chitosan solubility during the impregnation process. In all the samples, the residual element corresponds to the oxygen, from 8.2 to 13.8 wt.%, meaning that a substantial functionalization with oxygen groups is attained, especially in the sample prepared by using strong acidic conditions (HCl and H_2SO_4).

The highly porous nature of CH carbons was revealed by TEM measurements, which show the presence of carbon flakes characterized by round shape mesopores, all with diameters between 15 and 20 nm. TEM images of Fig. S1 in the Supporting Information (SI) file show the formation of an interconnected porous structure, which is the result of the interconnection of quasi-round pores created by the imprinting action of the SiO_2 NPs.

The synthesized NMCs showed a high specific BET surface area (S_{BET}): 714.6, 872.3, 1041 and 1037 $m^2\ g^{-1}$ for CH1 to CH4, respectively. It is evident that the resulting S_{BET} is sensitive to the different acids used for increasing the chitosan solubility in water, which in turn affects the disposition of chitosan chain around the P20 particles. These values are greater than that measured for commercial CMK-3 (Table S1 and Fig. S2 in SI) and significantly greater than that obtained for commercial Vulcan® XC-72 (Table S1 and Fig. S3 in SI).

Fig. 2 shows the total pore, micropore and mesopore volumes: all the samples showed a larger volume of mesopores (V_{meso}) as compared to that of micropores (V_μ). This is especially evident when H_2SO_4 was employed as acid ($V_{meso} = 2.408\ m^2\ g^{-1}$ and $V_\mu = 0.108\ m^2\ g^{-1}$), but V_{meso} tended to decrease and V_μ tended to increase upon transition from CH1 to CH4. Note that as V_μ increased, V_{meso} decreased together with the total pore volume ($V_{tot} = V_\mu + V_{meso}$). Thus, V_{meso}/V_μ ratio was 22.7, 21.7, 6.1 and 1.9 for CH1, CH2, CH3 and CH4, respectively. The higher microporosity of CH3 and CH4 agrees with their larger BET area measured, greater than 1000 $m^2\ g^{-1}$. On the other hand, CMK-3 presented V_{tot}, V_{meso} and V_μ values of 0.923, 0.638 and 0.142 $cm^3\ g^{-1}$, respectively, whereas the values for Vulcan® XC-72 were 0.629, 0.260 and 0.055 $cm^3\ g^{-1}$, respectively, with the corresponding V_{meso}/V_μ ratios of 4.5 and 4.7 for CMK-3 and XC-72, respectively (Table S1 in the SI).

The graphitization degree of the CH-derived carbonaceous materials was evaluated by means of Raman spectroscopy. The spectra of all these mesoporous carbons were similar and have been exemplified in Fig. 3. As shown in this figure, these carbons did not present defined second-order Raman spectra (2400–2700 cm^{-1} region), and only a smeared flat band was present, which overlapped with the background noise. The spectra of all the CH1-CH4 carbons could be deconvoluted in the first-order region between 1100 and 1700 cm^{-1} by using four Gaussian bands, being D1, D3, D4 and G, corresponding to disordered graphitic lattice (D1 and D4), amorphous carbon (D3) and ideal graphitic lattice (G) [46]. D2, corresponding also to disordered graphitic lattice, has been also sometimes used, and it is generally located at 1620 cm^{-1}. However, it was not considered in the present case because a very good fitting of the experimental data was already obtained, even by keeping a minimum number of gaussian components. Note that the position of the main bands D1 and G did not significantly change when comparing the four NMCs, thus evidencing a very similar graphitization degree and content of amorphous carbon. In Fig. 3, the ratios of the peak areas corresponding to the different spectral bands with respect to that of the G band were determined as: $A_{D1}/A_G = 1.85$, $A_{D3}/A_G = 0.62$, $A_{D4}/A_G = 0.55$ and $A_{2D}/A_G = 0.38$.

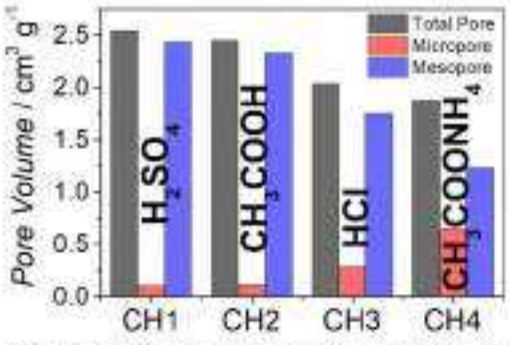

Fig. 2. Histogram for the pore volume of the four synthesized carbons.

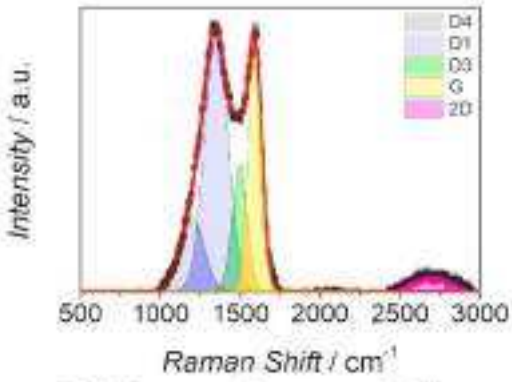

Fig. 3. Raman spectrum for mesoporous carbon CH3.

An index that can be used for evaluating the degree of organization in carbon materials is *R2*, which can be calculated using Equation (1) [42,47]:

$$R2 = A_{G2} / (A_{D1} + A_G + A_{D2}) \quad (1)$$

where A_i is the area of the corresponding deconvolution peak and A_{D2} was considered to be equal to zero. Values of *R2* lower or greater than 0.5 are then indicative of the presence of lower or higher amounts of defective graphitic lattice in the carbonaceous material, respectively. The values of *R2* for the different CH-derived carbons did not substantially change, ranging between 0.55 and 0.65, which denoted the relative dominance of disordered graphitic lattice in these mesoporous materials.

The surface compositions of the synthesized carbons were analysed by XPS. They showed the presence of surface of oxygen, carbon and nitrogen and the absence of silica. The C 1 s biding energy (*BE*) region of CH3 presented a broad peak (Fig. 4a), which could be fitted with five main components, assigned to C sp^2 (C–C, *BE* = 284.4 eV), C sp^2 species bond to N (C–N, *BE* = 286.1 eV), C–O–C groups at 287.5 eV, carboxylic carbon (COOH, *BE* = 289.3 eV) and carbonate groups (CO_3^{2-}, *BE* = 290.8 eV) [48]. The same deconvolution was performed for all the synthesized carbons, with the exception that no significant carbonate peak was ascertained for CH1. As expected, the XPS spectrum of CH1 showed a S 2p peak, absent in the other CH-derived carbons, which could be assigned to one singular S-thiophene species (C – S – C, *BE* = 163.6 eV) [40,49].

The high-resolution XPS spectra in the N 1 s region of CH3 is depicted in Fig. 4b, where two main contributions could be deconvoluted, corresponding to pyrrolic and pyridinic nitrogen, as indicated. The relative

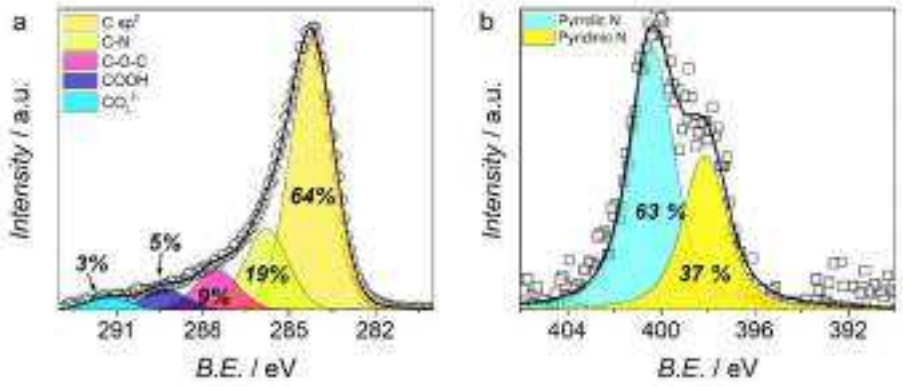

Fig. 4. High-resolution XPS analyses of mesoporous carbon CH3 in the *BE* region of (a) carbon and (b) nitrogen. Hollow symbols (○ and □) correspond to the experimental data and the solid lines to fitting after deconvolution in the indicated bonds.

peak areas corresponding to the different chemical species of C and N for the synthesized carbons have been collected in Table 1. It is worth mentioning the higher amount of the C sp^2 species and the dominance of pyrrolic N in CH2, CH3 and CH4 when compared to CH1.

The presence of pyridinic and/or pyrrolic N in these carbons is of additional interest, since a strong interaction between N and Pt may result in excellent catalytic activity toward the ORR, as shown previously by dispersing Pt NPs on N functionalized commercial mesoporous carbons [30].

It is then shown that inexpensive mesoporous carbons with variable mesoporosity to microporosity ratio can be obtained from an abundant precursor in disposable biomass, chitosan, modulated by the precursor treatment in different acids, with the help of cheap P20 hard templating silica. The obtained carbons, apart from oxygenated functional groups, presented pyridinic and pyrrolic N, which can operate as active sites for the catalyst anchoring.

3.2. Structural characteristics of the catalysts

Fig. 5a shows the XRD diffractograms of the different PtCu/NMCs, which are compared to PtCu/CMK-3 and Pt/C. All the diffractograms have a similar shape in which the dominance of the *fcc* Pt peaks is clear. However, the Pt-like XRD peaks for the PtCu samples show a slight shift with respect to those of Pt/C, what is better observed in the magnification shown in Fig. 5b.

The absence of peaks corresponding to Cu crystalline structures means that, if there were pure Cu or oxidized Cu crystallites, they had no sufficient size to be detected or they should be amorphous. The peaks at 2θ of 40.0, 46.3 and 67.5° correspond to (111), (200) and (220) *fcc* Pt planes, respectively [50]. In Fig. 5b, the (111) and (200) *fcc* Cu peaks have been marked, corresponding to 2θ angles of 43.3 and 50.5°, showing that those of PtCu fall between the peaks of pure Pt and pure Cu, although displaced toward the Pt peaks. These peak shifts strongly support the formation of PtCu alloy crystallites, since the Cu atomic radius (145 pm) is smaller than that of Pt (177 pm).

The composition of the PtCu alloys shown by these XRD analyses was estimated through Vegard's law, Eq. (2), which relates the lattice parameter of the PtCu alloy (a_{PtCu}) to the atomic fraction of Cu (x) and the lattice parameters of pure Pt (a_{Pt} = 0.3916 nm) and Cu (a_{Cu} = 0.3600 nm) [50]:

$$a_{PtCu} = (1 - x)a_{Pt} + xa_{Cu} \quad (2)$$

The Pt:Cu atomic ratios, collected in Table 2, show that the PtCu alloy crystallites formed are Pt-rich, with Pt amounts 5–9 times higher than Cu. The alloy formation indicates that in the galvanic replacement that takes place in the presence of Pt(IV), Cu is oxidized and replaced by Pt with some lattice reordering, which results in a PtCu alloy, in agreement with previous literature [18,19,51]. Note, however, that the peak broadness shown in Fig. 5 can be due to a small crystallite size and also to a peak superposition of phases having slightly different compositions [52]. For this reason, the alloy composition measured should be regarded as a mean value.

Despite not being pure metals, the crystallite sizes d can be estimated using Scherrer's equation:

$$d = \frac{K\lambda}{B\cos\theta} \quad (3)$$

where K = 0.9, λ is the wavelength of the X-ray radiation, and B is the width of the peak (in radians) at half the maximum intensity. The mean crystallite sizes obtained were around 3–4 nm (Table 2), slightly higher than that of the Pt nanoparticles in commercial Pt/C, but they can also be considered useful for fuel cell applications.

The PtCu/NMCs catalysts were also examined by TEM and compared to PtCu/CMK-3 and Pt/C (Fig. 6). According to the corresponding images, the PtCu NPs presented a rather spherical form, with sizes consistent with those estimated from XRD (Table 2). There is clear evidence of the successful attachment of the nanoparticles to the carbon supports, displaying some aggregation. However, the distribution and aggregation of the nanoparticles appear to be affected by the texture of the support. The corresponding EDS analyses provided the metallic overall compositions, also included in Table 2. Note that all the PtCu catalysts presented similar Pt contents in the range 22–33 wt.%, comparable to that of Pt/C, with Cu contents in the range 14–21 wt.%. The overall amounts of Pt and Cu did not vary too much from one catalyst to another, what is not strange because they were prepared in the same way. It is important to note, however, that the overall Pt:Cu atomic ratios in the catalyst were in the range 30–40 at.% Pt and 60–70 at.% Cu, which are very different from the alloy composition identified by XRD. Similar results were obtained by us when using CMK-3 and other

Table 1
Relative atomic composition (%) of the different oxidation states of C and N, obtained from the corresponding XPS high-resolution spectra.

Mesoporous carbon	C sp^2	C-N	COOH	C-O-C	CO_3^{2-}	Pyrrolic N	Pyridinic N
CH1	62	24	7	17	0	68	32
CH2	70	16	4	6	4	61	39
CH3	64	19	5	9	3	63	37
CH4	60	17	5	8	3	60	40

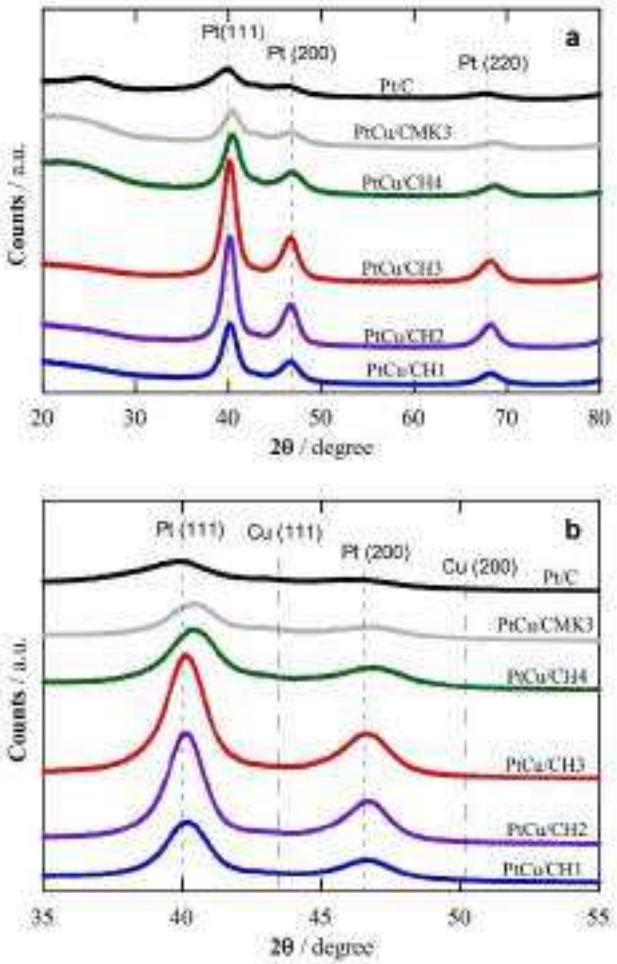

Fig. 5. XRD diffractograms of (a) the PtCu supported catalysts and (b) magnification of the main peaks observed, which correspond to Pt (111) and (200) plains.

Table 2
Metallic composition and crystallite size of the PtCu alloys identified by XRD (see Fig. 5), and overall metal contents of the catalysts measured from the EDS analyses.

Catalyst	Pt:Cu at.%	Crystallite size / nm	Metal content* / wt.%	
			Pt	Cu
PtCu/CH1	83:17	3.1	36	16
PtCu/CH2	87:13	4.7	26	20
PtCu/CH3	90:10	4.2	33	21
PtCu/CH4	84:16	3.3	22	19
PtCu/CMK-3	98:2	3.2	25	14
Pt/C	100:0	2.6	19	-

* Mean standard deviation of 2 wt.%

supports, although with different synthesis procedure [10,26]. This can be explained considering that the composition of the crystallites obtained from XRD refers to the Pt and Cu zero-valent elements and by the presence of significant amounts of Cu oxidized species on the carbon surface, resulting from the galvanic exchange. It was shown that the latter were easily removed by Ar^+ sputtering in the XPS analyses, and it is also expected that they should be also dissolved in the acidic electrolyte and electrochemical cleaning before the electrochemical tests.

These results show that the PtCu alloy nanoparticles, about 4 nm in size, were successfully attached to the mesoporous carbon supports, with some aggregation and composition dependence on the textural properties of the latter.

3.3. Electrochemical tests

The cyclic voltammograms of the PtCu/NMCs were first obtained in deaerated 0.5 M H_2SO_4 at 20 mV s^{-1} to examine the hydrogen adsorption/desorption peaks. The steady cyclic voltammograms obtained after electrochemical cleaning for representative PtCu/NMCs catalysts are shown in Fig. 7a. They have been compared to commercial Pt/C after normalizing to the respective mean value of the hydrogen adsorption and desorption charges, which are proportional to the number of active sites. Three distinct potential regions can be observed in all the cyclic voltammograms of the PtCu/NMCs, which match to those of commercial Pt/C: i) the hydrogen adsorption/desorption region (0.0–0.3 V), from which the coulombic charge of H adsorption and desorption (Q_H) can be obtained to estimate the electrochemical active surface area; ii) the

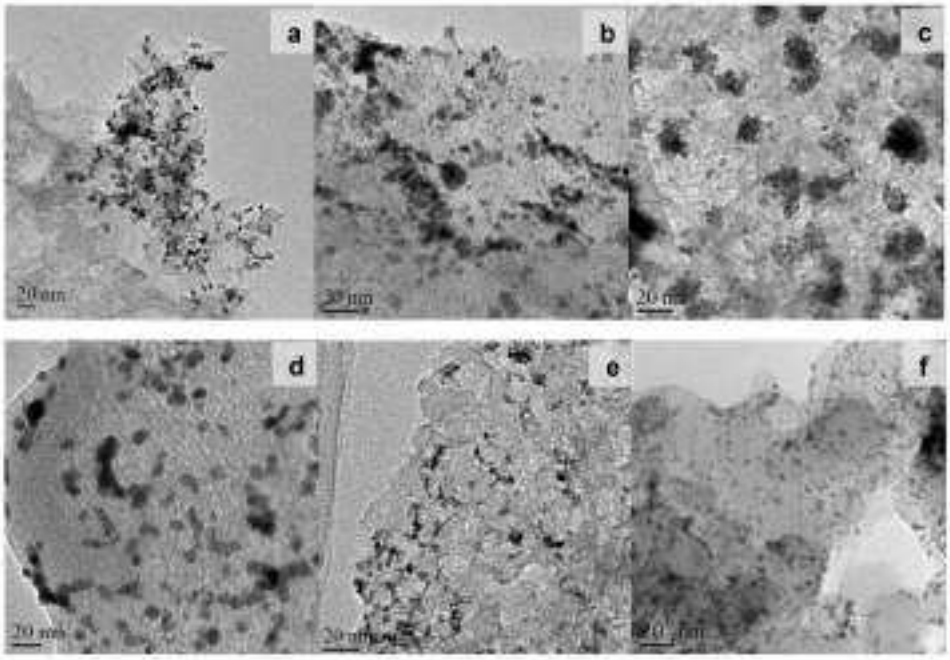

Fig. 6. TEM micrographs of the different specimens studied: (a) PtCu/CH1, (b) PtCu/CH2, (c) PtCu/CH3, (d)PtCu/CH4, (e) PtCu/CMK-3 and (f) commercial Pt/C.

pseudocapacitive region (0.3–0.7 V), which is proportional to the specific surface area of the carbon support; and iii) the oxidation/reduction of the surface Pt/PtO couple around 0.80 V (Pt oxidation from 0.80 V in the anodic sweep with the corresponding PtO reduction peak potential in the cathodic sweep at about 0.75 V). Note that the currents corresponding to the pseudocapacitive region for the PtCu/NMCs are higher than those of commercial Pt/C. This can be explained by the different specific total surface areas of the different carbons, which is of 225 m^2 g^{-1} for commercial Vulcan® XC-72 (Table S2 in SI), whereas they are over three-times greater for the mesoporous carbons of this work, as indicated above. Any evidence about Cu oxidation peaks in the cyclic voltammograms of the PtCu/NMCs was obtained, thus indicating the dominance of Pt on the PtCu surface NPs, achieved by the galvanic replacement and further CV cleaning [18,36]. Note in addition that the adsorption/desorption peaks of hydrogen in the PtCu/NMCs were not as well defined as those on Pt/C, most probably due to the Cu alloying, which can condition the Pt structural ordering on the surface of the nanoparticles [9,18].

The cyclic voltammograms of the CO stripping experiments have been depicted in Fig. 7b, where the oxidation of the CO monolayer that was previously adsorbed appear as the peak in the anodic sweep in the potential range between 0.6 and 1.0 V, although the onset and peak potentials depend on the catalyst. Note also that these curves have been normalized to the corresponding CO stripping charges for a better comparison, because these charges are proportional to the number of Pt active sites in each specimen.

It can be observed in the voltammograms shown in Fig. 7b that the stripping peaks for the PtCu/NMCs are shifted to more negative potentials than that corresponding to Pt/C. As shown in this figure, the onset potentials for the CO oxidation were about 0.70 V for the latter and about 0.65 V for the former, in agreement with previous results of the authors using PtCu NPs obtained also by galvanic exchange, although for different carbon supports [36,56]. This shift in the negative direction indicates improved activity toward CO oxidation (i.e., better CO tolerance), and can be explained by the electronic effects of Cu on Pt, which combine the compressive strain of the Pt lattice due to the smaller size of Cu (geometric effect) and the electron-donation of Cu on Pt due to the smaller electronegativity of the former (ligand effect), eventually weakening the CO bond and allowing its easier removal [9,18,36,53].

The electrochemical active surface area *ECSA* of each specimen was obtained from the hydrogen adsorption/desorption charges ($ECSA_H$) and from CO stripping ($ECSA_{CO}$), according to the following equations:

$$ECSA_H = \frac{Q_H}{210 \cdot m_{Pt}} \quad (4)$$

$$ECSA_{CO} = \frac{Q_{CO}}{420 \cdot m_{Pt}} \quad (5)$$

where Q_H and Q_{CO} are, respectively, the mean charge involved in the hydrogen adsorption/desorption and in the CO stripping charge (μC), m_{Pt} is the load of Pt (g) on the GCE, and 210 and 420 are the charges (μC cm^{-2}) associated to the oxidation of a monolayer of adsorbed H atoms (one-electron) and CO molecules (two-electron), also, respectively [54]. The *ECSA* values of the catalysts have been summarized in Table 3, showing a good agreement between those obtained from the hydrogen adsorption/desorption and CO stripping. Except for PtCu/CH4, they are in the range 15–22 m^2 g_{Pt}^{-1}, being smaller than for Pt/C. These rather low values can be explained, apart from the abovementioned larger nanoparticle size of PtCu/NMCs (Table 3), by the agglomeration of the PtCu NPs, which could reduce the number of accessible Pt active sites. This is in agreement with the TEM pictures shown in Fig. 6, in which more aggregation for CH3 is appreciated when compared to CH2. This is apparently related to the carbon microporosity. In fact, the microporosity of CH1 and CH2 is low and comparable (V_{micro}/V_t ratios of 22.7 and 21.7), whereas it is significantly higher for CH3 and CH4 (V_{micro}/V_t ratios 6.1 and 1.9). Accordingly, the ECSAs of CH1 and CH2 are comparable, and decreased when moving from CH2 to CH4. The higher microporosity of CH3 and CH4 allowed increasing their specific surface

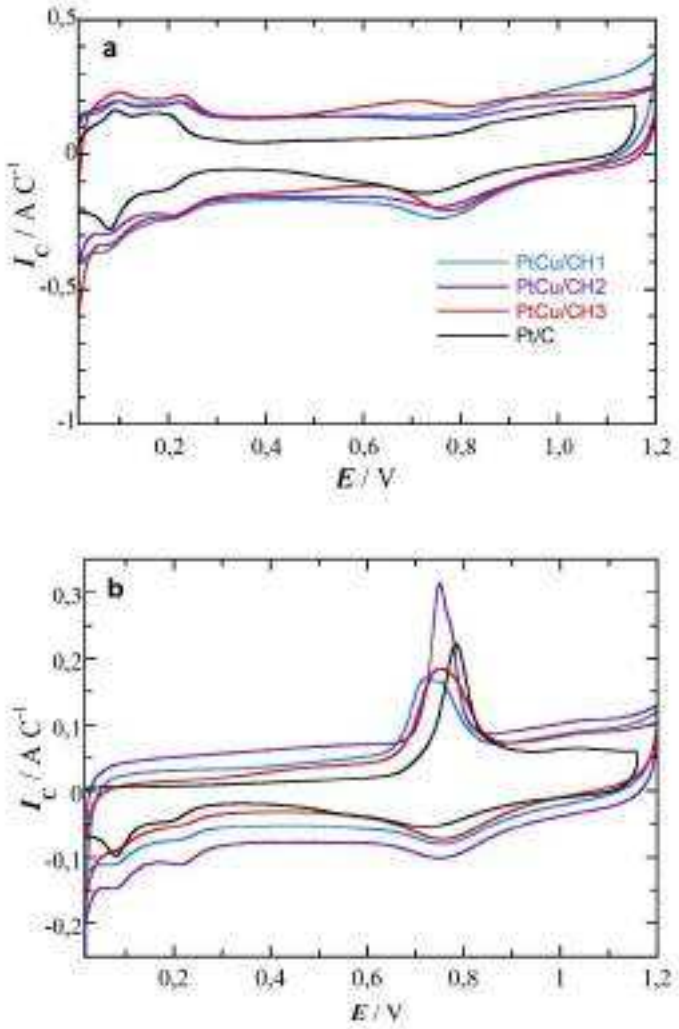

Fig. 7. (a) Cyclic voltammograms of the indicated PtCu/NMCs catalysts and (b) CO stripping curves of the same catalysts as in (a), compared to commercial Pt/C. Obtained in deaerated 0.5 M H_2SO_4 at a scan rate of 20 mV s^{-1}.

Table 3
ECSAs measured from the hydrogen adsorption/desorption (H) and from the CO stripping (CO) charges in the corresponding cyclic voltammograms.

Catalyst	Pt loading/ μg cm^{-2}	$ECSA_H$/ m^2 g$_{Pt}^{-1}$	$ECSA_{CO}$/ m^2 g$_{Pt}^{-1}$
PtCu/CH1	22.3	21.4	21.7
PtCu/CH2	22.4	23.7	21.6
PtCu/CH3	38.7	16.2	16.9
PtCu/CH4	23.5	9.5	9.7
PtCu/CMK-3	21.4	15.6	15.7
Pt/C	20.4	84.3	85.2

area, but could stimulate the nanoparticles aggregation.

The linear sweep voltammograms to study the ORR performance of the different catalysts in O_2-saturated 0.5 M H_2SO_4 solution at 5 mV s^{-1} and an RDE rotation rate of 1500 rpm, are shown in Fig. 8. Fig. 8a refers to the Pt mass (mass activity, j_m) and shows single waves in all cases, with limiting currents depending on the catalyst. When referred to the electrode section, the limiting current densities were comparable and about 2.5-3 mA cm^{-2} (see Fig. S4 in the SI file), except for PtCu/CH4 and PtCu/CMK-3, which were somewhat smaller. As shown in Fig. 8a, the Pt/C mass activity is the highest, which is an expected result, since its ECSA is about four times greater than those of PtCu/NMCs and PtCu/CMK-3, with about the same Pt loading. If, conversely, comparison is made in terms of current per *ECSA* (specific activities, j_s, in Fig. 8b), it is now the Pt/C that exhibits the smallest values. As the specific activities give the activity per unit of active area, higher values indicate greater catalytic activity and thus, all the PtCu catalysts appear to be more active than Pt/C.

The better activity of the PtCu/NMCs for ORR agrees with the CO stripping results of Fig. 7b, in which Cu alloying makes Pt more active in front of the CO oxidation and can also be explained by the electronic effects of Cu on Pt. As a method to quantify this specific activity, the potentials to attain a given j_m were determined in the Tafel region of the ORR (E_{mass} and $E_{0.1}$ at −0.01 and −0.1 mA cm$_{Pt}^{-2}$, respectively) and the

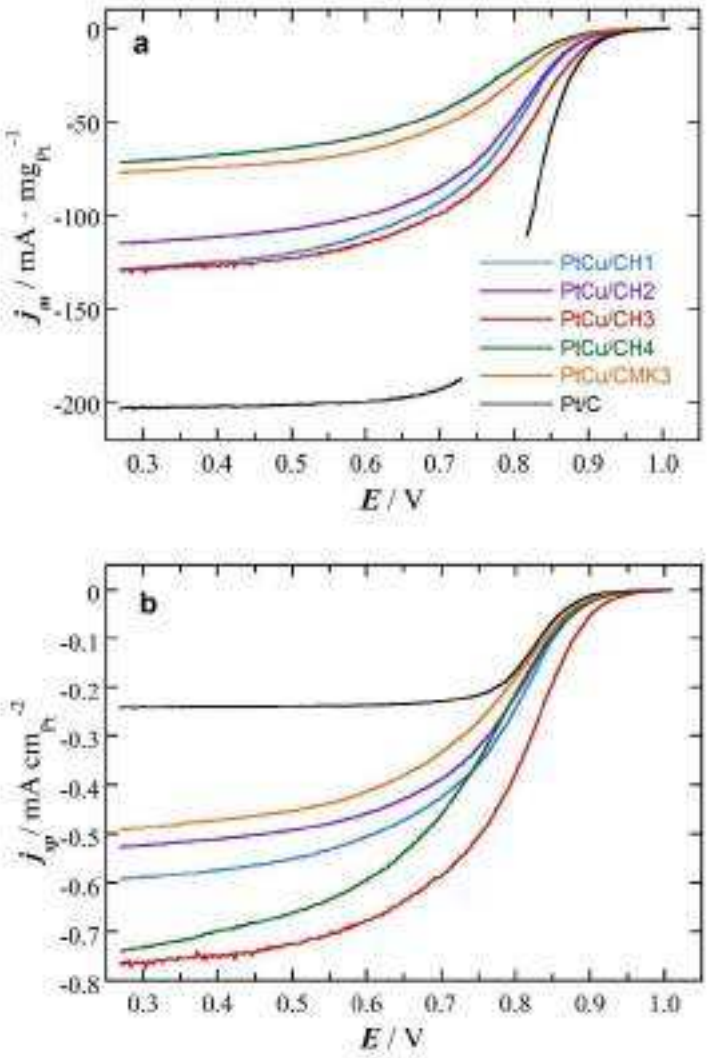

Fig. 8. Linear sweep voltammograms at 5 mV s^{-1} for the ORR in O_2-saturated 0.50 M H_2SO_4, the current densities being referred to the (a) Pt mass (j_m, mass activity) and (b) ECSA (j_{sp}, specific activity). RDE rotation rate of 1500 rpm.

j_{sp} values at 0.9 V ($j_{sp(0.9\,V)}$) were additionally considered. These data have been listed in Table 4, revealing a clear advantage of PtCu/CH3, with E_{onset} and $E_{0.5}$ values about 45 mV more positive than those of Pt/C, also with the highest j_{sp} at 0.9 V. The other PtCu/NMCs present intermediate values between both and again, the PtCu/NMCs exhibit better catalytic activity than commercial Pt/C. Note in addition that better ORR results have been obtained using the present NMCs as compared to commercial CMK-3. In the case of the RDE experiments, the limiting currents referred to the electrode section are not expected to significantly depend on the carbon porosity. However, the carbon porosity can be responsible for the dispersion of the PtCu NPs and their accessibility to the Pt(IV) species in the further galvanic exchange. Evidence about this point is that the composition of the crystallites depended on the support (see Table 2), that corresponding to PtCu/CH3 having the smallest Cu content (10 at.%) in the synthesized NMCs. In the case of PtCu/CMK-3, the Cu content of the crystallites was too small (2 at.%) and presented the lowest activity toward the ORR. It has been shown that building up a suitable structure of the PtCu surface is essential for a good catalytic performance and that an excessive Cu content of the PtCu

Table 4
Catalytic activity data obtained from LSV for the ORR using the RDE at 1500 rpm and for the MOR without rotation.

Catalyst	ORR			MOR	
	E_{onset} / mV	$E_{0.5}$ / mV	$j_{sp(0.9\,V)}$ / mA cm_{Pt}^{-2}	$E_{0.5}$ (mV)	j_f / j_b
PtCu/CH1	934	850	26	660	1.4
PtCu/CH2	936	847	23	649	1.2
PtCu/CH3	952	878	54	644	1.1
PtCu/CH4	922	846	27	658	1.2
PtCu/CMK-3	928	829	22	727	1.8
Pt/C	909	832	14	700	0.9

crystallites was not suitable [55,56]. Therefore, it is interpreted that the final composition and surface structure of the PtCu nanoparticles was conditioned by the different textural properties of the NMCs.

The cyclic voltammograms in deaerated 1.0 M MeOH + 0.5 M H_2SO_4 to study the MOR showed the same profile (Fig. S5 in SI), with an initial current growth leading to a forward peak (f) and a reverse one (r), with respective peak current densities j_f and j_r. As examples, Fig. S5a in the SI file shows the CV profile for PtCu/CH3 and Fig. S5b that of Pt/C. The j_f/j_r ratio has been taken in previous reports as a measure of the catalyst poisoning by the intermediates generated during the MeOH oxidation, the oxidation of such intermediates being easier in the forward scan as the j_f/j_r ratio increases [57]. As shown in Fig. S5 and Table 4, $j_f > j_r$ for all the PtCu catalysts and, conversely, $j_f < j_r$ for commercial Pt/C. However, this interpretation has been criticized sometimes because in situ surface-enhanced infrared measurements during the methanol oxidation on Pt showed that the forward and backward peaks shared the same origin, i.e. the oxidation of freshly chemisorbed $MeOH_{ads}$ species [17, 58]. Normalization with respect to the Pt mass and/or to the ECSA was then suggested as the best way of comparing the corresponding catalysts activities. This is done in Fig. 9, which compares the linear sweep voltammograms for the MOR considering the mass (j_m) and specific activities (j_{sp}).

It is shown in Fig. 9a that the mass activities of PtCu/CH2 and PtCu/CH3 competed with those of commercial Pt/C. Note, however, that this may arise from the smaller size and lower aggregation of the Pt NPs in the latter, since according to the data listed in Table 3 and despite using the same Pt loading on the GCE, the ECSAs of the PtCu/NMCs were about four times smaller. Therefore, the catalytic activities would be better represented by the specific values referred to the ECSAs (j_{sp}), shown in Fig. 9b. For this comparison, the potentials corresponding to a j_{sp} = 0.1 mA cm^{-2} ($E_{0.1}$) were selected as representative of the activity of the different catalysts, those being less positive presenting a smaller overpotential and thus, a higher activity. These results are also listed in Table 4, where it is shown that the best values were obtained for PtCu/CH3, which were 56 mV more negative than that of Pt/C. The highest specific current density was also obtained for PtCu/CH3, with a value of

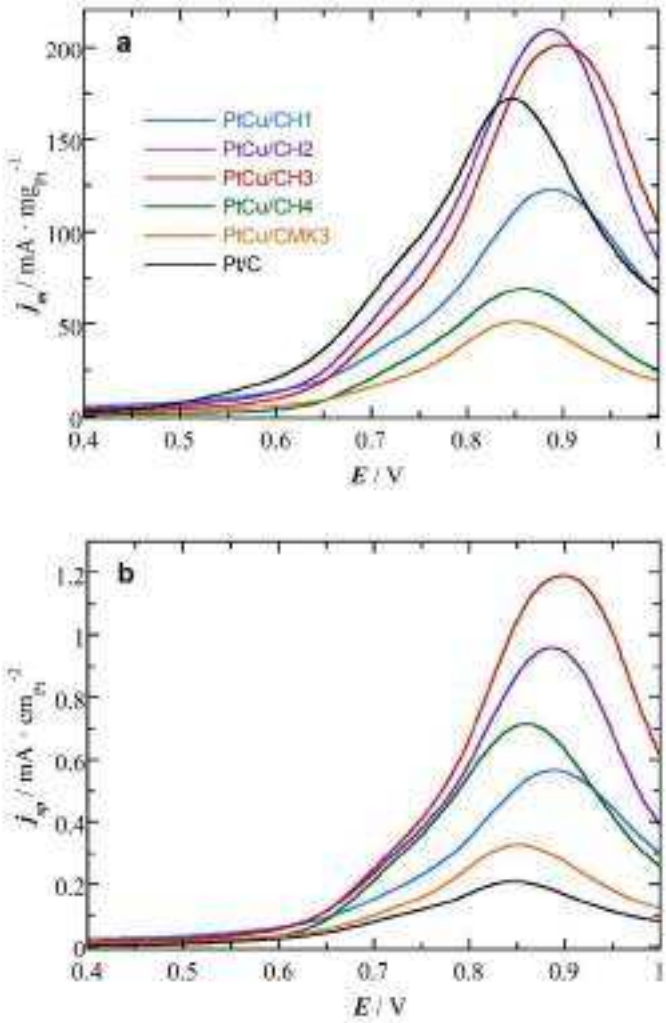

Fig. 9. Linear sweep of the cyclic voltammograms for the MOR in deaerated 1.0 M MeOH + 0.5 M H_2SO_4 solution corresponding to the (a) mass activities (j_m) and (b) specific activities (j_{sp}). Scan rate of 20 mV s^{-1}.

1.2 mA cm^{-2} at a peak potential of 0.90 V. The PtCu catalysts are more active for the MOR than commercial Pt/C, and there is a progress of activities, attributable, as indicated above, to the different surface structures of the PtCu nanoparticles produced on the different support textures. Note in addition, that the Pt loading of about 20 μg_{Pt} cm^{-2} has been fixed in this work for comparing the activity of the different catalysts. Changing such Pt load could plausibly enhance the obtained results, as shown in previous literature, but this aspect is out of the scope of the present paper [30].

Overall, the electrochemical tests showed that the synthesized PtCu/NMCs were more active than Pt/C in front of the CO stripping, the ORR and the MOR, and this can be attributed to the particular electronic structure of Pt in the PtCu alloy nanoparticles built up during the preparation procedure. There is, however, some dependence of the PtCu/NMC activity on the PtCu alloy nanoparticle composition. This can be due to the formation of different alloy surface structures resulting from the different textural properties of the NMCs, which could condition the transport of the species. The best activity results were obtained with PtCu/CH3, what could be assigned to the best compromise between meso and microporosity of CH3 with respect to the other NMCs.

4. Conclusions

PtCu alloy catalysts were supported on chitosan-derived N-doped mesoporous carbons (NMCs), with the double goal of reducing the need of Pt and investigating the viability of inexpensive greener carbons, eventually enhancing the sustainability of low-temperature fuel cells. Carbon supports with differently textural properties were synthesized from easily available chitosan present in disposable biomass, using the cheap silica P20 normally employed for chromatographic separation as hard templating agent. BET specific surface areas over 1000 m^2 g^{-1} were attained, with different mesopore-to-micropore volume ratios. This ratio was 6.1 for the NMC activated with H_2SO_4 (CH3), exhibiting better textural properties than the ordered mesoporous carbon CMK-3 and Vulcan® XC-72. The nitrogen content of the NMCs ranged between 5.2 and 7.4 wt.% and the XPS results showed about 19% atoms of carbon in C—N bonds, and pyridinic to pyrrolic forms with ratios in the range 40–50%. The Raman analyses indicated the formation of rather defective graphite lattices.

The supported PtCu catalysts for electrochemical tests were prepared sequentially in two steps. The dispersed PtCu nanocrystallites were identified by means of XRD, with compositions in the range 83–90 at.% Pt and mean size between 3.1 and 4.7 nm. The PtCu/NMCs presented CO oxidation peaks placed about 80 mV more negative than commercial Pt/C, thus indicating their higher CO tolerance. The specific activities (current densities relative to the ECSA) for the ORR and the MOR were also higher than those of commercial Pt/C and PtCu supported on commercial ordered mesoporous carbon CMK-3, PtCu/CH3 being the most active. The ECSA of the PtCu/NMCs was smaller than that of Pt/C and decreased with the microporosity of the NMCs, which was assigned to a higher nanoparticle aggregation, favoured by the microporosity increase. A soft dependence of the crystallite composition with the textural properties of the NMCs was also found, the Pt:Cu at.% ratio being 90:10, with the lowest Cu content, for PtCu/CH3. It is concluded that the compromise between meso and microporosity conditioned, through the mass transport of species, the surface structure of the final PtCu nanoparticles on the carbon supports.

Supporting information (SI) contains 5 figures and 1 table on: TEM micrographs of the synthesized mesoporous carbons; N_2 physisorption analyses; Linear sweep voltammograms for the ORR; Cyclic voltammograms for the MOR.

CRediT authorship contribution statement

Julia García-Cardona: Investigation, Formal analysis, Writing – original draft. **Ignasi Sirés:** Validation, Resources, Data curation, Writing – review & editing, Project administration, Funding acquisition. **Marco Mazzucato:** Investigation, Formal analysis, Writing – original draft. **Riccardo Brandiele:** Investigation, Formal analysis, Writing – original draft. **Enric Brillas:** Validation, Data curation. **Francisco Alcaide:** Conceptualization, Methodology. **Christian Durante:** Conceptualization, Methodology, Resources, Data curation, Writing – review & editing, Visualization, Supervision, Project administration, Funding acquisition. **Pere L. Cabot:** Conceptualization, Methodology, Resources, Writing – review & editing, Visualization, Supervision, Project administration.

Declaration of Competing Interest

The authors declare that they have no known competing financial interests or personal relationships that could have appeared to influence the work reported in this paper.

Data availability

Data will be made available on request.

Acknowledgments

The authors kindly acknowledge the University of Padova for the financial support through a P-DISC Grant project (Project No. P-DISC#03NEsiS_BIRD2021-UNIPD), funding from project PID2019-109291RB-I00 (MCIN/AEI/10.13039/501100011033, Spain) and the PhD scholarship 2020FISDU 00005 awarded to J.G.-C (AGAUR, *Generalitat de Catalunya*, Spain). TEM and XRD analyses from the *Centres Científics i Tecnològics de la UB* (CCiT-UB) are also acknowledged.

Supplementary materials

Supplementary material associated with this article can be found, in the online version, at doi:10.1016/j.electacta.2023.141911.

References

[1] X. Ren, Q. Lv, L. Liu, B. Liu, Y. Wang, A. Liu, G. Wu, Current progress of Pt and Pt-based electrocatalysts used for fuel cells, Sustain. Energy Fuels 4 (2020) 15, https://doi.org/10.1039/c9se00536a.

[2] E.H. Majlan, D. Rohendi, W.R.W. Daud, T. Husaini, M.A. Haque, Electrode for proton exchange membrane fuel cells: a review, Renew. Sustain. Energy Rev. 89 (2018) 117, https://doi.org/10.1016/j.rser.2018.03.007.

[3] A.B. Stambouli, E. Traversa, Fuel cells, an alternative to standard sources of energy, Renew. Sustain. Energy Rev. 6 (2002) 295, https://doi.org/10.1016/S1364-0321(01)00010-6.

[4] E. Antolini, Formation of carbon-supported PtM alloys for low temperature fuel cells: a review, Mater. Chem. Phys. 78 (2003) 563, https://doi.org/10.1016/S0254-0584(02)00369-9.

[5] Z. Liu, X.Y. Ling, X. Su, J.Y. Lee, Carbon-supported Pt and PtRu nanoparticles as catalysts for a direct methanol fuel cell, J. Phys. Chem. B 108 (2004) 8234, https://doi.org/10.1021/jp0494128.

[6] A. Velázquez-Palenzuela, E. Brillas, C. Arias, F. Centellas, J.A. Garrido, R. M. Rodríguez, P.L. Cabot, Structural analysis of carbon-supported Ru-decorated Pt nanoparticles synthesized using forced deposition and catalytic performance toward CO, methanol, and ethanol electro-oxidation, J. Catal. 298 (2013) 132, https://doi.org/10.1016/j.jcat.2012.11.008.

[7] M. Saleheen, J.P. Dellet, An extensive study about influence of the carbon support morphology on Pt activity and stability for oxygen reduction reaction, Appl. Catal. B 231 (2018) 62, https://doi.org/10.1016/j.apcatb.2018.02.059.

[8] Y. Song, J. Hwang, J.S. Chung, Characterization and activity correlations of Pt bimetallic catalysts for low temperature fuel cells, Int. J. Hydrogen Energy 34 (2009) 4007, https://doi.org/10.1016/j.ijhydene.2009.02.089.

[9] G. Cebollero-Manrique, A. Velázquez-Palenzuela, E. Brillas, F. Centellas, J. A. Garrido, R.M. Rodríguez, P.L. Cabot, Electrochemical synthesis and characterization of carbon-supported Pt and Pt-Ru nanoparticles with Cu cores for CO and methanol oxidation in polymer electrolyte fuel cells, Int. J. Hydrogen Energy 39 (2014) 12859, https://doi.org/10.1016/j.ijhydene.2014.06.080.

[10] E. Antolini, J.A.R. Van Veen, T.O. Maniwaagaa, S. Colelli, E.J.M. Hensen, F. A. de Bruijn, Oxygen reduction reaction (ORR) activity and durability of carbon-supported PtM (Co, Ni, Cu) alloys: influence of particle size and non-noble metals

Appl. Catal. B 515 (2012) 111–112, https://doi.org/10.1016/j.apcatb.2011.11.005.
[11] B. Geboes, I. Mintsouli, B. Wouters, J. Georgieva, A. Sakanoglou, S. Sotiropoulos, E. Valova, S. Armyanov, A. Hubin, T. Breugelmans, Surface and electrochemical characterization of a Pt–Co/C nano-structured electrocatalyst, prepared by galvanic displacement, Appl. Catal. B 150–151 (2014) 249, https://doi.org/10.1016/j.apcatb.2013.12.031.
[12] J. Georgieva, E. Valova, I. Mintsouli, S. Sotiropoulos, S. Armyanov, A. Sakanoglou, A. Hubin, O. Steenhaut, J. Dille, Carbon-supported Pt/(Ir) electrocatalysts for methanol oxidation prepared by (Ir) electroless deposition and its galvanic replacement by Pt, J. Appl. Electrochem. 44 (2014) 215, https://doi.org/10.1007/s10800-013-0618-0.
[13] J. Maya-Cornejo, R. Carrera-Cerritos, D. Sebastián, J. Ledesma-García, L. G. Arriaga, A.S. Aricò, V. Baglio, PtCu catalyst for the electro-oxidation of ethanol in an alkaline direct alcohol fuel cell, Int. J. Hydrogen Energy 42 (2017) 27910, https://doi.org/10.1016/j.ijhydene.2017.07.226.
[14] A. Sarkar, A. Manthiram, Synthesis of Pt@Co core-shell nanoparticles by galvanic displacement of Co by Pt^{2+} ions and their application as electrocatalysts for oxygen reduction reaction in fuel cells, J. Phys. Chem. C 114 (2010) 4725, https://doi.org/10.1021/jp9006013.
[15] E.J. Coleman, A.C. Co, Galvanic displacement of Pt on nanoporous copper: an alternative synthetic route for obtaining robust and reliable oxygen reduction activity, J. Catal. 316 (2014) 191, https://doi.org/10.1016/j.jcat.2014.05.012.
[16] H.Y. Park, J.H. Park, P. Kim, S.J. Yoo, Hollow $PtCu_3$@Pt core@shell nanoparticles with ordered intermetallic cores as efficient and durable oxygen reduction reaction electrocatalysts, Appl. Catal. B 215 (2016) 84, https://doi.org/10.1016/j.apcatb.2017.11.053.
[17] Y. Zhao, Y. Wu, J. Liu, P. Wang, Dependent relationship between quantitative lattice contraction and enhanced oxygen reduction activity over Pt-Co alloy catalysts, ACS Appl. Mater. Interfaces 9 (2017) 35740, https://doi.org/10.1021/acsami.7b08437.
[18] J. García-Cardona, I. Sirés, F. Alcaide, E. Brillas, F. Centellas, P.L. Cabot, Electrochemical performance of carbon-supported Pt(Co) electrocatalysts for low-temperature fuel cells, Int. J. Hydrogen Energy 45 (2020) 20582, https://doi.org/10.1016/j.ijhydene.2020.02.034.
[19] V. Vassiliadou, A. Alekseenko, V. Guterman, A. Nechitailov, N. Glebova, A. Tomasov, G. Spiridonova, S. Belenov, N. Zolotina, O. Safronenko, Effective platinum-copper catalysts for methanol oxidation and oxygen reduction in proton-exchange membrane fuel cell, Nanomaterials 10 (2020) 742, https://doi.org/10.3390/nano10040742.
[20] S. Sanad, Y.S. Loh, W.Y. Wong, T.K. Lee, J. Sasano, S.T. Chong, M.R.W. Daud, Carbon and non-carbon support materials for platinum-based catalysts in fuel cells, Int. J. Hydrogen Energy 43 (2018) 7823, https://doi.org/10.1016/j.ijhydene.2018.02.154.
[21] E. Antolini, Carbon supports for low-temperature fuel cell catalysts, Appl. Catal. B 88 (2009) 1, https://doi.org/10.1016/j.apcatb.2008.09.038.
[22] A.L. Dicks, The role of carbon in fuel cells, J. Power Sources 156 (2006) 128, https://doi.org/10.1016/j.jpowsour.2006.02.057.
[23] F. Rodriguez-Reinoso, The role of carbon materials in heterogeneous catalysis, Carbon N Y 36 (1998) 159, https://doi.org/10.1016/S0008-6223(97)00170-5.
[24] S. Shahgaldi, J. Hamelin, Improved carbon nanostructures as a novel catalyst support in the cathode side of PEMFC: a critical review, Carbon N Y 94 (2015) 705, https://doi.org/10.1016/j.carbon.2015.07.015.
[25] S. Sharma, B.G. Pollet, Support materials for PEMFC and DMFC electrocatalysts—a review, J. Power Sources 208 (2012) 96, https://doi.org/10.1016/j.jpowsour.2012.02.018.
[26] I.M. Rees, C.H. Paik, T.D. Jarvi, Electrocatalytic corrosion of carbon support in PEMFC cathodes, Electrochem. Solid State Lett. 7 (2004) B, https://doi.org/10.1149/1.1810425.
[27] Y. Shao, G. Yin, Y. Gao, Understanding and approaches for the durability issues of Pt-based catalysts for PEM fuel cell, J. Power Sources 171 (2007) 558, https://doi.org/10.1016/j.jpowsour.2007.07.009.
[28] M. Esteria, J.L. Figueiredo, Nanostructured mesoporous carbons: Tuning texture and surface chemistry, Carbon N Y 108 (2016) 79, https://doi.org/10.1016/j.carbon.2016.05.066.
[29] W. Li, J. Liu, D. Zhao, Mesoporous materials for energy conversion and storage devices, Nat. Rev. Mater. 1 (2016) 16023, https://doi.org/10.1038/natrevmats.2016.23.
[30] S. Günay, F.Ç. Gökbir, Synthesis of OMC supported Pt catalysts and the effect of the metal loading technique on their PEM fuel cell performances, Chem. Eng. Commun. 207 (2020) 961, https://doi.org/10.1080/00986445.2019.1629869.
[31] G. Alvarez, F. Alcaide, O. Miguel, E. Cabello, M.J. Lázaro, J.J. Quintana, J. C. Calderón, E. Pastor, Technical electrodes catalyzed with PdPt on mesoporous ordered carbons for liquid direct methanol fuel cells, J. Solid State Electrochem. 14 (2010) 1027, https://doi.org/10.1007/s10008-009-0915-3.
[32] J.R.C. Salgado, F. Alcaide, G. Álvarez, L. Calvillo, M.J. Lázaro, E. Pastor, Pt-Ru Electrocatalysts supported on ordered mesoporous carbon for direct methanol fuel cell, J. Power Sources 195 (2010) 4022, https://doi.org/10.1016/j.jpowsour.2010.01.001.
[33] L. Calvillo, M. Gangeri, S. Perathoner, G. Centi, R. Moliner, M.J. Lázaro, Synthesis and performance of platinum supported on ordered mesoporous carbons as catalyst for PEM fuel cells: effect of the surface chemistry of the support, Int. J. Hydrogen Energy 36 (2011) 8805, https://doi.org/10.1016/j.ijhydene.2011.03.033.
[34] G. Gupta, D.A. Slanac, P. Kumar, J.D. Wiggins-Camacho, X. Wang, S. Swinnea, K. L. More, S. Dai, R.J. Stevenson, K.P. Johnston, Highly stable and active Pt-Co oxygen reduction electrocatalysts based on mesoporous graphitic carbon supports, Chem. Mater. 21 (2009) 4515, https://doi.org/10.1021/cm901201e.
[35] E.P. Ambrosio, C. Francia, M. Manzoli, N. Penazzi, P. Spinelli, Platinum catalyst supported on mesoporous carbon for PEMFC, Int. J. Hydrogen Energy 33 (2008) 3142, https://doi.org/10.1016/j.ijhydene.2008.03.045.
[36] J. García-Cardona, F. Alcaide, E. Brillas, I. Sirés, P.L. Cabot, Tuning PtCu nanoparticles supported on highly ordered mesoporous carbons CMK3 and CMK8 as catalysts for low-temperature fuel cells, Catalysts 11 (2021) 724, https://doi.org/10.3390/catal11060724.
[37] X. Long, F. Yin, Y. Lei, K. Wang, Z. Chen, Methanol electro-oxidation on Cu@Pt/C core-shell catalysts derived from Cu MOF, Appl. Catal. B 260 (2020), 118187, https://doi.org/10.1016/j.apcatb.2019.118187.
[38] E. Brandiele, C. Durante, M. Zerbetto, N. Vicentini, T. Sounala, D. Badocco, P. Pastore, G.A. Rizzi, A.A. Isse, A. Gennaro, Probing the correlation between Pt support interaction and oxygen reduction reaction activity in mesoporous carbon materials modified with Pt/N active sites, Electrochim. Acta 277 (2018) 307, https://doi.org/10.1016/j.electacta.2018.04.162.
[39] E. Brandiele, F. Poli, L. Picelli, F. Pilot, G.A. Rizzi, F. Soavi, C. Durante, Nitrogen doped mesoporous carbon electrodes prepared from templating propylamine-functionalized silica, ChemElectroChem 92 (2020) 422, https://doi.org/10.1002/celc.202000694.
[40] E. Brandiele, M. Zerbetto, M.C. Dalconi, G.A. Rizzi, A.A. Isse, C. Durante, A. Gennaro, Mesoporous carbon with different density of thiophenic-like functional groups and their effect on oxygen reduction, ChemSusChem 12 (2019) 4229, https://doi.org/10.1002/cssc.201901568.
[41] E. Brandiele, L. Picelli, B. Pilot, V. Causin, A. Marinoni, G.A. Rizzi, A.A. Isse, C. Durante, A. Gennaro, Nitrogen and sulfur doped mesoporous carbons, prepared from templating silica, as interesting material for supercapacitors, Chemistryselect 2 (2017) 7082, https://doi.org/10.1002/slct.201701404.
[42] G. Daniel, Y. Zhang, S. Lanzalaco, E. Brandiele, T. Sounala, G. Granozzi, A. Wang, E. Brillas, I. Sirés, C. Durante, Chitosan-derived nitrogen-doped carbon electrocatalyst for a sustainable upgrade of oxygen reduction to hydrogen peroxide in UV-assisted electro-Fenton water treatment, ACS Sustain. Chem. Eng. 9 (2020) 14425, https://doi.org/10.1021/acssuschemeng.1c05268.
[43] G. Daniel, T. Kosmala, F. Brombin, M. Mazzucato, A. Facchin, M.C. Dalconi, D. Badocco, P. Pastore, G. Granozzi, C. Durante, Highly graphitized Fe-N-C electrocatalysts prepared from chitosan hydrogel frameworks, Catalysts 11 (2021) 390, https://doi.org/10.3390/catal11030390.
[44] H. El Knidri, R. Belaabed, A. Addaou, A. Laajeb, A. Lahsini, Extraction, chemical modification and characterization of chitin and chitosan, Int. J. Biol. Macromol. 120 (2018) 1181, https://doi.org/10.1016/j.ijbiomac.2018.08.168.
[45] J. Solla-Gullón, V. Montiel, A. Aldaz, J. Clavilier, Synthesis and electrochemical decontamination of platinum–palladium nanoparticles prepared by water-in-oil microemulsion, J. Electrochem. Soc. 150 (2003) 104, https://doi.org/10.1149/1.1534600.
[46] A. Salzsky, H. Muckenhuber, H. Grothe, H. Niessner, D. Fischl, Raman microspectroscopy of soot and related carbonaceous materials: spectral analysis and structural information, Carbon N Y 43 (2005) 1731, https://doi.org/10.1016/j.carbon.2005.02.018.
[47] O. Beyssac, B. Goffé, J.P. Petitet, E. Froigneux, M. Moreux, J.N. Rouzaud, On the characterization of disordered and heterogeneous carbonaceous materials by Raman spectroscopy, Spectrochim. Acta A Mol. Biomol. Spectrosc. 59 (2003) 2267, https://doi.org/10.1016/S1386-1425(03)00070-2.
[48] M. Mazzucato, G. Daniel, A. Mehmood, T. Sounala, G. Granozzi, A. Ruocchi, C. Durante, Effects of the induced micro- and nano-porosity on the single site density and turn over frequency of Fe-N-C carbon electrodes for the oxygen reduction reaction, Appl. Catal. B 291 (2021), 120068, https://doi.org/10.1016/j.apcatb.2021.120068.
[49] G. Daniel, M. Mazzucato, E. Brandiele, L. De Lazzari, D. Badocco, P. Pastore, T. Sounala, G. Granozzi, C. Durante, Boron doping versus hierarchical pore structure: the dominating effect on the Fe-N-C site density, activity, and selectivity in oxygen reduction reaction electrocatalysis, ACS Appl. Mater. Interfaces 13 (2021) 42690, https://doi.org/10.1021/acsami.1c09459.
[50] Powder Diffraction File (2016): International Centre for Diffraction Data 0CDD), 12 Campus Boulevard., Newtow Square, Pennsylvania 19073-3273, USA.
[51] V.V. Pryadchenko, S.V. Belenov, D.B. Shrimpf, V.V. Srabionyan, L.A. Avakyan, V. A. Volochaev, A.S. Mikheykin, K.E. Ivlyeyon, I. Zizak, V.E. Guterman, L.A. Bugaev, Effect of thermal treatment on the atomic structure and electrochemical characteristics of bimetallic PtCu core-shell nanoparticles in PtCu/C electrocatalysts, J. Phys. Chem. C 122 (2018) 17299, https://doi.org/10.1021/acs.jpcc.8b02006.
[52] A.A. Alekseenko, S.V. Belenov, V.A. Menshikov, V.E. Guterman, Pt(Cu)/C electrocatalysts with low platinum content, Russ. J. Electrochem. 54 (2018) 415, https://doi.org/10.1134/S1023193518050026.
[53] J.R. Ritchie, J.K. Nørskov, M.A. Barteau, J.G. Chen, Modification of the surface electronic and chemical properties of Pt(111) by subsurface 3d transition metals, J. Chem. Phys. 120 (2004) 10240, https://doi.org/10.1063/1.1737365.
[54] I. Espuelas, E. Brillas, F. Centellas, J.A. Garrido, R.M. Rodríguez, C. Arias, P. L. Cabot, Structure and electrocatalytic performance of carbon-supported platinum nanoparticles, J. Power Sources 196 (2009) 201, https://doi.org/10.1016/j.jpowsour.2009.10.075.
[55] A. Pavlets, A. Alekseenko, V. Menshchikov, S. Belenov, V. Volochaev, L. Pavlov, O. Safronenko, V.E. Guterman, Influence of electrochemical postreactor conditions of PtCu/C alloy electrocatalyst on its activity, Nanomaterials 11 (2021) 1499, https://doi.org/10.3390/nano11061499.

[56] L. Vega, J. García-Cardona, F. Viñes, P.L. Cabot, E.M. Sánchez, Nanostructuring determines poisoning: tailoring CO adsorption on PtCu bimetallic nanoparticles, Mater. Adv. 3 (2022) 9199, 10.1007/s10800-006-9202-0.
[57] Z. Liu, L. Hong, Electrochemical characterization of the electrooxidation of methanol, ethanol and formic acid on Pt/C and PtRu/C electrodes, J. Appl. Electrochem. 37 (2007) 585, https://doi.org/10.1007/s10800-006-9202-0.
[58] A. Holewinski-Duffy, D.J. Chen, S.G. Sun, Y.J. Tong, Origin of the current peak of negative scan in the cyclic voltammetry of methanol electro-oxidation on Pt-based electrocatalysts: a revisit to the current ratio criterion, J. Mater. Chem. 22 (2012) 5265, https://doi.org/10.1039/C2JM15942K.

SUPPORTING INFORMATION

On the viability of chitosan-derived mesoporous carbons as supports for PtCu electrocatalysts in PEMFC

Julia Garcia-Cardona,[†] Ignasi Sirés,[†] Marco Mazzucato,[‡] Riccardo Brandiele,[‡] Enric Brillas,[†] Francisco Alcaide,[†,§] Christian Durante*,[‡], Pere L. Cabot**,[†]

[†] *Laboratori d'Electroquímica dels Materials i del Medi Ambient, Departament de Química Física, Facultat de Química, Universitat de Barcelona, Martí i Franquès 1-11, 08028 Barcelona, Spain*

[‡] *Department of Chemical Sciences, University of Padua, Via Marzolo 1, 35131 Padova, Italy*

[§] *CIDETEC, Basque Research and Technology Alliance (BRTA), P°. Miramón, 196, 20014 Donostia-San Sebastián, Spain (permanent address)*

* Corresponding author: Tel.: +39 0498275112; Fax: +39 0498275829.
E-mail address: christian.durante@unipd.it (C. Durante)

** Corresponding author: Tel.: +34 934039236; Fax: +34 934021231.
E-mail address: p.cabot@ub.edu (P.L. Cabot)

This document includes 5 figures and 2 tables.

TEM observation of the synthesized mesoporous carbons

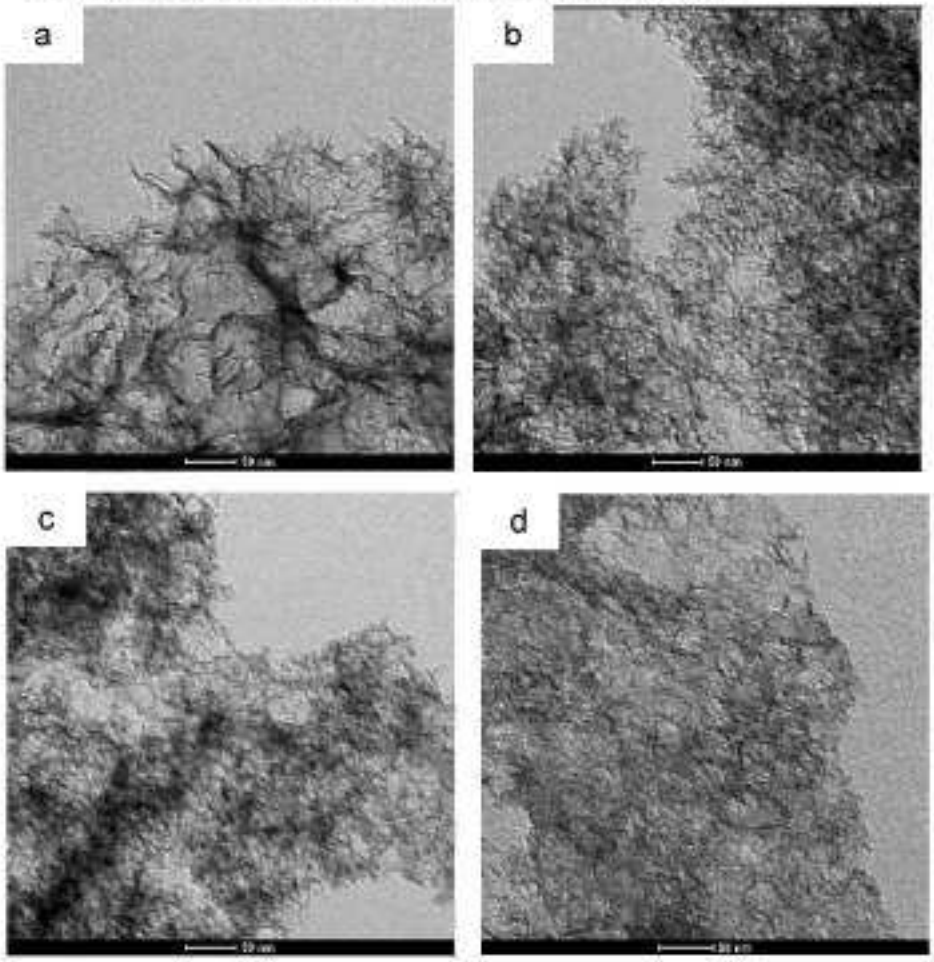

Figure S1. TEM images of the mesoporous carbons synthesized from chitosan. (a) CH1; (b) CH2; (c) CH3; and (d) CH4.

N_2 physisorption analyses

The physisorption analysis to measure the specific surface area and the pore size distribution (PSD) was carried out at 77.3 K on a Micromeritics ASAP 2020 Plus instrument. The adsorption isotherm for CMK-3 mesoporous carbon is shown in Figure S2a. Overall, the isotherm resembles a hybrid II/IV Type with H4 hysteresis which coupled with initial uptake, thus suggesting a double nature of material, with both micro and mesopores, and a certain component of macropore/larger mesopores. QSDFT deconvolution was obtained using the general Slit/Cylindrical/Spherical adsorption model, which gave a good fit of experimental data (Figure S2b). The specific surface area S_{BET} was determined using the Brunauer-Emmet-Teller (BET) model. QSDFT model allowed determining the specific surface area and volume of micropores (S_μ and V_μ), those of mesopores (S_{meso} and V_{meso}) and the overall specific surface area and volume of the pores ($S_{0.3-10nm}$ and $V_{0.3-10nm}$). Gurvich rule was applied to obtain the total pore volume V_{tot}.

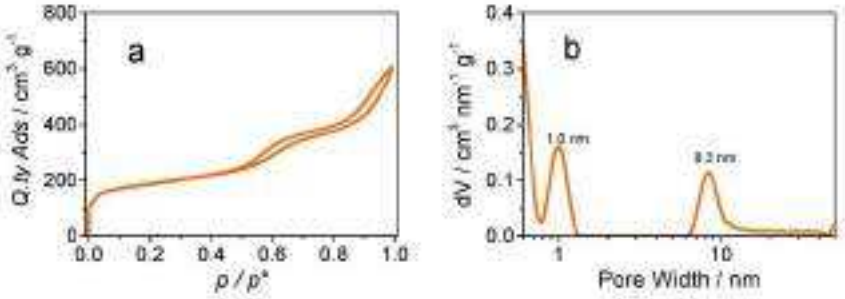

Figure S2. (a) Isotherm for N_2 physisorption and (b) PSD derived from QSDFT analysis for CMK-3.

Table S1 lists the data derived from the isotherm analysis of CMK-3 and shows a good content of micropores and mesopores. QSDFT gave a micropore volume of 0.142 $cm^3\ g^{-1}$ peaked at 1 nm, which resulted in a micropore surface area of 456 $m^2\ g^{-1}$. Mesopores were instead peaked at 8.3 nm for a volume of 0.638 $cm^3\ g^{-1}$ and a surface area of 294 $m^2\ g^{-1}$. Gurvich rule gave a total pore volume of 0.923 $cm^3\ g^{-1}$.

The N_2 adsorption isotherm for Vulcan® XC-72 carbon is shown in Figure S3a. It has the typical shape of carbon black (like Vulcan®) and resembles Type I (presence of micropores) with a final growth due to large mesopore/macropore textures, as confirmed

by PSD (Figure S3b). The data derived from the isotherm of the Vulcan® sample have also been collected in Table S1.

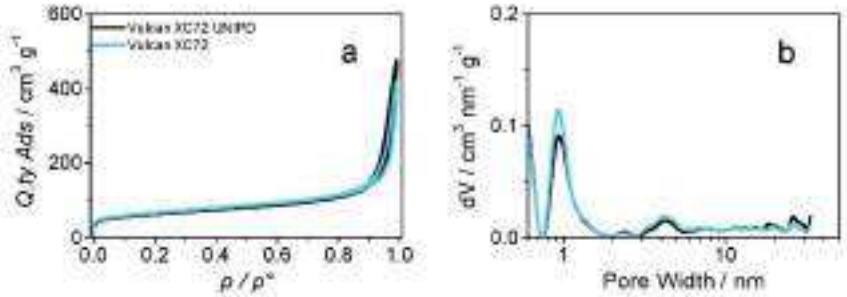

Figure S3. (a) Isotherm for N_2 physisorption and (b) PSD derived from QSDFT analysis for Vulcan® carbon. Vulcan® XC-72 carbons from two furnishers are compared, the two being almost superimposable.

Table S1. Physisorption data analysis, derived from BET model (orange), QSDFT model (green) and Gurvich rule (yellow) for CMK-3. Symbols are defined in the text.

	S_{bet}	S_{ip}	S_{micro}	$S_{0.5-10nm}$	V_{ip}	V_{micro}	$V_{0.5-10nm}$	V_{tot}
	$m^2 g^{-1}$	$m^2 g^{-1}$	$m^2 g^{-1}$	$m^2 g^{-1}$	$cm^3 g^{-1}$	$cm^3 g^{-1}$	$cm^3 g^{-1}$	$cm^3 g^{-1}$
CMK-3	620	456	294	750	0.142	0.638	0.780	0.923
XC-72	226	144	93	237	0.055	0.260	0.315	0.629

Linear sweep voltammograms for the ORR

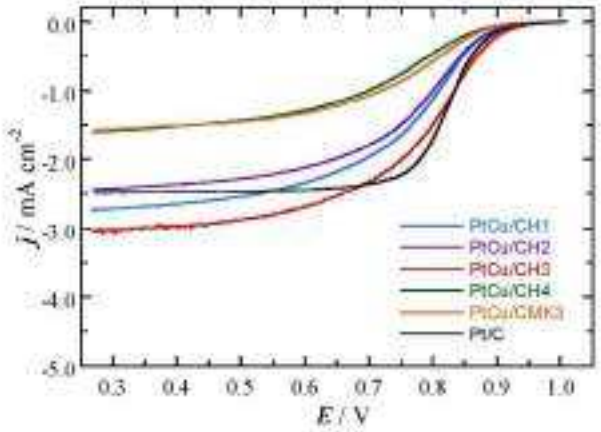

Figure S4. Linear sweep voltammograms at 5 mV s^{-1} for the ORR in O_2-saturated 0.50 M H_2SO_4, the current densities being referred to the electrode section (j). RDE rotation rate of 1500 rpm.

Cyclic voltammograms for the MOR

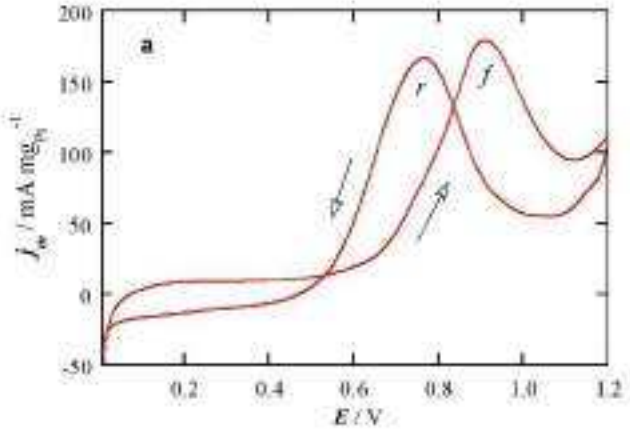

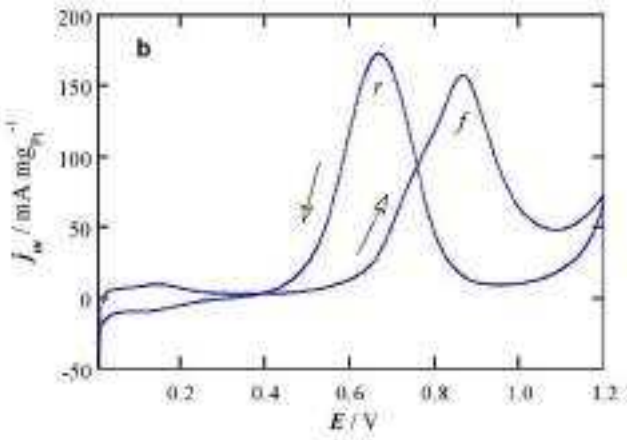

Figure S5. Cyclic voltammograms in deaerated 1.0 M MeOH + 0.5 M H_2SO_4 of (a) PtCu/CH3 and b) Pt/C. Scan rate of 20 mV s^{-1}.

5. Conclusions

Pt(Cu) and Pt(Ni) nanoparticles supported on conventional and advanced carbons were synthesised to accomplish the objectives defined in Section 2. The catalysts obtained were then characterised by means of structural and electrochemical techniques to ascertain their activity related to CO oxidation, ORR and MOR.

The synthesis of the catalysts started with the Cu or Ni deposition by different methods: reduction by HCHO in the presence of Na_2-EDTA, PVP and the carbon powder (A); reduction by $NaBH_4$ in the presence of the carbon powder (B); and reduction by $NaBH_4$ in a water-in-oil microemulsion prior to the carbon powder addition (C). After the Cu and Ni deposition, Pt was incorporated by galvanic exchange with Pt(IV) species.

Taking into account all the work performed in this thesis, the following conclusions can be drawn, organized according to the different sections presented:

1. **Pt(Cu) and Pt(Ni) supported on carbon black.**
   - Pt(Cu) and Pt(Ni) nanoparticles 2-4 nm in size with Pt-rich shells, as suggested by the CV results, supported on carbon blacks XC-72 and XC-72R, respectively, were synthesised. Pt(Cu) were prepared following methods A, B, and C, whereas the method B was applied for Pt(Ni). They presented higher CO tolerance than commercial Pt/C, their higher activity being explained by the electronic effect of the metallic core on the Pt shell. In the case of PtNi, two anodic peaks were observed in the CO oxidation, thus suggesting the presence of two distinct structural domains in the catalyst surface, probably Pt on hexagonal Ni-rich domains and on cubic Pt-rich ones.
   - Despite the fact that most of the Pt(Cu) catalysts were more tolerant to CO than commercial Pt/C, this was not the case when consisting of too small nanoparticles of about 1.5 nm. The computational study to calculate the CO adsorption energies on different sites of the nanoparticles showed that the presence of surface defects could affect the CO tolerance of the catalysts, which could be critical for too small nanoparticles, as observed in our experimental results.
   - The catalytic activity of PtNi/C for the MOR was higher than that of Pt/C. The kinetic analysis suggested that the mechanism of the MOR on the former

presented a different determining step than on the latter, related to the ligand effect of Ni on Pt, which facilitated the desorption of CO intermediates.

2. Pt(Cu) supported on carbon nanotubes and carbon nanofibers.

- The Pt(Cu) catalysts supported on CNFs, MWCNTs, and XC-72 by method B presented PtCu alloy crystallites about 3 nm in size and having a Pt-like *fcc* structure, as suggested by the slight shift of the Pt peaks with respect to pure Pt in the XRD diffractograms, complemented by TEM observations. The XPS analyses revealed that the Pt(Cu) nanoparticles were composed by a PtCu alloy core and a Pt-rich shell. The best dispersion was achieved for Pt(Cu)/CNF, with an ECSA about 70 $m^2\ g_{Pt}^{-1}$, comparable to those of Pt(Cu)/XC-72 and commercial Pt/C and PtCu/C, and higher than that for Pt(Cu)/MWCNT, with was about 40 $m^2\ g_{Pt}^{-1}$.
- The onset potentials for CO oxidation were about 50 mV more negative for Pt(Cu)/CNF, Pt(Cu)/MWCNT and Pt(Cu)XC-72 compared to commercial Pt/C and even commercial PtCu/C, indicating a higher tolerance of the synthesised catalysts due to the electronic effect of Cu on Pt. Pt(Cu)/CNF presented the best mass activity in front of the ORR followed by commercial PtCu/C, followed by Pt(Cu)/MWCNT, Pt(Cu)/XC-72, and Pt/C with comparable values, although Pt(Cu)/MWCNT presented the higher specific activity.
- The accelerated degradation tests showed that the catalysts with the highest relative stability were Pt(Cu)/MWCNT and Pt(Cu)/CNF.
- The activation of the carbonaceous materials used did not allow obtaining greater results of ECSAs or catalytic activity towards CO or ORR, although nanoparticle sizes were closer to those to commercial Pt/C, since no better distribution of the nanoparticles on the carbon support was obtained.

3. Pt(Cu) supported on commercial and chitosan-derived mesoporous carbons.

- Pt(Cu) nanoparticles of about 4–5 nm in size were successfully deposited on highly ordered commercial mesoporous carbons CMK-3 and CMK-8 using synthesis B, with ECSAs about 70 $m^2\ g_{Pt}^{-1}$. The XRD diffractograms and the XPS analyses indicated, also in this case, that the nanoparticles consisted of a PtCu alloy core and a Pt-rich shell. Although carbon activation led to somewhat smaller crystallite size, it did not enhance the particle dispersion, which resulted in lower ECSA values.

- Pt(Cu)/CMK3 and Pt(Cu)/CMK8 presented higher CO tolerance and specific activities in front of the ORR than commercial Pt/C, which were assigned, according to the XRD and XPS analyses, to the geometric and ligand effects of Cu on Pt.
- The Pt(Cu) catalysts supported on CMK-3 and CMK-8 exhibited much better stability than Pt/C in the accelerated degradation tests. However, the activation of the supports reduced the stability of the catalysts, probably due to a concomitant modification of the texture of the mesoporous channels.
- Pt(Cu) nanoparticles were dispersed on nitrogen-doped chitosan-derived mesoporous carbons with variable texture following synthesis C, resulting in crystallite sizes of about 3-5 nm. The Pt(Cu)/NMC catalysts presented ECSAs of about 20 m^2 g_{Pt}^{-1}, thus suggesting a significant aggregation of the crystallites, which were probably due to their accumulation in the mesoporous channels in the dispersion process, since the nanoparticles were synthesised prior to their dispersion on the carbon supports.
- Apart from the increased CO tolerance of Pt(Cu)/NMC with respect to commercial Pt/C observed for all the Pt(Cu) catalysts, the specific activities of the former in front of the ORR and the MOR were also higher than those of commercial Pt/C and Pt(Cu)/CMK3, the latter synthesised also by method C. The specific activities in front of the ORR and the MOR depended on the mesoporosity to microporosity ratio of the NMCs, thus suggesting that a compromise between mesoporosity and microporosity conditioned, through the mass transport of species, the surface structure of the final Pt(Cu) nanoparticles on the carbon supports.

6. References

[1] Maja, M. M.; Ayano, S. F. The impact of population growth on natural resources and farmers' capacity to adapt to climate change in low-income countries. *Earth Systems and Environment* 5 (2021) 271-283. https://doi.org/10.1007/s41748-021-00209-6

[2] Kamat, P. V. Meeting the clean energy demand: Nanostructure architectures for solar energy conversion. *The Journal of Physical Chemistry C* 111(7) (2007) 2834-2860. https://doi.org/10.1021/jp066952u

[3] Abdin, Z.; Zafaranloo, A.; Rafiee, A.; Mérida, W.; Lipiński, W.; Khalilpour, K. R. Hydrogen as an energy vector. *Renewable and Sustainable Energy Reviews* 120 (2020) 109620. https://doi.org/10.1016/j.rser.2019.109620

[4] Daud, W.; Rosli, R.; Majlan, E.; Hamid, S.; Mohamed, R; Husaini, T. PEM fuel cell system control: A review. *Renewable Energy* 113 (2017) 620-638. https://doi.org/10.1016/j.renene.2017.06.027

[5] Lucia, U. Overview on fuel cells. *Renewable and Sustainable Energy Reviews* 30 (2014) 164-169. https://doi.org/10.1016/j.rser.2013.09.025

[6] Kirubakaran, A.; Jain, S.; Nema, R. A review on fuel cell technologies and power electronic interface. *Renewable and Sustainable Energy Reviews* 13 (2009) 2430-2440. https://doi.org/10.1016/j.rser.2009.04.004

[7] Majlan, E.; Rohendi, D.; Daud, W.; Husaini, T.; Haque, M. Electrode for proton exchange membrane fuel cells: A review. *Renewable and Sustainable Energy Reviews* 89 (2018) 117-134. https://doi.org/10.1016/j.rser.2018.03.007

[8] Alcaide, F.; Cabot, P. L.; Brillas, E. Fuel cells for chemicals and energy cogeneration. *Journal of Power Sources* 153(1) (2006) 47-60. https://doi.org/10.1016/j.jpowsour.2005.11.041

[9] Mehta, V.; Cooper, J. S. Review and analysis of PEM fuel cell design and manufacturing. *Journal of Power Sources* 114(1) (2003) 32-53. https://doi.org/10.1016/s0378-7753(02)00542-6

[10] Wang, Y.; Ruiz Diaz, D. F.; Chen, K. S.; Wang, Z.; Adroher, X. C. Materials, technological status, and fundamentals of PEM fuel cells – A review. *Materials Today* 32 (2020) 178-203. https://doi.org/10.1016/j.mattod.2019.06.005

[11] Eikerling, M.; Kornyshev, A. A.; Stimming, U. Electrophysical properties of polymer electrolyte membranes: A random network model. *The Journal of Physical Chemistry B* 101(50) (1997) 10807-10820. https://doi.org/10.1021/jp972288t

[12] Kocha, S. S.; Deliang Yang, J.; Yi, J. S. Characterization of gas crossover and its implications in PEM fuel cells. *AIChE Journal* 52(5) (2006) 1916-1925. https://doi.org/10.1002/aic.10780

[13] Holdcroft, S. Fuel cell catalyst layers: A polymer science perspective. *Chemistry of Materials* 26(1) (2013) 381-393. https://doi.org/10.1021/cm401445h

[14] Park, S.; Lee, J. W.; Popov, B. N. A review of gas diffusion layer in PEM fuel cells: Materials and designs. *International Journal of Hydrogen Energy* 37(7) (2012) 5850-5865. https://doi.org/10.1016/j.ijhydene.2011.12.148

[15] Cindrella, L.; Kannan, A.; Lin, J.; Saminathan, K.; Ho, Y.; Lin, C.; Wertz, J. Gas diffusion layer for proton exchange membrane fuel cells—A review. *Journal of Power Sources* 194(1) (2009) 146-160. https://doi.org/10.1016/j.jpowsour.2009.04.005

[16] Cropper, M. A.; Geiger, S.; Jollie, D. M. Fuel cells: a survey of current developments. *Journal of Power Sources* 131(!-2) (2004) 57-61. https://doi.org/10.1016/j.jpowsour.2003.11.080

[17] Cano, Z. P.; Banham, D.; Ye, S.; Hintennach, A.; Lu, J.; Fowler, M.; Chen, Z. Batteries and fuel cells for emerging electric vehicle markets. *Nature Energy* 3(4) (2018) 279-289. https://doi.org/10.1038/s41560-018-0108-1

[18] Lewis, J. Stationary fuel cells – Insights into commercialisation. *International Journal of Hydrogen Energy* 39(36) (2014) 21896-21901. https://doi.org/10.1016/j.ijhydene.2014.05.177

[19] Edwards, P.; Kuznetsov, V.; David, W.; Brandon, N. Hydrogen and fuel cells: Towards a sustainable energy future. *Energy Policy* 36(12) (2008) 4356-4362. https://doi.org/10.1016/j.enpol.2008.09.036

[20] Kamarudin, S.; Achmad, F.; Daud, W. Overview on the application of direct methanol fuel cell (DMFC) for portable electronic devices. *International Journal of Hydrogen Energy* 34(16) (2009) 6902-6916. https://doi.org/10.1016/j.ijhydene.2009.06.013

[21] Mallick, R. K.; Thombre, S. B.; Shrivastava, N. K. Vapor feed direct methanol fuel cells (DMFCs): A review. *Renewable and Sustainable Energy Reviews* 56 (2016) 51-74. https://doi.org/10.1016/j.rser.2015.11.039

[22] Chen, C.; Yang, P.; Lee, Y.; Lin, K. Fabrication of electrocatalyst layers for direct methanol fuel cells. *Journal of Power Sources* 141(1) (2005) 24-29. https://doi.org/10.1016/j.jpowsour.2004.09.011

[23] Qi, Z.; Kaufman, A. Open circuit voltage and methanol crossover in DMFCs. J*ournal of Power Sources* 110(1) (2002) 177-185. https://doi.org/10.1016/s0378-7753(02)00268-9

[24] O'Hayre, R.; Cha, S.; Colella, W.; Prinz, F. B. Fuel Cell Fundamentals. Chapter 2: Fuel Cell Thermodynamics, pp. 25-76. Wiley, 3rd Ed., 2016.

[25] EG&G Technical Services, Inc. Fuel Cell Handbook. U.S. Department of Energy, 7th Ed., 2016.

[26] Srinivasan, S. Fuel Cells: From Fundamentals to Applications. Springer Publishing, 2006.

[27] Bard, A. J.; Faulkner, L. R. Electrochemical Methods: Fundamentals and Applications. Wiley, 2000.

[28] Vasquez, L. O. Fuel Cell Research Trends. MacMillan Publishers, 2007.

[29] Jerkiewicz, G. Hydrogen sorption ATIN electrodes. *Progress in Surface Science* 57(2) (1998) 137-186. https://doi.org/10.1016/s0079-6816(98)00015-x

[30] Oliveira, A. M.; Beswick, R. R.; Yan, Y. A green hydrogen economy for a renewable energy society. *Current Opinion in Chemical Engineering* 33 (2021) 100701. https://doi.org/10.1016/j.coche.2021.100701

[31] Maeda, N.; Matsushima, T.; Kotobuki, M.; Miyao, T.; Uchida, H.; Yamashita, H.; Watanabe, M. H_2O-tolerant monolithic catalysts for preferential oxidation of carbon monoxide in the presence of hydrogen. *Applied Catalysis A: General* 370(1-2) (2009) 50-53. https://doi.org/10.1016/j.apcata.2009.09.010

[32] Aizawa, H.; Tsuneyuki, S. First-principles study of CO bonding to Pt(111): Validity of the Blyholder model. *Surface Science* 399(2-3) (1998) L364-L370. https://doi.org/10.1016/s0039-6028(98)00042-9

[33] Wasmus, S.; Küver, A. Methanol oxidation and direct methanol fuel cells: a selective review. *Journal of Electroanalytical Chemistry* 461(!-2) (1999) 14-31. https://doi.org/10.1016/s0022-0728(98)00197-1

[34] Ramaswamy, N.; Mukerjee, S. Influence of inner- and outer-sphere electron transfer mechanisms during electrocatalysis of oxygen reduction in alkaline media. *The Journal of Physical Chemistry C* 115(36) (2011) 18015-18026. https://doi.org/10.1021/jp204680p

[35] Ge, X.; Sumboja, A.; Wuu, D.; An, T.; Li, B.; Goh, F. W. T.; Hor, T. S. A.,; Zong, Y.; Liu, Z. Oxygen reduction in alkaline media: From mechanisms to recent advances of catalysts. *ACS Catalysis* 5(8) (2015) 4643-4667. https://doi.org/10.1021/acscatal.5b00524

[36] Rana, M.; Mondal, S.,; Sahoo, L.; Chatterjee, K.; Karthik, P. E.; Gautam, U. K. Emerging materials in heterogeneous electrocatalysis involving oxygen for energy harvesting. *ACS Applied Materials & Interfaces* 10(40) (2018) 33737-33767. https://doi.org/10.1021/acsami.8b09024

[37] Damjanovic, A.; Dey, A.; Bockris, J. Kinetics of oxygen evolution and dissolution on platinum electrodes. *Electrochimica Acta* 11(7) (1966) 791-814. https://doi.org/10.1016/0013-4686(66)87056-1

[38] Wroblowa, H. S.; Yen-Chi-Pan; Razumney, G. Electroreduction of oxygen. *Journal of Electroanalytical Chemistry and Interfacial Electrochemistry* 69(2) (1976) 195-201. https://doi.org/10.1016/s0022-0728(76)80250-1

[39] Zinola, C. F. Electrocatalysis: Computational, Experimental, and Industrial Aspects. Surface Science Series, Vol. 149. CRC Press, 1st Ed., 2010.

[40] Markovic, N. Surface science studies of model fuel cell electrocatalysts. *Surface Science Reports*, 45(4-6) (2002) 117-229. https://doi.org/10.1016/s0167-5729(01)00022-x

[41] Nørskov, J. K.; Rossmeisl, J.; Logadottir, A.; Lindqvist, L.; Kitchin, J. R.; Bligaard, T.; Jónsson, H. Origin of the overpotential for oxygen reduction at a fuel-cell cathode. *The Journal of Physical Chemistry B* 108(46) (2004) 17886-17892. https://doi.org/10.1021/jp047349j

[42] Fletcher, S. Tafel slopes from first principles. *Journal of Solid State Electrochemistry* 13(4) (2008) 537-549. https://doi.org/10.1007/s10008-008-0670-8

[43] Agyekum, E. B.; Ampah, J. D.; Wilberforce, T.; Afrane, S.; Nutakor, C. Research progress, trends, and current state of development on PEMFC - New insights from a bibliometric analysis and characteristics of two decades of research output. *Membranes*, 12(11) (2022) 1103. https://doi.org/10.3390/membranes12111103

[44] Lü, X.; Qu, Y.; Wang, Y.; Qin, C.; Liu, G. A comprehensive review on hybrid power system for PEMFC-HEV: Issues and strategies. *Energy Conversion and Management* 171 (2018) 1273-1291. https://doi.org/10.1016/j.enconman.2018.06.065

[45] Ren, X.; Wang, Y.; Liu, A.; Zhang, Z.; Lv, Q.; Liu, B. Current progress and performance improvement of Pt/C catalysts for fuel cells. *Journal of Materials Chemistry A* 8(46) (2020) 24284-24306. https://doi.org/10.1039/d0ta08312g

[46] Yang, Y.; Zhou, X.; Li, B.; Zhang, C. Recent progress of the gas diffusion layer in proton exchange membrane fuel cells: Material and structure designs of microporous layer. *International Journal of Hydrogen Energy* 46(5) (2021) 4259-4282. https://doi.org/10.1016/j.ijhydene.2020.10.185

[47] Guerrero Moreno, N.; Cisneros Molina, M.; Gervasio, D.; Pérez Robles, J. F. Approaches to polymer electrolyte membrane fuel cells (PEMFCs) and their cost. *Renewable and Sustainable Energy Reviews* 52 (2015) 897-906. https://doi.org/10.1016/j.rser.2015.07.157

[48] Sharma, S.; Pollet, B. G. Support materials for PEMFC and DMFC electrocatalysts—A review. *Journal of Power Sources* 208 (2012) 96-119. https://doi.org/10.1016/j.jpowsour.2012.02.011

[49] Lázaro, M. J.; Calvillo, L.; Celorrio, V.; Pardo, J. I.; Perathoner, S.; Moliner, R. Carbon Black: Production, Properties and Uses: Chapter 2: Study and application of carbon black Vulcan XC-72R in polymeric electrolyte fuel (UK ed.). Nova Science Publishers, 2011.

[50] Antolini, E. Carbon supports for low-temperature fuel cell catalysts. *Applied Catalysis B: Environmental* 88(1-2) (2009) 1-24. https://doi.org/10.1016/j.apcatb.2008.09.030

[51] Shao, Y.; Liu, J.; Wang, Y.; Lin, Y. Novel catalyst support materials for PEM fuel cells: current status and future prospects. *Journal of Materials Chemistry* 19(1) (2009) 46-59. https://doi.org/10.1039/b808370c

[52] Shao, Y.; Wang, J.; Kou, R.; Engelhard, M.; Liu, J.; Wang, Y.; Lin, Y. The corrosion of PEM fuel cell catalyst supports and its implications for developing durable catalysts. *Electrochimica Acta*, 54(11) (2009) 3109-3114. https://doi.org/10.1016/j.electacta.2008.12.001

[53] Samad, S.; Loh, K. S.; Wong, W. Y.; Lee, T. K.; Sunarso, J.; Chong, S. T.; Wan Daud, W. R. Carbon and non-carbon support materials for platinum-based catalysts in fuel cells. *International Journal of Hydrogen Energy* 43(16) (2018) 7823-7854. https://doi.org/10.1016/j.ijhydene.2018.02.154

[54] Luo, C.; Xie, H.; Wang, Q.; Luo, G.; Liu, C. A review of the application and performance of carbon nanotubes in fuel cells. *Journal of Nanomaterials* (2015) 560392. https://doi.org/10.1155/2015/560392

[55] Akbari, E.; Buntat, Z. Benefits of using carbon nanotubes in fuel cells: a review. *International Journal of Energy Research* 41(1) (2016) 92-102. https://doi.org/10.1002/er.3600

[56] Tang, S.; Sun, G.; Qi, J.; Sun, S.; Guo, J.; Xin, Q.; Haarberg, G. M. Review of new carbon materials as catalyst Supports in direct alcohol fuel cells. *Chinese Journal of Catalysis* 31(1) (2010) 12-17. https://doi.org/10.1016/s1872-2067(09)60034-6

[57] Din, I. U.; Shaharun, M. S.,; Naeem, A.; Alotaibi, M. A.; Alharthi, A. I.; Bakht, M. A.; Nasir, Q. Carbon nanofibers as potential materials for catalysts support, a mini-review on recent advances and future perspective. *Ceramics International* 46(11) (2020) 18446-18452. https://doi.org/10.1016/j.ceramint.2020.04.275

[58] Peera, S. G.; Koutavarapu, R.;Akula, S.; Asokan, A.; Moni, P.; Selvaraj, M.; Balamurugan, J.; Kim, S. O.; Liu, C.; Sahu, A. K. Carbon nanofibers as potential catalyst support for fuel cell cathodes: A review. *Energy & Fuels* 35(15) (2021) 11761-11799. https://doi.org/10.1021/acs.energyfuels.1c01439

[59] Xu, J. B.; Zhao, T. S. Mesoporous carbon with uniquely combined electrochemical and mass transport characteristics for polymer electrolyte membrane fuel cells. *RSC Advances* 3(1) (2013) 16-24. https://doi.org/10.1039/c2ra22279e

[60] Li, W.; Liu, J.; Zhao, D. Mesoporous materials for energy conversion and storage devices. *Nature Reviews Materials* 1 (2016) 6. https://doi.org/10.1038/natrevmats.2016.23

[61] Yang, Y. X.; Bourgeois, L.; Zhao, C.; Zhao, D.; Chaffee, A.; Webley, P. A. Ordered micro-porous carbon molecular sieves containing well-dispersed platinum nanoparticles for hydrogen storage. *Microporous and Mesoporous Materials* 119(1-3) (2009) 39-46. https://doi.org/10.1016/j.micromeso.2008.09.044

[62] Raghuveer, V.; Manthiram, A. Mesoporous carbons with controlled porosity as an electrocatalytic support for methanol oxidation. *Journal of The Electrochemical Society* 152(8) (2005) A1504. https://doi.org/10.1149/1.1940767

[63] Phan, T. N.; Gong, M. K.; Thangavel, R.; Lee, Y. S.; Ko, C. H. Enhanced electrochemical performance for EDLC using ordered mesoporous carbons (CMK-3 and CMK-8): Role of mesopores and mesopore structures. *Journal of Alloys and Compounds* 780 (2019) 90-97. https://doi.org/10.1016/j.jallcom.2018.11.348

[64] Suginta, W.; Khunkaewla, P.; Schulte, A. Electrochemical biosensor applications of polysaccharides chitin and chitosan. *Chemical Reviews* 113(7) (2013) 5458-5479. https://doi.org/10.1021/cr300325r

[65] Hammi, N.; Chen, S.; Dumeignil, F.; Royer, S.; El Kadib, A. Chitosan as a sustainable precursor for nitrogen-containing carbon nanomaterials: Synthesis and uses. *Materials Today Sustainability* 10 (2020) 100053. https://doi.org/10.1016/j.mtsust.2020.100053

[66] Ma, J.; Yogeshwar S. Chitosan biopolymer for fuel cell applications. *Carbohydrate Polymers* 92(2) (2013) 955-975. https://doi.org/10.1016/j.carbpol.2012.10.015

[67] Perazzolo, V.; Brandiele, R.; Durante, C.; Zerbetto, M.; Causin, V.; Rizzi, G. A.; Cerri, I.; Granozzi, G.; Gennaro, A. Density functional theory (DFT) and experimental evidences of metal–support interaction in platinum nanoparticles supported on nitrogen- and sulfur-doped mesoporous carbons: Synthesis, activity, and stability. *ACS Catalysis* 8(2) (2018) 1122–1137. https://doi.org/10.1021/acscatal.7b03942

[68] Perini, L.; Durante, C.; Favaro, M.; Perazzolo, V.; Agnoli, S.; Schneider, O.; Granozzi, G.; Gennaro, A. Metal–support interaction in platinum and palladium nanoparticles loaded on nitrogen-doped mesoporous carbon for oxygen reduction reaction. *ACS Applied Materials & Interfaces* 7(2) (2015) 1170–1179. https://doi.org/10.1021/am506916y

[69] Daniel, G.; Zhang, Y.; Lanzalaco, S.; Brombin, F.; Kosmala, T.; Granozzi, G.; Wang, A.; Brillas, E.; Sirés, I.; Durante, C. Chitosan-derived nitrogen-doped carbon electrocatalyst for a sustainable upgrade of oxygen reduction to hydrogen peroxide in UV-assisted electro-Fenton water treatment. *ACS Sustainable Chemistry & Engineering* 8(38) (2020) 14425–14440. https://doi.org/10.1021/acssuschemeng.0c04294

[70] Jiang, R.; Tung, S. O.; Tang, Z.; Li, L.; Ding, L.; Xi, X.; Liu, Y.; Zhang, L.; Zhang, J. A review of core-shell nanostructured electrocatalysts for oxygen reduction reaction. *Energy Storage Materials* 12 (2018) 260-276. https://doi.org/10.1016/j.ensm.2017.11.005

[71] Zhang, X.; Li, H.; Yang, J.; Lei, Y.;Wang, C.; Wang, J.; Tang, Y.; Mao, Z. Recent advances in Pt-based electrocatalysts for PEMFCs. *RSC Advances* 11(22) (2021) 13316-13328. https://doi.org/10.1039/d0ra05468b

[72] Corona, B.; Howard, M.; Zhang, L.; Henkelman, G. Computational screening of core@shell nanoparticles for the hydrogen evolution and oxygen reduction reactions. *The Journal of Chemical Physics* 145(24) (2016) 244708. https://doi.org/10.1063/1.4972579

[73] Caballero-Manrique, G.; Velázquez-Palenzuela, A.; Brillas, E.; Centellas, F.; Garrido, J. A.; Rodríguez, R. M.; Cabot, P. L. Electrochemical synthesis and characterization of carbon-supported Pt and Pt–Ru nanoparticles with Cu cores for CO and methanol oxidation in polymer electrolyte fuel cells. *International Journal of Hydrogen Energy* 39(24) (2014) 12859-12869. https://doi.org/10.1016/j.ijhydene.2014.06.089

[74] Caballero-Manrique, G.; Brillas, E.; Centellas, F.;Garrido, J.;Rodríguez, R.; Cabot, P. L. Electrochemical oxidation of the carbon support to synthesize Pt(Cu) and Pt-Ru(Cu) core-shell electrocatalysts for low-temperature fuel cells. *Catalysts* 5(2) (2015) 815-837. https://doi.org/10.3390/catal5020815

[75] Caballero-Manrique, G.; Nadeem, I.; Brillas, E.,; Centellas, F.; Garrido, J.; Rodríguez, R.; Cabot, P. L. Effects of the electrodeposition time in the synthesis of carbon-supported Pt(Cu) and Pt-Ru(Cu) core-shell electrocatalysts for polymer electrolye fuel cells. *Catalysts* 6(8) (2016) 125. https://doi.org/10.3390/catal6080125

[76] Mintsouli, I.; Georgieva, J.; Armyanov, S.; Valova, E.; Avdeev, G.; Hubin, A.; Steenhaut, O.; Dille, J.,; Tsiplakides, D.; Balomenou, S., Sotiropoulos, S. Pt-Cu electrocatalysts for methanol oxidation prepared by partial galvanic replacement of Cu/carbon powder precursors. *Applied Catalysis B: Environmental* 136-137 (2013) 160-167. https://doi.org/10.1016/j.apcatb.2013.01.059

[77] Geboes, B.; Mintsouli, I.; Wouters, B.; Georgieva, J.; Kakaroglou, A.; Sotiropoulos, S.; Valova, E.; Armyanov, S.; Hubin, A.; Breugelmans, T. Surface and electrochemical characterisation of a Pt-Cu/C nano-structured electrocatalyst, prepared by galvanic displacement. *Applied Catalysis B: Environmental* 150-151 (2014) 249-256. https://doi.org/10.1016/j.apcatb.2013.12.020

[78] Georgieva, J.; Valova, E.; Mintsouli, I.;Sotiropoulos, S.; Armyanov, S.; Kakaroglou, A.; Hubin, A.; Steenhaut, O.; Dille, J. Carbon-supported Pt(Cu) electrocatalysts for methanol oxidation prepared by Cu electroless deposition and its galvanic replacement by Pt. *Journal of Applied Electrochemistry* 44(2) (2013) 215-224. https://doi.org/10.1007/s10800-013-0618-2

[79] Guterman, V. E.; Belenov, S. V.; Alekseenko, A. A.; Lin, R.; Tabachkova, N. Y.; Safronenko, O. I. Activity and stability of Pt/C and Pt-Cu/C electrocatalysts. *Electrocatalysis* 9(5) (2018) 550-562. https://doi.org/10.1007/s12678-017-0451-1

[80] Pryadchenko, V. V.; Srabionyan, V. V.; Kurzin, A. A.; Bulat, N. V.; Shemet, D. B.; Avakyan, L. A.; Belenov, S. V.; Volochaev, V. A.; Zizak, I.; Guterman, V. E.; Bugaev, L. A. Bimetallic PtCu core-shell nanoparticles in PtCu/C electrocatalysts: Structural and electrochemical characterization. *Applied Catalysis A: General* 525 (2016) 226-236. https://doi.org/10.1016/j.apcata.2016.08.008

[81] Alekseenko, A. A.; Belenov, S. V.; Menshikov, V. S.; Guterman, V. E. Pt(Cu)/C electrocatalysts with low platinum content. *Russian Journal of Electrochemistry* 54(5) (2018) 415-425. https://doi.org/10.1134/s1023193518050026

[82] Alekseenko, A.; Guterman, V.; Belenov, S.; Menshikov, V.; Tabachkova, N.; Safronenko, O.; Moguchikh, E. Pt/C electrocatalysts based on the nanoparticles with the gradient structure. *International Journal of Hydrogen Energy* 43(7) (2018) 3676-3687. https://doi.org/10.1016/j.ijhydene.2017.12.143

[83] Maya-Cornejo, J.; Carrera-Cerritos, R.; Sebastián, D.; Ledesma-García, J.; Arriaga, L.; Aricò, A.; Baglio, V. PtCu catalyst for the electro-oxidation of ethanol in an alkaline direct alcohol fuel cell. *International Journal of Hydrogen Energy* 42(46) (2017) 27919-27928. https://doi.org/10.1016/j.ijhydene.2017.07.226

[84] Shao, Y.; Yin, G.; Gao, Y.; Shi, P. Durability study of Pt/C and Pt/CNTs catalysts under simulated PEM fuel cell conditions. *Journal of The Electrochemical Society* 153(6) (2006) A1093. https://doi.org/10.1149/1.2191147

[85] El-Deeb, H.; Bron, M. Microwave-assisted polyol synthesis of PtCu/carbon nanotube catalysts for electrocatalytic oxygen reduction. *Journal of Power Sources* 275 (2015) 893-900. https://doi.org/10.1016/j.jpowsour.2014.11.060

[86] Devrim, Y.; Arıca, E. D. Multi-walled carbon nanotubes decorated by platinum catalyst for high temperature PEM fuel cell. *International Journal of Hydrogen Energy* 44(34) (2019) 18951-18966. https://doi.org/10.1016/j.ijhydene.2019.01.051

[87] Gupta, G.; Slanac, D. A.; Kumar, P.; Wiggins-Camacho, J. D.; Wang, X.; Swinnea, S.; More, K. L.; Dai, S.; Stevenson, K. J.; Johnston, K. P. Highly stable and active Pt−Cu oxygen reduction electrocatalysts based on mesoporous graphitic carbon supports. *Chemistry of Materials* 21(19) (2009) 4515-4526. https://doi.org/10.1021/cm901203n

[88] Knudsen, J.; Nilekar, A. U.; Vang, R. T.; Schnadt, J.; Kunkes, E. L.; Dumesic, J. A.; Mavrikakis, M.; Besenbacher, F. A CU/PT Near-Surface alloy for Water−Gas shift catalysis. *Journal of the American Chemical Society*, 129(20) (2007) 6485–6490. https://doi.org/10.1021/ja0700855

[89] Andersson, K.; Calle-Vallejo, F.; Rossmeisl, J.; Chorkendorff, I. Adsorption-Driven surface segregation of the less reactive alloy component. *Journal of the American Chemical Society* 131(6) (2009) 2404–2407. https://doi.org/10.1021/ja8089087

[90] Bandarenka, A. S.; Varela, A. S.; Karamad, M.; Calle-Vallejo, F.; Bech, L.; Pérez-Alonso, F. J.; Rossmeisl, J.; Stephens, I. E. L.; Chorkendorff, I. Design of an Active Site towards Optimal Electrocatalysis: Overlayers, Surface Alloys and Near-Surface Alloys of Cu/Pt(111). *Angewandte Chemie* 51(47) (2012) 11845–11848. https://doi.org/10.1002/anie.201205314

[91] Stamenkovic, V. R.; Fowler, B.;Mun, B. S.; Wang, G.; Ross, P. N.; Lucas, C. A.; Marković, N. M. Improved oxygen reduction activity on $Pt_3Ni(111)$ via increased surface site availability. *Science* 315 (5811) (2007) 493-497. https://doi.org/10.1126/science.1135941

[92] Cui, C.; Gan, L.; Li, H. H.; Yu, S. H.; Heggen, M.; Strasser, P. Octahedral PtNi nanoparticle catalysts: Exceptional oxygen reduction activity by tuning the alloy particle surface composition. *Nano Letters* 12(11) (2012) 5885-5889. https://doi.org/10.1021/nl3032795

[93] Choi, S. I.; Xie, S.; Shao, M.; Odell, J. H.; Lu, N.; Peng, H. C.; Protsailo, L.; Guerrero, S.; Park, J.; Xia, X.; Wang, J.; Kim, M. J.; Xia, Y. Synthesis and characterization of 9 nm Pt–Ni octahedra with a record high activity of 3.3 A/mg Pt for the oxygen reduction reaction. *Nano Letters* 13(7) (2013) 3420-3425. https://doi.org/10.1021/nl401881z

[94] Zhang, C.; Hwang, S. Y.; Trout, A.; Peng, Z. Solid-state chemistry-enabled scalable production of octahedral Pt–Ni alloy electrocatalyst for oxygen reduction reaction. *Journal of the American Chemical Society* 136(22) (2014) 7805-7808. https://doi.org/10.1021/ja501293x

[95] Beermann, V.; Gocyla, M.; Willinger, E.; Rudi, S.; Heggen, M.; Dunin-Borkowski, R. E.; Willinger, M. G., Strasser, P. Rh-doped Pt–Ni octahedral nanoparticles: Understanding the correlation between elemental distribution, oygen Reduction reaction, and shape sability. *Nano Letters* 16(3) (2016) 1719-1725. https://doi.org/10.1021/acs.nanolett.5b04636

[96] Choi, J.; Lee, Y.; Kim, J.; Lee, H. Enhancing stability of octahedral PtNi nanoparticles for oxygen reduction reaction by halide treatment. *Journal of Power Sources* 307 (2016) 883-890. https://doi.org/10.1016/j.jpowsour.2016.01.063

[97] Antolini, E.; Salgado, J.; Gonzalez, E. Carbon supported Pt75M25 (M = Co, Ni) alloys as anode and cathode electrocatalysts for direct methanol fuel cells. *Journal of Electroanalytical Chemistry* 580(1) (2005) 145-154. https://doi.org/10.1016/j.jelechem.2005.03.023

[98] Wu, J.; Gross, A.; Yang, H. Shape and composition-controlled platinum alloy nanocrystals using carbon monoxide as reducing agent. *Nano Letters* 11(2) (2011) 798-802. https://doi.org/10.1021/nl104094p

[99] Carpenter, M. K.; Moylan, T. E.; Kukreja, R. S.;Atwan, M. H.; Tessema, M. M. Solvothermal synthesis of platinum alloy nanoparticles for oxygen reduction electrocatalysis. *Journal of the American Chemical Society* 134(20) (2012) 8535-8542. https://doi.org/10.1021/ja300756y

[100] Shen, Y.; Zhang, M. Z.; Xiao, K.; Xi, J. Synthesis of Pt, PtRh, and PtRhNi alloys supported by pristine graphene nanosheets for ethanol electrooxidation. *ChemCatChem* 6(11) (2014) 3254-3261. https://doi.org/10.1002/cctc.201402629

[101] Mohanraju, K.; Cindrella, L. One-pot surfactant-free synthesis of high surface area ternary alloys, PtMCo/C (M = Cr, Mn, Fe, Ni, Cu) with enhanced electrocatalytic activity and durability for PEM fuel cell application. *International Journal of Hydrogen Energy* 41(22) (2016) 9320-9331. https://doi.org/10.1016/j.ijhydene.2016.04.109

[102] Jiang, Q.; Jiang, L.; Hou, H.; Qi, J.; Wang, S., Sun, G. Promoting effect of Ni in PtNi bimetallic electrocatalysts for the methanol oxidation reaction in alkaline media: Experimental and density functional theory studies. *The Journal of Physical Chemistry C* 114(46) (2010) 19714-19722. https://doi.org/10.1021/jp1039755

[103] Zhou, X. W.; Zhang, R. H.; Zhou, Z. Y.; Sun, S. G. Preparation of PtNi hollow nanospheres for the electrocatalytic oxidation of methanol. *Journal of Power Sources* 196(14) (2011) 5844-5848. https://doi.org/10.1016/j.jpowsour.2011.02.088

[104] Zignani, S. C.; Baglio, V.; Sebastián, D.; Rocha, T. A.,; Gonzalez, E. R.; Aricò, A. S. Investigation of PtNi/C as methanol tolerant electrocatalyst for the oxygen reduction reaction. *Journal of Electroanalytical Chemistry* 763 (2016) 10-17. https://doi.org/10.1016/j.jelechem.2015.12.044

[105] Glüsen, A.; Dionigi, F.; Paciok, P.; Heggen, M.; Müller, M.; Gan, L.; Strasser, P.; Dunin-Borkowski, R. E.; Stolten, D. Dealloyed PtNi-core–sShell nanocatalysts enable significant lowering of Pt electrode content in direct methanol fuel cells. *ACS Catalysis* 9(5) (2019) 3764-3772. https://doi.org/10.1021/acscatal.8b04883

[106] Wang, Z. B.; Zuo, P. J.; Wang, G. J.; Du, C. Y.; Yin, G. P. Effect of Ni on PtRu/C catalyst performance for ethanol electrooxidation in acidic medium. *The Journal of Physical Chemistry C* 112(16) (2008) 6582-6587. https://doi.org/10.1021/jp800249q

[107] Ribadeneira, E.; Hoyos, B. A. Evaluation of Pt–Ru–Ni and Pt–Sn–Ni catalysts as anodes in direct ethanol fuel cells. *Journal of Power Sources* 180(1) (2008) 238-242. https://doi.org/10.1016/j.jpowsour.2008.01.084

[108] Erini, N.; Rudi, S.; Beermann, V.; Krause, P.; Yang, R.; Huang, Y.; Strasser, P. Exceptional activity of a Pt-Rh-Ni ternary nanostructured catalyst for the electrochemical oxidation of ethanol. *ChemElectroChem* 2(6) (2015) 903-908. https://doi.org/10.1002/celc.201402390

[109] Gao, F.; Zhang, Y.; Song, P.; Wang, J.; Yan, B.; Sun, Q.; Li, L.; Zhu, X.; Du, Y. Shape-control of one-dimensional PtNi nanostructures as efficient electrocatalysts for alcohol electrooxidation. *Nanoscale* 11(11) (2019) 4831-4836. https://doi.org/10.1039/c8nr09892a

[109] Puthiyapura, V. K.; Lin, W. F.; Russell, A. E.; Brett, D. J. L.; Hardacre, C. Effect of mass transport on the electrochemical oxidation of acohols over electrodeposited film and carbon-supported Pt electrodes. *Topics in Catalysis* 61(3-4) (2018) 240-253. https://doi.org/10.1007/s11244-018-0893-6

[110] Hodnik, N.; Zorko, M.; Bele, M.; Hočevar, S.; Gaberšček, M. Identical location scanning electron microscopy: A case study of electrochemical degradation of PtNi nanoparticles using a new nondestructive method. *The Journal of Physical Chemistry C* 116(40) (2012) 21326-21333. https://doi.org/10.1021/jp303831c

[111] Wang, Q.; Wang, G.; Tao, H.; Li, Z.; Han, L. Highly CO tolerant PtRu/PtNi/C catalyst for polymer electrolyte membrane fuel cell. *RSC Advance*, 7(14) (2017) 8453-8459. https://doi.org/10.1039/c6ra28198b

[112] Calvillo, L.; Lázaro, M.; García-Bordejé, E.; Moliner, R.; Cabot, P.; Esparbé, I.; Pastor, E.; Quintana, J. Platinum supported on functionalized ordered mesoporous carbon as electrocatalyst for direct methanol fuel cells. *Journal of Power Sources* 169(1) (2007) 59-64. https://doi.org/10.1016/j.jpowsour.2007.01.042

[113] Brandiele, R.; Picelli, L.; Pilot, R.; Causin, V.; Martucci, A.; Rizzi, G. A.; Isse, A. A.; Durante, C.; Gennaro, A. nitrogen and sulfur doped mesoporous carbons, prepared from templating silica, as interesting material for supercapacitors. *ChemistrySelect*, 2(24) (2017) 7082-7090. https://doi.org/10.1002/slct.201701404

[114] Solla-Gullón, J.; Montiel, V.; Aldaz, A.; Clavilier, J. Synthesis and electrochemical decontamination of platinum-palladium nanoparticles prepared by water-in-oil

microemulsion. *Journal of The Electrochemical Society* 150(2) (2003) E104. https://doi.org/10.1149/1.1534600

[115] Hosseini, M. G.; Mahmoodi, R. Preparation method of Ni@Pt/C nanocatalyst affects the performance of direct borohydride-hydrogen peroxide fuel cell: Improved power density and increased catalytic oxidation of borohydride. *Journal of Colloid and Interface Science* 500 (2017) 264-275. https://doi.org/10.1016/j.jcis.2017.04.016

[116] Nikolic, J.; Expósito, E.; Iniesta, J.; González-Garcia, J.; Montiel, V. Theoretical concepts and applications of a rotating disk electrode. *Journal of Chemical Education* 77(9) (2000) 1191. https://doi.org/10.1021/ed077p1191

Document signat digitalment per: Julia Garcia Cardona

Publications and Meetings

Publications in scientific indexed journals

[1] J. Garcia-Cardona, I. Sires, M. Mazzucato, R. Brandiele, E. Brillas, F. Alcaide, C. Durante, P. Cabot. On the viability of chitosan-derived mesoporous carbons as supports for PtCu electrocatalysts in PEMFC. Electrochimica Acta 442 (2023) 141911. https://doi.org/10.1016/j.electacta.2023.141911

[2] Vega, L.; Garcia-Cardona, J.; Viñes, F.; Cabot, P.L.; Neyman, K.M. Nanostructuring determines poisoning: Tailoring CO adsorption on PtCu bimetallic nanoparticles. Mater. Adv. 3 (2022) 5159-4169. https://doi.org/10.1039/D2MA00196A .

[3] J. Garcia-Cardona, F. Alcaide, E. Brillas, I. Sirés, P. L. Cabot. Testing PtCu nanoparticles supported on highly ordered mesoporous carbons CMK3 and CMK8 as catalysts for low-temperature fuel cells. Catalysts 11 (2021) 724 https://doi.org/10.3390/catal11060724 .

[4] Garcia-Cardona, J., Sirés, I., Alcaide, F., Brillas, E., Centellas, F., Cabot, P.L. Electrochemical performance of carbon-supported Pt(Cu) core-shell electrocatalysts for low-temperature fuel cells. International Journal of Hydrogen Energy 45 (2020) 20582-20593 https://doi.org/10.1016/j.ijhydene.2020.02.038

[5] Caballero-Manrique, G., Garcia-Cardona, J., Brillas, E., Jaén J.A., Sánchez J.M., Cabot, P.L. Synthesis and Evaluation of PtNi Electrocatalysts for CO and Methanol Oxidation in Low Temperature Fuel Cells. Catalysts 10 (2020) 563 https://doi.org/10.3390/catal10050563

Presentations in meetings

[1] J. Garcia-Cardona, L. Zhao, I. Sirés, E. Brillas, F. Alcaide, P. L. Cabot. 6^{th} – 8^{th} of July 2022. “Catalizadores de PtCu soportados a partir de redes metal-orgánicas” XLII Reunión del Grupo Especializado de Electroquímica de la RSEQ (42 GERSEQ 2022), Santander (Spain). *POSTER*

[2] J. Garcia-Cardona, I. Sirés, F. Alcaide, E. Brillas, P. L. Cabot. 30^{th} de June – 3^{rd} of July 2020. Reprogramed for 6^{th} – 9^{th} of July 2021. “Supporting Pt(Cu) nanoparticles on

mesoporous carbons for PEMFC". XLI Reunión del Grupo de Electroquímica de la Real Sociedad Española de Química y 1st French-Spanish Atelier/Workshop on Electrochemistry, Paris (France). *ORAL*

[3] J. Garcia-Cardona, I. Sirés, M. Mazzucaro, R. Brandiele, E. Brillas, C. Durante, P. L. Cabot. 3rd – 6th of April 2022. "Carbonos mesoporosos derivados del quitosano como soportes para electrocatalizadores PtCu en PEMFCs" XXV Congreso Virtual de la SIBAE, México (Online). *POSTER*

[4]: J. Garcia-Cardona, I. Sirés, E. Brillas, P. L. Cabot. 7th - 10th of Decembre 2020 "Electrocatalizadores de Pt(Cu) y Pt(Ni) soportados para pilas de combustible tipo PEM". XXIV Congreso de la Sociedad Iberoamericana de Electroquímica, (online). *POSTER*

[5] J. García-Cardona, I. Sirés, F. Alcaide, E. Brillas, P. L. Cabot. 28th – 31st of October 2020. "Sistemas bimetálicos soportados sobre diferentes materiales como catalizadores para PEMFC" V Workshop de la Red E3TECH / I Workshop Iberoamericano a Distancia 'Aplicaciones Medioambientales y Energéticas de la Tecnología Electroquímica' (V E3TECH)", (online). *ORAL*

[6] J. García-Cardona, I. Sirés, F. Alcaide, E. Brillas, P. L. Cabot. 28th – 31st of October 2020. "Electrocatalizadores sintetizados mediante intercambio galvánico para pilas de combustible". V Workshop de la Red E3TECH / I Workshop Iberoamericano a Distancia 'Aplicaciones Medioambientales y Energéticas de la Tecnología Electroquímica' (V E3TECH)", (online). *POSTER*

[7] J. Garcia-Cardona, I. Sirés, F. Alcaide, E. Brillas, F. Centellas, P. L. Cabot. 31st of August – 4th of September 2020. "Ordered mesoporous carbons as supports for bimetallic Pt(Cu) catalysts in PEMFCs". 71st Annual Meeting of the International Society of Electrochemistry, (online). *POSTER*

[8] Garcia-Cardona, J. 9th – 12th of July 2019 "Synthesis and characterization of nanoparticulated supported catalysts for porous electrodes and environmental applications." XL Meeting of Specialized Group of Electrochemistry of the Royal Spanish Society of Chemistry and XX Iberian Meeting of Electrochemistry, Huelva (Spain). *ORAL*

[9]: Garcia-Cardona, J., Sirés, I., Alcaide, F., Brillas, E., Centellas, F., Cabot, P.L. 1st – 3rd of July 2019. "Electrochemical performance of carbon-supported Pt(Cu) core-shell electrocatalysts for low-temperature fuel cells" VII Symposium on Hydrogen, Fuel Cells and Advanced Batteries, HYCELTEC, Barcelona (Spain). *ORAL*

[10] Garcia-Cardona, J., Sirés, I., Alcaide, F., Brillas, E., Centellas, F., Cabot, P.L. 26th - 30th of May 2019. "Nanopartículas de Pt(Cu) soportadas sobre materiales carbonosos como electrocatalizadores para pilas de combustible de baja temperatura" XXXVII Reunión Bienal de la RSEQ, Donostia-San Sebastián (Spain). *POSTER*

[11] Garcia-Cardona, J., Sirés, I., Alcaide, F., Brillas, E., Centellas, F., Cabot, P.L. 14th -15th of May 2019. "Properties and electrochemical performance of supported Pt(Cu) core-shell catalysts for hydrogen oxidation" 3rd Workshop of the Excellence Network on Environmental and Energy Applications of the Electrochemical Technology, Toledo (Spain). *ORAL*

[12] Garcia-Cardona, J., Sirés, I., Alcaide, F., Brillas, E., Centellas, F., Cabot, P.L. 10th -15th of May 2019. "Pt(Cu) core-shell nanoparticles supported on advanced carbonaceous materials as electrocatalysts for low-temperature PEM fuel cells." 25 th Topical Meeting of the International Society of Electrochemistry, Toledo (Spain). *POSTER*

Document signat digitalment per: Julia Garcia Cardona

Document signat digitalment per: Julia Garcia Cardona